Lappeenranta
University of Technology

Kari Myöhänen

MODELLING OF COMBUSTION AND SORBENT REACTIONS IN THREE-DIMENSIONAL FLOW ENVIRONMENT OF A CIRCULATING FLUIDIZED BED FURNACE

Thesis for the degree of Doctor of Science (Technology) to be presented with
due permission for public examination and criticism in the Auditorium 1381
at Lappeenranta University of Technology, Lappeenranta, Finland on the
2nd of December, 2011, at noon.

Acta Universitatis
Lappeenrantaensis 449

Supervisor Professor Timo Hyppänen
Department of Energy Technology
Faculty of Technology
Lappeenranta University of Technology
Finland

Reviewers Professor Reijo Karvinen
Department of Energy and Process Engineering
Faculty of Science and Environmental Engineering
Tampere University of Technology
Finland

Docent Ernst-Ulrich Hartge
Institute of Solids Process Engineering and Particle Technology
Technical University of Hamburg-Harburg
Germany

Opponents Professor Reijo Karvinen
Department of Energy and Process Engineering
Faculty of Science and Environmental Engineering
Tampere University of Technology
Finland

Professor Markus Haider
Institute for Energy Systems and Thermodynamics
Vienna University of Technology
Austria

ISBN 978-952-265-160-0
ISBN 978-952-265- 161-7 (PDF)
ISSN 1456-4491
Lappeenrannan teknillinen yliopisto
Digipaino 2011

Abstract

Kari Myöhänen
Modelling of combustion and sorbent reactions in three-dimensional flow environment of a circulating fluidized bed furnace
Lappeenranta 2011
161 pages
Acta Universitatis Lappeenrantaensis 449
Diss. Lappeenranta University of Technology
ISBN 978-952-265-160-0, ISBN 978-952-265- 161-7 (PDF), ISSN 1456-4491

This thesis presents a three-dimensional, semi-empirical, steady state model for simulating the combustion, gasification, and formation of emissions in circulating fluidized bed (CFB) processes.

In a large-scale CFB furnace, the local feeding of fuel, air, and other input materials, as well as the limited mixing rate of different reactants produce inhomogeneous process conditions. To simulate the real conditions, the furnace should be modelled three-dimensionally or the three-dimensional effects should be taken into account. The only available methods for simulating the large CFB furnaces three-dimensionally are semi-empirical models, which apply a relatively coarse calculation mesh and a combination of fundamental conservation equations, theoretical models and empirical correlations. The number of such models is extremely small.

The main objective of this work was to achieve a model which can be applied to calculating industrial scale CFB boilers and which can simulate all the essential sub-phenomena: fluid dynamics, reactions, the attrition of particles, and heat transfer. The core of the work was to develop the model frame and the required sub-models for determining the combustion and sorbent reactions.

The objective was reached, and the developed model was successfully used for studying various industrial scale CFB boilers combusting different types of fuel. The model for sorbent reactions, which includes the main reactions for calcitic limestones, was applied for studying the new possible phenomena occurring in the oxygen-fired combustion. The presented combustion and sorbent models and principles can be utilized in other model approaches as well, including other empirical and semi-empirical model approaches, and CFD based simulations. The main achievement is the overall model frame which can be utilized for the further development and testing of new sub-models and theories, and for concentrating the knowledge gathered from the experimental work carried out at bench scale, pilot scale and industrial scale apparatus, and from the computational work performed by other modelling methods.

Keywords:
circulating fluidized bed, comprehensive model, steady state, large-scale modelling, 3D, combustion, limestone, sulphur capture
UDC 66.096.5:662.93:536.46:51.001.57

Acknowledgements

This work was carried out in the Department of Energy Technology at Lappeenranta University of Technology, Finland, between 2005 and 2011. The research leading to these results has received funding from the European Community's Seventh Framework Programme (FP7/2007-2013) under grant agreement No. 239188, from the Academy of Finland under grant No. 124368, from the Research Fund for Coal and Steel of the European Community (Contract No. RFCR-CT-2005-00009), from the Finnish Funding Agency for Technology and Innovation (Tekes), and from Foster Wheeler Energia Oy.

I express my deepest gratitude to my supervisor Professor Timo Hyppänen for all the support and encouragement he provided during this work.

I humbly thank my reviewers, Professor Reijo Karvinen and Docent Ernst-Ulrich Hartge, for their valuable comments and suggestions.

The development work in this dissertation has been supported by co-operation between Foster Wheeler Energia Oy, VTT (Technical Research Centre of Finland), and LUT. Many thanks to all my friends and colleagues in these organizations.

Especially I would like to thank Mr. Reijo Kuivalainen and Mr. Timo Eriksson from Foster Wheeler Energia Oy for their sharp and professional comments on different articles and presentations. Mr. Jouni Miettinen and Mr. Ossi Sippu have provided material related to several application studies. Moreover, this dissertation would not have been possible without the kind support of Mr. Arto Hotta and Mr. Ari Kettunen.

I express my gratitude to the whole VTT's CFB team in Jyväskylä for the fruitful co-operation and data exchange and especially to Dr. Antti Tourunen, Dr. Jaakko Saastamoinen, Mr. Toni Pikkarainen, Mr. Timo Leino, and Ms. Heidi Nevalainen.

The discussions with Ms. Sirpa Kallio from VTT have been very instructive for deeper understanding of the problematics of fluid dynamics modelling.

The people at LUT, who have contributed to this work, include Dr. Jouni Ritvanen, Ms. Sirpa Takkinen, Mr. Ari Vepsäläinen, Mr. Vesa Tanskanen, Mr. Markku Nikku, and Mr. Matti Koski.

Finally, I express my heartfelt appreciation to my family for the loving support and motivation during this long project.

Kari Myöhänen
November 2011
Lappeenranta, Finland

Contents

Abstract

Acknowledgements

Contents

List of publications supporting present monograph **9**

Nomenclature **11**

1 Introduction **15**

2 State of the art **17**
2.1 Overview of circulating fluidized bed technology for combustion 17
2.2 Modelling approaches for fluidized bed systems 23
2.2.1 Classification of multiphase modelling approaches 23
2.2.2 Particle scale modelling 26
2.2.3 Lagrangian-Eulerian modelling 27
2.2.4 Eulerian-Eulerian modelling 29
2.2.5 Empirical and semi-empirical models 33
2.2.6 Combinations 35
2.3 Comprehensive 3D CFB models 36
2.3.1 Fluid dynamics 37
2.3.2 Comminution 40
2.3.3 Combustion reactions 41
2.3.4 Sorbent reactions 43
2.3.5 Heat transfer 45
2.3.6 Comparison of 3D CFB model features 47

3 Model frame **49**
3.1 Model features 49
3.2 Model structure and flow chart of the main solver 51
3.3 Particle size fractions and comminution of solids 53
3.4 Modelling of solid concentration and solid flow fields 54
3.5 Modelling of pressure and gas flow field 59
3.6 Combustion model 60
3.7 Sorbent model 60
3.8 Solution of inert materials 60
3.9 Solving of gas species 61
3.10 Energy equation 62
3.11 NOx-model 64

4 Combustion model **65**
4.1 Composition of fuel 65
4.2 Combustion model 73
4.3 Continuity equations for fuel 76
4.4 Evaporation and devolatilization rate 78
4.5 Composition of devolatilized gases 80
4.6 Combustion of char 84
4.7 Gasification of char 87
4.8 Homogeneous combustion reactions 89
4.9 Shift conversion 92
4.10 Heat from combustion reactions 93

5 Sorbent model **97**
5.1 Concentration and velocity fields of sorbent fractions 98
5.2 Continuity equations for sorbent species 100
5.3 Calcination and carbonation 102
5.4 Sulphation and direct sulphation 104
5.5 Desulphation 106
5.6 Enthalpy change in sorbent reactions 108
5.7 Sources of sulphur dioxide emissions 108

6 Applications **109**
6.1 Validation study of a 15 MWe CFB combusting recycled wood 109
6.2 Conceptual study of an oxy-fuel CFB boiler 117
6.3 Modelling of a Flexi-Burn® demonstration plant 122

7 Discussion **137**

8 Conclusions **139**

References **141**

List of publications supporting present monograph

The present monograph contains both unpublished material and material, which has been published previously by the author elsewhere. A large part of the present monograph is related to the following papers. The rights have been granted by publishers to include the material in dissertation.

Scientific journal articles

I. Myöhänen, K., Hyppänen, T., Pikkarainen, T., Eriksson, T., and Hotta, A. (2009). Near zero CO2 emissions in coal firing with oxy-fuel CFB boiler. *Chemical Engineering & Technology*, 32(3), pp. 355-363. John Wiley & Sons.

II. Myöhänen, K., and Hyppänen, T. (2011). A three-dimensional model frame for modelling combustion and gasification in circulating fluidized bed furnaces. *International Journal of Chemical Reactor Engineering*, 9, Article A25, 55 p. Berkeley Electronic Press.

Refereed conference articles

III. Myöhänen, K., Hyppänen, T., Miettinen, J., and Parkkonen, R. (2003). Three-dimensional modeling and model validation of circulating fluidized bed combustion. In: Pisupati, S., ed., *Proceedings of the 17th International Conference on Fluidized Bed Combustion*. New York: ASME.

IV. Myöhänen, K., Hyppänen, T., and Loschkin, M. (2005). Converting measurement data to process knowledge by using three-dimensional CFB furnace model. In: Cen, K., ed., *Proceedings of the 8th International Conference on Circulating Fluidized Beds*, pp. 306-312. Beijing: International Academic Publishers.

V. Myöhänen, K., Hyppänen, T., and Vepsäläinen, A. (2006). Modelling of circulating fluidized bed combustion with a semi-empirical three-dimensional model. In: Juuso, E., ed., *SIMS 2006: Proceedings of the 47th Conference on Simulation and Modelling*, pp. 194-199. Helsinki: Finnish Society of Automation.

VI. Myöhänen, K., Tanskanen, V., Hyppänen, T., Kyrki-Rajamäki, R., Nevalainen, T. (2006). CFD modelling of fluidized bed systems. In: Juuso, E., ed., *SIMS 2006: Proceedings of the 47th Conference on Simulation and Modelling*, pp. 88-93. Helsinki: Finnish Society of Automation.

VII. Myöhänen, K., Ritvanen, J., Eriksson, T., Kuivalainen, R., and Hyppänen, T. (2011). Three-dimensional modelling of a 300 MWe Flexi-Burn CFB for multifuel combustion in oxygen-fired and air-fired modes. In: *2nd Oxyfuel Combustion Conference*. 12-16 September 2011, Queensland, Australia. IEA Greenhouse Gas R&D Programme.

Author's contribution and relation to present thesis

In all of the above papers, Kari Myöhänen has been the corresponding author and responsible of the work related to development and application of the three-dimensional model code, which is the subject of this thesis.

Publication I includes the application studies of air-fired and oxygen-fired combustion, which are presented in Chapter 6.2. Moreover, it includes some of the material, which is presented in the state of the art review in Chapter 2.1.

Publication II constitutes most of the material, which are presented in the literature review of modelling approaches (Chapter 2.2) and the description of the model frame (Chapter 3). It also contains overall description of the combustion and sorbent models presented in Chapters 4 and 5.

Material from Publications III – V has been used in Chapters 3 and 4.

The findings of the other modelling fields in Chapter 2.2 are partly based on Publication VI.

Publication IV includes the validation study presented in Chapter 6.1.

Publication VII includes the validation study presented in Chapter 6.3.

Nomenclature

In the present work, variables and constants are denoted using *slanted style*, vectors are denoted using **bold regular style**, and abbreviations are denoted using regular style. The chemical formulas are denoted using regular style (e.g. CO_2).

Latin alphabet

A	area	m^2
A_m	specific surface area	m^2/kg
a,b,c,d	model parameter (variable unit)	
C	molar concentration (e.g. C_{CO})	mol/m^3
c_p	specific heat capacity at constant pressure	J/(kgK)
D	diffusion / dispersion coefficient	m^2/s
d_p	particle size	m
E	activation energy	J/mol
f_x	force per unit mass in x-direction	m/s^2
f_0	target solid concentration	kg/m^3
g	acceleration due to gravity	m/s^2
H	total height	m
H_0	formation enthalpy	J/mol
h	height	m
k	rate constant	1/s
L	latent heat	J/kg
M	molecular weight	kg/mol
m	mass	kg
P	pressure	Pa
P_{fs}	flow potential of solids	kg/(ms)
p	partial pressure	atm
q	heat flow	W
q_m	mass flow	kg/s
R	universal gas constant (8.3143)	J/(mol K)
R'''	reaction source term	kg/m^3s
r'''	reaction source term in molar units	mol/m^3s
T	temperature	K
t	time	s
u,v,w	velocity	m/s
w	weight fraction, mass ratio	-
V	volume	m^3
X	molar fraction	-
x	x-coordinate (width)	m
y	y-coordinate (depth)	m
z	z-coordinate (height)	m

Greek alphabet

α	heat transfer coefficient	$W/(m^2K)$
β	drag coefficient	$kg/(m^3s)$
β_m	macroscopic drag coefficient	1/s
γ	molar share	-
γ_{char}	molar share $CO/(CO + CO_2)$ for char burning	-
γ_{vol}	molar share $CO/(CO + CO_2)$ for devolatilization	-
ε	volume fraction	-
η_{RC}	share of recirculated fly ash	-
θ_s	granular temperature	m^2/s^2
μ	dynamic viscosity	kg/(ms)
ρ	density	kg/m^3
τ	stress	N/m^2
ϕ'''	source term	$kg/(m^3s)$
φ'''	volumetric heat source	W/m^3

Subscripts

btm	bottom zone
B	bottom ash
boud	Boudouard reaction
C	comminution
c	core or main cell
carb	carbonation
calc	calcination
char	char
daf	dry, ash-free
desu	desulphation
di	dilute zone
dirs	direct sulphation
E	elutriation to fly ash
eq	equilibrium
F	feed
f	additional solid phase
fuel	fuel
g	gas
i	particle size fraction
ib	back flow from internal circulation
ic	internal circulation
in	inside
j	particle size fraction

kin	kinetic
l	liquid
max	maximum
meas	measured
out	outside
p	particle
pt	product
r	species; material
reac	reaction
ref	reference
rt	reactant
RC	recirculated fly ash
s	solid
shift	shift conversion
sorb	sorbent
sulf	sulphation
top	top zone
tot	total
tr	transient zone
vol	volatiles or devolatilization
w	wall
wat	water or evaporation
watg	water-gas reaction
wl	wall layer

Abbreviations

0D	zero-dimensional (lumped)
1D	one-dimensional
1.5D	one-and-half-dimensional core-annulus approach
2D	two-dimensional
3D	three-dimensional
ASU	air separation unit
CCDM	combined continuum and discrete model
CCS	carbon capture and storage
CFB	circulating fluidized bed
CFD	computational fluid dynamics
CPU	compression and purification unit
CUT	Chalmers University of Technology
DEM	discrete element method
DNS	direct numerical simulation
DPM	discrete particle model

DSMC	direct simulation Monte Carlo
EMMS	energy minimization multiscale
KTGF	kinetic theory for granular flow
LBM	lattice Boltzmann method
LES	large eddy simulation
MP-PIC	multiphase particle-in-cell
MWe	power capacity, megawatts of electricity
MWt	thermal capacity, megawatts of thermal power
OTU	once-through-unit
TFM	two-fluid method
TUHH	Technical University of Hamburg-Harburg

1 Introduction

In a circulating fluidized bed furnace, the combustion occurs in a granular gas-solid suspension which is fluidized by gas at the velocity higher than the terminal velocity of solids. This creates the elutriation of solids which are then separated from gas at the top of the furnace and returned back to the base of the furnace, thus creating a circulating flow of solids (Figure 1.1).

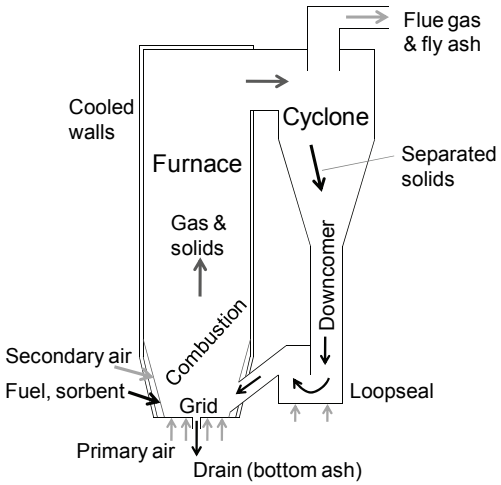

Figure 1.1. The principle of a circulating fluidized bed combustor.

The amount of energy produced by the circulating fluidized bed (CFB) technology has been constantly growing since the first CFB boilers in late 1970's. The driving forces have been the inherent features of the CFB combustion: fuel flexibility, good combustion efficiency, the ability to capture sulphur emissions in the furnace by sorbents, and smaller nitrogen oxide emissions due to low combustion temperatures.

Recently, the unit capacities have increased up to 300 – 500 MWe, and plans exist for a further increase up to 600 – 800 MWe. New CFB combustion processes based on oxygen-fired combustion are being developed, allowing carbon sequestration and thus providing a more sustainable method for the energy production from fossil fuels. The ability to use biomasses, waste derived fuels, and other low-grade fuels will continue as one of the major benefits of the CFB combustion technology. In the future, the selection of fuels is likely to increase and include new renewable energy sources, such as algae.

The development of larger CFB units and new CFB processes and the wide fuel range require modelling tools which can simulate the complex process phenomena and model full-scale units. This work presents methods for the three-dimensional modelling of combustion and sorbent reactions in a furnace of a CFB boiler. The main objective was to achieve a model which combines fundamental conservation equations with empirical correlations, thus enabling the modelling of industrial scale CFB furnaces.

Chapter 2 presents an overview of the CFB combustion technology and the current modelling approaches of the CFB combustion process. These determine the background and motivation of this work. The modelling approaches of the CFB process can be categorized into fundamentals-oriented and practice-oriented models. Although the recent development of the fundamentals-oriented models has been fast and the different model approaches are starting to near each other, the comprehensive modelling of a large-scale CFB process is still a challenge, which requires a simplified, practice-oriented model approach. Despite the clear need for comprehensive, three-dimensional CFB models, only a few models capable of simulating industrial scale CFB furnaces have been published. Moreover, except for the model presented in this work, none of these includes the ability to model sorbent reactions.

Chapter 3 describes the model frame which has been developed in this work. The descriptions of the model development related to the modelling of flow and heat transfer are included in this chapter, as they have an impact on the main subject of the study as well. Chapters 4 and 5 present the core of this work; the developed model approaches for combustion and sorbent reactions in detail. Chapter 6 presents studies, in which the model has been applied to study full-scale CFB boilers, including comparisons to the measurements. The final chapters include discussion, future plans, and the conclusions of the work.

The following is a summary of the most significant contributions of this work in the order in which they appear in the thesis:

- The description of a three-dimensional model frame which can be utilized for the modelling of industrial scale CFB furnaces and for the further development of sub-models describing the furnace process.
- Studies of char and volatile compositions, and a correlation model for determining them approximately for various solid fuel types used in CFB combustion.
- A combustion model for solid fuels which has been implemented to the three-dimensional model frame.
- A sorbent model for calcitic limestone which includes all the essential sorbent reactions occurring in circulating fluidized bed combustion and which has been implemented to the three-dimensional model frame.
- Studies of combustion and sorbent reactions illustrating various sub-phenomena inside a large-scale CFB furnace.
- The application of the developed model approaches for studying real, large-scale CFB units with air-fired and oxygen-fired combustion.

The presented combustion and sorbent models can be utilized in other model approaches as well, including the empirical and semi-empirical model approaches and CFD based simulations.

2 State of the art

This chapter provides a literature study of the state-of-the-art relating to present work. Chapter 2.1 provides a short overview of the circulating fluidized bed technology and its possibilities and challenges, which determine the motivation and background of this work. Chapter 2.2 reviews the model approaches for fluidized bed systems at different scales to relate the presented model to other modelling field, and to justify the need for semi-empirical modelling approach. Chapter 2.3 presents the currently existing, comprehensive three-dimensional models for full-scale CFB combustors. This chapter is divided to subchapters describing the main modelling fields: fluid dynamics, comminution of solids, combustion reactions, sorbent reactions, and heat transfer.

2.1 Overview of circulating fluidized bed technology for combustion

The circulating fluidized bed (CFB) technology for combustion was developed in 1970's and 1980's by several engineering companies. The background of the CFB development for combustion was different in different companies and in different countries, but in all cases, the development can be traced back to one or several of the following technological predecessors:

- development of first fluidized bed application by Winkler in 1920's for gasification of coal (Winkler, 1922; Basu et al., 2009),
- development of fluidized catalytic cracking of crude oil in 1940's (Squires, 1986; Lim et al., 1995),
- development of calciners for alumina industry in 1950's (Barner et al., 1985; Reh, 1986; Reh, 2003),
- development of bubbling bed combustion in 1960's and 1970's (Roeck, 1982; Pai and Engström, 1999; Koornneef et al., 2007; Yue et al., 2009)

A typical layout of a CFB boiler is presented in Figure 2.1. The bed of solid material is fluidized by combustion air, which enters the furnace through a grid at the bottom of the furnace. The bed consists typically of unburnt fuel, fuel ash, make-up sand and sorbent. The fuel and the other solid feed points are located at the bottom part of the furnace. The secondary air is injected above the fuel feed points at various locations and heights in order to accomplish staged combustion. The furnace temperature is below the agglomeration temperature of solids, typically in the range of 750 – 950 °C, thus much lower than in pulverized coal combustion or grate combustion.

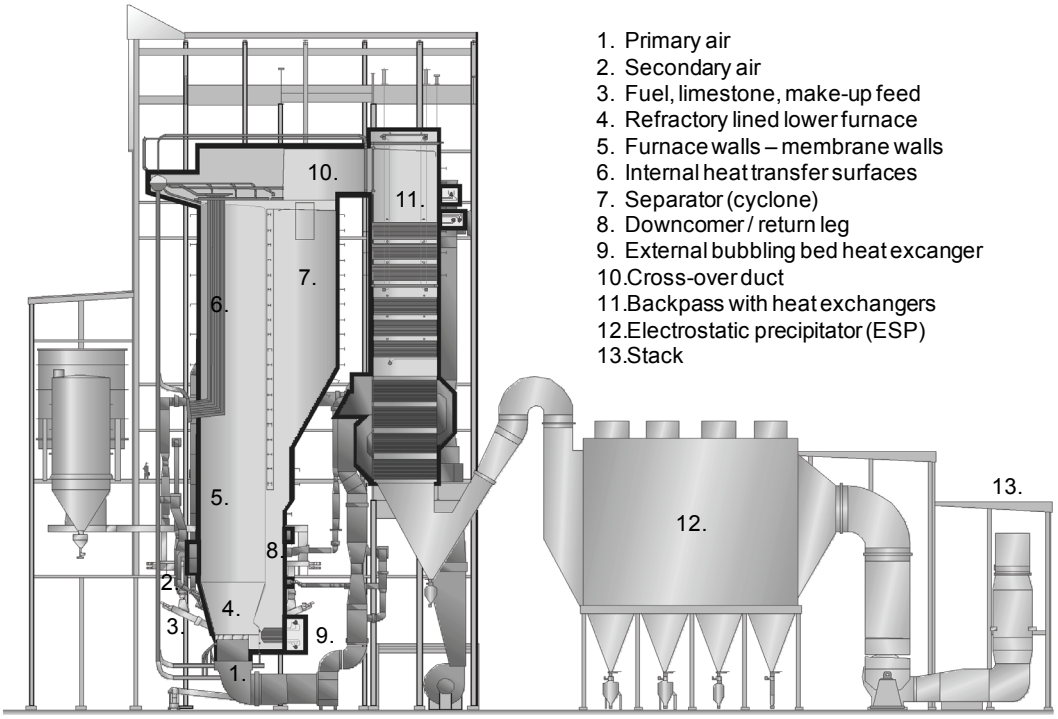

Figure 2.1. Layout of a CFB boiler (courtesy of Foster Wheeler Energia Oy).

The heat from combustion is recovered to water and steam by various heat transfer surfaces, which can be located in the furnace, separator, return leg and backpass. The furnace is constructed of membrane wall tubes, inside which a cooling fluid, typically saturated water, circulates. The bottom section of the furnace is refractory lined in order to protect the wall tubes from erosion and corrosion. At the upper section of the furnace, the solids and gas travel upwards while releasing heat to the heat transfer walls. Additional heat transfer surfaces can be located inside the furnace. These can be e.g. superheater panels extending across the furnace, wingwall panels located at the walls of the furnace (item 6 in Figure 2.1) and superheaters hanging from the roof.

At the top of the furnace, the gas-solid-suspension enters the separator section, in which the solids are separated and returned back to circulation while gas passes through to backpass section, filter system and finally to stack. A bubbling bed heat exchanger unit can be located in the return leg system for increased heat recovery in the furnace section. The heat exchangers in the backpass typically include superheaters, reheaters, air preheaters, and feed water preheaters (economizers).

In a typical arrangement (Figure 2.1), the fluid in furnace walls is saturated water. Steam is separated in a drum and then superheated in separate heat transfer sections, which are located in backpass, furnace and return leg. The resulting superheated steam is used to generate electricity in a steam turbine. Various other arrangements are

possible, e.g. utilizing steam as process heat, operating in supercritical steam conditions, and operating below saturation temperature, i.e. without evaporation (hot water boiler).

Different manufacturers have different solutions regarding, e.g. the shape of the furnace, grid design, location of the fuel and air inlets and the separator and return leg designs. Figure 2.1 shows a design concept, in which the separator is integrated to the furnace. Other alternative designs include for example:

- an internally recirculated CFB, in which the primary separator has been replaced by U-beams (Kavidass et al., 2000),
- a design with the cyclone placed inside the furnace (Karppanen, 2000),
- a pant-leg design, in which the bottom of the furnace is divided to two sections (Xianbin and Minhua, 2009),
- a horizontal CFB, in which the furnace consists of subsequent riser, downcomer and riser sections before the primary cyclone (Li et al., 2009).

One of the main advantages of fluidized bed combustion is the fuel flexibility. Due to presence of hot solids, even low-grade fuels can be combusted at high combustion efficiency. During the history of CFB combustion, all types of coals, coal wastes, different biomasses, waste material from industry and consumers, and a wide variety of other fuels have been used for fuel (Anthony, 1995; Koornneef et al., 2007).

Figure 2.2 presents the applicability of different fuel types for fluidized bed combustion. In this chart, the challenges increase when moving towards right. The major encountered challenges are the fouling and corrosion of heat transfer surfaces, agglomeration of bed, feeding problems, and problems to remove incombustible coarse material from furnace (Hiltunen et al., 2008; Barisic et al., 2009).

Each fuel type has unique chararacteristics, which affect the feeding and combustion properties, and formation of emissions. Most of the energy produced by CFB boilers is originating from burning of fossil fuels, peat, biomasses, and petroleum coke. Only a minor proportion is originating from burning of different waste materials and other fuels (Koornneef et al., 2007). The main fuel types are presented shortly below.

The classification of different coal types varies between different countries. In general, as the geological age of a coal increases, the amount of volatiles decreases and the heat value increases. In a standard ASTM D388 (1992), the coal types are divided to anthracitic, bituminous, subbituminous, and lignitic coals based on amount of volatiles and the heat value of mineral matter free coal. Each main type is further divided to subtypes. Peat is a precursor of coal. Depending on political decisions in different countries, it can be regarded as fossil fuel or slowly regenerating biomass (Rowlands, 2005). Wood and other biomasses are non-fossil fuels and have a higher volatile content and a lower heat value than the fossil fuels. The exact composition of the different biomasses is highly diversified (Vassilev et al., 2010). A petroleum coke is carbonous solid derived from oil refinery industry.

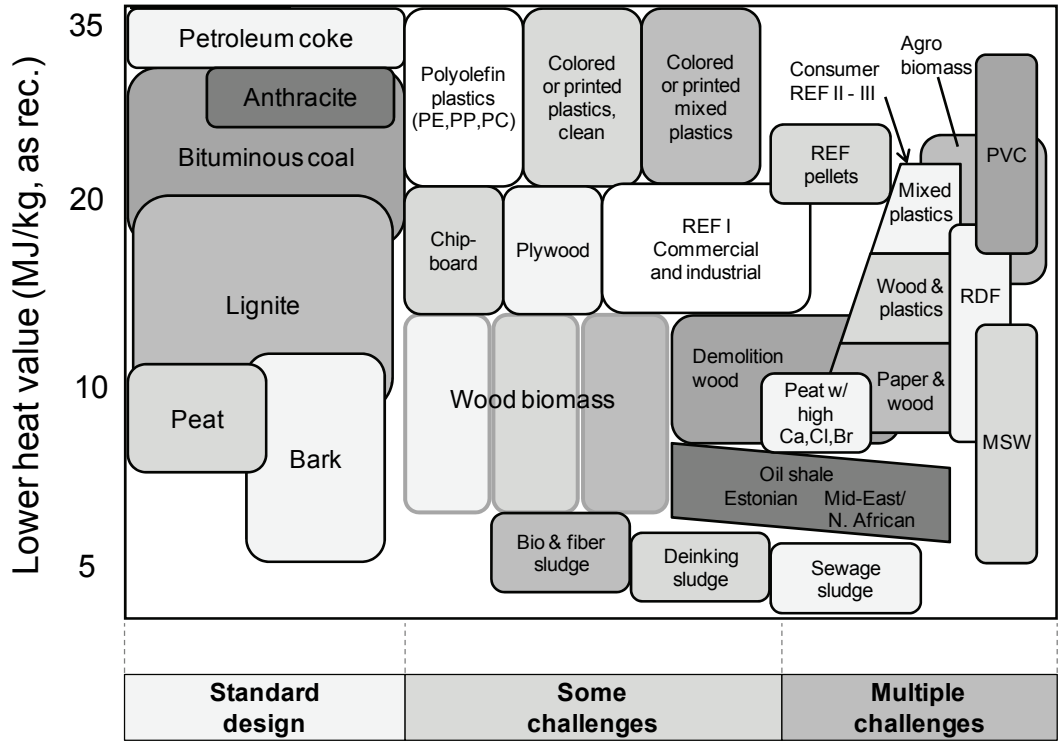

Figure 2.2. Applicability of fuel types for fluidized bed combustion (modified by author from original material received from Foster Wheeler Energia Oy, cf. Makkonen (1999, p. 109)).

Table 2.1 presents main boiler data of some CFB boilers commissioned during the history of CFB combustion. The table presents boiler units, which have been often referred to in literature, and which can be regarded as major milestones during the history of CFB development or which have otherwise contributed to the knowledge development.

During the last three decades, there has been an increase in the use of large CFB units for energy production. The maximum boiler unit sizes have increased up to range 300...500 MWe. At the same time, the steam parameters have increased up to operation at supercritical steam parameters (Patel, 2009; Jäntti and Parkkonen, 2009). The current trend is to further increase the unit sizes so that the CFB boilers will be competing with pulverized coal (PC) boilers in the utility scale, 600 – 800 MWe (Utt et al., 2009; Hotta et al., 2010).

Table 2.1: Examples of CFB units.

Plant, Country	Manuf.	Year	Unit capacity		Main steam data		Main fuels
			MWe	MWth	Press. (bar,abs)	Temp. (°C)	
Pihlava, Finland	FW	1979	5	15	84	520	Peat, wood residue
Kauttua, Finland	FW	1981	20	65	83	500	Peat, bituminous coal
Uvalde, TX, USA	BS	1982	-	15	168	352	Coals, petroleum coke
Lünen, Germany	LL	1982	9	84	65	480	Coal washery residues
Duisburg, Germany	LL	1985	96	208	145	535	Coal
Tri-State, Nucla, USA	FW	1987	110	294	105	541	Coal
Kajaani, Finland	FW	1989	95	240	136	535	Peat, coal, wood residue, sludge
Emile Huchet, Carling, France	AL	1990	125	285	127	542	Coal, slurry
Ebensburg, PA, USA	BW	1991	55	n.a.	106	512	Waste coal
Nova Scotia, Canada	FW	1993	180	409	128	540	Coal
Provence/Gardanne, France	AL	1996	250	557	169	567	Subbituminous coal
SIU, Carbondale, IL, USA	BW	1997	n.a.	35	44	399	Bituminous coal
NPS, Tha Toom, Thailand	FW	1998	150	370	161	542	Anthracite, bit.coal, rice husk, bark
Turow, Poland	FW	1998	235	520	132	540	Lignite
Alholmen, Finland	MP	2001	240	550	165	545	Bark, peat, biomass
Jacksonville, FL, USA	FW	2001	300	689	182	540	Petroleum coke, bituminous coal
EC Tychy, Poland	BW	2002	90	250	120	540	Bituminous coal, biomass, sludge
Seward, PA, USA	AL	2004	293	644	175	541	Waste coal, bituminous
Baima, China	AL	2006	300	708	175	540	Anthracite
Łagisza, Poland	FW	2009	460	966	283	563	Bituminous coal

Manufacturers: FW = Foster Wheeler, LL = Lurgi Lentjes, AL = Alstom, MP = Metso Power (Kvaerner), BW = Babcock&Wilcox. BS = Battelle/Struthers. See Koornneef et al. (2007, p. 33) for overview of the joint ventures, takeovers and mergers in CFB manufacturing industry.
References: Roeck (1982), Reh (1986), Boyd and Friedman (1991), Anthony (1995), Sapy (1998), Kavidass et al. (2000), Belin et al. (2001), EPRI (2002), Goidich and Lundqvist (2002), Dutta and Basu (2003), Marchetti et al. (2003), Morin (2003), Lemasle and Sculy-Logotheti (2004), Kokko and Nylund (2005), Basu (2006, p. 274), Peltier (2006), Salamov (2007), Hotta (2009).

In an industrial scale unit, the cross-section of a furnace can be about 30 x 10 m^2 and the height close to 50 m. In a large furnace, the lateral mixing of solids and gas is slower than vertical convection and combustion reactions (Hartge et al., 1999). This results in uneven distribution of the different gaseous and solid species (e.g. oxygen and fuel) and spatially non-uniform combustion process, which is observed in measurements (Werther, 2005). The design of larger CFB units requires modelling tools, which can be used to study the three-dimensional mixing of different reactants and the resulting reactions, and to support the design of furnace layout for maximal combustion efficiency and minimal emissions.

Naturally, the CFB units will always be applied to burning the different low grade or challenging fuel types, which cannot be efficiently combusted by other technologies. The capacities of these units are usually less than 100 MWe. With these applications, the challenges and demands for valid computational models are as high as with large

size units, due to difficulties in characterizing the fuels and due to needs to minimize the operational problems and emissions, and to maximize the performance (Jäntti et al., 2005)

An emerging technology is to apply CFB technology for oxy-fuel combustion thus enabling carbon capture and storage (Buhre et al., 2005; Czakiert et al., 2006; Zhao et al., 2009). In oxy-fuel combustion, the fuel burns in a mixture of oxygen and recirculated flue gas. This generates CO_2 rich flue gas, from which CO_2 can be separated and compressed (Figure 2.3). In oxy-fuel CFB, the combustion takes place in gas with high proportion of CO_2 and H_2O but very small proportion of N_2. The oxygen content can be similar as in air-fired systems or it can be higher, thus resulting in higher adiabatic combustion temperature. One currently studied alternative is a flexible operation of a CFB unit, which allows using either air-combustion or oxygen-combustion (Myöhänen et al., 2009). The operating mode can be decided depending on the economical conditions and the availability of CO_2 storage, for example. The oxygen-fired combustion sets new demands on the modelling tools as the changing gas atmosphere affects the reactions and the heat transfer.

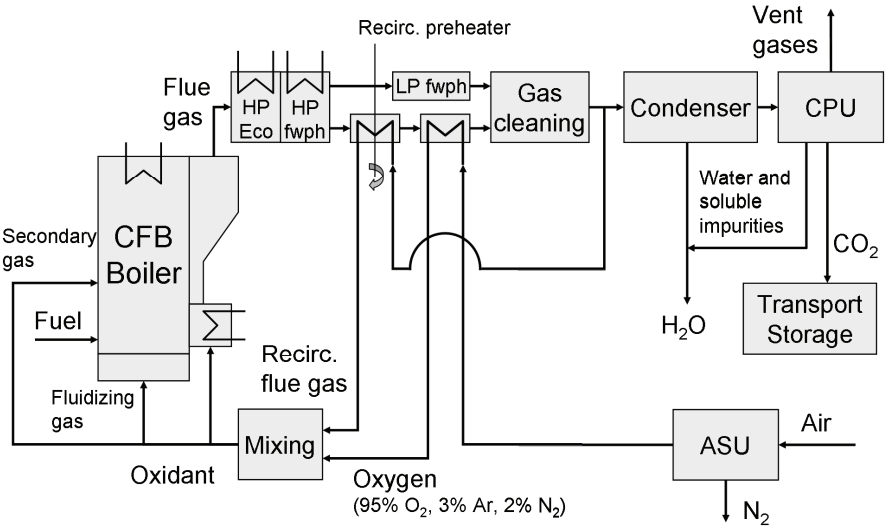

Figure 2.3. Process flow scheme of an oxy-fuel CFB (Myöhänen et al., 2009).

Yet another developing fuel conversion technology utilizing circulating fluidized bed is the chemical looping combustion (CLC). In a CLC process, the oxygen is transferred from combustion air to gaseous fuel by means of an oxygen carrier (Lyngfelt et al., 2001). The oxygen carrier is typically a metal oxide, such as Fe_2O_3 or NiO, but calcium sulphate has been suggested as well (Deng et al., 2008). In air reactor, the oxygen carrier is oxidized by air and then transported to fuel reactor, in which it is reduced in the presence of gaseous fuel C_xH_y (Figure 2.4). This results to a nitrogen free flue gas, from which the CO_2 can be captured. The heat is produced in the air reactor and recovered similar to conventional CFB boilers.

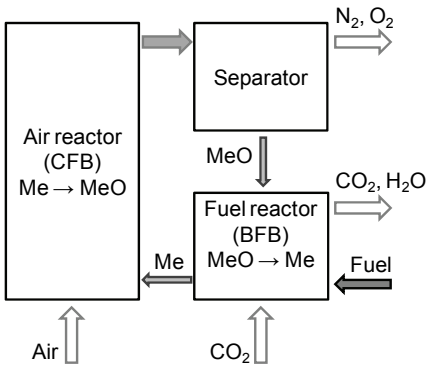

Figure 2.4. Principle of CLC combustion.

The development of the CFB combustion technology requires valid modelling tools, which can be used to study novel designs and the effects of scale-up, to optimize the process in terms of efficiency, availability and emissions, and to carry out trouble-shooting and risk assessment studies. The following chapter describes the modelling approaches which have been applied for fluidized bed systems.

2.2 Modelling approaches for fluidized bed systems

2.2.1 Classification of multiphase modelling approaches

For a transient single phase flow (e.g. gas flow), the basic equations of motion are the unsteady Navier-Stokes equations, first developed by Navier in 1822. This set of continuum equations, derived for the conservation of mass, momentum and energy, are accepted as the governing equations for the flow of a Newtonian fluid (Tannehill et al., 1997). For example, the momentum equation in direction x of Cartesian coordinate system is written as

$$\frac{\partial \rho u}{\partial t} + \frac{\partial}{\partial x}(\rho u^2 + P - \tau_{xx}) + \frac{\partial}{\partial y}(\rho uv - \tau_{xy}) + \frac{\partial}{\partial z}(\rho uw - \tau_{xz}) = \rho f_x \tag{2.1}$$

where the components of the viscous stress tensor τ are given by

$$\tau_{xx} = \frac{2}{3}\mu\left(2\frac{\partial u}{\partial x} - \frac{\partial v}{\partial y} - \frac{\partial w}{\partial z}\right) \tag{2.2}$$

$$\tau_{xy} = \mu\left(\frac{\partial u}{\partial y} + \frac{\partial v}{\partial x}\right) \tag{2.3}$$

$$\tau_{xz} = \mu\left(\frac{\partial w}{\partial x} + \frac{\partial u}{\partial z}\right) \tag{2.4}$$

Applying the full Navier-Stokes equations to solve a flow field is called direct numerical simulation (DNS). Due to computation costs related to solving all the relevant length and time scales starting from the smallest turbulent eddies, the DNS method is viable only for relatively simple flows at low Reynolds number. The computation cost can be reduced by large-eddy simulation (LES), in which only the large scale turbulent eddies are computed directly and the small-scale turbulence is modelled by averaged equations. However, this method is still too demanding for industrial case studies, as the dimension of the large scale eddies is in the order of millimetres.

For practical calculations, most of the industrial scale modelling of turbulent flows is being carried out by applying Reynolds average (time averaged) Navier-Stokes (RANS) equations. Time averaging the equations of motion generates new terms associated with the turbulent motion. These new terms must be related to the mean flow variables through turbulence models or closure models, which are needed to close the system of equations. Thus, the RANS models have not been derived from the first principles and assumptions and approximations have been done to achieve the solvable equations.

Many turbulence models have been derived. The mostly used are the eddy-viscosity model (k-ε model) with many modifications and the Reynolds stress model. More profound descriptions of the different modelling approaches for one phase flow are found in textbooks (Tannehill et al., 1997; Ferziger and Peric, 2002).

In a fluidized bed process, the solids are interpreted as additional phase, which can be handled as discrete particles in Lagrangian frame, or as a continuous phase in Eulerian frame. Depending on the point of view, the flow can be called as a "two-phase flow", in which the solids are forming the second phase or a "multiphase flow", in which the different separate solid materials are forming several additional phases.

When studying a fluidized bed, different space and time scales can be noticed in terms of modelling of fluid dynamics and mixing of solids and gas. Literature applies terms micro-, meso- and macro-scale to distinguish the different scales, although the usage of the terms has not been fully established and the boundaries between the scales have not been exactly specified. The following descriptions are generally used in literature (Hartge et al., 1999; Reh, 2003):

- Micro-scale: scale ranging from molecular level to particle level.
- Meso-scale: scale related to forming of clusters and streamers and other small-scale flow structures; scale between microscale and macroscale.
- Macro-scale: large scale flow and mixing

Figure 2.5 presents a scale-based classification of the most popular model approaches used for fluidized bed systems.

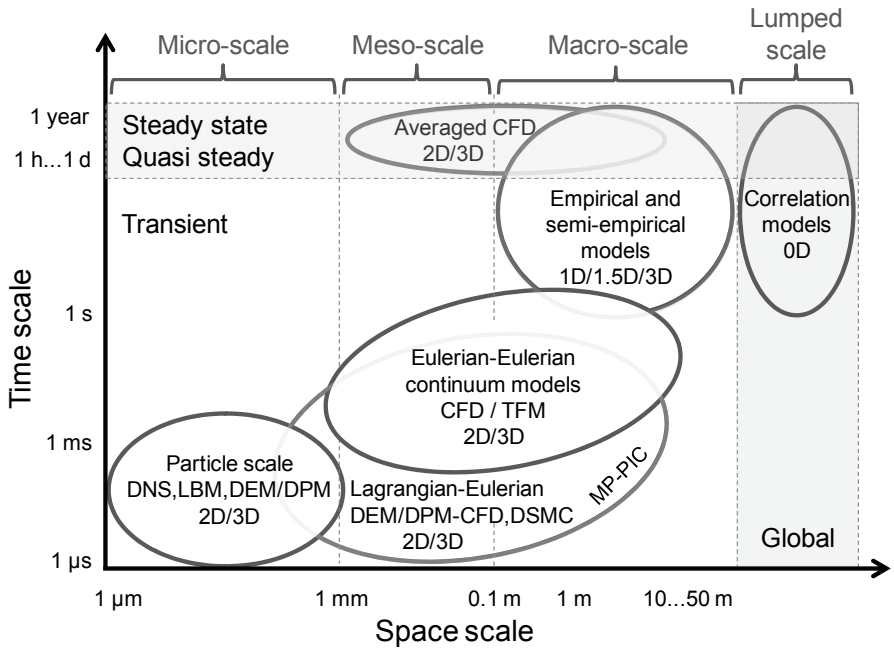

Figure 2.5. Scale based classification of multiphase model approaches for fluidized beds.

The purpose of Figure 2.5 is to show roughly the different scales for which the different models are applied and to relate the presented semi-empirical steady state 3D model to other model approaches. The ranges of space and time scales cannot be exact, but the given values provide some idea of the vast range of different scales, which are encountered when modelling the fluidized bed systems. The literature has only a few estimations of the actual numerical values for separating the different scales. The values in Figure 2.5 are in agreement with the data in literature (Lim et al., 1995; Lefebvre et al., 2004; Zhu et al., 2007, p. 3390), but the boundaries should be regarded as indicative only.

The terms have not been fully established in literature. For example, Tsuji (2007) states that the macro-scale term would be limited to combustor scale only: the macro-scale flow field would be solved only one-dimensionally or globally and not divided to small cells. This dissertation applies the definition used by Hartge et al. (1999) and Reh (2003) that the term macro-scale is used for large-scale three-dimensional flow and mixing, as this provides a clearer definition between the different approaches. A combustor scale or a zero-dimensional model can be termed as lumped scale.

The top region of Figure 2.5 includes area for steady state modelling. Due to different long-term phenomena (e.g. segregation, fouling, rusting), the real physical processes are

never actually steady state, if the observation time is long enough (e.g. years or decades). Thus, the steady state is a virtual state, which can be reached only in models, in which the number of affecting variables is limited. The measurements are always quasi-steady values. The averaged values of transient calculations are often quasi-steady values because the calculation capacity limits the averaging times.

The classification could be based separately on particle motion and fluid motion as presented by Tsuji (2007). For example, in a typical Lagrangian-Eulerian model, the particle motion is solved in micro-scale as trajectories of individual particles and the fluid motion is solved in meso-scale or macro-scale using local averaged equations for fluid flow. In Figure 2.5, the ranges of different model approaches have been set to extend across the different scales in terms of both particle and fluid motion (cf. Zhu et al., 2007, p. 3390). The following chapters describe shortly the different model groups and model approaches, which have been used to model fluidized bed systems.

2.2.2 Particle scale modelling

The "particle scale" group includes the models, which have been targeted to study the flow dynamics at particle level, i.e. the micro-scale movement of individual particles caused by momentum exchange between the particle and the surrounding fluid and other particles. The separation to "Lagrangian-Eulerian" group is that in the latter, the fluid has been modelled by using volume-averaged equations. In both of these groups, the particles are treated as discrete elements; hence, the terms DEM (discrete element method) and DPM (discrete particle model) have been applied, although the terminology is diverse, as discussed in Chapter 2.2.3.

The most rigorous method is the direct numerical simulation (DNS), in which the flow of fluid is solved based on the full Navier-Stokes equations and particles are treated as moving boundaries (Hu, 1996). Resolving all the temporal and spatial scales associated with the size of the solid particles and turbulent eddies of fluid motion is numerically very demanding and DNS is restricted to low Reynolds numbers and small number of particles and mainly applied for particle-liquid systems. The handling of particle collisions is difficult, thus in the DNS models, the inter-particle effects are often neglected (Boivin et al., 1998), prevented by artificial repulsive force (Glowinski et al., 1999; Pan et al., 2002), or prevented by using fixed particle assemblies (Tenneti et al., 2010). Applications of actual collision models in DNS calculations are rare. A soft-sphere collision model was applied by Tenneti et al. (2010) in a study of particle velocity fluctuations in a gas flow with moderate Reynolds number (Re = 20). Chapter 2.2.3 presents the different collision models in more details.

In lattice Boltzmann method (LBM), the gas flow is approximated by treating the gas phase as discrete elements, which are much larger than the size of single molecules but still smaller than the size of solid particles. These gas ”particles” obey the Boltzmann equations and transport the momentum in a lattice. Similar to DNS, the handling of collisions is challenging and it is usually avoided in studies applying LBM. The method

has been used to improve the formulations of gas-solid drag force (Hill et al., 2001; Deen et al., 2006), while the particle-particle interactions have been modelled by separate, larger scale modelling. Compared with DNS, the LBM has been applied for flows with higher Reynolds numbers, e.g. in a study by Beetstra et al. (2007) up to Re = 1000. Feng et al. (2010) coupled the LBM and soft-sphere collision approach in a three-dimensional case with number of particles 5086 and the maximum Re = 137 360.

2.2.3 Lagrangian-Eulerian modelling

The Lagrangian-Eulerian model approach in Figure 2.5 refers to model approaches, in which the particles are solved in Lagrangian frame, i.e. as discrete particles, and the fluid is solved in Eulerian frame, i.e. as a continuum. In these model approaches, the translational and rotational particle motion is solved based on Newtonian equations and trajectories of individual particles are calculated.

The Lagrangian-Eulerian approaches can be classified based on the particle-fluid and particle-particle coupling schemes (Loth, 2006):

- One-way coupled: fluid affects particle motion, but not vice versa.
- Two-way coupled: above plus particle motion affects fluid motion.
- Three-way coupled: above plus particle disturbance of the fluid locally affects another particle's motion, e.g. drafting of a trailing particle.
- Four-way coupled: above plus particle collisions.

Based on Elghobashi (2006), a four-way coupling, i.e. including the inter-particle effects, is required, if the volume fraction of solids (ε_s) is above $10^{-4}...10^{-3}$, the exact limit depending on the properties of particles and turbulent flow. In a CFB furnace, the typical range can be $\varepsilon_s = 10^{-4}...0.4$ or even wider. Thus, in general, in a circulating fluidized bed, the flow conditions require modelling of particle-particle interactions to describe the flow dynamics correctly. This is achieved by collision models, which are classified to hard-sphere models and soft-sphere models.

In a hard-sphere model (or event-driven model), the interactions between particles are assumed to be instantaneous and expressed by binary collisions (Hoomans et al., 1996). Each collision is an event between a pair of particles or between a particle and a wall. The calculation is progressed as successive events and multiple collisions at the same instant cannot be accounted for.

In a soft-sphere model (or time-driven model), the interaction between solid particles is expressed by the Hertzian contact theory and the particles are allowed to overlap slightly (Tsuji et al., 1993). Every particle can have multiple contacts with neighbouring particles simultaneously. The calculation is progressed using a fixed time step.

The particle tracking and collision models are commonly named as discrete (or distinct) element method (DEM) or discrete particle modelling (DPM). The names are often equivalent in meaning, but the usage is diverse and the terminology is not universally fixed. Some researchers limit the DEM strictly for the soft-sphere collision approach according to original usage of the term (Cundall and Strack, 1979; Tsuji et al., 1993). Some researchers have expanded the usage of DEM to include hard-sphere collision models as well (Zhu et al., 2007; Gui and Fan, 2009; Stratton and Wensrich, 2010). The DPM term has been used instead of DEM in some papers as a generic term for both collision models (Deen et al., 2007). Often, the DPM term has been applied to refer to one-way or two-way coupled particle tracking as well. Another possible generic term for different particle models is granular dynamics (GD) (Hoomans et al., 1996).

When the Lagrangian particle modelling is coupled with Eulerian modelling of fluid, the usual terms are DPM-CFD or DEM-CFD. Feng et al. (2010) used a term CCDM for combined continuum and discrete model. A safe generic term is "Lagrangian-Eulerian modelling" to avoid confusion about the possible collision model.

Tracking a large number of particles and collisions is computationally demanding, thus the Lagrangian-Eulerian models have been mostly limited to studying small-scale systems. Van Wachem et al. (2001a) and Zhou et al. (2002) presented two-dimensional model studies with the hard-sphere approach. Goldschmidt et al. (2002) applied a hard-sphere model with 24 750 particles to study a pseudo two-dimensional fluidized bed. Chu and Yu (2008) presented simulation results of a three-dimensional circulating fluidized bed by applying a soft-sphere model using 20 000 particles. Tsuji et al. (2008) performed a soft-sphere modelling with more than 4.5 million particles to study a bubbling fluidized bed with a cross section of 1.2 x 1.2 m^2. He et al. (2009) applied a hard-sphere model with 20 260 particles to study a binary particle system in a 30 cm high CFB riser. In a study by Jalali and Hyppänen (2010), the particle-particle interactions of two granular phases, each consisting of 5000 particles, were simulated by a soft-sphere model.

As the computing capacities and methods are improving, the Lagrangian-Eulerian models will be applied to study ever-larger systems with larger number of particles. A large-scale CFB furnace can have a bed inventory in the order of 100 000 kg. With typical mean particle size ranging 200...300 μm and particle density about 2500 kg/m^3, the estimated number of mean sized particles in such a system would be $10^{12}...10^{13}$. To model the large proportion of finer particles, the number would be considerably higher. Consequently, a detailed particle-by-particle modelling of large-scale CFB processes by Lagrangian-Eulerian method will not be feasible in any near future.

The calculation cost is reduced in a direct simulation Monte Carlo method (DSMC), in which each simulated particle represents a large number of physical particles and the collisions are described in a statistical manner. Even with this simplification, the calculations are limited to small-scale and relatively low solid phase volume fractions (Tanaka et al., 1996; Wang et al., 2009). A further simplification is applied in recently

suggested distinct cluster method (Liu and Xu, 2009). In this approach, the particle clusters are considered as discrete phase. Naturally, this will result in numerous approximations and assumptions regarding the turbulence, interphase forces and solid phase stress terms. This method has not yet been applied to large-scale studies.

Another concept of speeding the calculation of Lagrangian-Eulerian simulation is a multiphase particle-in-cell method (MP-PIC). This technique was suggested by Andrews and O'Rourke (1996) and later extended by Patankar and Joseph (2001) and Snider (2001). In this method, the particles are treated both as a continuum and as discrete particles, while fluid phase is treated as continuum. Particles are grouped into clouds that contain a fixed number of identical particles, instead of tracking individual particles. Collisions between particles are not resolved explicitly, but the effect of particle collisions is accounted for in an average manner using a continuum model for the solid-phase stress. Recently, O'Rourke et al. (2009) presented an improved collision sub-model. With the MP-PIC method, the calculation cost is smaller than with Lagrangian-Eulerian methods using collision models, thus it can be applied for larger scale systems, while allowing simulating particles of different sizes and materials. At the moment, the published fluidized bed applications of MP-PIC are still limited to small-scale studies, with vessel diameters less than one meter (Leboreiro et al., 2008; Snider and Banerjee, 2010; Karimipour and Pugsley, 2010).

The Lagrangian-Eulerian calculations in one-way or two-way coupled manner, i.e. without interparticle effects, cannot predict the dense phase gas-solid flows correctly. However, they have been successfully applied for studying gas-solid flows in separators (Zhao and Su, 2007; Wan et al., 2008). Thus, they can be used to support studies of overall fluid dynamics of CFB boilers.

2.2.4 Eulerian-Eulerian modelling

In the Eulerian–Eulerian approach, the gas and the solid phases are handled as interpenetrating continua in Eulerian frame. This is also called the two-fluid method (TFM) as the solid phase is treated as a fluid. This is the most commonly used approach for simulating flow dynamics of fluidized bed applications (Myöhänen et al., 2006).

The formulation of the averaged transport equations for two-fluid models is usually credited to Ishii (1975) or Anderson and Jackson (1967). Both of them have derived the flow equations from first principles. Originally, the equations by Ishii were developed for modelling liquid-gas flows in nuclear processes and the equations by Anderson and Jackson for modelling fluidized beds. Van Wachem et al. (2001b) showed that the difference between the two formulations was in the effect of fluid stress tensor on the solid phase and that the Ishii's treatment was appropriate for a dispersed phase consisting of fluid droplets and Anderson and Jackson's treatment was appropriate for dispersed phase consisting of solid particles.

The following presents governing equations for locally averaged variables following the formulations of Anderson and Jackson.

Continuity equations for gas and solids:

$$\frac{\partial \varepsilon_g}{\partial t} + \nabla \cdot \left(\varepsilon_g \mathbf{v}_g\right) = 0 \tag{2.5}$$

$$\frac{\partial \varepsilon_s}{\partial t} + \nabla \cdot \left(\varepsilon_s \mathbf{v}_s\right) = 0 \tag{2.6}$$

Momentum equations (gas phase *g*, solid phases *s, f*):

$$\frac{\partial}{\partial t}\left(\varepsilon_g \rho_g \mathbf{v}_g\right) + \nabla \cdot \left(\varepsilon_g \rho_g \mathbf{v}_g \mathbf{v}_g\right) = -\varepsilon_g \nabla P + \nabla \cdot \boldsymbol{\tau}_g + \sum_f \beta_{fg}\left(\mathbf{v}_f - \mathbf{v}_g\right) + \varepsilon_g \rho_g \mathbf{g} \tag{2.7}$$

$$\begin{aligned} &\frac{\partial}{\partial t}\left(\varepsilon_s \rho_s \mathbf{v}_s\right) + \nabla \cdot \left(\varepsilon_s \rho_s \mathbf{v}_s \mathbf{v}_s\right) \\ &\quad = -\varepsilon_s \nabla P + \nabla \cdot \boldsymbol{\tau}_s - \nabla P_s + \beta_{gs}\left(\mathbf{v}_g - \mathbf{v}_s\right) + \sum_f \beta_{fs}\left(\mathbf{v}_f - \mathbf{v}_s\right) + \varepsilon_s \rho_s \mathbf{g} \end{aligned} \tag{2.8}$$

In some formulations in literature, the solid pressure (P_s) may have been written inside solid phase stress ($\boldsymbol{\tau}_s$) (Arastoopour, 2001; Gidaspow et al., 2004). The interphase exchange force between multiple solid phases is often neglected because the studies are limited to one solid phase. Moreover, the interphase forces could include lift force and virtual mass force, but these are generally considered insignificant compared with the drag force due to large density difference between the phases. The challenges of the two-fluid models are related to correct definition of the stress terms, solid pressure and interphase drag coefficients (β).

The mostly used approach is to apply kinetic theory concepts for defining the terms due to particle-particle interactions, i.e. the solid phase stress tensor (τ_s) and solid pressure (P_s); hence, the model approach is named as kinetic theory of granular flow (KTGF).

Bagnold (1954) is credited for starting the kinetic theory approach of granular flow. Major efforts to the development of KTGF theory and the closure models have been contributed by Ogawa et al. (1980), Jenkins and Savage (1983), Lun et al. (1984), Sinclair and Jackson (1989), Ma and Ahmadi (1990), Ding and Gidaspow (1990), Gidaspow et al. (1992) and Syamlal et al. (1993).

In the granular theory, the analogy with kinetic gas theory is attempted. The kinetic energy related to random movement of solid particles is interpreted as granular temperature θ_s. On the other hand, the granular temperature can be understood as some kind of turbulent kinetic energy or solids fluctuating energy. The instant particle

velocity v can be thought to be decomposed into a mean velocity $\bar{v}$ and a superimposed fluctuating velocity v'.

$$v = \bar{v} + v' \tag{2.9}$$

The basic principle of KTGF is that analogous to the thermodynamic temperature for gases, a granular temperature θ_s can be introduced, which is associated with the random fluctuating velocity of the particles.

$$\theta_s = \frac{1}{3}\overline{(v')^2} \tag{2.10}$$

The granular temperature can be solved from a transport equation (Ding and Gidaspow, 1990; Arastoopour, 2001) or by algebraic formulation, in which the convection and diffusion of θ_s have been neglected (Syamlal et al., 1993). The stress terms are then functions of the granular temperature.

The gas-solid momentum exchange is defined by drag coefficient β_{gs}, which has been empirically determined by different researchers for different conditions. The formulation by Syamlal and O'Brien (1989) applies equations developed by Dalla Valle (1948) and Garside and Al-Dibouni (1977). The formulation by Gidaspow et al. (1992) applies equations by Ergun (1952) for dense flows and equations by Wen and Yu (1966) for dilute flows, but resulting in a step change at solid volume fraction 0.2. Equations for solid-solid drag term β_{fs} have been proposed by Gidaspow et al. (1986), Syamlal (1987) and Bell (2000).

The different closure models and correlations have been reviewed by van Wachem et al. (2001b). There are no unique formulations in the literature for the closure models defining the different terms in the momentum equations.

In order to capture the meso-scale flow features, the calculation mesh spacing should be relatively fine, in the order of 10...100 particle diameters (Agrawal et al., 2001; Andrews et al., 2005). In a typical CFB combustor, the average particle size is in the order of 200...300 µm, which would mean a cell size of 2...30 mm. For a large-scale furnace, this would mean calculation mesh sizes in the order of 10^9...10^{12} elements, which is too demanding for any practical calculations. Consequently, large-scale studies need to be performed with coarse calculation meshes. The clusters smaller than the cell size cannot be resolved, which in coarse mesh leads to overestimating the drag force between the gas and solid phases and false macroscopic flow fields. Thus, the modelled volume fraction of solids tends to be too small at the lower part of the furnace or too high at the upper part of the furnace. Several researchers have addressed this problem by suggesting modifications to the drag term or development of sub-grid models (Agrawal et al., 2001; Zhang and VanderHeyden, 2002; Yang et al., 2003; Andrews et

al., 2005; Kallio, 2005; Qi et al., 2007; Igci et al., 2008). Lately, especially the EMMS (energy minimization multiscale) method, which is based on correcting the drag coefficient, has been extensively used and has succeeded matching the axial solid profiles with the measurements (Wang, W. et al., 2010).

The time step of the transient calculations must be sufficiently small to capture fast movements of solid phase and to achieve stable calculation process. Typically, the time steps are in the order of 1 ms. Increasing the time step size and, ultimately, achieving a steady state CFD simulation is an attractive alternative for time-consuming transient simulations. This has been pursued by De Wilde et al. (2007) and Kallio et al. (2008).

Naturally, a steady state macroscopic flow field can be generated by averaging over a transient simulation, but due to long calculation times, the averaging times are often relatively small, in the order 20 s of simulated process time (Shah et al., 2009; Zhang et al., 2010). Considering the possible slow fluctuations of the CFB process, these kind of averaging times may be too small to represent the actual steady state model results and the sensitivity of results on the averaging time should be checked.

Another item to consider when applying averaged CFD calculations is that the effects of transient phenomena on the mixing are lost in the averaging process. These transient phenomena have an effect e.g. on the mixing of reactants and the combustion process. In the averaged, steady state flow equations, these effects create new terms, analogous to single phase turbulence models, and the challenge is how to determine proper closure models for the new terms.

Due to challenges related to modelling the large-scale CFB processes with two-fluid models, most of the published studies, including quite recent ones, are limited to two-dimensional cases or small-scale applications (Mathiesen et al., 2000; Flour and Boucker, 2002; Yue et al., 2008; Zhang et al., 2008; Hartge et al., 2009; Nikolopoulos et al., 2009; Özel et al., 2009; Wang, J., 2010; Wang, X.Y. et al., 2010). The published industrial scale 3D CFD studies are very scarce and none of them includes modelling of combustion and heat transfer. Myöhänen et al. (2006) present model results of a 102 MWe CFB, in which a three-dimensional slice of the furnace was modelled, but the simulated process times were very short. Shah et al. (2009) show calculation of a full furnace with two solid phases to better simulate the measured vertical pressure profile. Zhang et al. (2010) performed a simulation of a 150 MWe boiler modelling a full CFB loop including two cyclones and the return leg system. The simulated process time was 40 seconds. The results compared well with the measurements, when the interphase drag term had been modified based on the EMMS method.

Many researchers are working together with boiler industry on improving the applicability of the TFM models for practical calculations of CFB combustors. In near future, the number of large-scale studies will certainly increase due to improvement of calculation capacity, numerical methods, model theories, and, especially, with support of advanced measurement techniques for validating the models.

2.2.5 Empirical and semi-empirical models

The empirical and semi-empirical models are targeted in modelling the complete process, including the reactions and heat transfer. These are currently the only methods, which have been used for comprehensive modelling of industrial scale CFB combustors and gasifiers.

The simplest model approaches are steady state zero-dimensional or lumped models, which are correlation based models fulfilling the basic continuity equations for the total process. In a coal combustion model by Lee and Hyppänen (1989), a zero-dimensional approach is used for determining overall mass balances of solids (Figure 2.6). Recent examples of steady state 0D CFB models are gasification models by Li et al. (2004) and Doherty et al. (2009). The strength of the lumped models is that they are fast and simple to use. However, they are not very flexible, cannot take account for the spatial effects, such as fuel feed distribution, do not provide details of the in-furnace phenomena and cannot usually predict the effects of changing boundary conditions and geometry, if the conditions differ from the ones for which the model has been validated for.

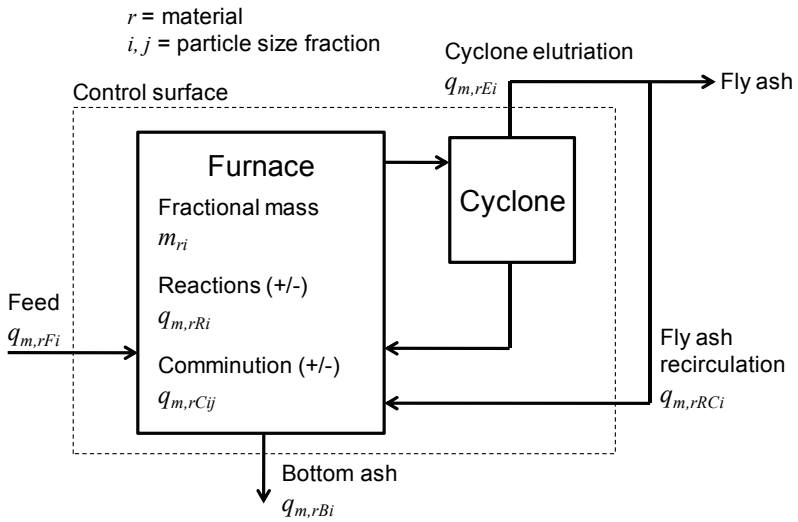

Figure 2.6. Zero-dimensional model (cf. Lee and Hyppänen, 1989).

A more detailed description of the furnace process is achieved in 1D models, in which the furnace is divided to vertical sections (Lee and Hyppänen, 1989; Sotudeh-Gharebaagh et al., 1998; Corella and Sanz, 2005; Krzywanski et al., 2010). These model types lack the characteristic feature of large-scale circulating fluidized beds: the downflow of solids near the walls. The vertical concentration profile of solids is typically based on empirical correlations (Li and Kwauk, 1980; Johnsson and Leckner, 1995) or simple models (Smolders and Baeyens, 2001).

A popular model approach is a core-annulus approach (Adánez et al., 1995; Wang et al., 1999; Huilin et al., 2000; Hua et al., 2004). These model types have often been referred as 1.5D models, but in some articles as 1D (Gungor, 2009b) or 2D (Kruse and Werther, 1995; Wang et al., 2003). The principle is the same: the suspension flow is divided into dilute and dense regions. In dilute core region, the solids are flowing upwards and in dense annulus region downwards (Figure 2.7). The gas velocity in the core is above the superficial velocity through the riser, while in the annulus it is close to zero. The bottom bed is usually regarded as a separate section. The flow behaviour and the mixing between the regions are determined by empirical correlations. Each of the sections can be divided to several control volumes. A population balance model is usually applied to simulate the real, continuous particle size distribution and the effects of attrition.

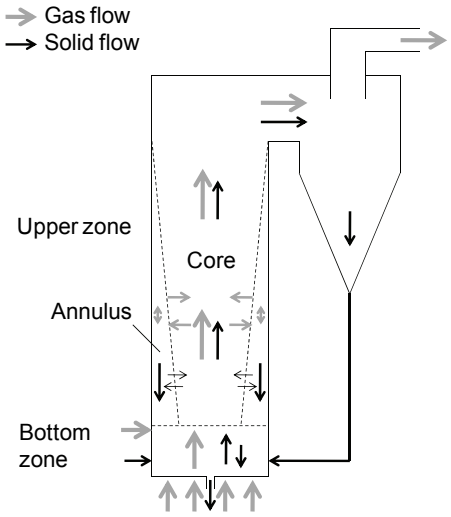

Figure 2.7. Core-annulus approach.

Transient macroscopic models usually use 0D, 1D, 1.5D or 2D approaches (Muir et al., 1997; Park and Basu, 1997; Costa et al., 2001; Kettunen et al., 2003; Gungor and Eskin, 2008). These are applied for analysis of boiler operation in transient conditions, e.g. during load changes or fault situations, and for development of control systems. A 3D transient model for gasification has been presented by Petersen and Werther (2005b).

The number of comprehensive three-dimensional CFB furnace models, which are capable of modelling industrial scale combustors, is very small. The model presented in this work is based on the original code developed in 1989 (Rainio, 1989; Hyppänen et al., 1991). In addition, the current literature presents only two models: one developed by Technical University Hamburg-Harburg (Wischnewski et al., 2010) and one developed by Chalmers University of Technology (Pallarès et al., 2008b). The validation of the models requires measurement data from commercial boilers, thus the model development of the semi-empirical models is more or less linked to various boiler manufacturers and the dissemination of the specific correlation data is often limited.

The advantage of the 3D models is that they can simulate the real three-dimensional nature of the furnace process (Figure 2.8). The simulation of flow and mixing relies on empirical models, thus these are simpler to solve than in fundamentals-oriented CFD models and calculation of large-scale units is possible. Naturally, the prediction capability of these models is limited by the available validation data. These models have been reviewed in more detail in Chapter 2.3.

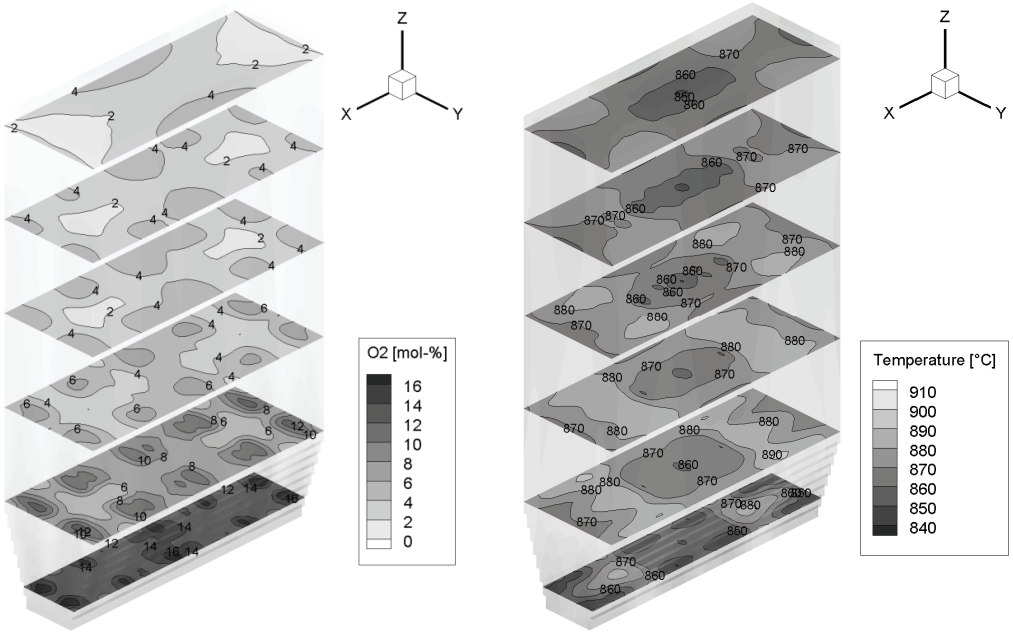

Figure 2.8. Modelled O_2 and temperature fields of a 460 MWe CFB (Myöhänen et al., 2009).

2.2.6 Combinations

The model approaches presented in Figure 2.5 and Chapters 2.2.2 - 2.2.5 can be combined by numerous ways. It is reasonable to use the models, which are best suited for the task and if necessary, combine the modelling by different methods to achieve the wanted results. The following lists some combinations, but naturally, many others are possible as well.

In multiscale model approaches, the principle is to apply smaller scale models to provide information for higher scale models (van der Hoef et al., 2004; Wang, W. et al., 2010), emphasizing the importance of small scale structures.

An interesting approach is to combine Eulerian-Eulerian modelling and Lagrangian tracking of particles (Liu and Chen, 2010). In this study, the solution of flow fields was based on Eulerian-Eulerian method and tracer particles, following the Eulerian solid flow field, were applied to study dispersion of particles.

Shah et al. (2009) applied Eulerian-Eulerian CFD modelling of fluid dynamics to provide data for a semi-empirical 3D combustion model. Hartge et al. (2009) have indicated plans to use CFD modelling as a basis for their 3D reactor model. In future, these modelling approaches are likely to be linked more, as the CFD models can be applied to larger scale and may include reactions due to increasing computing capacity, and the semi-empirical models will have more detailed flow models or can apply CFD based calculations for defining the flow and mixing in the combustor models.

2.3 Comprehensive 3D CFB models

This chapter reviews the comprehensive three-dimensional models, which are capable of simulating industrial scale CFB combustors.

Modelling of a total CFB process can be divided to four main fields: fluid dynamics of gas and solids, comminution of solids, reactions (e.g. combustion and sorbent reactions) and heat transfer. All of the different fields are affecting each other, but the fluid dynamics has the largest effect on the other modelling fields (Pallarès and Johnsson, 2006b). This is illustrated below in Figure 2.9.

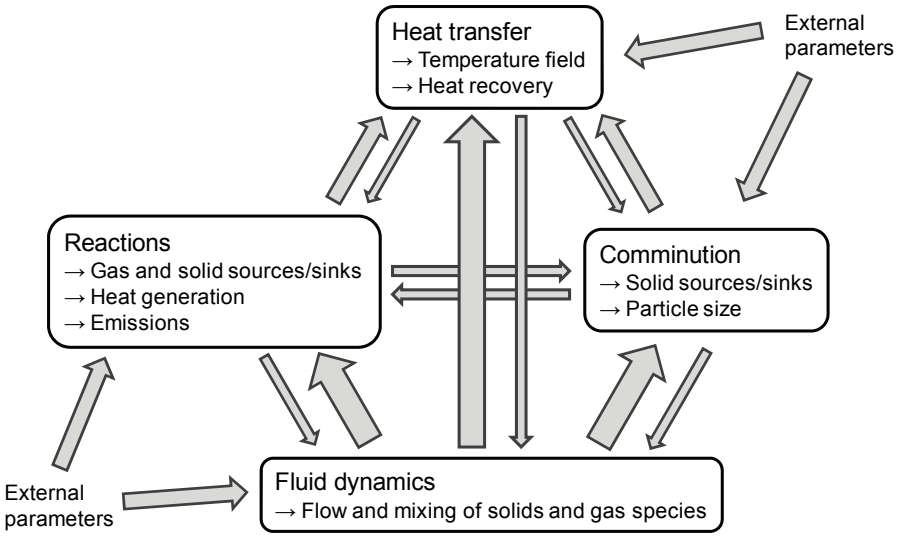

Figure 2.9. Relationships between CFB modelling fields (cf. Pallarès and Johnsson, 2006b).

The following subchapters present a review of how the different modelling fields are handled in the existing comprehensive 3D models. In the following, the model by Technical University Hamburg-Harburg (Knoebig et al., 1999; Luecke et al., 2004; Wischnewski et al., 2010) will be referred to as the TUHH-model and the model by Chalmers University of Technology (Pallarès et al., 2008b) will be referred to as the CUT-model.

2.3.1 Fluid dynamics

The literature has large amount of data concerning the flow and mixing processes occurring in a circulating fluidized bed combustor. These are based on visual observations of cold and hot test facilities (Yerushalmi et al., 1976; Lackermeier et al., 2001; Pallarès and Johnsson, 2006a; Kallio et al., 2009), measurements of solid concentration, gas concentration and velocity profiles (Zhang et al., 1995; Issangya et al., 2000; Schlichthaerle and Werther, 2001; Johansson, 2005; Werther, 2005) and CFD modelling (Tossavainen et al., 2003; Liu and Chen, 2010). Reviews are found in articles (Lim et al., 1995; Hartge et al., 1999; Reh, 2003; Breault, 2006; Pallarès and Johnsson, 2008a) and in textbooks (Basu, 2006). The following figure illustrates the main macroscopic flow and mixing processes, which are usually identified in a CFB combustor (cf. Reh, 2003, p. 190).

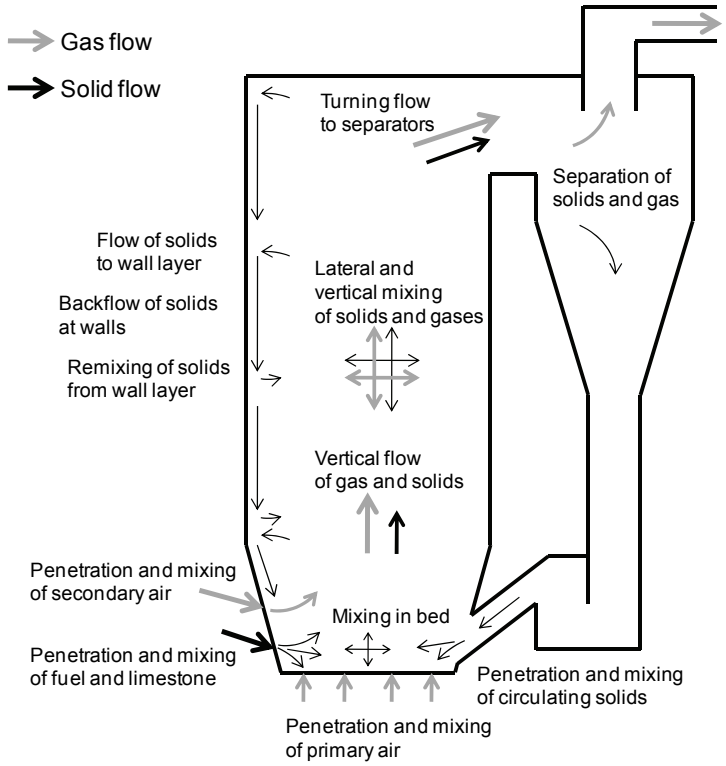

Figure 2.10. Macroscale flow and mixing processes in a CFB combustor.

The main flow pattern – the circulating fluidized bed – is achieved by fluidizing the bed of solids with gas at a velocity, which exceeds the terminal velocity of particles. At the top of the furnace, the elutriated solids are recovered and returned back to the base of the furnace to maintain the bed inventory. Another term, which has been often used for this type of fluidization regime, is "fast bed" or "fast fluidized bed" coined by Yerushalmi et al. (1976).

The solid flow mechanisms are determined by the different forces acting on particles: drag force between the fluidization gas and solids, gravity, interparticle forces and forces between particles and vessel walls. The main flow pattern is characterized by a core-annulus flow profile (Pallarès and Johnsson, 2008a). In the core, the solids are flowing mostly upwards as dispersed particles and clusters of particles. Occasionally, the clusters become too dense to be suspended by gas flow, which results in downwards falling clusters. The flow is transient: clusters are forming and breaking continuously and the direction and magnitude of flow is fluctuating. Some of the solids flow towards the walls, where they tend to form backflow of solids due to smaller gas velocity near the walls (Werther and Hirschberg, 1997). The average solids flow at the walls is downwards, but, again, this process is transient: the downfalling solid clusters at the walls may break and the solids are remixed back to the upwards flowing suspension in the core. The backflow of solids has a large effect on the furnace process, as it is essentially forming an internal circulation of solids parallel to the external circulation across the separator and return leg system. The main flow patterns are illustrated in Figure 2.11. Due to the main flow patterns, the concentration of the solids is higher at the bottom of the furnace and near the walls. Typically, a separate dense bubbling bed section is identified at the bottom of the furnace, but some large-scale units may operate with relatively lean bottom bed and with more homogeneous axial distribution of solids (Werther, 2005).

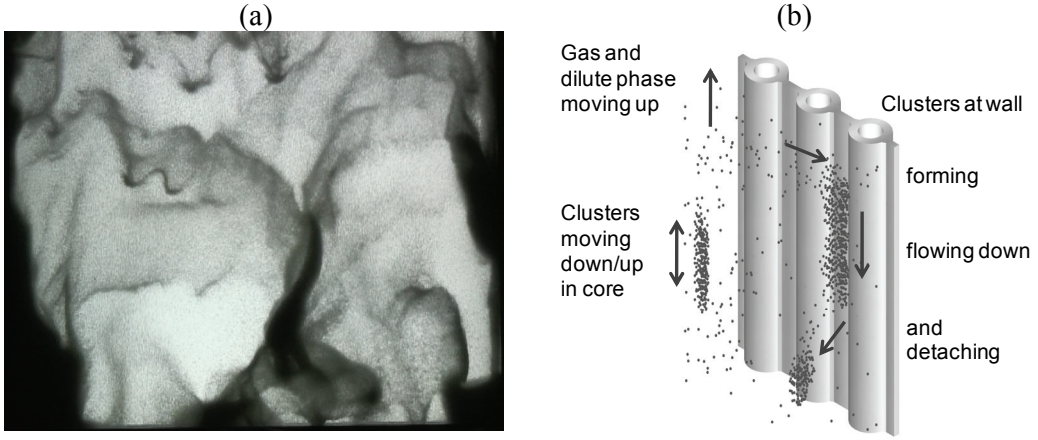

Figure 2.11. Flow mechanisms of a circulating fluidized bed.
(a) Photograph of a small-scale 2D CFB unit (courtesy of Sirpa Kallio, cf. Kallio et al., 2009).
(b) Illustration of the main flow mechanisms.

In the TUHH-model, the furnace is divided to four sections: bottom zone, splash zone, upper dilute zone and exit zone (Wischnewski et al., 2010). Momentum balances are not solved, but the flow fields are based on empirical models and potential flow approach. The mixing of solids and gases are controlled by diffusion in analogy to Fick's law. The dispersion coefficients in different furnace sections and in axial and lateral directions are adopted from literature. The external solid circulation rate is given as a model parameter.

In the bottom zone, a shallow bubbling bed is assumed. The height of the bottom bed is experimentally set, for example 0.53 m (Luecke et al., 2004). A wall region with descending solids is determined so that the thickness of the wall region increases linearly from zero at the floor of the furnace to a value at the bottom of the splash zone (Wischnewski et al., 2010). In the bottom zone, the solids are assumed to be ideally mixed in the vertical direction. The horizontal mixing of solids is simulated by a dispersion model applying a constant solid dispersion coefficient of 0.12 m^2/s (Luecke et al., 2004). The gas flow is assumed to flow vertically in a plug flow, i.e. mixing of gas is not considered in vertical or horizontal directions. The gas flows in two phases: a bubble phase and a suspension phase. In the other furnace sections, the gas flows in a single phase.

In the splash zone and the upper dilute zone, a core-annulus flow structure is assumed based on the model by Pugsley and Berruti (1996). In the splash zone, the solids are accelerated to a constant upward velocity and the thickness of the wall region decreases with height. In the upper dilute zone, the vertical velocity of solids and the thickness of the wall layer are constant. Horizontal gas and solids velocities are calculated with a two-dimensional potential flow field approach for each row of the calculation cells. The sources and sinks account for the gas and solid streams entering and leaving the furnace, the sources due to devolatilization, and combustion reactions of char and volatiles. In the wall region, the gas is entrained by the descending solids thus creating back-mixing of gas.

The exit zone is modelled as a continuous stirred-tank reactor with an infinitely small height. The exit zone and the bottom zone are connected by a model describing the operation of the separator and the return leg system.

The sources of char, devolatilized gases and evaporated moisture are solved at the start of the calculation and these are assumed to remain constant throughout the simulation. The influence of local temperature on the devolatilization and evaporation are neglected. The model assumes that the fuel releases the volatile content continuously and the primary char is formed at the end of the devolatilization. The resulting distributions of primary char and volatile sources are the input data for the second modelling step, which describes the combustion of char and gas components (Wischnewski et al., 2010).

The fluid dynamics model of the CUT-model is based on a macroscopic model by Pallarès and Johnsson (2006b), which has been derived from initial 1.5-dimensional model by Pallarès and Johnsson (2002). The furnace is divided to three sections: bottom bed, freeboard and exit zone. The exit zone and the bottom bed are connected by sub-models for exit duct, cyclone and return leg system.

Similar to TUHH-model, the bottom bed consists of two phases: a dense phase formed by the solids and the interstitial gas flow, and a bubble phase formed by upflowing gas bubbles, which are assumed free of solids. However, in the CUT-model, the backmixing

of solids through a wall region is not considered in the bottom bed. The vertical mixing of fuel is assumed perfect, while the horizontal mixing is approximated by diffusion (Pallarès and Johnsson, 2008a).

The freeboard section comprises the height between the bottom zone and the exit zone. This section can be further divided to a splash zone and a transport zone (Johnsson and Leckner, 1995). In the freeboard section, the solid (and fuel) flow is divided to a cluster flow and dispersed phase flow. The cluster flow pattern dominates the splash zone and it is characterized by ballistic movement of clustered solids originating from the bottom zone. The transport zone is dominated by a dispersed phase flow, which forms a typical core-annulus flow structure with descending solids at wall regions. The vertical solid concentration profile is determined by equation given by Johnsson and Leckner (1995). The gas flow is modelled as vertical plug flow. The secondary gas injections are assumed to join the plug flow at the injection height.

In the exit zone, the solids are either internally recirculated through the wall layers (backflow of solids) or they follow the gas flow out of the furnace. The backflow ratio is determined by an empirical correlation.

2.3.2 Comminution

In a fluidized bed, the solid particles are in vigorous movement and in close contact with each other. Figure 2.12 illustrates the possible mechanisms of how the particle size of the solids can change in a fluidization process. Agglomeration is an undesired phenomenon, which can be avoided by keeping the furnace temperature below agglomeration temperature of the solids by means of temperature control and by avoiding accumulation of alkali salts and other compounds with low melting temperature by means of additives and make-up feed. Normally, the particle size is decreasing due to mechanical wear of particles, temperature shocks and effects of different chemical reactions (e.g. breaking of char particles during combustion) and the comminution is occurring from larger particles to smaller particles.

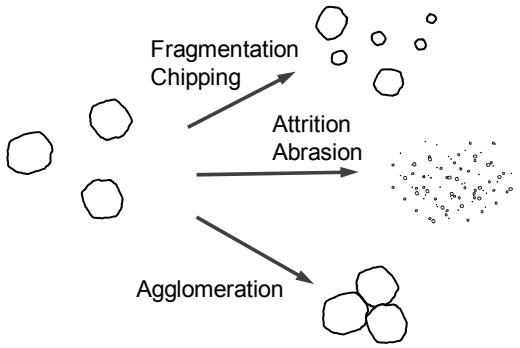

Figure 2.12. Mechanisms of changing particle size.

In the TUHH-model, primary fragmentation of char is assumed to occur after the end of devolatilization, but secondary fragmentation is neglected (Luecke et al., 2004). In the furnace, the char particles experience a changing particle size due to combustion of char following a shrinking particle model. This is simulated by population balance approach using eight particle size intervals. The comminution of inert solids or ash is not considered.

In the CUT-model, the fragmentation of fuel is defined as a given fragmentation pattern, e.g. assuming fragmentation to 10 pieces after 75% of the devolatilization time (Pallarès and Johnsson, 2008a). The comminution of other solid material is not considered.

2.3.3 Combustion reactions

The combustion of a fuel particle consists of the following stages:

- heating of a fuel particle,
- evaporation of moisture,
- devolatilization (or pyrolysis),
- combustion of char.

In addition, the primary fragmentation at the end of the devolatilization and the secondary fragmentation of the remaining char particles are identified. In many simplified descriptions in textbooks, the above stages are illustrated as subsequent processes (e.g. Basu, 2006, p.104). For a local point of a single fuel particle, this may be true, but in a group of particles, the phenomena are overlapping as the different particles can be at different stages of the phenomena. This happens with a single particle as well: the devolatilization may start at the surface of the particle, while the evaporation is still continuing in the core of the particle (Saastamoinen, 2006).

The devolatilization produces different combustible gases, which are then burned in a presence of oxygen.

The following description of the TUHH-model is based on Luecke et al. (2004) and Wischnewski et al. (2010). In the TUHH-model, the heating of the fuel particles is neglected. The model assumes parallel evaporation and devolatilization, thus, the water vapour is included in the devolatilized gas species, which consist of CO, CO_2, CH_4, H_2, H_2O, O_2, N_2 and SO_2. The char is assumed to consist of carbon, after which the elemental composition of volatiles can be determined from proximate and ultimate analysis. The devolatilization produces gaseous species according to following rules:

- Sulphur is completely converted to SO_2.
- Carbon and hydrogen form CH_4. Initially 75% of the hydrogen is assumed to form CH_4. The remaining carbon is released as CO and CO_2 depending on the oxygen content of the fuel.

- Remaining oxygen forms H_2O if enough hydrogen is left, otherwise O_2 is released.
- Remaining hydrogen is released as H_2.
- All nitrogen is converted to N_2.

The devolatilization time is determined by an empirical correlation as a function of particle size based on Ross et al. (2000):

$$t_{vol} = a d_p^b \qquad (b \approx 1) \tag{2.11}$$

A shrinking particle size model is applied for modelling the combustion of char. As the char is assumed to consist of only carbon, the combustion produces CO and CO_2. The split is determined by an empirical correlation as a function of particle size and temperature. The reaction rate of char combustion k_{char} is limited by kinetic reaction rate constant k_{kin} (determined by Arrhenius type correlation) and mass transfer coefficient k_g (determined by empirical correlations for the Sherwood number):

$$k_{char} = \frac{1}{1/k_{kin} + 1/k_g} \qquad (\text{units m/s}) \tag{2.12}$$

The combustible gas species (CO, CH_4 and H_2) burn in the presence of oxygen. The reaction rates are defined by Arrhenius type expressions.

The CUT-model considers drying, devolatilization and char combustion as well as the homogeneous combustion reactions (Pallarès et al., 2008b). The main concepts are similar to TUHH-model, but applying different correlations for determining the governing equations. The composition of the devolatilized gases is based on Thunman et al. (2001), which solves a system of equations formed by mass balances on the fuel ultimate analysis, an energy balance, and empirical parameters. The resulting gas species are formed of CO, CO_2, H_2O, H_2, C_iH_j (light hydrocarbons, methane and ethene), and $C_nH_mO_k$ (heavy hydrocarbons). The char is presumably considered as carbon and sulphur is neglected.

Neither of the two models considers gasification of char or homogeneous gasification reactions. However, TUHH has presented a separate, transient 3D gasifier model, which includes a comprehensive set of combustion and gasification reactions (Petersen and Werther, 2005b).

2.3.4 Sorbent reactions

Combustion of sulphur containing fuels produces sulphur oxides, which are harmful emissions causing acid rain. In a CFB furnace, the sulphur capture is possible by addition of sorbents. The mainly used sorbents are calcitic limestones and the sorbent feed usually consists mainly of calcium carbonate. In atmospheric combustion with air, the furnace temperature is usually above the calcination temperature and the $CaCO_3$ is first calcined to CaO as it enters the hot furnace and then sulphated to $CaSO_4$ in the presence of SO_2. In pressurized combustion or oxycombustion, the partial pressure of CO_2 is high, which may prevent calcination, and the sulphur capture is possible by direct sulphation. In reducing conditions, the calcium sulphate may decompose back to CaO. Furthermore, in reducing conditions, the reactions involving calcium sulphide (CaS) and hydrogen sulphide are possible. (Mattisson and Lyngfelt, 1998b; Zevenhoven et al., 1998; Anthony and Granatstein, 2001; Stanmore and Gilot, 2005)

The following figure illustrates the reaction paths of the most common reactions:

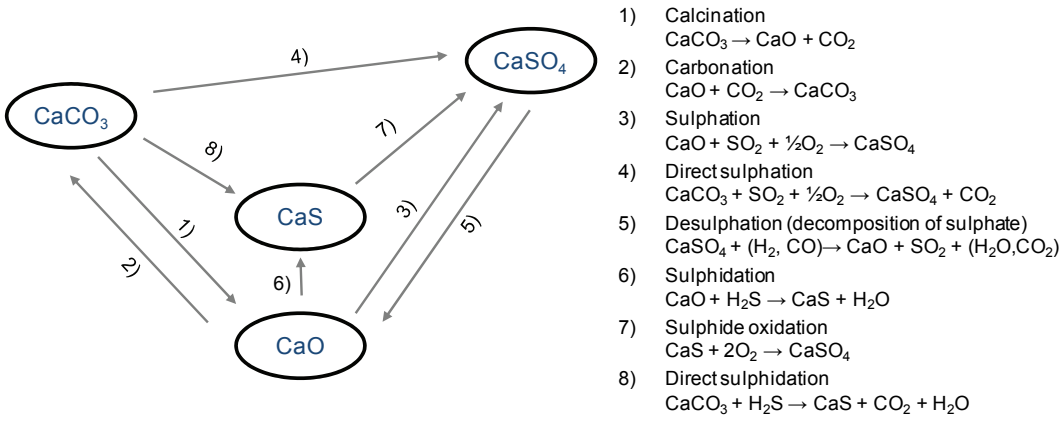

Figure 2.13. Limestone reaction paths. Exothermic reactions indicated by arrows going upwards.

The limestone reactions at particle level has been modelled by different model approaches: pore models, grain models, changing internal structure models, and unreacted shrinking core models (Adánez et al., 1996; Zevenhoven et al., 1998; Stanmore and Gilot, 2005; Saastamoinen, 2007; Bouquet et al., 2009). In principle, the particle models could be integrated to modelling of a full CFB process by Lagrangian-Eulerian approach. However, for practical calculations, the number of calculated particle trajectories should be restricted, for example by applying the MP-PIC-method (see Chapter 2.2.3). These kinds of studies have not yet been published however.

Li et al. (1995) combined a particle model for calcination and sulphation and Lagrangian modelling of particle trajectories in a 1D-model. Wang et al. (1999) applied

the same model in a 1.5D core-annulus-model, but the description of the model principles was superficial.

In most of the lumped, 1D- and 1.5D- models considering the limestone reactions, the reactions have been modelled by a simplified manner using effective reaction rate constants. The models are usually handling only a restricted set of limestone reactions, for example only sulphation or only carbonation. None of the published models has combined the different limestone reactions shown in Figure 2.13.

Mattisson and Lyngfelt (1998a) presented a lumped sulphur capture model for the sulphation reaction. The model used an exponential decay function to describe the decreasing reactivity of CaO as a function of molar conversion X to $CaSO_4$:

$$\frac{dX}{dt} = a\, e^{-bX} p_{SO_2} \tag{2.13}$$

The particle size distribution of the limestone bed was considered by dividing the solids to 11 – 12 particle size fractions. The parameters a and b were determined as functions of particle size and the residence time of each size fraction was determined from the estimated bed masses and exiting mass flows and assuming a well mixed reactor. The partial pressure of SO_2 was determined from the measured SO_2 in flue gas.

The model by Adánez et al. (2001) was targeted for simulating the operation in turbulent regime. It combined a simplified modelling of combustion and a semi-empirical model for reactivity of CaO, in which the reactivity decreased exponentially as a function of residence time. The calcination was considered instantaneous, thus, only the sulphation reaction was modelled.

In a coal combustion model by Huilin et al. (2000), the sulphation rate was controlled by an empirical correlation and affected mainly by SO_2 concentration, temperature and the conversion degree of CaO to $CaSO_4$. The same sulphation model was applied in a dynamic model by Gungor and Eskin (2008) and in a steady-state model by Gungor (2009b). The applied model frame in these studies was a core-annulus-model.

Alonso et al. (2009) and Abanades et al. (2011) presented one-dimensional modelling of carbonator and combustor-carbonator reactor respectively. The reaction rate of carbonation was proportional to a determined average reaction surface and the difference between the partial pressure and the equilibrium pressure of CO_2.

The limestone reactions are not considered in the three-dimensional TUHH-model or CUT-model (Luecke et al., 2004; Pallarès et al., 2008b; Wischnewski et al., 2010). The earlier version of the model presented in this thesis included simplified modelling of calcination and sulphation (Rainio, 1989; Myöhänen et al., 2003). The calcination rate was determined by a fixed reaction rate constant. The sulphation rate was determined by

an empirical equation considering a given maximum calcium utilization degree and local concentration of SO_2. However, the model did not consider flow or mixing of limestone species, and the solid concentration fields of the limestone species were determined by fixed concentration profiles. Local variation in the sorbent composition was not simulated and the applicability of the model was limited. There is a clear need for a model, which can simulate the sorbent reactions in a three-dimensional flow environment of a circulating fluidized bed furnace.

2.3.5 Heat transfer

The heat transfer mechanism of a circulating fluidized bed has been widely studied. The methods to predict the heat transfer can be categorized to dimensional and dimensionless empirical correlations and mechanistic models, such as single particle models, continuous film models and cluster renewal models. The different model approaches have been compared in Basu and Nag (1996) and Dutta and Basu (2003).

Most of the currently used mechanistic heat transfer models are based on cluster renewal model, first described by Subbarao and Basu (1986) based on packet theory by Mickley and Fairbanks (1955). This model has been later refined by Basu and Nag (1987) and Dutta and Basu (2003). Similar or simplified model approaches have been presented by several researchers (Wang et al., 1996; Golriz and Grace, 2002; Gnanapragasam and Reddy, 2008). Gungor has presented a modified cluster renewal model and studied the effect of different operating parameters (Gungor, 2009a). The following describes generally accepted principles of the heat transfer mechanisms, which have been described in the above-mentioned literature. The main mechanisms have been illustrated in Figure 2.14.

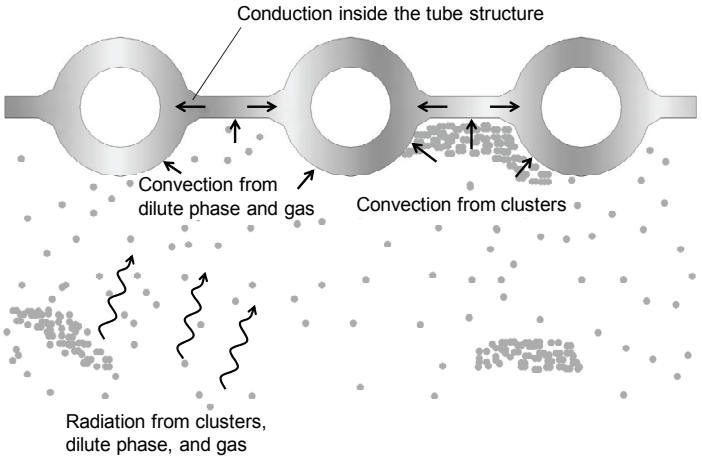

Figure 2.14. Main heat transfer modes.

The fluid dynamics of gas-solid suspension has a crucial effect on the heat transfer to walls. In a circulating fluidized bed, clusters are forming and breaking constantly and moving vertically and laterally. The movement of solids transports heat from the hot core of the furnace towards the heat transfer walls, which is mostly the basis for improved heat transfer in fluidized bed conditions. In the vicinity of furnace walls, the clusters tend to move downwards.

The total heat transfer to furnace walls can be divided to particle convection, gas convection and thermal radiation. The mechanism can be different in the inclined lower part of the furnace, near the furnace outlets and at the roof, but because these parts are refractory lined, they are not usually contributing much to the total heat transfer.

The gas convective component is often considered insignificant compared with other heat transfer modes. In measurements of commercial scale units, the increase of secondary air flow (and thus the gas velocity) has not affected considerably the heat flow to walls (Basu and Nag, 1996). However, with small boiler loads, the solid concentration and the temperature can be small at the upper part of the furnace, in which case, the gas convection can be dominating (Dutta and Basu, 2002).

The particle convection can be divided to convection from dense phase (or clusters), and from dilute phase (or dispersed or emulsion phase). With industrial sized heat transfer surfaces, the dense phase convection due to clusters falling downwards at the walls is usually dominating over the dilute phase convection.

The thermal radiation is occurring from hot clusters and dispersed phase as well as from radiative gas components (mainly CO_2 and H_2O) flowing in the core of the furnace. As the temperature of the clusters near the walls is usually much smaller, the radiative heat transfer from the clusters beside the walls is small.

The dominating heat flux modes are changing depending on the local conditions, especially the solid concentration and temperature. At the lower parts of the furnace, with higher solid concentration, the convective heat transfer is dominating. At the upper parts of the furnace, the radiation is dominating (Baskakov and Leckner, 1997).

The heat transfer in a circulating fluidized bed is a transient process. At any location, the heat transfer modes are constantly varying between convection and radiation, as the clusters are forming, flowing and breaking at the furnace walls. In a steady-state formulation, the total heat transfer is a time-averaged integral over the different transient heat transfer forms.

The geometry of the membrane wall structure affects the local distribution of the heat flux on the wall. The radiation exchange factors (or visibilities) are different due to shape of the wall, thus the radiative heat flux is higher on the tube crest than on the valley between the tubes, i.e. the tube sides and the fin. Both the radiative and convective heat transfer is affected by layer of solids flowing mostly downwards near

the walls. The concentration of downflowing solids is likely to be higher in the valley, which may increase the heat transfer coefficient between the suspension and the fin. However, the temperature of the downflowing solids is smaller than that of the surrounding suspension, and the temperature of the fin is higher than the temperature of the cooled tube, which will reduce the heat flux to fin. Moreover, a denser, or more frequent, layer of solids decreases the radiative heat transfer to this section.

The heat transfer within the gas-solid suspension is an important aspect of the overall heat transfer process. Convection of gas and solids transports the energy within the furnace and results to a fairly uniform temperature field, typical for a CFB. Another form of energy transfer within the suspension is by radiation. In dilute suspension, the radiation can occur across longer distances thus affecting the heat transfer especially at the upper parts of the furnace. In addition, the gas and solid flows are fluctuating, both in lateral and vertical direction. The different heat transfer mechanisms transport energy within the suspension and result to a more uniform temperature.

In measurements of large-scale units, the temperature profiles are often fairly uniform in the core of the furnace (Hartge et al., 2005). The temperature decreases towards the furnace wall due to heat transfer mechanisms described above. In many cases, the temperature profile measurements are limited however and cannot extend across the whole furnace cross-section due to technical issues related to handling of instrumentation and durability of long but narrow temperature probes in hot CFB conditions.

In the earlier TUHH-model, the furnace was isothermal and heat transfer was not modelled (Luecke et al., 2004). In the recent version, the enthalpy balance equation has been included, which includes terms for gas and solid convection, heat sources from combustion reactions and heat sinks due to evaporation and heat recovery (Wischnewski et al., 2010). As the solid flow field is modelled by core-annulus approach, this then simulates the main heat transfer pattern, i.e. mixing of energy due to internal backmixing of solids.

The CUT-model includes modelling of heat transfer by convection and radiation, but the enthalpy equation has not been explicitly given (Pallarès et al., 2008b). At the bottom zone and the exit zone, a perfect thermal mixing is assumed.

2.3.6 Comparison of 3D CFB model features

The following table summarizes the features of the above described three-dimensional models for CFB furnaces. In addition, the features are compared with the status of the presented model prior to the work carried out in this thesis.

The most important feature, which is lacking in these models, is the capability of modelling sorbent reactions and sulphur capture. A three-dimensional description of sorbent reactions can be a very valuable tool when optimizing the sulphur capture.

Moreover, the sorbent reactions may have a large impact on other process phenomena, such as fluid dynamics and heat transfer, and they should be included to a comprehensive CFB furnace model.

Table 2.2: Comparison of 3D CFB model features.

	TUHH-model	CUT-model	Earlier version of presented model
Fluid dynamics of gas and solids	Yes (semi-empirical)	Yes (semi-empirical)	Yes (semi-empirical)
Particle size distribution	Yes	Yes	Yes
Comminution			
Fuel (char)	Yes	Yes	Yes
Sorbent	No	No	Yes
Inert	No	No	Yes
Combustion reactions			
Evaporation	Yes	Yes	Yes (source volume given)
Devolatilization	Yes	Yes	Yes (fixed constant rate)
Char combustion	Yes	Yes	Yes
Homogeneous comb. reactions	Yes	Yes	Yes
Gasification	No	No	No
Sorbent reactions			
Calcination	No	No	Yes (fixed constant rate)
Carbonation	No	No	No
Sulphation	No	No	Yes
Direct sulphation	No	No	No
Desulphation	No	No	No
NOx reactions	No	No	Yes
Heat transfer	Yes	Yes	Yes

3 Model frame

The main purposes of the present model are to support the development and the design of new CFB units, to provide a tool for optimization, trouble-shooting and risk assessment studies of existing units, and to provide a frame for further development of various sub-models. The model code is written in Fortran-95 language. The model frame is illustrated in Figure 3.1. It includes a three-dimensional description of the furnace, which is linked to separate sub-models, which describe the hot loop processes: separators, return legs, and possible external heat exchangers. The following subchapters describe the model frame and different sub-models at general level. The sub-models for fuel and sorbent reactions are presented in more details in Chapters 4 and 5.

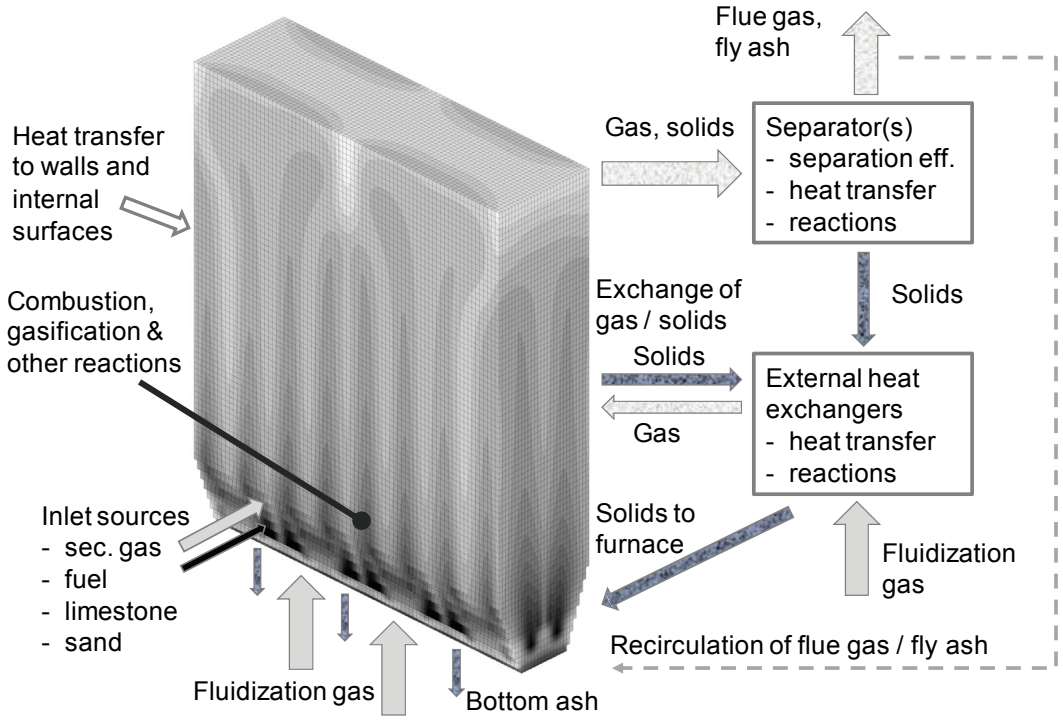

Figure 3.1. Model frame (Myöhänen and Hyppänen, 2011).

3.1 Model features

The model combines fundamental balance equations with empirical correlations, which enables practical calculation of full-scale CFB furnaces. The sub-models include fluid dynamics of solids and gases, fuel combustion and limestone reactions, comminution of solid materials, homogeneous reactions, heat transfer, sub-models for separators and external heat exchangers, and a post-solver for nitrogen oxides.

The furnace of the CFB boiler is modelled three-dimensionally by applying a control volume method to discretize and solve the various balance equations in a steady state condition. The calculation mesh is structural with hexahedral calculation cells. The balance equations are solved by the first order upwind differencing scheme and the Gauss-Seidel method with successive overrelaxation. The solved 3D balance equations include:

- total gas (continuity and momentum),
- total solids,
- fuel reactions and species (moisture, volatiles, char),
- sorbent reactions and species ($CaCO_3$, CaO, $CaSO_4$, CaS, inert),
- homogeneous reactions and gaseous species (O_2, CO_2, H_2O, SO_2, CO, H_2, CH_4, C_2H_4, C_g, H_2S, NO, N_2O, HCN, NH_3, Ar, N_2),
- energy (heat transfer within suspension and to surfaces, temperature field).

The boundary conditions of the model include the different gas and solid feeds as local volumetric source terms and temperature profile of cooling fluid (i.e. water or steam) specified as a function of height for furnace walls and specified separately for each internal heat transfer surface (e.g. superheaters).

The solid feeds can be fuels, sorbents (limestones) and inert make-up (sand) materials. The number of each solid feed material is not limited, thus the model can simulate multifuel and multisorbent cases. All solid materials are divided to six particle size fractions in order to simulate the continuous particle size distributions and the comminution of particles.

The gaseous feed types include primary gas through grid, secondary gas, fluidization gases entering the external heat exchangers and return legs, and burner gases. The number of each gas feed type is not limited and each of them can be divided to number of feed points, e.g. secondary air to various nozzles.

Recirculation of flue gas and/or fly ash can be included to the model. These are then specified as separate sources appearing in the furnace model. The compositions of recirculated streams are the mass flow averaged compositions of the flue gas and fly ash streams exiting the separators and thus affected by various sub-models, e.g. mixing of reactants and combustion modelling in furnace and fractional collection efficiencies of separators.

In addition to basic process calculation, formation and reduction of different NOx-species (NO, N_2O, HCN, NH_3) can be determined by a post-solver.

The visualization of the three-dimensional model results is done either in a dedicated Matlab-application written for this model or in a generic visualization software Tecplot. The overall model results and averaged one-dimensional profiles are written to text files.

3.2 Model structure and flow chart of the main solver

Figure 3.2 illustrates the model structure. The code is divided into a main program and four module groups, each of which consisting of various modules and subroutines. The different module groups exchange data with each other as indicated by the arrows. The main tasks of the module groups are described below.

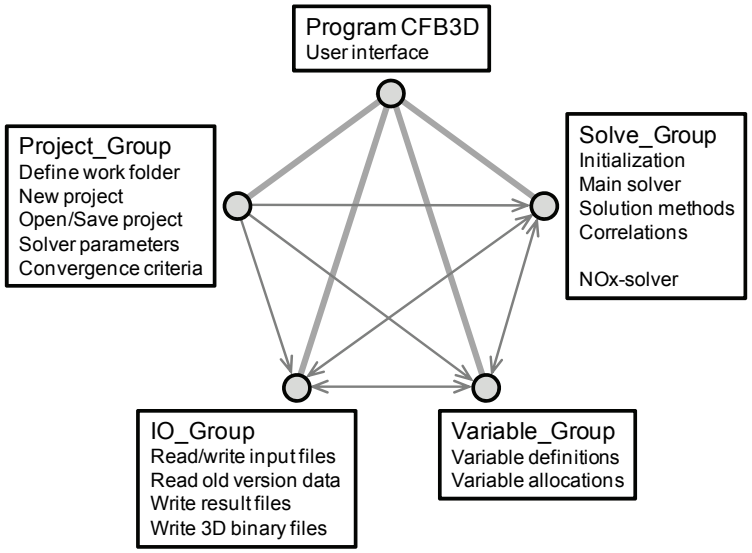

Figure 3.2. Model structure and module groups.

The execution of the code is controlled by a graphical user interface, which is determined in the main program. The main program calls the various modules, which are handling the project definitions, file operations, definition and allocation of variables, and calculations.

The project group defines project specific general data, such as the project name, work folder, short description of project, solver parameters (selection of models), and convergence criteria. The general data are saved to a project file.

The input/output group reads and writes the input and output data files. The input data is given in two files, which are generated by using Excel: one defines the boundary conditions and model parameters and the other defines the geometry and mesh. The model can read input files produced by earlier versions of the code as well. The overall results and one-dimensional average profile data are written to comma separated text files (CSV) for further processing in Excel. The three-dimensional results are written to binary files, which can be studied by visualization software. In addition, this module group allows writing the whole calculation data in binary format enabling to use this as an initial state for a subsequent calculation or for other calculation cases.

The variable group includes the definition and allocation of shared variables. Calculation variables are dynamically allocated based on the input data, e.g. number of gas and solid feeds and mesh size.

The solver group includes initialization of the calculation variables, the main solver, different solution algorithms, correlations and a post-solver for nitrogen oxides. Figure 3.3 presents a flow chart of the main solver.

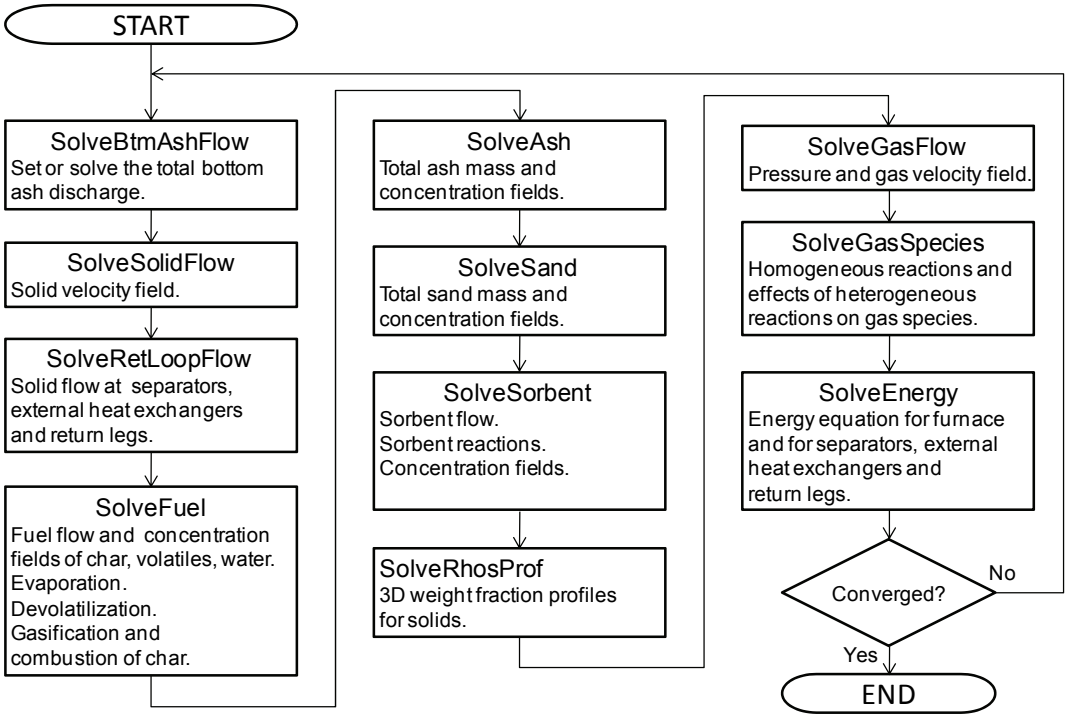

Figure 3.3. Flow chart of the main solver.

Before invoking the main solver, the calculation data must be initialized: either by an initialization subroutine or by reading existing earlier data as the starting state. Thus, during the first call of the main solver routine, the model has already defined reasonable flow fields, gas concentrations and temperature fields enabling the calculation. The execution of different solver modules is controlled by user, e.g. the solution of energy equation (SolveEnergy) can be skipped, if this is wanted for any purposes. Similarly, the material specific modules are not called, if the material does not exist, for example, if the model case does not include any limestone feed, the SolveSorbent-module is not called.

3.3 Particle size fractions and comminution of solids

In a population balance approach, the continuous particle size distribution is discretized to particle size fractions. Each particle size fraction then represents a group of particles with defined range (e.g. 125 – 180 µm). In this model, all solid materials (combustible fuel, ash, sand, limestone) are divided to six particle size fractions and the comminution of solids is simulated by a rate model, in which the mass change is proportional to the mass (Loschkin, 2001; Pikkarainen, 2001). For example, the mass change due to comminution from particle size *i* to particle size *j* can be expressed:

$$q_{m,Cij} = k_{C,ij} m_i \tag{3.1}$$

In the above, the term $k_{C,ij}$ is a comminution coefficient, which is defined in the input data. Figure 3.4 illustrates comminution paths from coarser to finer fractions. The comminution coefficients are determined between each size fraction. Agglomeration of particles can be simulated as well, but normally the particle size is decreasing due to mechanical wear of particles, temperature shocks and effects of chemical reactions (e.g. breaking of char particles during combustion).

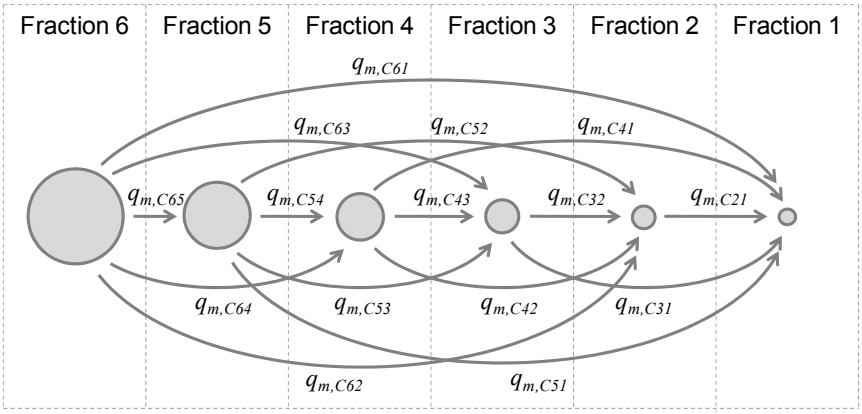

Figure 3.4. Comminution paths from coarser to finer fractions.

The number of size fractions is relatively small mostly due to practical limitations of the laboratory analyses, which are applied for characterization of solid materials and validation of the model. In characterization and validation studies, the different solid samples are fractionated by sieving and compositions analyzed for each particle size fraction. Increasing the number of size intervals would increase the time and cost of the analyses and increase the measurement errors related to sieving as the mass share of each fraction would be smaller.

For fuel and limestone, the comminution effects have been included to three-dimensional transport equations. The mass of solids in cell volume dV can be expressed with volume fraction of solids ε_s and material density ρ_s:

$$m_{i,dV} = \int_V \varepsilon_{s,i}\rho_{s,i}\, dV \tag{3.2}$$

The steady state total mass change due to comminution for particle size fraction i in cell volume dV includes comminution from fraction i to other size fractions j and comminution from other fractions j to size fraction i. The net mass flow due to comminution for fraction i is then:

$$\int_V q'''_{m,Ci}\, dV = \int_V \sum_{j,j\neq i} k_{C,ij}\varepsilon_{s,i}\rho_{s,i}\, dV - \int_V \sum_{j,j\neq i} k_{C,ji}\varepsilon_{s,j}\rho_{s,j}\, dV \tag{3.3}$$

Ash and sand are not taking part to any reactions, thus, the solution process is simplified and the mass change due to comminution is included to zero-dimensional balance equations and determined for total fractional masses m_i. The total net mass flow due to comminution for particle size i is

$$q_{m,Ci} = \sum_{j,j\neq i} k_{C,ij}m_i - \sum_{j,j\neq i} k_{C,ji}m_j \tag{3.4}$$

Examples of determined comminution rate coefficients for different solid materials are found in works by Loschkin (2001) and Pikkarainen (2001).

3.4 Modelling of solid concentration and solid flow fields

The SolveRhosProf module determines three-dimensional weight fraction fields for different materials and particle size fractions by applying empirical equations for solid concentration profiles. The total vertical solid concentration profile as a function of height follows an equation given by Johnsson and Leckner (1995):

$$\varepsilon_s(h) = \left(\varepsilon_{s,btm} - \varepsilon_{s,top}e^{c_{di}H}\right)e^{-c_{tr}h} + \varepsilon_{s,top}e^{c_{di}(H-h)} \tag{3.5}$$

The parameters include volume fraction of solids at bottom and top of the furnace ($\varepsilon_{s,btm}$, $\varepsilon_{s,top}$), coefficients for transient and dilute section (c_{tr}, c_{di}), and total height (H). These

are based on measured vertical pressure profiles or separate correlation models, which have been developed from field measurements.

The material and particle size fraction specific profiles of inert materials and total sorbent have similar shape as the total profile, but the equation parameters are adjusted so that the total integrated masses over the total height match the different masses solved from furnace mass balance. The solid concentration fields of fuel and sorbent species have been solved separately as described in Chapters 4 and 5.

In horizontal direction, the solid concentration is assumed flat, except for a denser wall layer, which is solved as superimposed over the main furnace model. The volume fraction of solids at wall layer is determined as a function of the local average volume fraction of solids (ε_s) across the cross-section of the furnace:

$$\varepsilon_{s,wl} = \varepsilon_{max}\left[1 - \exp\left(-a\frac{\varepsilon_s}{\varepsilon_{max}}\right)\right] \tag{3.6}$$

In the above equation, the term ε_{max} is the maximum volume fraction (e.g. packing density) of solids and the term a is an empirical constant. Figure 3.5 compares the equation with literature data from Zhang et al. (1993) and Nicolai et al. (1993).

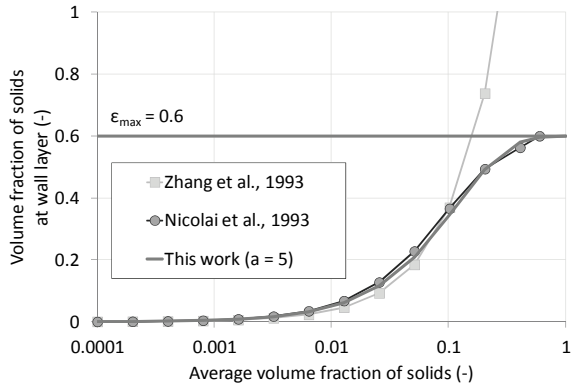

Figure 3.5. Volume fraction of solids at wall layer vs. average volume fraction of solids.

The internal circulation of solids due to downflow of solids at the walls is modelled by a wall layer model, which is superimposed over the main furnace model. A wall layer is formed to all vertical walls in the furnace, including the internal heat exchanger structures. It is reasonable to assume that large internal panels, e.g. hanging superheaters, have the same effect as the furnace walls on the solids flow (Reh, 2003), thus they have been modelled by the same principles.

The mass balance of a wall layer cell is defined by Equation 3.7 and illustrated in Figure 3.6. The solid mass flow entering the wall layer ($q_{m,ic}$) and the back mixing from wall

layer to main flow ($q_{m,ib}$) are proportional to local solid concentration, which has been determined from empirical correlations (Equations 3.5 and 3.6). The down flowing mass flow at the wall layer is determined from Equation 3.7. This is solved from roof to bottom of the furnace, each wall layer cell receiving mass flow from above and exchanging mass with the main furnace domain.

$$q_{m,wl,btm} = q_{m,wl,top} + q_{m,ic} - q_{m,ib} \tag{3.7}$$

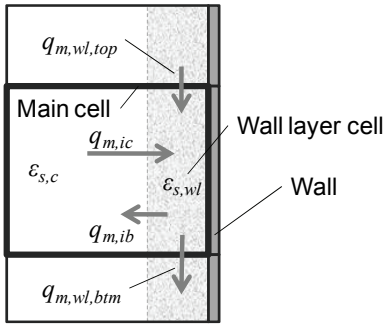

Figure 3.6. Mass flows in wall layer.

At the bottom of the furnace, the accumulated mass flow at wall layer is released back to main furnace flow. In the case of internal walls, which are not extending to the bottom of the furnace, e.g. hanging superheaters, the wall layer flow is released back to main furnace flow at the lower edge of the internal wall.

Figure 3.7 illustrates the mass flows by internal and external circulation of solids. The internal flow of solids through the wall layers has a large effect on the thermal balance of the furnace. Similar to external circulation of solids through the separators, the internal circulation of solids creates a heat capacity flow or a thermal wheel, which reduces the temperature gradients and results in a more uniform vertical temperature profiles. Thus, the model parameters, which define the local mass flow values to and from wall layer, are determined experimentally based on vertical temperature profile measurements.

The flow of solids through the wall layer and the heat exchange from wall layer to heat transfer walls produces a heat transfer model similar to mechanistic heat transfer models based on cluster renewal model (Dutta and Basu, 2003), but allowing for a more accurate description of the local temperatures by the three-dimensional description of the flow.

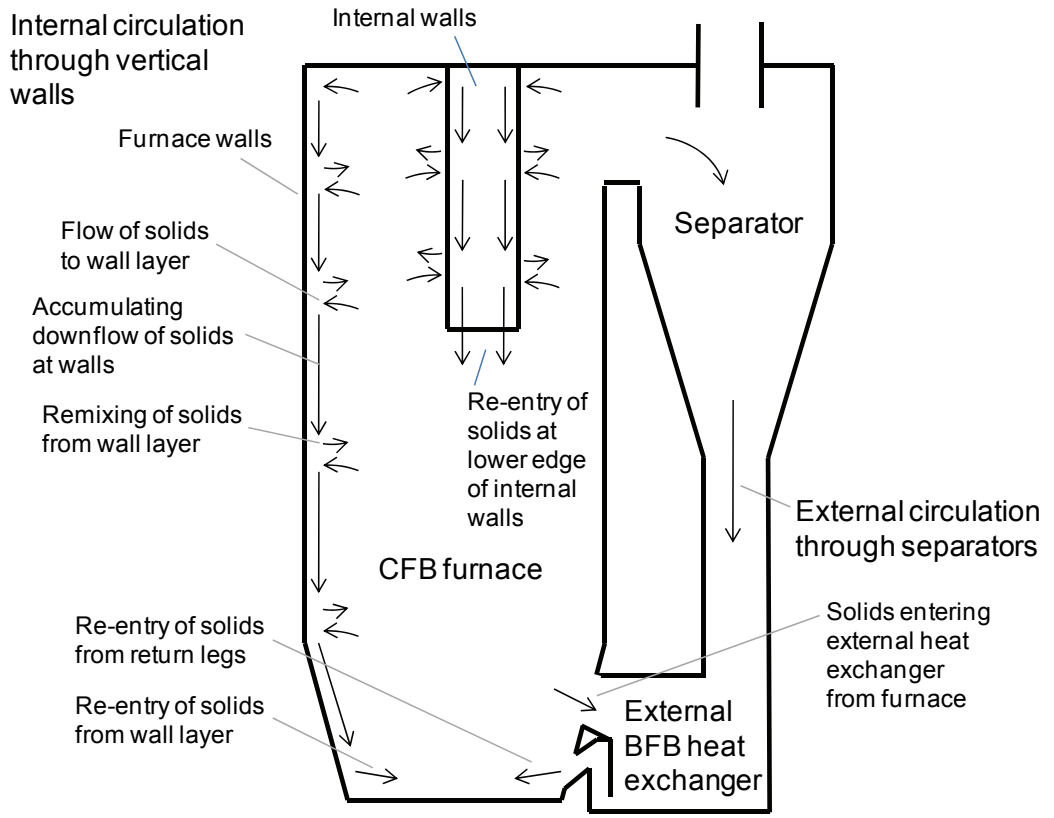

Figure 3.7. Internal and external circulation of solids in the model.

As the model only requires the knowledge of solid mass flows and heat capacity flows through the internal circulation and the wall layer model is superimposed over the main furnace model, the thickness or the velocity of the wall layer does not need to be solved. The solid concentration of the wall layer (Equation 3.6) is applied in the correlations defining the heat transfer coefficients.

The external circulation of solids entering the separators, i.e. the net solid flux across the furnace is determined by an empirical correlation, which is a function of superficial fluidization velocity and the average solid concentration at the upper part of the furnace, just below the furnace outlets. This sets the velocity of the solids at the furnace outlets. The velocity is assumed constant at all outlet faces and used for determining the boundary condition for solid flow model.

The solid mass flows to fly ash are determined by fractional collection efficiencies of the separators. The fractional collection efficiencies are based on measured fractional mass balances of circulating solids and fly ash. The remaining mass flow from separators is then released to downcomer legs and further to return legs or to external heat exchangers located in the return loop.

The solid mass flow from furnace to external heat exchangers is controlled by empirical correlation, which sets the velocity of solids and the maximum solid mass flux at the interfaces. The solid mass flow entering an external heat exchanger is then added to the circulating mass flow coming from a separator.

As the three-dimensional solid concentration field has been fixed by the empirical correlations and the different solid sources and sinks are known, the solution of the net velocity field of solids is possible by a potential flow approach. This is a steady state description of the flow field without the effects of vortices or transient mixing of solids. In the future, the target is to apply more comprehensive CFD flow model approaches (cf. Shah et al., 2009) , but for the moment, this is a simple method to produce an approximation of the solid convection to be applied in the energy equation. The local mixing effects due to vortices and fluctuating flow are considered by dispersion terms.

A flow potential P_{fs} is defined according to Equation 3.8, i.e. the gradient of P_{fs} is equal to mass flux of solids. The continuity equation for total solids includes convection, a source term and a reaction term (Equation 3.9).

$$\varepsilon_s \rho_s \mathbf{v}_s = \nabla P_{fs} \tag{3.8}$$

$$\oint_A \varepsilon_s \rho_s \mathbf{v}_s \cdot d\mathbf{A} = \int_V \phi_s''' \, dV + \int_V R_s''' \, dV \tag{3.9}$$

The source term includes the sources due to flow from return legs and solid feeds and sinks due to flow to bottom ash, wall layer and possible external heat exchangers connected to the furnace. The reaction rate term includes the mass changes due to different reactions. The potential difference across the furnace outlet faces is set based on the determined constant outlet velocity. This is necessary to set a reasonable velocity profile at the outlets. With a constant potential at the outlet, the mass flow would be much higher through the bottom section of the outlets, which would be contrary to the experience from measurements and modelling results by CFD models.

Combining the above equations, the potential field P_{fs} is solved, after which the solid velocity field is defined from Equation 3.8. The solved solid velocity field represents the net velocity of total solids, i.e. combined solid materials and particle size fractions. The flow fields for fuel and sorbent are solved separately – these are presented in Chapters 4 and 5. However, at the furnace outlets, all solid materials are assumed to flow at the same velocity, which has been solved from the total solid flow field. This assumption does not have a large effect on the solved flow fields inside the furnace: if a solid material has been able to flow to the furnace outlet, it can be removed at the same velocity as all the other solids.

The bottom ash is removed from the furnace at the specified locations and according to specified discharge rates or according to solved mass balance. The composition of the

bottom ash flow depends on the composition of solids at the bottom discharge points. Classification of bottom ash can be included, i.e. returning certain particle size fractions back to furnace at the discharge points.

The solution of the total mass balance can be based on two optional methods. In the first method, the total bed mass is known, in which case the total bottom ash flow rate is solved in module SolveBtmAshFlow from the overall mass balance. In the second method, the bottom ash flow rate is known and the total bed mass is solved based on the solution of the total mass of each solid material (fuel, ash, sand, sorbent). Both methods produce the same results, but either the total bed mass or the total bottom ash flow rate must be fixed to reach the steady state result.

3.5 Modelling of pressure and gas flow field

The pressure field and the gas velocity field are solved in SolveGasFlow. The solution is based on defining the continuity of gas (Equation 3.10) and a simplified momentum balance for gas (Equation 3.11), in which the momentum exchange between the solids and gas is defined by a macroscopic drag term β_m.

$$\oint_A \varepsilon_g \rho_g \mathbf{v}_g \cdot d\mathbf{A} = \int_V \phi_g''' \, dV + \int_V R_g''' \, dV \tag{3.10}$$

$$\int_V \beta_m \varepsilon_s \rho_s (\mathbf{v}_g - \mathbf{v}_s) \, dV = -\int_V \varepsilon_g \nabla P \, dV \tag{3.11}$$

The continuity equation includes terms for convection (left side), sources, and reactions. The source term includes the different gas feeds as volumetric sources. Thus, for example the penetration of secondary air jets is not solved in the model, but must be provided based on measurements or additional CFD modelling. The reaction term includes sources and sinks due to different heterogeneous reactions.

In the momentum equation, the drag force (left side) is assumed equal to the force due to pressure gradient, which is the same assumption as in the initial model version (Rainio, 1989). Many affecting forces, e.g. inertia, gravity, and viscous stress, have been neglected and this approach does not work in cases with very small solid concentration. A more universal formulation is being developed, but this has not been included to this thesis work.

Combining the above equations, the pressure P is solved, after which the gas velocity field is defined from Equation 3.11. The solved velocity field is the net velocity of gas. In addition, the gases are mixing by dispersion, which is considered when solving the gas species.

3.6 Combustion model

The SolveFuel module solves fuel flow field, evaporation, devolatilization, and gasification and combustion of char as well as comminution of fuel particles. From this, the three-dimensional concentration fields of moisture, volatiles and char in fuel for each particle size fraction are determined. The development of the combustion model has been a core part of this work and it is presented in details in Chapter 4.

3.7 Sorbent model

The SolveSorbent module solves the flow fields, reactions and comminution of sorbents. From these, the concentration fields of sorbent species are determined for each particle size fraction. The sorbent model is targeted for calcitic limestones. The sorbent is simulated as a mixture of main reacting species ($CaCO_3$, CaO, $CaSO_4$, and CaS) and inert material. The current model solves the reactions, which are occurring in combustion conditions: calcination, carbonation, sulphation, direct sulphation and desulphation. The development of the sorbent model has been a core part of this work and it is presented in details in Chapter 5.

3.8 Solution of inert materials

The SolveAsh and SolveSand modules solve the total masses of ash and sand and their three-dimensional solid concentration fields. The residence time of ash and make-up sand is long and these compounds do not participate in the reactions, thus the solution principle is simpler than with combustible fuel and sorbent. The flow field of the inert materials is set to follow the flow field of total solids, which is solved in SolveSolidFlow. The total mass balances of ash and sand for each particle size i are determined by Equation 3.12, which takes account for feed rates ($q_{m,F,i}$), comminution between fractions (k_C), discharge rates to bottom ash ($k_{B,i}$) and fly ash ($k_{E,i}$), and recirculation of fly ash ($\eta_{RC,i}$) (cf. Figure 2.6):

$$q_{m,F,i} = \left[k_{B,i} + (1 - \eta_{RC,i}) k_{E,i} + \sum_{j,j \neq i} k_{C,ij} \right] m_i - \sum_{j,j \neq i} k_{C,ji} m_j \tag{3.12}$$

The rate constants for bottom ash and fly ash flow rates are defined from the solved material and fraction specific mass flows. The fractional bottom ash flow is determined from the specified total bottom ash flow and the composition of solids in the discharge points. The fractional fly ash flow is determined from the total sum of the fly ash flows solved for each separator, thus these are affected by the mass flow of solids entering the separators and the grade efficiencies of each separator. The recirculation of fly ash can be accounted for by user-defined coefficients. The comminution rates are defined

directly in the input data as well. The total (fractional) masses of sand and ash are distributed to furnace by using empirical correlations, which are set in SolveRhosProf.

3.9 Solving of gas species

The heterogeneous reaction rates are solved in material specific modules: SolveFuel and SolveSorbent. The effect of the heterogeneous reactions on the gas species is included in the SolveGasSpecies, which is solving the homogeneous reaction rates and the weight fractions w_r of different gas species r. A species transport equation is defined as follows for all modelled gas species:

$$\oint_A w_r \varepsilon_g \rho_g \mathbf{v}_g \cdot d\mathbf{A} - \oint_A \varepsilon_g \rho_g D_g \nabla w_r \cdot d\mathbf{A} = \int_V \phi_r''' \, dV + \int_V R_r''' \, dV \tag{3.13}$$

The equation includes 1) convection, 2) dispersion, 3) source term, and 4) reaction term. The net velocity field of gas was solved earlier (Chapter 3.5).

The dispersion coefficient (D_g) is determined in input data separately for lateral and vertical directions and separately for different furnace sections. This allows for tuning the mixing of gas species at different sections of the furnace: the dense bottom zone, the splash zone, the dilute upper section and the exit zone.

As the direction of the gas flow in the furnace is mostly vertical, the convection is governing the vertical mixing and the dispersion is governing the lateral mixing of gas species. The dispersion coefficient can be determined based on gas profile measurements in large-scale CFB units. However, in most cases, the measurements are too scarce for detailed, zone specific setting of the dispersion coefficient and acceptable results have been achieved by using constant values for the whole furnace.

The model can simulate for example the gas mixing pattern presented in the model by Luecke et al. (2004), in which the horizontal dispersion is neglected at the bottom zone and considered at the upper zones. However, in many studies, the lateral gas dispersion is higher in the bottom and splash zones than in the dilute zone (Gayán et al., 1997; Sternéus et al., 2000). In these studies, the lateral dispersion coefficients were in the order of 0.02 m^2/s or lower. In the 3D modelling study by Luecke et al. (2004), the dispersion coefficients validated by measurements were however much higher, in the order of 0.07 m^2/s. An extensive review of the dispersion coefficients is given in a work by Tanskanen (2005).

The source term includes the different gaseous feeds. The reaction term includes the species-specific effects of heterogeneous and homogeneous reactions. The combustion reactions are modelled by Arrhenius-type equations, which are described in more details in Chapter 4. Due to relatively coarse mesh and the transient, fluctuating flow, complete

mixing of gas species within a calculation cell cannot be assumed and the kinetic reaction rate expressions from literature cannot be directly applied, but need to be adjusted based on field measurements.

3.10 Energy equation

The SolveEnergy module combines the heat effects of different input mass flows, reactions and heat transfer inside the furnace and to the surfaces and solves the temperature field. The heat balance of the furnace domain is controlled by Equation 3.14. It includes:

- convection of gas and solids (line 1),
- dispersion of gas and solids (line 2),
- source terms due to sensible enthalpies of gas and solid sources and additional volumetric heat sources (line 3),
- reaction enthalpies, i.e. heat due to different heterogeneous and homogeneous reactions as a difference between formation enthalpies of products (*pt*) and reactants (*rt*) (line 4),
- direct heat transfer from cell to surrounding walls (line 5).

$$
\begin{aligned}
&\oint_A \varepsilon_g \rho_g c_{pg} T_c \mathbf{v}_g \cdot d\mathbf{A} + \oint_A \varepsilon_s \rho_s c_{ps} T_c \mathbf{v}_s \cdot d\mathbf{A} \\
&- \oint_A \varepsilon_g \rho_g D_g c_{pg} \nabla T_c \cdot d\mathbf{A} - \oint_A \varepsilon_s \rho_s D_s c_{ps} \nabla T_c \cdot d\mathbf{A} \\
&\quad = \int_V \left(\phi_g''' c_{pg} T_g + \phi_s''' c_{ps} T_s + \varphi''' \right) dV \\
&+ \int_V \left(\sum_{rt} \frac{\partial m_{rt}'''}{\partial t} \frac{H_{0,rt}}{M_{rt}} - \sum_{pt} \frac{\partial m_{pt}'''}{\partial t} \frac{H_{0,pt}}{M_{pt}} \right) dV \\
&- \oint_A \alpha_c (T_c - T_w) \cdot d\mathbf{A}
\end{aligned}
\tag{3.14}
$$

Most of the terms in the energy equation have been solved by the other sub-models, for example the gas and solid velocities and the reaction rates, or can be directly calculated from the solved parameters, such as the local heat capacities of solid and gas from the solved compositions. The heat transfer in return loop systems, i.e. separators, external heat exchangers and return legs, are solved in separate sub-models and the effects are included to the energy equation, for example as a source of solids from return legs.

The dispersion terms simulate the diffusion of energy within the suspension due to transient fluctuation and local mixing of gas and solids and due to radiation. The

dispersion coefficients have a large effect on the horizontal temperature gradients and these are validated by temperature profile measurements.

The total heat transfer to walls q_{tot} is combined of convective and radiative heat transfer from cell (i.e. dilute phase, cell temperature T_c) and convective heat transfer from wall layer (i.e. dense phase, wall layer temperature T_{wl}) as presented in Equation 3.15 and Figure 3.8.

$$q_{tot} = \alpha_c(T_c - T_w)A + \alpha_{wl}(T_{wl} - T_w)A \tag{3.15}$$

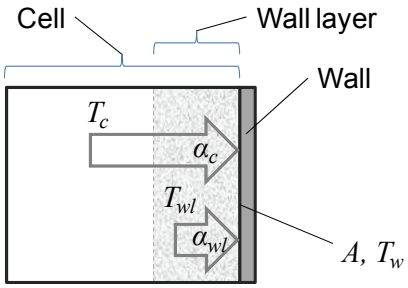

Figure 3.8. Heat transfer mechanism in the model.

The model principle is that the hot solids can flow from a main cell located beside a vertical wall to a superimposed wall layer cell. At the wall layer, the solids are accumulated and flow downwards while cooling and releasing heat to the wall. In Equation 3.14, the heat capacity flows of solids entering and exiting the wall layer are included in the solid convection term and source term respectively. The local temperature of the wall layer (T_{wl}) is solved from the energy balance, which includes the convection of solids between the main cell and the wall layer cell, convection of solids between the subsequent wall layer cells, and the heat transfer from the wall layer to the wall. The heat transfer coefficients are determined by empirical correlations.

The local fluid temperature, i.e. the temperature of water and steam inside membrane tubes, is given as a boundary condition. The temperature at the hot surface of the wall (T_w) is solved taking account for the effective wall thickness, heat conductivity of the wall and possible refractory lining, which can be specified for any heat transfer surfaces in the model. The heat transfer surface can be a furnace wall or an internal surface, in which case the surface is modelled as a zero thickness wall located between neighbouring cells. The mass transfer and energy transfer across an internal wall is prevented and the heat transfer properties (i.e. thermal conductivity and wall thickness) can be specified separately for both sides of the wall allowing simulating for example heat transfer panels, which have a refractory lining on one side of the panel.

3.11 NOx-model

The nitrogen oxide chemistry can be solved by an integrated NOx-solver after the main process calculation has converged. The principle is that the NOx-reactions do not have any significant effect on other process phenomena, such as fluid dynamics and heat transfer, thus they can be calculated by a post-processor without coupling the effects to other sub-models.

Figure 3.9 presents the considered reaction paths. Nitrogen in fuel is divided to nitrogen in volatiles and nitrogen in char as presented in Chapter 4. During devolatilization, the volatile nitrogen forms hydrogen cyanide (HCN) and ammonia (NH_3). As the char is combusted, the char nitrogen forms nitrous oxide (NO) and nitric oxide (N_2O). The different compounds react with each other and the surrounding gas atmosphere in different homogeneous and heterogeneous or catalytic reactions with char and CaO. The homogeneous reactions do not affect the concentration of main gas species (e.g. O2 and CO), only the NOx-species are solved (HCN, NH_3, NO and N_2O).

The validation of the NOx-model is still at an early stage and the results are mostly qualitative, but the model can be applied to study the different reaction mechanisms and the effects of changing fuel and air feeding arrangements (Vepsäläinen et al., 2009).

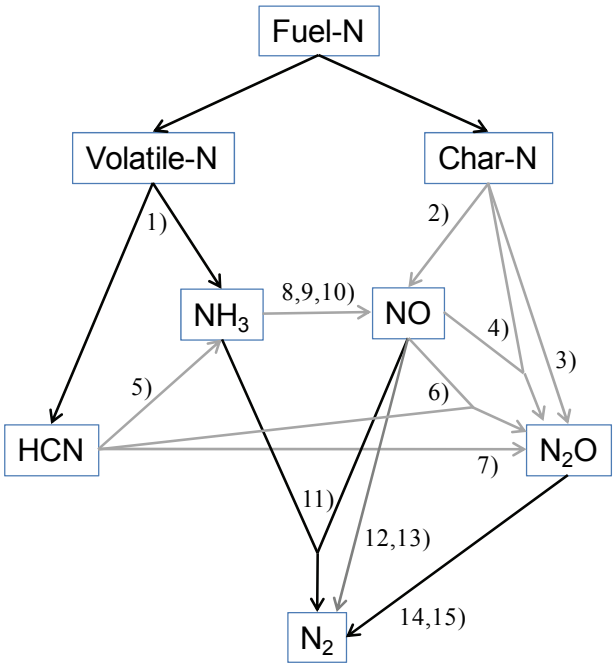

1) $N_{vol} \rightarrow \gamma\ HCN + (1-\gamma)\ NH_3$
2) $N_{char} + O_2 \rightarrow NO$
3) $2\ N_{char} + O_2 \rightarrow N_2O$
4) $N_{char} + O_2 + NO \rightarrow N_2O$
5) $HCN + O_2 \rightarrow NH_3$
6) $HCN + O_2 + NO \rightarrow N_2O$
7) $2\ HCN + O_2 \rightarrow N_2O$
8) $NH_3 + O_2 \rightarrow NO$
9) $NH_3 + O_2 + CaO \rightarrow NO$
10) $NH_3 + O_2 + char \rightarrow NO$
11) $NH_3 + NO \rightarrow N_2$
12) $NO + char \rightarrow N_2$
13) $NO + CO + CaO \rightarrow N_2$
14) $N_2O \rightarrow N_2$
15) $N_2O + CaO \rightarrow N_2$

Figure 3.9. Reaction paths of NOx-model.

4 Combustion model

4.1 Composition of fuel

As shown in Chapter 2.1, the circulating fluidized bed boilers apply a wide variety of fuel types extending from low grade fuels, such as waste derived fuels and biomasses, to high grade fuels, such as bituminous coal or anthracite. The composition of fuel has a major effect on the combustion behaviour and formation of emissions and it should be known to enable valid modelling of the furnace process.

In standard fuel analyses, the composition of fuel is determined by proximate (technical) and ultimate (elemental) analyses (Perry and Green, 1997). In a proximate analysis, the fuel is divided to char, volatiles, moisture and ash. In an ultimate analysis, the elemental composition of dry and ash free fuel (daf) is determined. In standard analyses, the elemental composition of char and volatiles is not separately determined, but the ultimate analysis shows the elemental composition of the total burning proportion of the fuel (Figure 4.1).

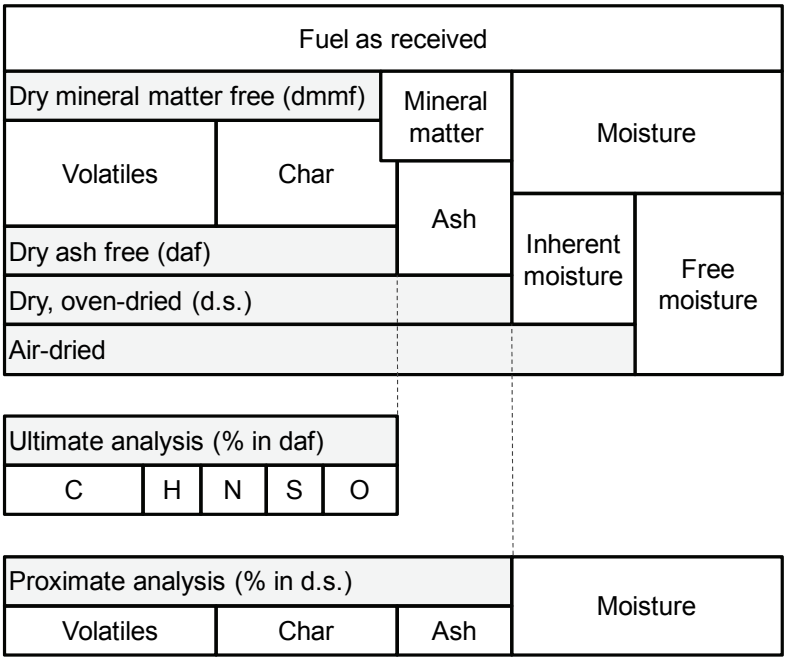

Figure 4.1. Standard fuel analyses and definitions.

In many simplified combustion models, the char is assumed to consist of carbon only and the elemental composition of volatiles is determined from the balance. This approach has been selected for example in the comprehensive 3D model presented by Luecke et al. (2004) and Wischnewski et al. (2010). This approach is valid for

approximate simulation of the combustion process and heat generation because in typical solid fuels over 90% of the char consists of carbon. However, in terms of emission modelling, this approach would be false as the nitrogen and sulphur are found both in char and in volatiles (Perry and Green, 1997). These elements produce the NO_x and SO_x emissions and as the combustion process is fundamentally different for char and volatiles, the distribution of these elements should be known in order to simulate the formation of emissions three-dimensionally.

In this work, different fuel samples were analyzed for determining the elemental composition of char and volatiles. Table 4.1 presents standard fuel analyses of these samples as analyzed at Foster Wheeler Karhula R&D Center (Myöhänen and Takkinen, 2009). The coal samples have been categorized according to standard classification of coals by rank (ASTM D388, 1992). Other fuel types have been categorized by using commonly used terms for different fuel types. Figure 4.2 shows the higher heat value versus volatile content in dry, ash-free fuel samples. The tested fuels represent well the whole range of the typical fuels used in CFB combustion.

Table 4.1: Proximate and ultimate fuel analyses.

Fuel	Proximate analysis (% in d.s.)			Moisture	Ultimate analysis (% in daf)				
	Char	Volatiles	Ash	(%)	C	H	N	S	O
Petroleum coke	89.48	10.10	0.42	5.43	87.67	3.72	1.66	5.65	1.31
Anthracite	81.80	6.80	11.40	7.20	92.10	3.36	1.38	0.58	2.58
Medium volat. bituminous coal	56.50	22.60	20.90	7.80	87.61	4.91	1.45	0.51	5.52
High volat. bituminous coal	54.00	32.80	13.20	5.20	79.72	5.29	2.67	0.39	11.92
Subbituminous A coal (high S)	45.80	35.80	18.40	14.60	73.65	5.36	2.02	5.48	13.49
Subbituminous A coal	44.60	29.20	26.20	12.93	74.93	4.88	1.29	1.72	17.18
Subbituminous B coal	48.51	45.00	6.49	22.30	72.51	4.97	1.51	0.72	20.30
Subbituminous C coal	43.50	44.90	11.60	21.70	75.79	5.48	1.14	1.52	16.07
Lignite A coal	41.90	44.00	14.10	38.70	72.76	5.77	1.13	0.52	19.81
Lignite B coal (1)	36.50	46.10	17.40	45.76	68.64	5.81	0.65	0.70	24.19
Lignite B coal (2)	40.98	53.60	5.42	51.10	70.21	5.17	0.94	0.34	23.35
Lignite B coal (3)	28.90	42.60	28.50	51.50	64.48	5.36	1.39	2.98	25.79
Peat, foreign	31.68	61.80	6.52	48.50	57.55	5.11	2.32	0.50	34.51
Peat, domestic	25.97	66.70	7.33	46.70	56.98	6.13	2.95	0.23	33.72
Wood, Salix	16.99	80.80	2.21	48.40	51.95	5.85	0.33	0.04	41.83
Wood, chips	18.74	79.40	1.86	46.60	52.27	6.12	0.36	0.02	41.23
Wood, bark	18.92	78.40	2.68	58.10	52.71	6.06	0.25	0.02	40.96
Demolition wood (1)	17.92	76.00	6.08	30.43	50.36	5.72	1.97	0.13	41.82
Demolition wood (2)	19.10	76.00	4.90	24.90	50.68	6.26	0.99	0.16	41.91
Waste, recovered fuel (REF)	13.10	74.70	12.20	22.00	52.51	6.78	0.85	0.33	39.53
Waste, refuse derived fuel (RDF)	11.30	75.80	12.90	28.28	57.75	8.06	1.13	0.20	32.87

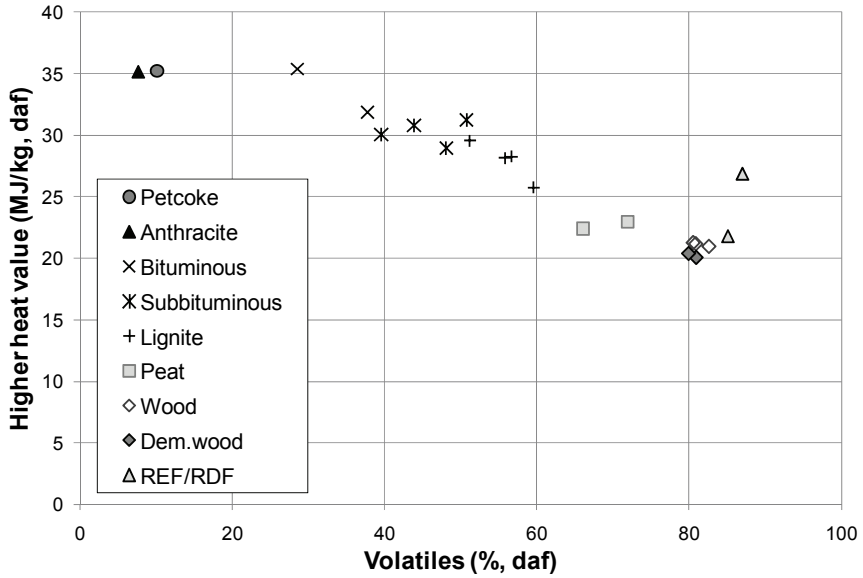

Figure 4.2. Higher heat value versus volatile content of the analyzed fuels.

The above samples were further analyzed by determining the elemental composition of char and volatiles. First, a standard determination of volatiles was performed according to DIN 51720. After this, the elemental composition of C, H, N and S in the remaining fuel residue (char + ash) was determined by using elemental analyzers. The amount of oxygen was then calculated from balance. In most fuel samples, the analyzed amount of oxygen in char was small and in some cases, the calculation from balance produced negative values (Figure 4.3). The determination of oxygen from balance is not accurate, because during determination of ash content, oxygen can be bound to inorganic ash compounds thus increasing the share of ash. Because of the uncertainties in the distribution of oxygen and in order to keep the combustion model simple, the oxygen was assumed to exist only in volatiles. From this, the composition of char could be determined. When the composition of char is known, the composition of volatiles can be determined from the difference to ultimate analysis of total fuel.

Table 4.2 presents the analyzed compositions of char. The elemental distribution in char is given for dry, ash free fuel so that it can be directly compared with values of total fuel given in Table 4.1. The relative distribution shows how the different elements are divided between char and volatiles. Figure 4.4 presents how the relative ratios are depending on the ratio of char in dry, ash free fuel. The relative ratio of carbon in char depends on the ratio of char, but the dependence is not linear. The relative ratio of hydrogen is small and it is approximately linearly depending on the ratio of char. The ratios of nitrogen and sulphur are not showing any clear dependence on the ratio of char.

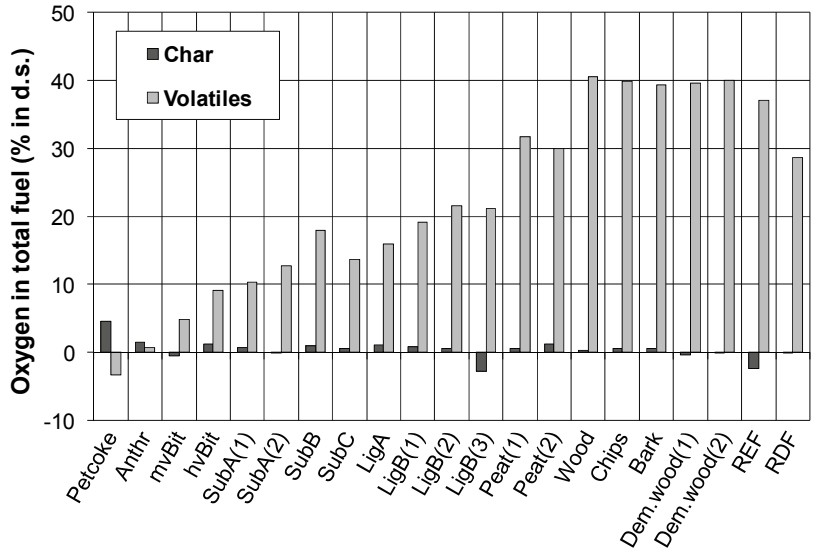

Figure 4.3. Determined distribution of oxygen in char and volatiles.

Table 4.2: Analyzed composition of char (assuming no oxygen in char).

Fuel	Elements in char (% in daf)				Relative distribution (-)			
	C	H	N	S	Cchar/Ctot	Hchar/Htot	Nchar/Ntot	Schar/Stot
Petroleum coke	82.94	0.52	1.66	4.73	0.946	0.141	1.000	0.837
Anthracite	89.86	0.51	1.38	0.58	0.976	0.153	1.000	1.000
Medium volat. bituminous coal	69.54	0.33	1.15	0.41	0.794	0.067	0.794	0.805
High volat. bituminous coal	60.00	0.39	1.56	0.26	0.753	0.073	0.583	0.667
Subbituminous A coal (high S)	51.64	0.24	1.17	3.08	0.701	0.045	0.581	0.562
Subbituminous A coal	58.24	0.19	0.92	1.08	0.777	0.039	0.714	0.629
Subbituminous B coal	50.33	0.29	0.89	0.37	0.694	0.058	0.590	0.511
Subbituminous C coal	47.55	0.23	0.73	0.69	0.627	0.043	0.641	0.458
Lignite A coal	47.50	0.23	0.77	0.27	0.653	0.041	0.682	0.524
Lignite B coal (1)	43.08	0.22	0.57	0.32	0.628	0.038	0.868	0.457
Lignite B coal (2)	42.25	0.26	0.62	0.19	0.602	0.051	0.655	0.573
Lignite B coal (3)	37.87	0.21	0.74	1.60	0.587	0.040	0.532	0.536
Peat, foreign	32.77	0.13	0.70	0.29	0.569	0.025	0.300	0.580
Peat, domestic	27.01	0.21	0.69	0.10	0.474	0.035	0.235	0.449
Wood, Salix	17.10	0.05	0.21	0.01	0.329	0.009	0.642	0.343
Wood, chips	18.81	0.07	0.21	0.01	0.360	0.012	0.589	0.319
Wood, bark	19.16	0.05	0.22	0.01	0.363	0.008	0.899	0.445
Demolition wood (1)	18.52	0.01	0.45	0.09	0.368	0.002	0.228	0.728
Demolition wood (2)	19.51	0.06	0.40	0.11	0.385	0.010	0.401	0.716
Waste, recovered fuel (REF)	14.42	0.01	0.25	0.24	0.275	0.001	0.289	0.734
Waste, refuse derived fuel (RDF)	12.62	0.02	0.29	0.05	0.219	0.002	0.258	0.241

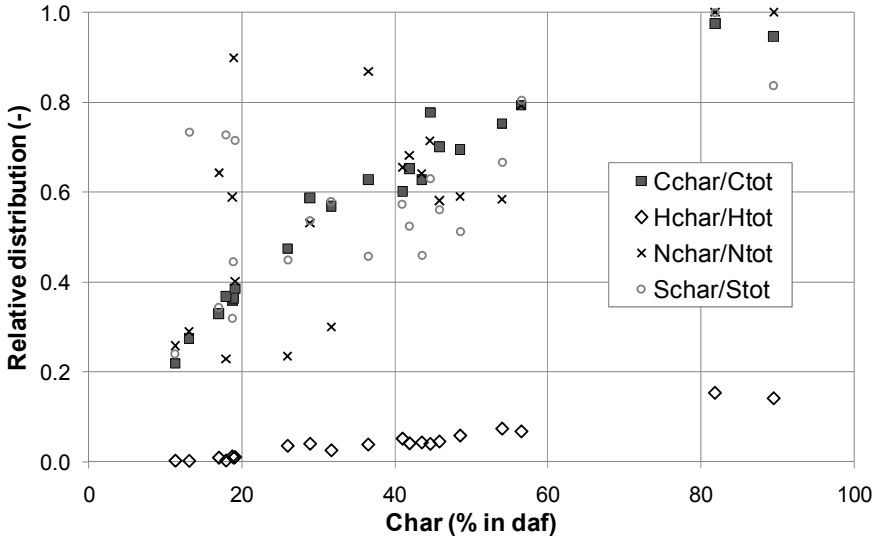

Figure 4.4. Relative distribution of elements in char versus proportion of char in dry, ash free fuel.

Correlations were developed for predicting the approximate relative distribution of hydrogen, nitrogen and sulphur. These were created by analyzing the dependencies between the relative distribution values (Table 4.2), and the values from standard fuel analyses (Table 4.1). The following correlations were achieved:

$$\frac{\mathrm{H}_{char}}{\mathrm{H}_{tot}} = 0.52 \exp\left[-33\left(\frac{\mathrm{H}}{\mathrm{C}}\right)\right] \tag{4.1}$$

$$\frac{\mathrm{N}_{char}}{\mathrm{N}_{tot}} = 0.088\, w_{char,daf}^{0.6}\left(\frac{\mathrm{N}}{\mathrm{C}}\right)^{-0.6} \tag{4.2}$$

$$\frac{\mathrm{S}_{char}}{\mathrm{S}_{tot}} = 0.14\, w_{char,daf}^{0.2}\left(\frac{\mathrm{H}}{\mathrm{C}}\right)^{-0.6} \tag{4.3}$$

in which

$\left(\frac{\mathrm{H}}{\mathrm{C}}\right), \left(\frac{\mathrm{N}}{\mathrm{C}}\right)$ = mass ratios of elements in ultimate analysis (-)

$w_{char,daf}$ = mass ratio of char in dry, ash free fuel (-)

The content of hydrogen, nitrogen and sulphur in char can be estimated with the above correlations. The content of carbon in char and the composition of volatiles can then be calculated from balance.

Figure 4.5 compares the relative elemental ratios calculated by correlations and the analyzed values. The coefficients of determination indicate a good fit for hydrogen and nitrogen. With sulphur, three fuels are behaving different to others: the two demolition wood samples and the recovered waste fuel sample (REF). Without these three samples, the correlation shows a good fit for sulphur as well. In these waste derived fuel types, the forms of sulphur can be different from the other fuel types, which is probably the reason for the deviation. Moreover, the analysis of sulphur may contain errors, because some of the sulphur may be bound to ash during the proximate analysis.

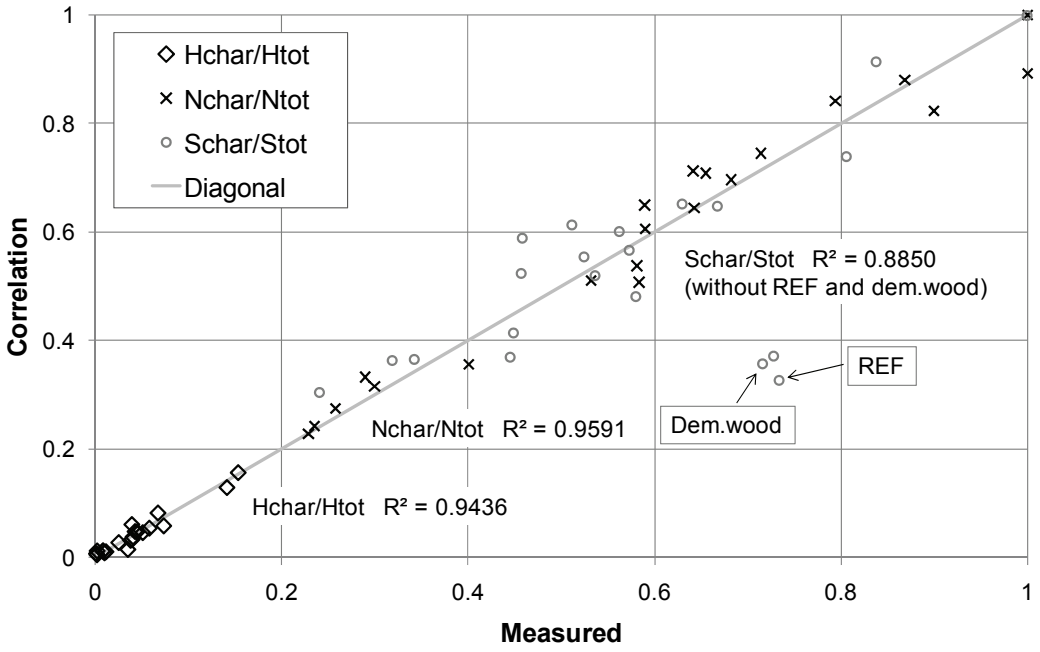

Figure 4.5. Measured vs. modelled elemental ratios.

Figures 4.6 – 4.9 compare the modelled and measured elemental compositions. The correlations predict the elemental compositions well and the absolute errors are small.

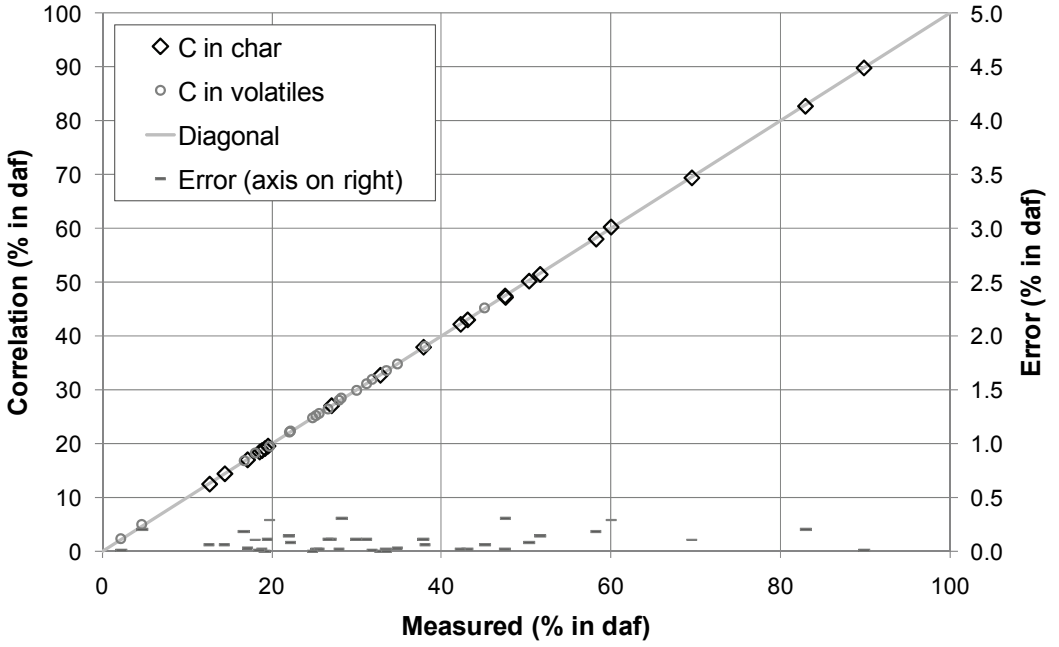

Figure 4.6. Carbon in char and volatiles. Measured values versus calculated from correlations.

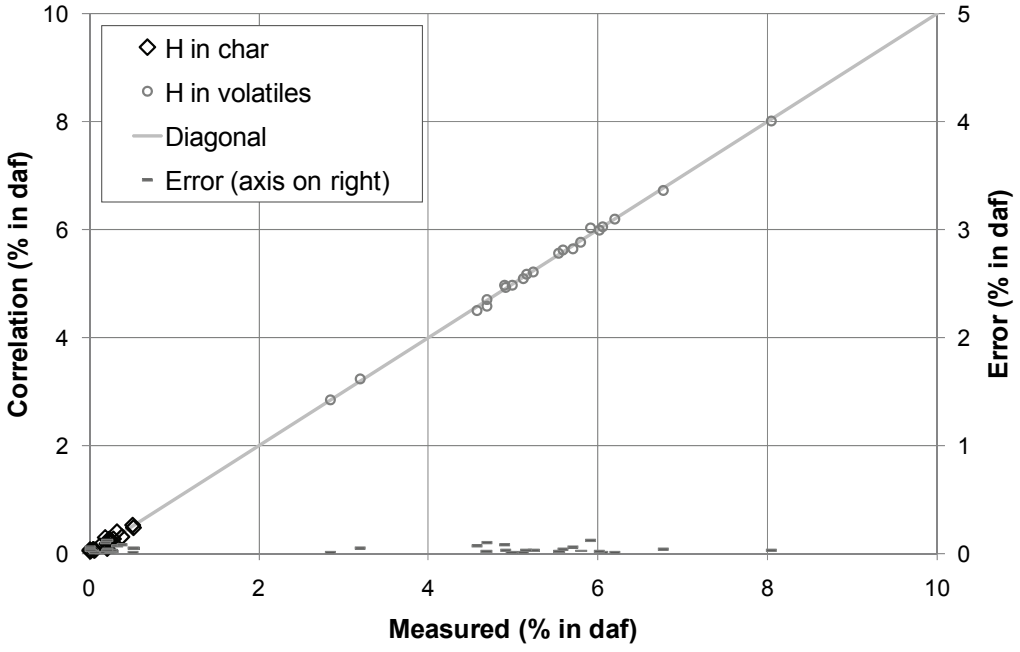

Figure 4.7. Hydrogen in char and volatiles. Measured values versus correlation.

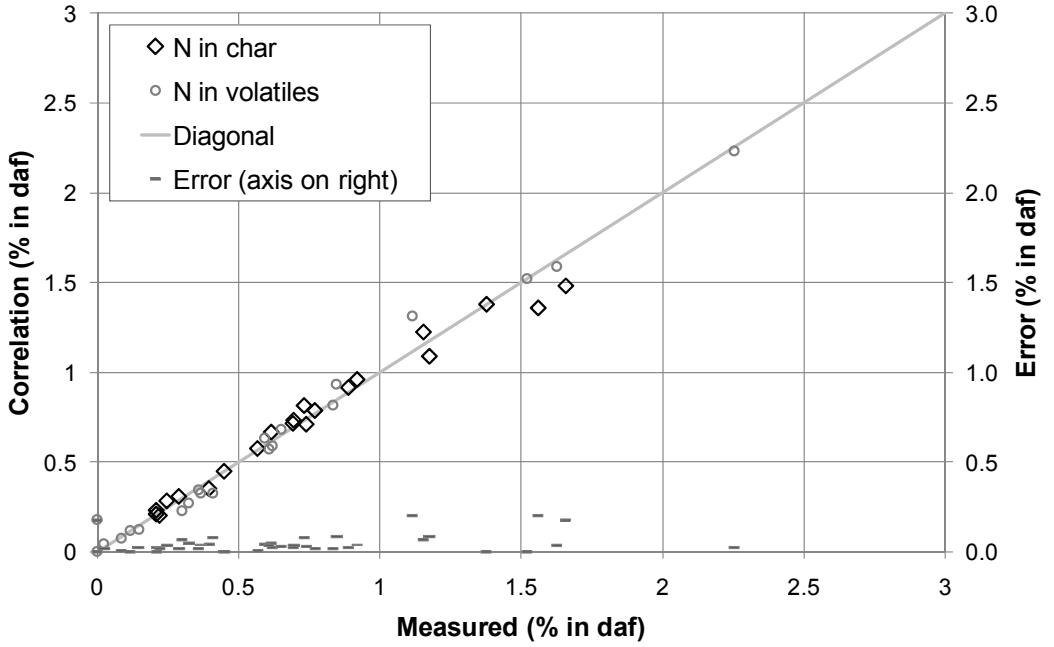

Figure 4.8. Nitrogen in char and volatiles. Measured values versus correlation.

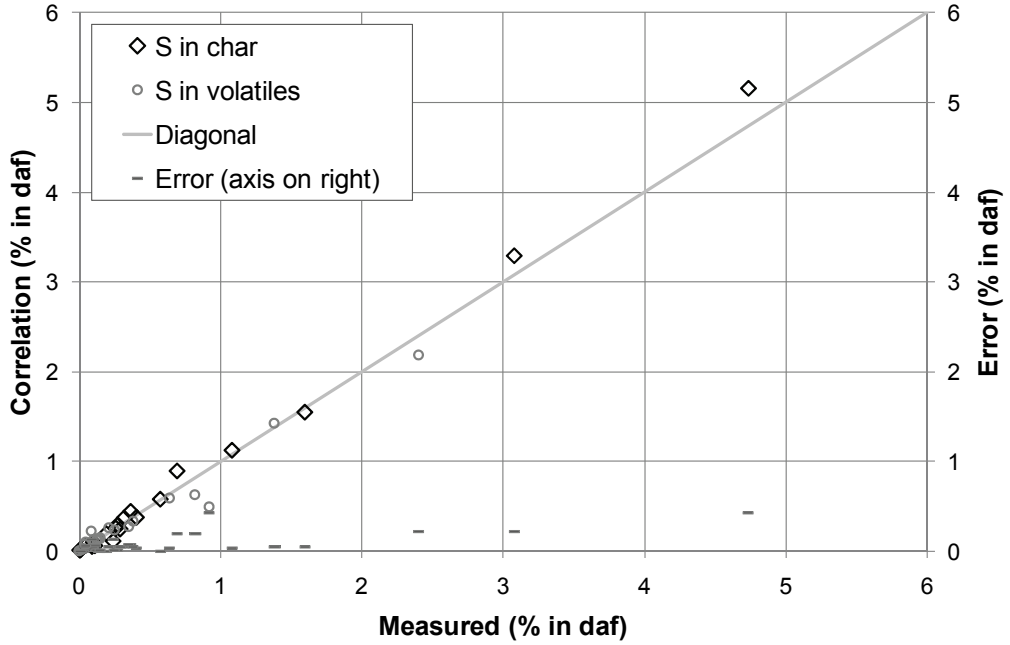

Figure 4.9. Sulphur in char and volatiles. Measured values versus correlation.

The above figures show that the developed correlations fit very well with the analyzed compositions. However, the formation of volatiles in actual furnace conditions is different from laboratory conditions. The devolatilization process of a fuel particle is affected for example by the surrounding temperature and gas atmosphere, heating rate of the particle, particle shape and size and the internal structure of the particle (Hayhurst and Lawrence, 1995; Migliavacca et al., 2005; Saastamoinen, 2006). Moreover, the real devolatilization process is transient: the lighter hydrocarbons are likely to be released faster than the heavy hydrocarbons, and the limit between the volatile proportion and remaining char is not exact, but depends on the retention time.

For example, the studies by Garcia-Labiano et al. (1996, fig. 2) of a lignite coal show how the release of sulphur to volatiles increases as a function of time and temperature and at 900 °C, the maximum yield to volatiles is about 45%. Based on the above defined correlation (Equation 4.3), the proportion of volatile sulphur with the given ultimate and proximate analysis is 51%, which would be approximately correct. On the other hand, another lignite sample in the same article shows a much smaller proportion of volatile sulphur (maximum about 17%) while the above correlation predicts 47%, thus the correlations are not valid for all fuels and conditions.

The developed correlations can be applied for approximate model estimations when no better data is available and when the combustion model needs to be kept simple to enable practical calculations of full-scale processes.

4.2 Combustion model

Figure 4.10 illustrates the combustion model. The fuel is divided to char, volatiles, moisture and ash by proximate analysis. As the fuel enters the furnace, the moisture is evaporated and the volatile components released due to presence of hot circulating solids and gas. The remaining char is burned in presence of oxygen or may react with water vapour and carbon dioxide in gasification reactions. The retention time of ash is very long compared with the other fuel components and in the model, the ash is handled separately (Chapter 3.8).

The total elemental composition of the burning fuel, i.e. char and volatiles, is determined by ultimate analysis. The elemental composition of char and volatiles can be specified as input values, if they have been determined e.g. by bench scale studies. If better data is not available, then the compositions can be estimated with the correlations presented in Chapter 4.1. The compositions are assumed constant during the reactions.

The combustible fuel and the ash materials are divided to six particle size fractions to allow simulation of fragmentation (Chapter 3.3). The compositions are assumed the same for all size fractions because usually the chemical analyses have been done for total samples only and fractional data is not available. The evaporation and devolatilization rate and the combustion rate of char are defined separately for each size fraction.

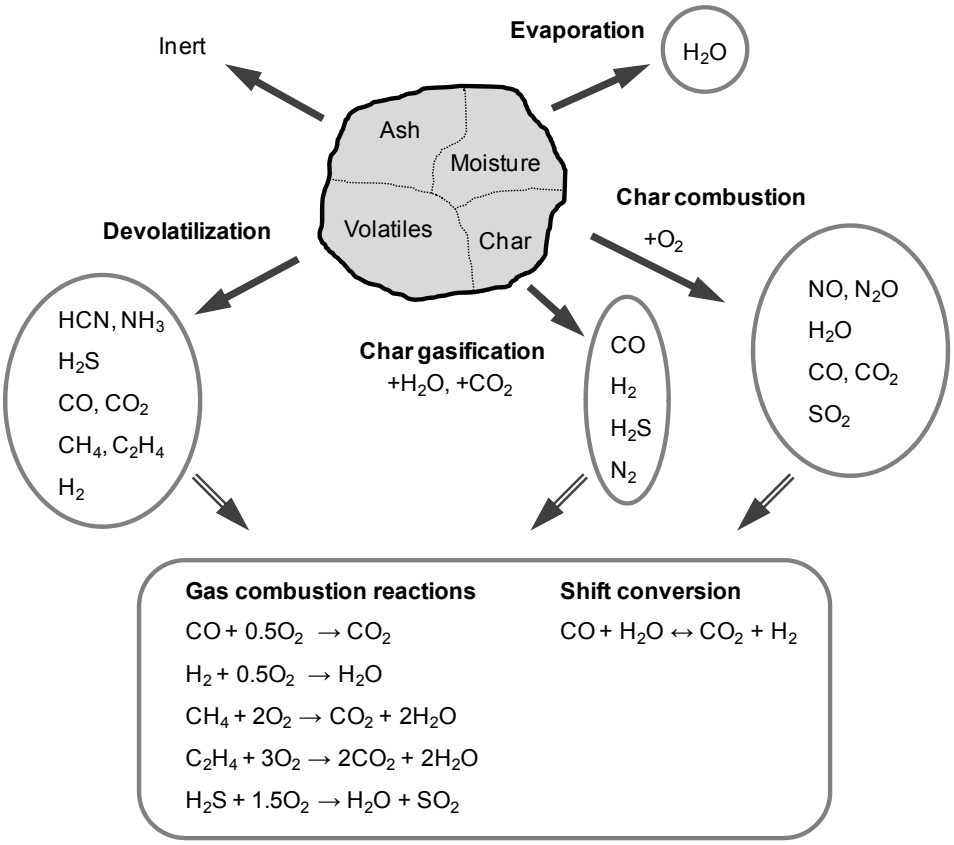

Figure 4.10. Principle of the combustion model.

In the model, a particle size fraction simulates a group of particles with particle diameter falling to defined range (e.g. 125 – 180 μm). This fraction of particles is represented by "effective particle size" d_p, which can be assumed to be close to arithmetic average. The evaporation, devolatilization and char combustion processes are occurring simultaneously, but they have indirect effects on each other. For example, during the devolatilization, combustible gases are released, which consume oxygen and thus reduce the combustion rate of char in the locations with high devolatilization rate.

The different combustible gaseous species, which are produced from devolatilization and char combustion and gasification, burn in the presence of oxygen. In gasification conditions, the carbon monoxide can react with water vapour to form carbon dioxide and hydrogen in shift conversion, which is a reversible reaction.

The following chapters present the different topics of the combustion model in details. The different phenomena have been illustrated by model results of a 300 MWe CFB furnace (Myöhänen, 2010). The furnace dimensions were 25.2 m x 7.6 m x 44.0 m. The fuel was a mixture of anthracite and petroleum coke. The layout of the furnace and the locations of fuel and air inlets and the calculation mesh are presented below.

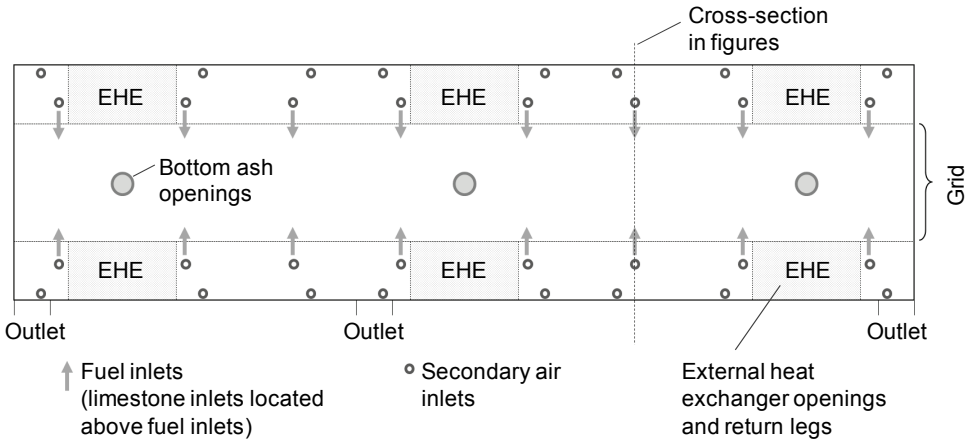

Figure 4.11. Furnace layout of a 300 MWe CFB looking from top.

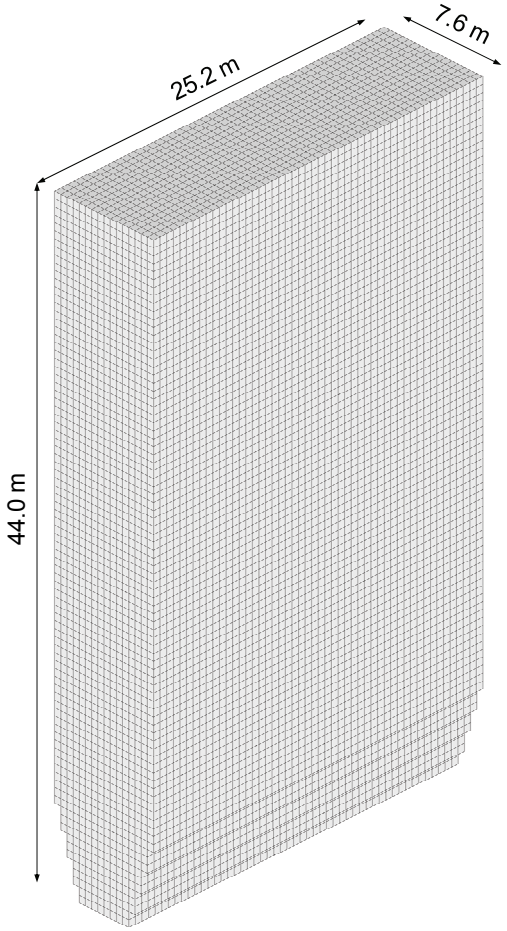

Figure 4.12. Calculation mesh of a 300 MWe CFB.

4.3 Continuity equations for fuel

The three-dimensional transport equations are defined for continuity of char, volatiles, and moisture and solved for each particle size fraction. The continuity equation for particle size fraction *i* of char is defined as follows:

$$\begin{aligned}&\oint_A \varepsilon_{char,i}\rho_{char}\mathbf{v}_{fuel,i}\cdot d\mathbf{A} - \oint_A D_{fuel,i}f_{0,i}\nabla\left(\frac{\varepsilon_{char,i}\rho_{char}}{f_{0,i}}\right)\cdot d\mathbf{A}\\ &= \int_V \phi'''_{char,i}\,dV - \int_V R'''_{char,i}\,dV\\ &- \int_V \sum_{j,j\neq i} k_{C,fuel,ij}\varepsilon_{char,i}\rho_{char}\,dV + \int_V \sum_{j,j\neq i} k_{C,fuel,ji}\varepsilon_{char,j}\rho_{char}\,dV\end{aligned} \tag{4.4}$$

The terms in the continuity equation are 1) convection, 2) dispersion, 3) sources, 4) reactions, 5) comminution to other size fractions, 6) comminution from other size fractions.

With usual fuel types (e.g. coal), the horizontal mixing of fuel at the lower part of the furnace can be approximated by dispersion which has a diffusional gradient function form (Pallarès and Johnsson, 2008a). At the upper part of the furnace, the vertical mixing is governed by ballistic movement, which leads to exponential decay in the concentration field.

In this model, the dispersion term includes a target profile f_0. This is a three-dimensional solid concentration field profile for char, which is based on an empirical function. The shape of the profile in vertical dimension is similar to the concentration field of total solids (Equation 3.5). In horizontal dimension, the target profile is assumed flat, which then eliminates the effect of term f_0 and reduces the dispersion term in horizontal direction similar to common diffusive flux by Fick's law (cf. Pallarès and Johnsson, 2008 and Luecke et al., 2004).

This approach means that the char is attempting to flow from input cells towards the target profile limited by dispersion coefficient D_{fuel}. If the reaction rate of char is fast compared with the dispersion term, then the char will burn close to the feed points. The dispersion coefficient can be defined separately for lateral and vertical directions, and for different regions of the furnace. Thus, it is possible to set different mixing behaviour for the bottom zone of the furnace, for example.

With usual fuel types, the mixing of fuel is governed by the above mechanism and the convection of fuel is set to zero, i.e. the fuel is spreading by dispersion only. With some fuels, the mixing of fuel can be different, for example, fine fuel particles (e.g. sawdust) can be entrained by gas and solid flow and not enter the bottom bed. A more

fundamental flow model applying a momentum balance between the fuel and gas-solid suspension is being developed, which may then eliminate the empirical target profile.

The source term (ϕ'''_{char}) includes the sources due to fuel flow feed and the solid flow from the return legs. In addition, it includes sinks due to bottom ash flow and mass flow to external heat exchangers, if they are exchanging material with the furnace. The reaction term (R'''_{char}) includes the sinks due to combustion and gasification of char. The comminution terms include the comminution between the different particle size fractions as described in Chapter 3.3.

The transport equations for volatiles and moisture are defined similarly as for char. It should be noticed that in this work, the term "volatiles" refers to volatiles in solid state, i.e. before devolatilization, not the gaseous species produced by devolatilization.

As the burning fuel is a mixture of char, volatiles and moisture, then the convection, dispersion and comminution terms for volatiles and moisture can be formulated from the above-defined terms for char. The following terms are introduced for determining the mass ratios between the reacting fuel species:

$$w_{vol,i} = \frac{\varepsilon_{vol,i}\rho_{vol}}{\varepsilon_{char,i}\rho_{char}} \tag{4.5}$$

$$w_{wat,i} = \frac{\varepsilon_{wat,i}\rho_{wat}}{\varepsilon_{char,i}\rho_{char}} \tag{4.6}$$

The earlier solved terms for convection, dispersion and comminution for char can be applied by multiplying the terms with the corresponding mass ratios for volatiles and moisture. Equation 4.7 presents a continuity equation for volatiles.

$$\begin{aligned}
&\oint_A w_{vol,i}\varepsilon_{char,i}\rho_{char}\mathbf{v}_{fuel,i}\cdot d\mathbf{A} - \oint_A w_{vol,i}D_{fuel,i}f_{0,i}\nabla\left(\frac{\varepsilon_{char,i}\rho_{char}}{f_{0,i}}\right)\cdot d\mathbf{A} \\
&= \int_V \phi'''_{vol,i}\,dV - \int_V R'''_{vol,i}\,dV \\
&- \int_V \sum_{j,j\neq i} w_{vol,i}k_{C,fuel,ij}\varepsilon_{char,i}\rho_{char}\,dV + \int_V \sum_{j,j\neq i} w_{vol,j}k_{C,fuel,ji}\varepsilon_{char,j}\rho_{char}\,dV
\end{aligned} \tag{4.7}$$

The continuity equation is the same for moisture, but replacing w_{vol} by w_{wat}.

The code solves the solid concentration field of char ($\varepsilon_{char,i}\ \rho_{char}$) and the mass ratios for volatiles and moisture ($w_{vol,i}$ and $w_{wat,i}$). The solid concentration fields for volatiles and moisture are then calculated from Equations 4.5 and 4.6.

The volumetric mass flow rates of the different heterogeneous reactions are controlled by empirical reaction rate equations, which are presented in Chapters 4.4 - 4.7.

The different combustible gaseous species, which are produced from devolatilization and char combustion and gasification, burn in the presence of oxygen. In gasification conditions, the carbon monoxide can react with water vapour to form carbon dioxide and hydrogen in shift conversion, which is a reversible reaction. These homogeneous reactions are handled in Chapters 4.8 and 4.9.

4.4 Evaporation and devolatilization rate

In simplified model approaches, the evaporation may be approximated to occur parallel to the devolatilization and controlled by the same conversion rate (Luecke et al., 2004). Thunman et al. (2004) separate three different conversion mechanisms for evaporation and devolatilization process and suggest a drying number (Dr) for identifying them. With a low drying number the evaporation and devolatilization are subsequent processes – the devolatilization starts after evaporation has been completed. With a high drying number, the processes are parallel and the devolatilization is controlled by drying. With $Dr \approx 1$, the processes are partly parallel and the devolatilization is affected by the moisture content. In a group of particles with a continuous particle size distribution, the different particles are in different stages of the evaporation and devolatilization and the two processes are always more or less parallel. This is often true for a single particle as well (Saastamoinen, 2006).

In this model, the evaporation and devolatilization rates are handled separately by two correlations and the effect of remaining moisture content on the devolatilization can be considered. The empirical parameters can be determined based on validation studies or based on more detailed particle models, e.g. Saastamoinen (2006).

The evaporation rate is controlled by a local rate constant k_{wat} (Equation 4.8). This is defined separately for each particle size fraction i, thus allowing to simulate the effect of the particle size. The rate constant can be given directly in the input data for each particle size fraction i or it may be defined according to Equation 4.9, which takes account for the particle size of the fuel fraction ($d_{p,i}$) and the local temperature (T):

$$R'''_{wat,i} = k_{wat,i}\varepsilon_{wat,i}\rho_{wat} \tag{4.8}$$

$$k_{wat,i} = a_{wat}\left(\frac{d_{p,i}}{d_{ref}}\right)^{b_{wat}} \exp\left(\frac{-E_{wat}}{RT}\right) \tag{4.9}$$

Parameters a_{wat}, b_{wat} and E_{wat} are constant model parameters and the term d_{ref} is a reference particle size, which has been set to 1250 µm.

The devolatilization process is similar to evaporation. The devolatilization rate is defined separately for each particle size either by a given rate constant k_{vol} or by a correlation, which considers the particle size ($d_{p,i}$), local temperature (T) and the local remaining moisture content of the fuel in each fuel fraction ($w_{H2O,i}$):

$$R'''_{vol,i} = k_{vol,i}\varepsilon_{vol,i}\rho_{vol} \tag{4.10}$$

$$k_{vol,i} = a_{vol}\left(\frac{d_{p,i}}{d_{ref}}\right)^{b_{vol}}\left(1 - w_{H2O,i}\right)^{c_{vol}}\exp\left(\frac{-E_{vol}}{RT}\right) \tag{4.11}$$

The proposed correlations can be adjusted to suit different drying/devolatilization mechanisms. For example, setting the activation energies (E_{wat}, E_{vol}) and the parameter controlling the effect of moisture (c_{vol}) to zero allows simulating the devolatilization rate applied in the TUHH-model (Equation 2.11). Changing the parameter c_{vol} allows simulating the different characteristic conversion behaviours as shown in Figure 4.13.

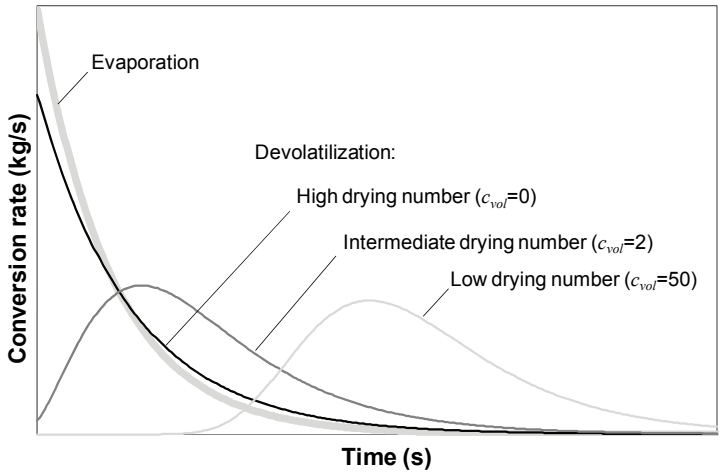

Figure 4.13. Characteristic conversion behaviour with different model parameters c_{vol}.

Figure 4.14 compares the evaporation and devolatilization of the example calculation. The evaporation rate is high near the fuel inlets and the moisture is quickly evaporated when fuel enters the furnace. The devolatilization process is similar to evaporation, however, the devolatilization continues further as the devolatilization is slower than evaporation and the volatiles in solid state in fuel can flow to the bottom of the furnace with the fuel. The local devolatilization process produces high local concentrations of combustible gases above the fuel inlets. This phenomenon has been observed in field measurements of large CFB furnaces (Werther, 2005).

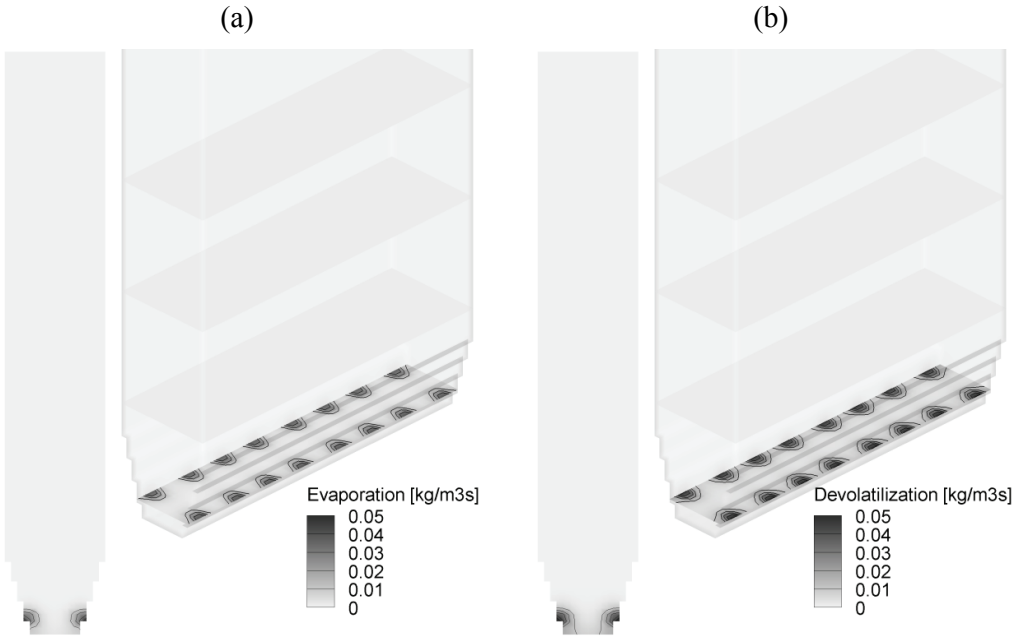

Figure 4.14. Modelled evaporation (a) and devolatilization (b) rate. Model parameters d_{ref} = 1250 µm, a_{evap} = 1.4 s^{-1}, a_{vol} = 0.8, b_{evap} = b_{vol} = -0.5, E_{evap} = E_{vol} = 88 J mol^{-1}, c_{vol} = 0.5 for both fuels.

4.5 Composition of devolatilized gases

The elemental composition of volatiles is determined either directly by user or by applying the correlations, which were presented earlier. Table 4.3 shows the predicted composition of volatiles of different fuel samples studied in Chapter 4.1. The composition of the produced gases from devolatilization is determined by simple rules:

- Nitrogen (N) forms hydrogen cyanide (HCN) and ammonia (NH_3). The split is determined by an empirical correlation, which is used by the NO_x-model.
- Sulphur (S) forms hydrogen sulphide (H_2S).
- Oxygen (O) forms carbon monoxide (CO) and carbon dioxide (CO_2) based on given molar ratio γ_{vol} and limited by the amount of carbon left.
- Any excess oxygen forms molecular oxygen (O_2).
- Remaining carbon (C) and hydrogen (H) form methane (CH_4), ethene (C_2H_4), hydrogen (H_2) and "gaseous carbon" (C_g) according to following rules:
    - Molar amount of carbon and hydrogen: x C + y H
    - Species produced:
        - if x > y/2: (y/4) C_2H_4 + (x–y/2) C_g
        - else if x > y/4: (y/2–x) CH_4 + (x–y/4) C_2H_4
        - else: x CH_4 + (y/2–2x) H_2

Table 4.3: Predicted elemental composition of volatiles.

Fuel	Composition (weight fractions)				
	C	H	N	S	O
Petroleum coke	0.4860	0.3193	0.0175	0.0484	0.1287
Anthracite	0.2933	0.3700	0.0000	0.0000	0.3368
Medium volat. bituminous coal	0.6363	0.1576	0.0081	0.0046	0.1934
High volat. bituminous coal	0.5142	0.1318	0.0348	0.0036	0.3155
Subbituminous A coal (high S)	0.5051	0.1163	0.0213	0.0498	0.3075
Subbituminous A coal	0.4265	0.1158	0.0083	0.0151	0.4342
Subbituminous B coal	0.4624	0.0977	0.0123	0.0058	0.4218
Subbituminous C coal	0.5621	0.1026	0.0065	0.0123	0.3165
Lignite A coal	0.4935	0.1085	0.0067	0.0046	0.3868
Lignite B coal (1)	0.4584	0.1008	0.0014	0.0060	0.4334
Lignite B coal (2)	0.4936	0.0871	0.0048	0.0026	0.4119
Lignite B coal (3)	0.4446	0.0870	0.0114	0.0240	0.4329
Peat, foreign	0.3748	0.0752	0.0240	0.0039	0.5220
Peat, domestic	0.4148	0.0839	0.0310	0.0018	0.4685
Wood, Salix	0.4221	0.0699	0.0014	0.0003	0.5063
Wood, chips	0.4139	0.0749	0.0015	0.0002	0.5096
Wood, bark	0.4165	0.0744	0.0005	0.0002	0.5084
Demolition wood (1)	0.3936	0.0698	0.0188	0.0010	0.5168
Demolition wood (2)	0.3887	0.0776	0.0080	0.0013	0.5245
Waste, recovered fuel (REF)	0.4470	0.0791	0.0067	0.0026	0.4647
Waste, refuse derived fuel (RDF)	0.5192	0.0921	0.0094	0.0016	0.3777

The formation of gaseous species from volatiles resembles the TUHH-model (Chapter 2.3.3) with some differences, which allow better simulation of formation of emissions. The volatile nitrogen is released as HCN and NH_3, which are precursors of NO and N_2O typically formed from devolatilization (Migliavacca et al., 2005; Tourunen et al., 2009). The sulphur is released as H_2S, which is usually identified as the main sulphur-containing product from devolatilization (Garcia-Labiano et al., 1996). The other possible sulphur species (e.g. COS and CS_2) are ignored to keep the model simple.

The hydrocarbons are modelled as a mixture of CH_4, C_2H_4, H_2 and C_g. The latter is "gaseous carbon", which is a virtual compound required for simulation of some fuels with very large C/H-ratio, e.g. a heavy fuel oil. Usually, the hydrocarbons produced by devolatilization and subsequent thermal cracking have a low C/H-ratio (Hayhurst and Lawrence, 1995) and can be simulated as a mixture of methane, ethene and hydrogen.

The production of CO and CO_2 from oxygen in volatiles O_{vol} (and limited by available carbon in volatiles, C_{vol}) is controlled by parameter γ_{vol}, which can have values in range 0...1:

$$C_{vol} + (2 - \gamma_{vol})\, O_{vol} \rightarrow \gamma_{vol}\, CO + (1 - \gamma_{vol})\, CO_2 \qquad (4.12)$$

In literature, the molar share CO/CO_2 ranges between 0.37...3.4 (Thunman et al., 2001). Converted to above parameter, these would give γ_{vol} = 0.27...0.77. In a CFB combustor, the CO burns rapidly to CO_2, thus validation of this parameter from measurements in large-scale units is challenging and should be based on bench scale or pilot scale studies. Tables 4.4 and 4.5 present the composition of gas species produced from the devolatilization of different fuel types presented in Chapter 4.1. The parameter γ_{vol} has been set to one in Table 4.4 and zero in Table 4.5 to present the full effect on the devolatilized gas species. Thus, in the first case, no CO_2 is produced and in the second case, no CO is produced.

The volatile nitrogen produces HCN only from petroleum coke and some bituminous coals. With most fuels, the nitrogen is released as NH_3. The amount of hydrogen in volatiles is always large enough to produce the sulphur as hydrogen sulphide H_2S. In the earlier model version, the sulphur was released as SO_2, which generated calculation problems if the S/O-ratio in fuel was high and the fuel did not contain enough oxygen to oxidize all the sulphur.

Even with parameter γ_{vol} = 1.0, molecular oxygen is produced only from two fuel samples, and the amount is small. This is quite reasonable, as in reality the remaining oxygen is not likely to be in molecular form, but may be e.g. linked with complex hydrocarbons $C_xH_yO_z$ or carbonyl sulphide COS. Simulation of this kind of compounds has been avoided to keep the combustion model simple. If the γ_{vol} is increased, the production of molecular oxygen is zero with all fuels, amount of carbon for hydrocarbons increases and the amount of molecular hydrogen decreases.

With all fuels and γ_{vol} = 0...1, the hydrocarbons consist of methane, ethene and hydrogen. None of the studied fuel samples produces gaseous carbon (C_g). This virtual compound is only included to allow simulation of complex hydrocarbons with reasonable accuracy and to avoid definition of complex or arbitrary hydrocarbons ($C_xH_yO_z$). As an example, combustion of naphthalene can be modelled as follows:

Actual reaction: $C_{10}H_8 + 12\ O_2 \rightarrow 10\ CO_2 + 4\ H_2O$ $\Delta H_0 = -5052$ kJ/mol

Simulated: $2\ C_2H_4 + 6\ C_g + 12\ O_2 \rightarrow 10\ CO_2 + 4\ H_2O$ $\Delta H_0 = -5007$ kJ/mol

The molar balance of the elements is the same with both reactions and the product species are the same. The reaction rates can be set identical by the reaction rate parameters. The heat effect (reaction enthalpy) is approximately same by both reactions (error = 0.9%).

In normal calculation cases, the concept of gaseous carbon is not necessary because the used fuels are solid fuels, typically representing one of the fuel types shown above.

A more accurate simulation of gasification might require better description of heavy hydrocarbons (e.g. tar), but reasonable results have already been acquired with this simple model (Koski et al., 2011).

Table 4.4: Predicted production of gas species from devolatilization, $\gamma_{vol} = 1.0$.

Fuel	Production from devolatilization (kg/kg,volat)							
	HCN	NH_3	H_2S	CO	O_2	CH_4	C_2H_4	H_2
Petroleum coke	0.023	0.007	0.0515	0.225	0	0.507	0	0.187
Anthracite	0	0	0.0000	0.590	0	0.054	0	0.356
Medium volat. bituminous coal	0.008	0.005	0.0049	0.339	0	0.591	0.053	0
High volat. bituminous coal	0.013	0.034	0.0039	0.552	0	0.363	0	0.034
Subbituminous A coal (high S)	0.003	0.024	0.0529	0.538	0	0.364	0	0.017
Subbituminous A coal	0	0.010	0.0161	0.760	0	0.134	0	0.079
Subbituminous B coal	0	0.015	0.0061	0.738	0	0.195	0	0.046
Subbituminous C coal	0	0.008	0.0131	0.554	0	0.366	0.059	0
Lignite A coal	0	0.008	0.0048	0.677	0	0.271	0	0.039
Lignite B coal (1)	0	0.002	0.0064	0.759	0	0.178	0	0.055
Lignite B coal (2)	0	0.006	0.0028	0.721	0	0.246	0	0.024
Lignite B coal (3)	0	0.014	0.0255	0.758	0	0.160	0	0.043
Peat, foreign	0	0.029	0.0042	0.874	0.023	0	0	0.070
Peat, domestic	0	0.038	0.0020	0.820	0	0.084	0	0.056
Wood, Salix	0	0.002	0.0003	0.886	0	0.056	0	0.055
Wood, chips	0	0.002	0.0002	0.892	0	0.042	0	0.064
Wood, bark	0	0.001	0.0002	0.890	0	0.047	0	0.063
Demolition wood (1)	0	0.023	0.0011	0.905	0	0.007	0	0.064
Demolition wood (2)	0	0.010	0.0014	0.906	0.007	0.000	0	0.076
Waste, recovered fuel (REF)	0	0.008	0.0028	0.813	0	0.131	0	0.045
Waste, refuse derived fuel (RDF)	0	0.011	0.0017	0.661	0	0.315	0	0.011

Table 4.5: Predicted production of gas species from devolatilization, $\gamma_{vol} = 0.0$.

Fuel	Production from devolatilization (kg/kg,volat)							
	HCN	NH_3	H_2S	CO_2	O_2	CH_4	C_2H_4	H_2
Petroleum coke	0.023	0.007	0.0515	0.177	0	0.571	0	0.171
Anthracite	0	0	0.0000	0.463	0	0.223	0	0.314
Medium volat. bituminous coal	0.008	0.005	0.0049	0.266	0	0.494	0.222	0
High volat. bituminous coal	0.013	0.034	0.0039	0.434	0	0.474	0.041	0
Subbituminous A coal (high S)	0.003	0.024	0.0529	0.423	0	0.347	0.150	0
Subbituminous A coal	0	0.010	0.0161	0.597	0	0.352	0	0.025
Subbituminous B coal	0	0.015	0.0061	0.580	0	0.348	0.051	0
Subbituminous C coal	0	0.008	0.0131	0.435	0	0.207	0.336	0
Lignite A coal	0	0.008	0.0048	0.532	0	0.384	0.071	0
Lignite B coal (1)	0	0.002	0.0064	0.596	0	0.395	0	0.001
Lignite B coal (2)	0	0.006	0.0028	0.567	0	0.230	0.194	0
Lignite B coal (3)	0	0.014	0.0255	0.595	0	0.284	0.081	0
Peat, foreign	0	0.029	0.0042	0.718	0	0.239	0	0.010
Peat, domestic	0	0.038	0.0020	0.644	0	0.294	0.022	0
Wood, Salix	0	0.002	0.0003	0.696	0	0.244	0.058	0
Wood, chips	0	0.002	0.0002	0.701	0	0.296	0.001	0
Wood, bark	0	0.001	0.0002	0.699	0	0.289	0.010	0
Demolition wood (1)	0	0.023	0.0011	0.711	0	0.256	0.009	0
Demolition wood (2)	0	0.010	0.0014	0.721	0	0.256	0	0.011
Waste, recovered fuel (REF)	0	0.008	0.0028	0.639	0	0.252	0.098	0
Waste, refuse derived fuel (RDF)	0	0.011	0.0017	0.519	0	0.212	0.255	0

4.6 Combustion of char

The combustion rate of char depends on local, fraction specific concentration of char ($\varepsilon_{char,i}\ \rho_{char}$), molar concentration of oxygen (C_{O2}), particle size ($d_{p,i}$) and temperature (T):

$$R'''_{char,i} = k_{char,i}\varepsilon_{char,i}\rho_{char} \tag{4.13}$$

$$k_{char,i} = a_{char}\left(\frac{d_{p,i}}{d_{ref}}\right)^{b_{char}} C_{O_2}^{c_{char}} \exp\left(\frac{-E_{char}}{RT}\right) \tag{4.14}$$

Due to a relatively coarse calculation mesh and the transient, fluctuating flow, complete mixing of oxygen and char within a calculation cell cannot be assumed and the actual combustion rate is smaller than the kinetic reaction rate. In the current model, this limitation of incomplete mixing is considered by setting the model parameters experimentally so that the model results match the measurements, e.g. the determined total carbon conversion. Another possibility would be to limit the reaction rate based on kinetic reaction rate and the mixing rate, similar to Equation 2.12. Yet another possibility would be to define a separate sub-model for determining "effective oxygen", which would indicate the actual oxygen concentration available for char combustion. New modelling methods are currently being developed with the support of transient simulations, which can then be used for determining alternative correlation models.

In usual calculation studies, the exponent of the oxygen content has been in the range c_{char} = 0.75...1.0 and the exponent for the particle size effect has been b_{char} = -1, which makes the reaction rate proportional to the surface area of the group of particles. The temperature effect has been often eliminated (E_{char} = 0) to improve the convergence and the coefficient a_{char} has been tuned based on measured carbon conversion (Myöhänen et al., 2005).

The combustion rate of char is slower than the devolatilization rate. Consequently, with a typical fuel, char has time to penetrate to the furnace and flow to the bottom of the furnace. This results in a high local concentration of char at the bottom of the furnace. Thus, the maximum char combustion rate is located at the bottom of the furnace instead of the location of the fuel inlets (Figure 4.15). Naturally, local maximums are found at the location of the fuel inlets.

The elemental composition of char can be defined by user input or by using the correlations presented in Chapter 4.1. The elements of char burn in the presence of oxygen producing different gas species:

$$\text{Char} + O_2 \rightarrow NO, N_2O, SO_2, H_2O, CO, CO_2 \tag{4.15}$$

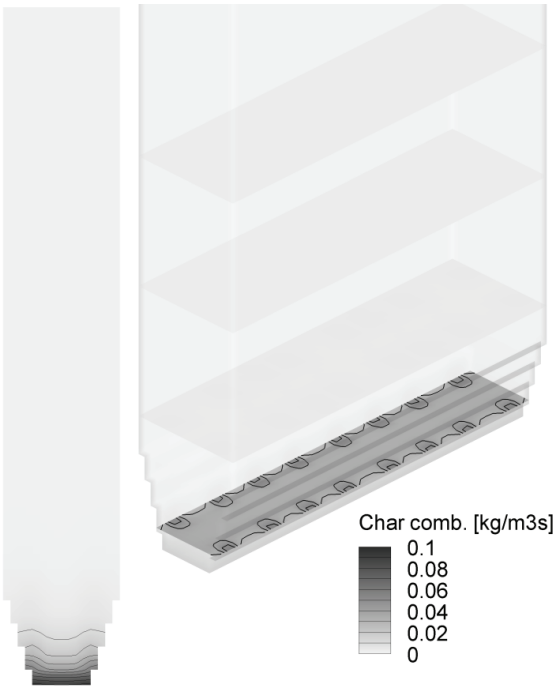

Figure 4.15. Modelled char combustion rate.

Nitrogen in char produces nitrogen oxides: NO (nitric oxide, nitrogen monoxide) and N_2O (nitrous oxide). The distribution is determined by the model parameters of the NOx-model.

The sulphur combusts to sulphur dioxide (SO_2). In real conditions, other forms of sulphur oxides may exist as well, e.g. SO_3, SO and S_2O. The amount of these is considerably smaller and these have been neglected in the model.

Hydrogen burns to water vapour.

Most of the char consists of carbon. The carbon in char (C_{char}) combusts to carbon monoxide and carbon dioxide as follows:

$$C_{char} + (1 - 0.5\,\gamma_{char})\,O_2 \rightarrow \gamma_{char}\,CO + (1 - \gamma_{char})\,CO_2 \tag{4.16}$$

Parameter γ_{char} is a user given input value, which determines the distribution of CO and CO_2 during combustion of char. In literature, many correlations have been presented for determination of CO/CO_2 –ratio of char combustion (Ma, 2006, p. 84). In general, the share of CO is increasing with increasing temperature, and the ratio could be estimated by an Arrhenius-type expression. At usual CFB temperatures, the molar share CO/CO_2 has been 1...10, which corresponds to γ_{char} = 0.5...0.9.

The following table presents the composition of gas species produced from the combustion of char of different fuel types presented in Chapter 4.1.

Table 4.6: Predicted production of gas species from char combustion.

Fuel	**Production from char combustion (kg/kg,char)** (γ_{CO} = 0.5)					**Oxygen consumption**
	Char-N	SO_2	H_2O	CO	CO_2	O_2 (kg/kg,char)
Petroleum coke	0.016	0.115	0.047	1.074	1.687	1.939
Anthracite	0.015	0.012	0.051	1.135	1.783	1.996
Medium volat. bituminous coal	0.017	0.010	0.050	1.133	1.781	1.992
High volat. bituminous coal	0.022	0.008	0.044	1.130	1.776	1.980
Subbituminous A coal (high S)	0.019	0.117	0.040	1.070	1.681	1.927
Subbituminous A coal	0.016	0.037	0.044	1.120	1.760	1.977
Subbituminous B coal	0.018	0.017	0.046	1.130	1.775	1.985
Subbituminous C coal	0.017	0.036	0.048	1.119	1.759	1.979
Lignite A coal	0.016	0.012	0.040	1.135	1.783	1.987
Lignite B coal (1)	0.013	0.017	0.037	1.136	1.785	1.989
Lignite B coal (2)	0.015	0.009	0.049	1.137	1.786	1.995
Lignite B coal (3)	0.018	0.076	0.040	1.096	1.722	1.951
Peat, foreign	0.022	0.014	0.037	1.128	1.772	1.973
Peat, domestic	0.026	0.007	0.029	1.129	1.773	1.963
Wood, Salix	0.012	0.002	0.038	1.146	1.800	1.998
Wood, chips	0.012	0.001	0.031	1.147	1.803	1.994
Wood, bark	0.010	0.001	0.033	1.149	1.806	1.998
Demolition wood (1)	0.024	0.005	0.033	1.131	1.778	1.970
Demolition wood (2)	0.018	0.006	0.025	1.139	1.790	1.977
Waste, recovered fuel (REF)	0.019	0.014	0.030	1.131	1.778	1.973
Waste, refuse derived fuel (RDF)	0.024	0.009	0.029	1.129	1.774	1.965

As most of the char is carbon, the production of carbon monoxide and carbon dioxide from burning of carbon is dominating. When considering the heat effect of char combustion, the other elements could be neglected and the char could be assumed to be 100% carbon without making any large errors. However, the nitrogen and sulphur in char have a large effect on formation of nitrogen oxides and sulphur dioxide, thus they must be known in order to determine the formation of emissions correctly. The amount of hydrogen in char is small so it has very little effect when char is combusted. For modelling gasification of char, the presence of hydrogen in the char model is beneficial as it allows simulating the release of sulphur as H_2S during gasification of char.

In real conditions, char contains some oxygen as well (Ma, 2006). In the above study, the oxygen in char was found to be small and it would not have a large effect on heat release or emissions. In the model, the oxygen in char can be specified, if the elemental composition of char is defined by user and not by the built-in correlations. During combustion, the oxygen in char is used for oxidizing the different combustible elements. During gasification, the oxygen in char is released as molecular oxygen, which then reacts in combustion reactions.

4.7 Gasification of char

Two gasification reactions of char have been implemented to the model based on work by Koski (2010), the water-gas reaction (Equation 4.17) and the Boudouard reaction (Equation 4.18):

$$C + H_2O \rightarrow H_2 + CO \tag{4.17}$$

$$C + CO_2 \rightarrow 2\,CO \tag{4.18}$$

The reaction rate equations have been simplified from expressions used by Petersen and Werther (2005a). In the simplified correlations, the effect of product gases has been eliminated to improve the convergence of the model and fraction specific correction factors ($k_{watg,i}$, $k_{boud,i}$) have been included for tuning the values based on measurements:

$$r'''_{watg,i} = 235.3\, k_{watg,i} C_{C,i} C_{H_2O} \exp\left(\frac{-15\,500}{T}\right) \tag{4.19}$$

$$r'''_{boud,i} = 7.696 \cdot 10^6\, k_{boud,i} C_{C,i} C_{CO_2} \exp\left(\frac{-30\,600}{T}\right) \tag{4.20}$$

The above equations define the molar reaction rate for carbon in char. Terms C_{H2O} and C_{CO2} are local molar concentrations of water vapour and carbon dioxide. The term $C_{C,i}$ is the local molar concentration of carbon in particle size fraction *i*. Assuming that the other elements in char are bound to carbon, the hydrogen, nitrogen, sulphur and oxygen are released at the same rate constant as the carbon is gasified. This approach enables simple handling, as the composition of char can be assumed constant during gasification. During gasification of char, nitrogen is released as molecular nitrogen and sulphur is released as hydrogen sulphide. The remaining hydrogen is released as molecular hydrogen. If the char contains oxygen, it is released as molecular oxygen, which would of course be quickly consumed in combustion reactions.

The units of the above equations are mol/m^{3}s. To get the mass change needed in the continuity equations of gaseous species and char (Equations 3.10 and 4.4), the above defined molar reaction rates are multiplied by the applicable molar mass. For example, the mass change of CO_2 (kg/m^{3}s) due to gasification of carbon in the Bouduard-reaction is a sum of the reactions in all particle size fractions:

$$R'''_{CO_2} = \sum_i \left(r'''_{boud,i} M_{CO_2}\right) \tag{4.21}$$

The amount of hydrogen in char has to be large enough to form hydrogen sulphide with sulphur during gasification of char. Table 4.7 presents the molar concentrations of elements in char in the different fuel types studied in Chapter 4.1. With all of these fuel types, the molar ratio of hydrogen to sulphur (H/S) is above 2, thus enabling the release of sulphur as H_2S.

Table 4.7: Predicted molar composition of char.

Fuel	Molar composition (mol/kg,char)				H/S
	C	H	N	S	
Petroleum coke	76.66	5.268	1.175	1.792	2.9
Anthracite	81.02	5.632	1.065	0.194	29.0
Medium volat. bituminous coal	80.93	5.584	1.222	0.163	34.3
High volat. bituminous coal	80.69	4.913	1.557	0.127	38.6
Subbituminous A coal (high S)	76.38	4.468	1.384	1.830	2.4
Subbituminous A coal	79.98	4.859	1.133	0.579	8.4
Subbituminous B coal	80.65	5.143	1.258	0.264	19.5
Subbituminous C coal	79.93	5.292	1.181	0.565	9.4
Lignite A coal	81.04	4.451	1.151	0.186	24.0
Lignite B coal (1)	81.13	4.152	0.929	0.259	16.0
Lignite B coal (2)	81.15	5.418	1.098	0.138	39.3
Lignite B coal (3)	78.24	4.397	1.255	1.194	3.7
Peat, foreign	80.51	4.148	1.543	0.223	18.6
Peat, domestic	80.58	3.241	1.821	0.104	31.1
Wood, Salix	81.82	4.227	0.866	0.027	157.4
Wood, chips	81.92	3.465	0.866	0.012	286.0
Wood, bark	82.05	3.616	0.746	0.012	296.9
Demolition wood (1)	80.79	3.648	1.679	0.077	47.1
Demolition wood (2)	81.33	2.734	1.253	0.087	31.3
Waste, recovered fuel (REF)	80.79	3.312	1.360	0.226	14.7
Waste, refuse derived fuel (RDF)	80.63	3.204	1.700	0.142	22.5

Figure 4.16 shows modelled reaction rates of char gasification in a combustion process. Compared with the char combustion, the effect of the gasification reactions is insignificant. The gasification reactions of char are highest at locations around the fuel inlets, where the gas atmosphere contains water vapour and carbon dioxide from evaporation and combustion reactions, the temperature is high, and the concentration of char is high. At the bottom of the furnace, the gasification reactions are suppressed due to lack of reacting gases, CO_2 and H_2O.

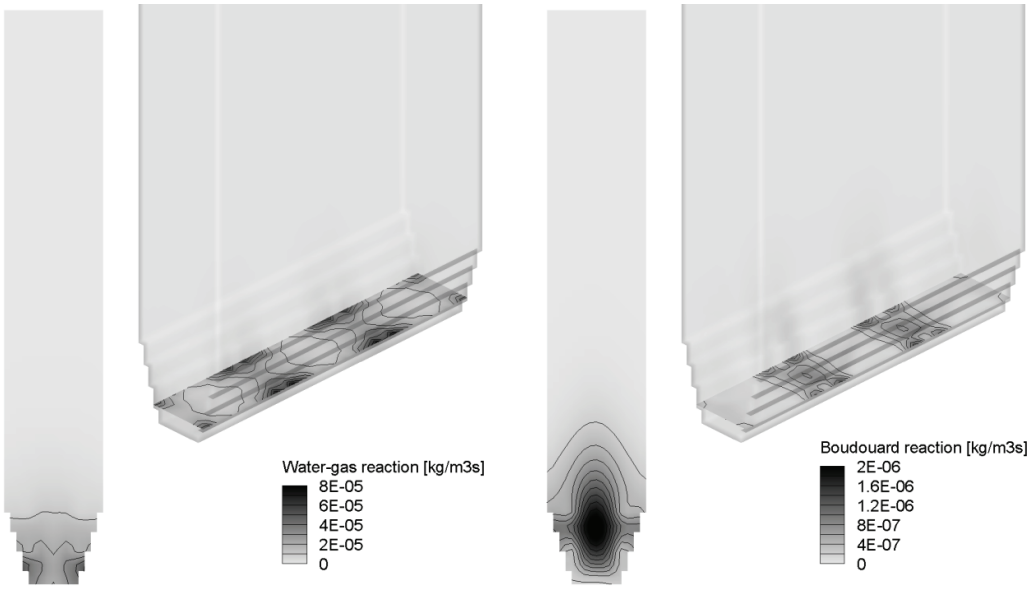

Figure 4.16. Modelled char gasification rates.

4.8 Homogeneous combustion reactions

The different combustible gases, which are produced from devolatilization and gasification and combustion of char, burn in presence of oxygen by the following six reactions:

$$H_2S + 1.5\ O_2 \rightarrow SO_2 + H_2O \tag{4.22}$$

$$CO + 0.5\ O_2 \rightarrow CO_2 \tag{4.23}$$

$$CH_4 + 0.5\ O_2 \rightarrow CO + 2\ H_2 \tag{4.24}$$

$$C_2H_4 + 0.5\ O_2 \rightarrow CH_4 + CO \tag{4.25}$$

$$H_2 + 0.5\ O_2 \rightarrow H_2O \tag{4.26}$$

$$C_g + 0.5\ O_2 \rightarrow CO \tag{4.27}$$

The reaction rates are modelled by empirical equations, which have the same generic form shown below for the combustion of carbon monoxide.

$$r'''_{CO} = k_{CO} X_{CO}^{a_{CO}} X_{O_2}^{b_{CO}} X_{H_2O}^{c_{CO}} \left(\frac{P}{P_{ref}}\right)^{d_{CO}} \exp\left(\frac{-E_{CO}}{RT}\right) \tag{4.28}$$

The correlation includes molar fraction of the reacting gas component (X_{CO} for carbon monoxide) and molar fractions of oxygen (X_{O2}) and water vapour (X_{H2O}). The effect of pressure (P) can be included, the reference pressure is P_{ref} = 101325 Pa. The temperature dependence is set by Arrhenius type exponential function applying the activation energy E_{CO}.

The above correlation uses molar fractions X, while in most of the reaction rate expressions in literature, the gas concentrations have been specified as molar concentrations. For example, in Petersen and Werther (2005a):

$$r'''_{\mathrm{CO}} = 1.78 \cdot 10^{10}\, C_{\mathrm{CO}} C_{\mathrm{O_2}}^{0.25} C_{\mathrm{H_2O}}^{0.5} \exp\left(\frac{-180\,032}{RT}\right) \tag{4.29}$$

The usage of molar concentrations is better justified and would eliminate the pressure term from the reaction rate expressions. However, the correlation form of Equation 4.28 can be easily adjusted to match the correlations found in literature as presented in Figure 4.17. In future, the reaction expressions are probably changed to apply molar concentrations, but for now, the format shown in Equation 4.28 has been used to maintain compatibility to validation studies carried out with the earlier model versions.

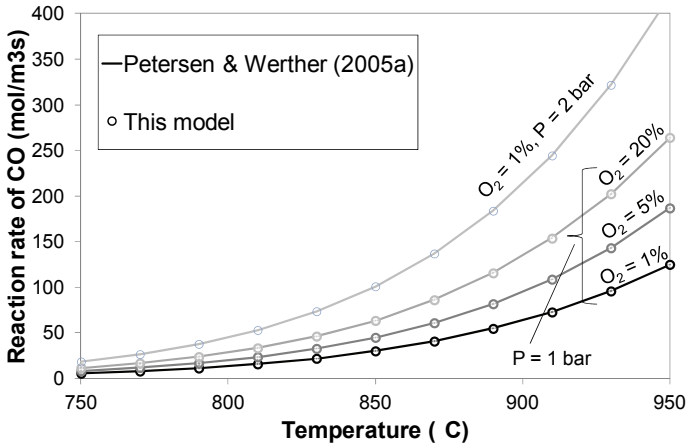

Figure 4.17. Example of fitting the reaction rate correlation for CO. Model parameters k_{CO} = 1.8636·10^{11}, a_{CO} = 1.0, b_{CO} = 0.25, c_{CO} = 0.5, d_{CO} = 1.75, E_{CO} = 163 000.
Boundary conditions 5% CO, 15% H_2O, total pressure 1 bar/2 bar, variable O_2 and temperature.

Figure 4.18 compares the combustion rate of hydrogen and carbon monoxide in the example calculation. Carbon monoxide is produced mainly from char combustion while hydrogen and other combustible gases are produced mainly from devolatilization. As shown in Chapters 4.4 and 4.6, the devolatilization and char combustion are different in nature: devolatilization is occurring near the fuel inlets and char is combusting more

evenly in the bottom of the furnace as well. Consequently, the distribution of CO is different from other combustible gases. The effect is seen in the combustion rates of CO and H_2 as shown in Figure 4.18. Hydrogen burns quickly near the fuel inlets, while carbon monoxide has a more uniform combustion profile and higher combustion rate at the bottom of the furnace.

The different mechanisms of how the combustible gases are formed are reflected on the gas concentration fields. Figure 4.19 presents the hydrogen and carbon monoxide concentration fields. Hydrogen is mostly originated from volatiles and it burns quickly near the fuel inlets. The profile of carbon monoxide shows how the concentration of CO is highest just above the bottom of the furnace. The CO concentration is higher in the core of the furnace than near the furnace walls. This is explained by the penetration and mixing of secondary air: the concentration of oxygen is small in the core of the furnace, which results in slower combustion rate and higher CO concentration. The concentration of CO decreases towards the top of the furnace, as the oxygen is mixing with the combustible gases and CO is burned. The local minimums in the horizontal slice at 1.25 m height are due to diluting effect of devolatilized gases, evaporated moisture and secondary air fed to fuel inlets.

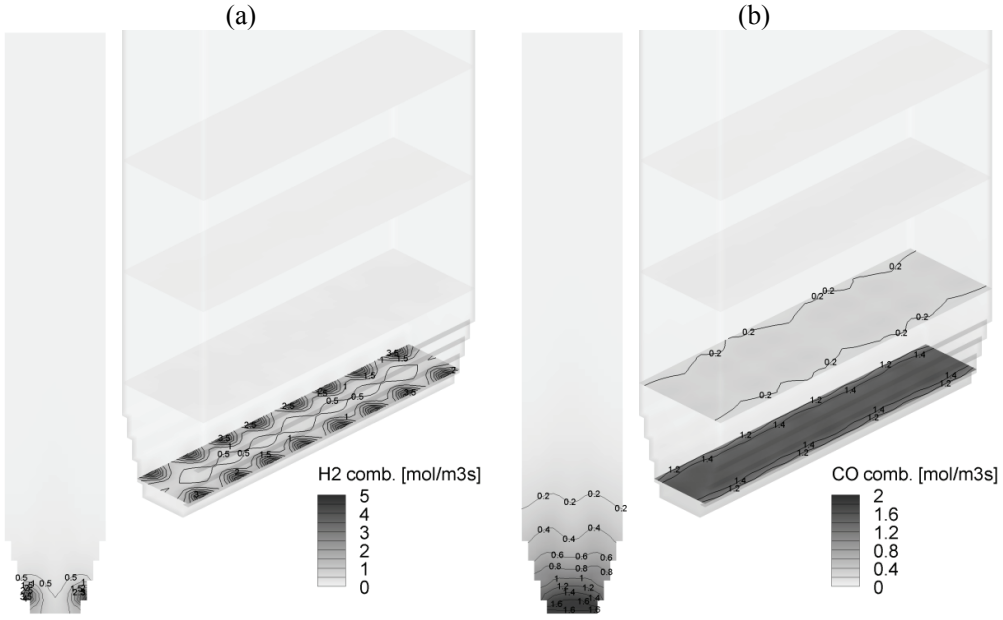

Figure 4.18. Modelled combustion rate of hydrogen (a) and carbon monoxide (b).

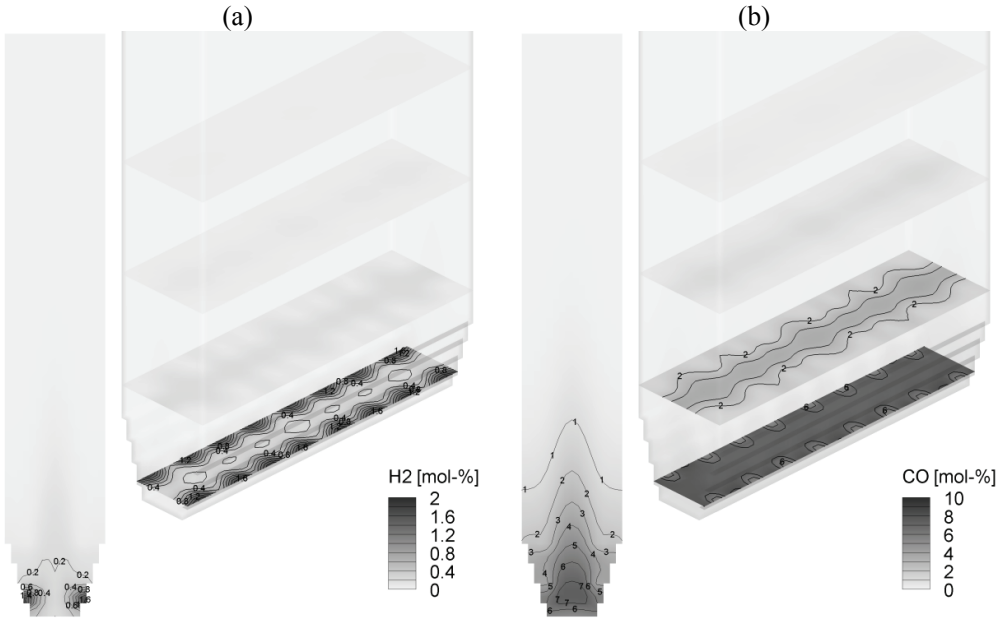

Figure 4.19. Modelled concentration of hydrogen (a) and carbon monoxide (b).

4.9 Shift conversion

The shift conversion is a reversible reaction, which is important in gasification conditions:

$$CO + H_2O \leftrightarrow CO_2 + H_2 \tag{4.30}$$

This has been implemented to the model based on work by Koski (2010). The reaction rate correlation is based on literature (Biba et al., 1978; Yoon et al., 1978):

$$r'''_{shift} = 2.78\, k_{shift} \exp\left(\frac{-1515.46}{T}\right)\left[C_{CO}C_{H_2O} - \frac{C_{CO_2}C_{H_2}}{0.0265 \exp\left(\frac{3956}{T}\right)}\right] \tag{4.31}$$

The correlation includes a correction factor k_{shift}, which can be applied for tuning the model results to match measurements. The terms include temperature (T) and the molar concentrations of CO, H_2O, CO_2, and H_2.

In a combustion process, the shift conversion can occur at the lower part of the furnace, where carbon monoxide and hydrogen have not yet been burned and the reacting species are available (Figure 4.20). The concentration of CO tends to be higher due to

slower combustion rate and higher input from fuel. This promotes the reaction towards right, i.e. producing hydrogen. Based on a calculation study, the shift conversion can have a significant effect on the combustion process. However, the applied correlation may exaggerate the shift conversion rate and the correction factor k_{shift} should be in the order of 0.1 (Petersen and Werther, 2005a).

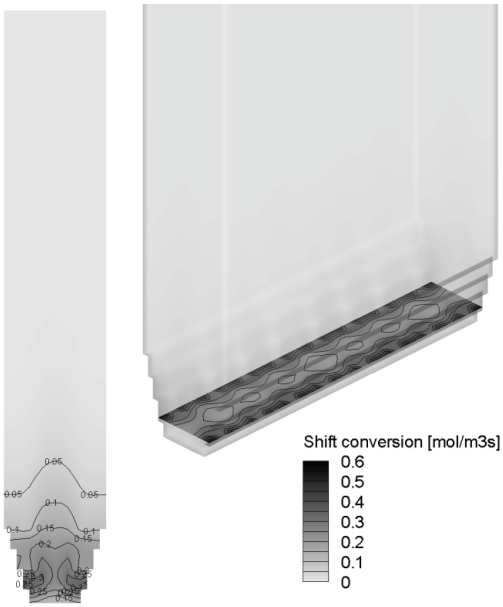

Figure 4.20. Modelled shift conversion rate (k_{shift} = 1).

4.10 Heat from combustion reactions

The heat from different reactions is determined based on formation enthalpies of different species in the above-described reactions. The heat from complete combustion of char is generated from the following reactions:

$$C_{char} + O_2 \rightarrow CO_2 \qquad \Delta H_0 = -393.505 \text{ kJ/mol} \qquad (4.32)$$

$$S_{char} + O_2 \rightarrow SO_2 \qquad \Delta H_0 = -296.813 \text{ kJ/mol} \qquad (4.33)$$

$$H_{char} + 0.25\ O_2 \rightarrow H_2O \qquad \Delta H_0 = -120.913 \text{ kJ/mol} \qquad (4.34)$$

The reaction heat due to formation of NO and N_2O is ignored as they are not contributing much to the total reaction heat and these compounds are only required for modelling the NOx-emissions.

The latent heat due to evaporation is determined as follows:

$$H_2O(l) \rightarrow H_2O(g) \qquad L = 2500.93 \text{ kJ/kg} \qquad (4.35)$$

The reaction heat from complete combustion of devolatilized combustible gas species is generated by the following reactions:

$$H_2S + 1.5\ O_2 \rightarrow SO_2 + H_2O \qquad \Delta H_0 = -518.039 \text{ kJ/mol} \qquad (4.36)$$

$$CO + 0.5\ O_2 \rightarrow CO_2 \qquad \Delta H_0 = -282.964 \text{ kJ/mol} \qquad (4.37)$$

$$CH_4 + 2\ O_2 \rightarrow CO_2 + 2\ H_2O \qquad \Delta H_0 = -802.284 \text{ kJ/mol} \qquad (4.38)$$

$$C_2H_4 + 3\ O_2 \rightarrow 2\ CO_2 + 2\ H_2O \qquad \Delta H_0 = -1323.129 \text{ kJ/mol} \qquad (4.39)$$

$$H_2 + 0.5\ O_2 \rightarrow H_2O \qquad \Delta H_0 = -241.826 \text{ kJ/mol} \qquad (4.40)$$

$$C_g + O_2 \rightarrow CO_2 \qquad \Delta H_0 = -393.505 \text{ kJ/mol} \qquad (4.41)$$

In the model, the different reactions occur through the different partial reactions as presented in Chapter 4.8, e.g. the combustion of ethene:

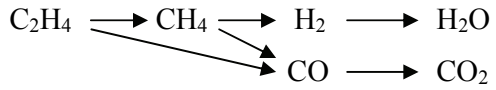

Figure 4.21. Reaction paths for combustion of ethene.

The summed reaction heat of the partial reactions is equal to the above reaction heats for complete combustion reactions, e.g. Equation 4.39 for ethene.

By summing the above combustion reactions for char and devolatilized gases, a computational reaction enthalpy can be determined for a fuel. However, this is not exactly the same as the analyzed heat value due to different simplifications in the reaction mechanism, and due to additional enthalpy change related to devolatilization process. In the model, the difference between the analyzed heat value and the computational reaction enthalpy has been defined as a formation enthalpy of the devolatilization (positive or negative). This creates an additional heat sink or source for the devolatilization process and thus the energy from complete combustion of fuel matches exactly the analyzed heat value of the fuel and the energy balance is correct. Usually the difference is small however, as shown in the following figure, which compares the two values determined for the fuel samples presented in Chapter 4.1.

The heat from different reactions is included in the energy equation (Equation 3.14). Naturally, in a usual calculation case, the combustion inside the furnace is not complete and the ash and the flue gas contain unburned components, char and combustible gases.

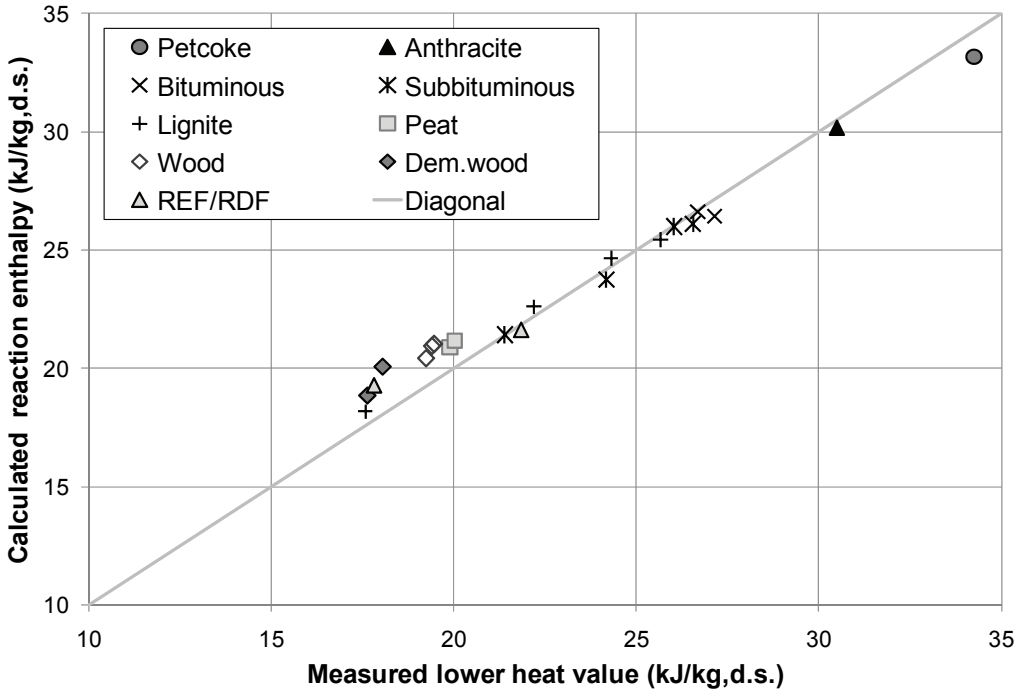

Figure 4.22. Calculated reaction enthalpy vs. measured lower heat value of fuel.

5 Sorbent model

The sorbent is simulated as a mixture of main reacting species and inert material:

- $CaCO_3$ calcium carbonate (limestone, calcite)
- CaO calcium oxide
- $CaSO_4$ calcium sulphate
- CaS calcium sulphide
- Inert inert material

Similar to other solid materials, the sorbent is divided to six particle size fractions, which allows simulating the effects of particle size distribution and comminution. The model solves the solid concentration fields of each sorbent fraction (i.e. the mixture of the above-defined species) by applying empirical concentration fields. The net velocity fields for each size fraction (=6) are solved by potential flow approach. Continuity equations are then determined for each reacting species (=4) and size fractions (=6), which then solve the species-specific concentration fields. Consequently, for calculation of one sorbent, the model needs to solve 30 three-dimensional transport equations, which makes this sub-model the most time-consuming part of the overall solution process. Moreover, many of the reactions are reversible (e.g. calcination – carbonation), which can create convergence problems.

The current model solves the reactions, which are occurring in air-fired and oxygen-fired combustion conditions: calcination, carbonation, sulphation, direct sulphation and desulphation. In future, the reactions involving CaS will be included to define sorbent reactions in reducing conditions and gasifiers.

The solution of sorbent reactions is an iterative process, in which the values of next iteration step are calculated from values of previous iteration step. The proper initialization of the values is crucial for successful calculations. In the current model, during initialization of the calculation, the whole sorbent in bed is set to be calcined (CaO) and the mass of each particle size fraction is determined from zero-dimensional mass balance without reactions (cf. Chapter 3.8). This is the logical initial state for normal air-fired cases, in which the calcination of fresh limestone occurs quickly. For oxygen-fired cases, the calcination might not occur and the sorbent could remain as calcium carbonate. In this case, the initial assumption of calcined limestone leads to very large reactions at the start of the calculation as the whole sorbent bed can go through carbonation. This could have a disproportional effect on gas flow, gas species and temperature fields. To avoid possible calculation problems, the coupling between the sorbent reactions and the other process phenomena is switched off during the first five global iteration loops: the sorbent reactions and the composition of sorbent phase are solved, but the reactions do not affect the gas species, gas flow field or temperature field. After a few calculation steps, the changes in the sorbent composition have subdued and the coupling can be switched on without causing divergence of the solution.

5.1 Concentration and velocity fields of sorbent fractions

The net velocity field of sorbent is defined separately for each particle size fraction. First, the total fractional mass of sorbent is determined based on results of the earlier iteration step or initialized values. For each size fraction, the mass is distributed in furnace by using empirical correlations for defining the three-dimensional weight fraction profiles (Chapter 3.4). Similar to determining the velocity field of total solids, a flow potential is defined, but now this is determined for each size fraction *i*:

$$\varepsilon_{sorb,i}\rho_{sorb}\mathbf{v}_{sorb,i} = \nabla P_{fs,sorb,i} \tag{5.1}$$

The potential difference across the furnace outlet faces is set based on the determined constant outlet velocity for total solids. The continuity of the sorbent fractions is defined as follows:

$$\begin{aligned}\oint_A \varepsilon_{sorb,i}\rho_{sorb}\mathbf{v}_{sorb,i}\cdot d\mathbf{A} &= \int_V \phi'''_{sorb,i}\,dV + \int_V R'''_{sorb,i}\,dV \\ -\int_V \sum_{j,j\neq i} k_{C,sorb,ij}\varepsilon_{sorb,i}\rho_{sorb}\,dV &+ \int_V \sum_{j,j\neq i} k_{C,sorb,ji}\varepsilon_{sorb,j}\rho_{sorb}\,dV\end{aligned} \tag{5.2}$$

Equation 5.2 includes terms for convection, sources and sinks (e.g. feeds and flow from return legs), reactions, and comminution between the size fractions.

Combining Equations 5.1 and 5.2, the potential fields $P_{fs,sorb,i}$ can be solved, after which the sorbent velocity for each fraction is defined from Equation 5.1.

Figure 5.1 presents an example of the sorbent velocity field for one particle size fraction. At the bottom section, the sorbent enters the system from the return legs and feed points and spreads to the furnace. Part of the sorbent flow is diverted to external heat exchangers, which exchange solids with the furnace. In the middle section, the velocity profile of the sorbent is mostly vertical with velocity increasing towards top. At the top of the furnace, the sorbent flow turns towards the furnace outlets and exits to the cyclones, from which the flow is returned back to the furnace through the return legs. The sorbent flow through the internal circulation, i.e. through the wall layers, has not yet been implemented to the model.

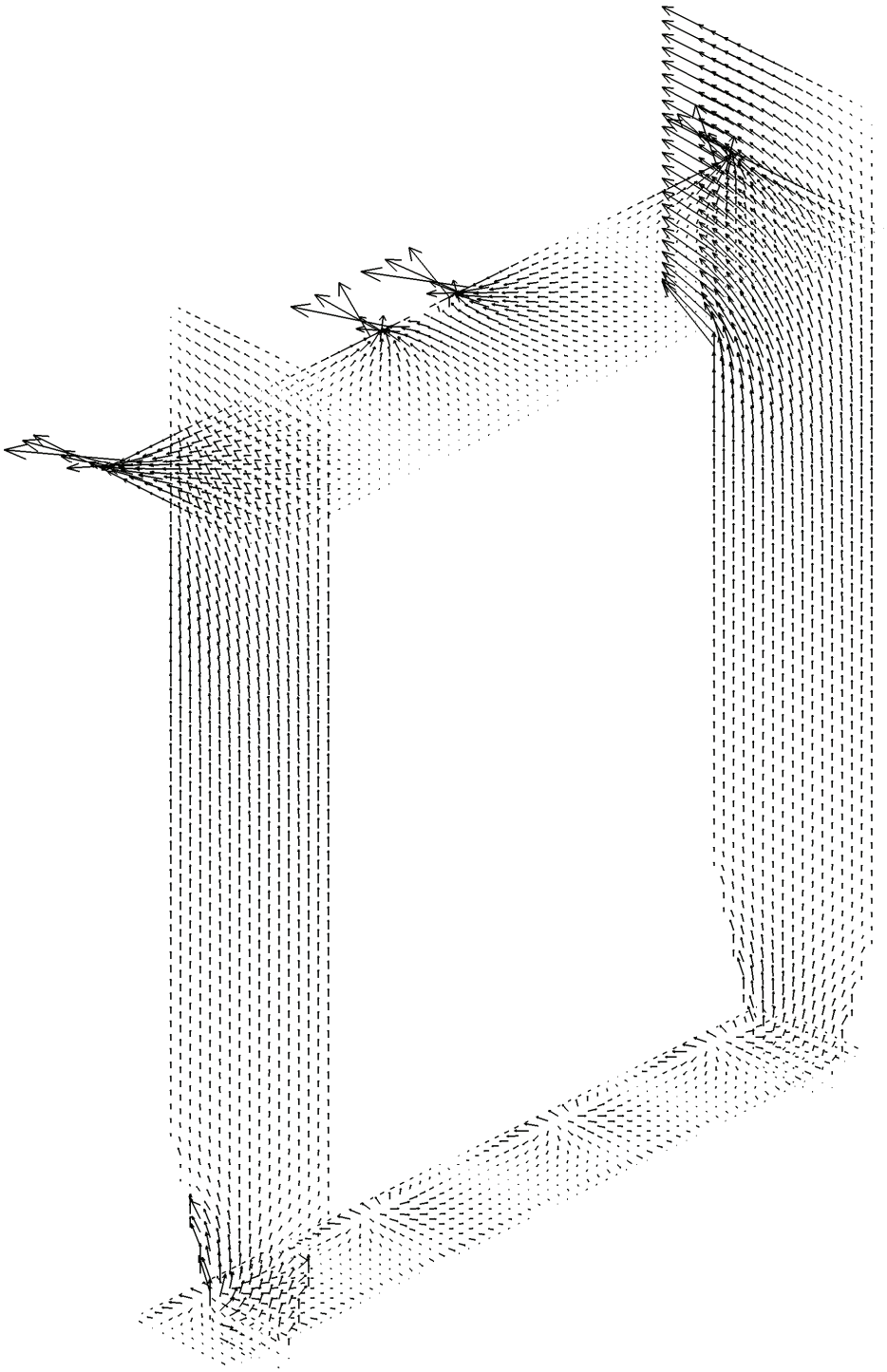

Figure 5.1. Tangential velocity vectors of sorbent fraction 3 (125-180 μm) in a 330 MWe CFB (Myöhänen et al., 2011).

5.2 Continuity equations for sorbent species

The continuity equations are defined for each particle size fraction *i* and for each reacting sorbent species *r* ($CaCO_3$, CaO, $CaSO_4$, CaS):

$$\begin{aligned}&\oint_A w_{r,i}\varepsilon_{sorb,i}\rho_{sorb}\mathbf{v}_{sorb,i}\cdot d\mathbf{A} - \oint_A \varepsilon_{sorb,i}\rho_{sorb}D_{sorb,i}\nabla w_{r,i}\cdot d\mathbf{A}\\ &= \int_V \phi'''_{r,i}\,dV + \int_V R'''_{r,i}\,dV\\ &- \int_V \sum_{j,j\neq i} w_{r,i}k_{C,sorb,ij}\varepsilon_{sorb,i}\rho_{sorb}\,dV + \int_V \sum_{j,j\neq i} w_{r,j}k_{C,sorb,ji}\varepsilon_{sorb,j}\rho_{sorb}\,dV\end{aligned} \tag{5.3}$$

Equation 5.3 includes the following terms: 1) convection, 2) dispersion, 3) sources, 4) reactions, 5) comminution to other size fractions, 6) comminution from other size fractions. The equation is similar to earlier equation for char (Chapter 4.3), but now the dispersion is defined in a conventional manner instead of applying a target profile. The term $w_{r,i}$ is a fraction specific weight fraction of species *r*.

The continuity of the sorbent species is fundamentally different than that of char. While char is combusted and only a minor amount of char is usually reaching the furnace outlet, the sorbent species are constantly flowing through the whole system and the residence time of sorbent species is much longer. Consequently, the net velocity field has a significant effect on the continuity and cannot be neglected, as could be done for char, where the mixing of char was modelled by dispersion only. On the other hand, the transient flow causes constant mixing of sorbent species, which is approximated by the dispersion term. The dispersion constants are defined separately for each furnace zone, each size fraction, and vertical and horizontal directions, but they are the assumed to be the same for all sorbent species.

The sources include the feeds and the solid flows from return legs as volumetric sources. The mass flows to bottom ash and to external heat exchangers have been defined as sinks in the source term. The mass flow to furnace outlets is included in the convection term. The mass flow of sorbent species through internal circulation is not yet considered.

The different sorbent reactions are controlled by fraction specific reaction rate expressions for each reaction *reac* and reacting sorbent species *r*:

$$R'''_{reac,i} = k_{reac,i}\varepsilon_{r,i}\rho_r \tag{5.4}$$

The following table presents the relation between different species (*r*) and reactions (*reac*) and the sign of reaction rate constants (k_{reac}). A negative rate constant indicates the reacting (i.e. consuming) species (e.g. $CaCO_3$ in calcination).

Table 5.1: Sign of reaction rate constants k_{reac} for different sorbent species.

Reaction (*reac*)	Abbr.	Equation	Species (*r*)		
			$CaCO_3$	CaO	$CaSO_4$
Calcination	calc	$CaCO_3 \rightarrow CaO + CO_2$	$-k_{calc}$	$+k_{calc}$	
Carbonation	carb	$CaO + CO_2 \rightarrow CaCO_3$	$+k_{carb}$	$-k_{carb}$	
Sulphation	sulf	$CaO + SO_2 + ½O_2 \rightarrow CaSO_4$		$-k_{sulf}$	$+k_{sulf}$
Direct sulphation	dirs	$CaCO_3 + SO_2 + ½O_2 \rightarrow CaSO_4 + CO_2$	$-k_{dirs}$		$+k_{dirs}$
Desulphation	desu	$CaSO_4 \rightarrow CaO + SO_2 + ½O_2$		$+k_{desu}$	$-k_{desu}$

The species-specific reaction term ($R'''_{r,i}$) in the continuity equation combines the different reactions for each species, for example the reactions defined for $CaSO_4$:

$$\begin{aligned} R'''_{\mathrm{CaSO_4},i} = &+k_{sulf,i}\varepsilon_{\mathrm{CaO},i}\,\rho_{\mathrm{CaO}}\frac{M_{\mathrm{CaSO_4}}}{M_{\mathrm{CaO}}} \\ &+ k_{dirs,i}\varepsilon_{\mathrm{CaCO_3},i}\,\rho_{\mathrm{CaCO_3}}\frac{M_{\mathrm{CaSO_4}}}{M_{\mathrm{CaCO_3}}} \\ &- k_{desu,i}\varepsilon_{\mathrm{CaSO_4},i}\,\rho_{\mathrm{CaSO_4}} \end{aligned} \tag{5.5}$$

The reaction rate constants are determined by empirical correlations based on literature, but including user defined correction factors for tuning the reaction rates based on characterization tests or validation studies. Moreover, the correlations can be easily modified or several alternative correlations can be defined as the knowledge of the sorbent reactions is improved. Example calculation of sorbent reactions in air-fired and oxygen-fired modes is given in Chapter 6.3.

The reactions involving CaS have not been implemented to the code yet. In combustion cases, these reactions usually have only a minor role, but in gasification conditions and in reducing zones of the furnace, these reactions can be significant.

The comminution rate constants are assumed the same for all sorbent species. In real conditions, the comminution is probably affected by the reactions, for example due to cycling calcination/carbonation reactions. This steady-state model does not predict the effect of such cycling, but the comminution rate constants should be adjusted to simulate the measured behaviour.

5.3 Calcination and carbonation

The calcination and carbonation are reversible reactions:

Calcination	$CaCO_3 \rightarrow CaO + CO_2$	(5.6)
Carbonation	$CaO + CO_2 \rightarrow CaCO_3$	(5.7)

In atmospheric combustion with air, the limestone is rapidly calcined as it enters the hot furnace. In pressurized combustion or oxycombustion, the partial pressure of CO_2 is high, which can prevent calcination. Figure 5.2 presents typical operation ranges of atmospheric air-fired and oxygen-fired combustion in relation to curves for equilibrium pressure of CO_2 based on Barker (1973) and Silcox et al. (1989).

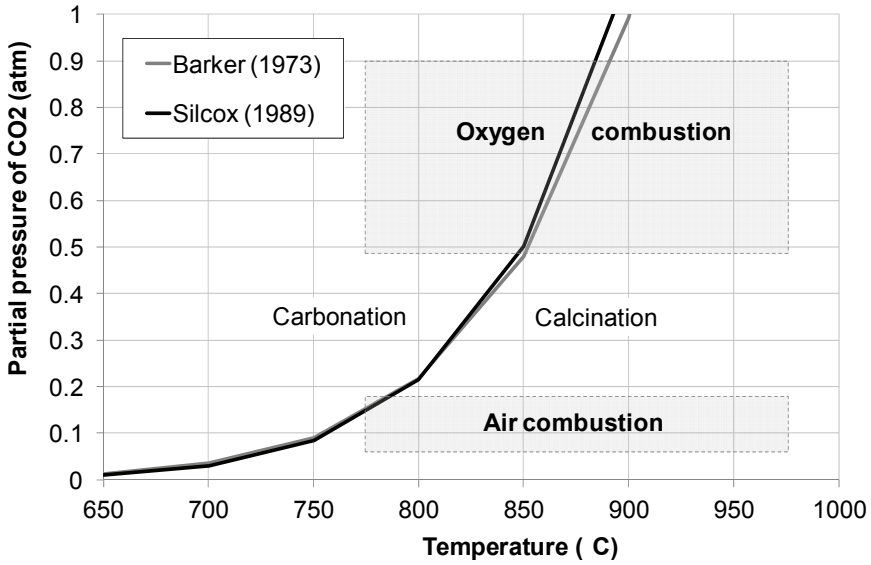

Figure 5.2. Calcination curves.

This model applies the equations by Silcox et al. (1989) to define the equilibrium pressure and the reaction rate constant for calcination:

$$p_{eq} = 4.137 \cdot 10^7 \exp\left(\frac{-20\,474}{T}\right) \quad \text{atm} \tag{5.8}$$

$$k_{calc,i} = 1.22\, a_{calc,i} \exp\left(\frac{-4026}{T}\right)\left(p_{eq} - p_{\mathrm{CO_2}}\right) A_{m0,\mathrm{CaCO_3}} M_{\mathrm{CaCO_3}} \tag{5.9}$$

The term $a_{calc,i}$ is a fraction specific correction factor. The term $A_{m0,CaCO3}$ is a default specific surface for $CaCO_3$, which has been set to 300 m^2/kg. The actual, effective reacting surface area for each particle size fraction *i* is thus defined as:

$$A_{m,CaCO_3,i} = a_{calc,i} A_{m0,\mathrm{CaCO_3}} \tag{5.10}$$

The carbonation rate has been defined based on Sun et al. (2008) and converted to apply pressure units $[p]$ = atm:

$$k_{carb,i} = 0.0169\, a_{carb,i} \exp\left(\frac{-3488}{T}\right)\left(p_{\mathrm{CO_2}} - p_{eq}\right) A_{m0,\mathrm{CaO}} M_{\mathrm{CaO}} \tag{5.11}$$

Similar to calcination equation, the carbonation equation applies a default specific reaction surface for CaO, which has been set to 20 000 m^2/kg. The actual, fraction specific reaction surfaces can be adjusted by parameter $a_{carb,i}$.

The specific reaction surfaces are limestone dependent. Cheng et al. (2004) reports values between 60...200 m^2/kg for limestones and 14 000...16 000 m^2/kg for calcined samples. Krishnan and Sotirchos (1994) report 300...700 m^2/kg for recarbonated limestones, 45 000...56 000 m^2/kg for calcined limestones and 27 000...34 000 m^2/kg for recalcined limestones. Typically, the reaction surface is higher with smaller particle diameter. However, because the reactions are not limited to particle surface, the reaction surface area cannot be set simply proportional to the integrated particle surface area. The above given default values are only initial settings, which provide meaningful results, but they should be adjusted by the fraction specific correction factors.

In oxycombustion conditions, the sorbent can be subject to cycling calcination/carbonation reactions. In cyclic conditions, the maximum carbonation conversion has been found to decay while complete calcination has been always achieved (Abanades and Alvarez, 2003; Bouquet et al., 2009). To take account for this kind of cyclic effects in a steady-state model, the rate constant for carbonation must be adjusted to match the average behaviour.

Figure 5.3 presents examples of determined reaction rate coefficients for calcination and carbonation in oxycombustion conditions. With the selected CO_2-concentration, the calcination temperature is about 870 °C. The reaction rate curves show how the carbonation rate decreases gradually when approaching the calcination temperature. Above the calcination temperature, the calcination rate increases rapidly with increasing temperature. As the calcination is endothermic and carbonation is exothermic reaction, the calculation can easily start to fluctuate between the two regions. In the code, this is prevented by damping the changes, especially when the operating conditions are near to the calcination temperature.

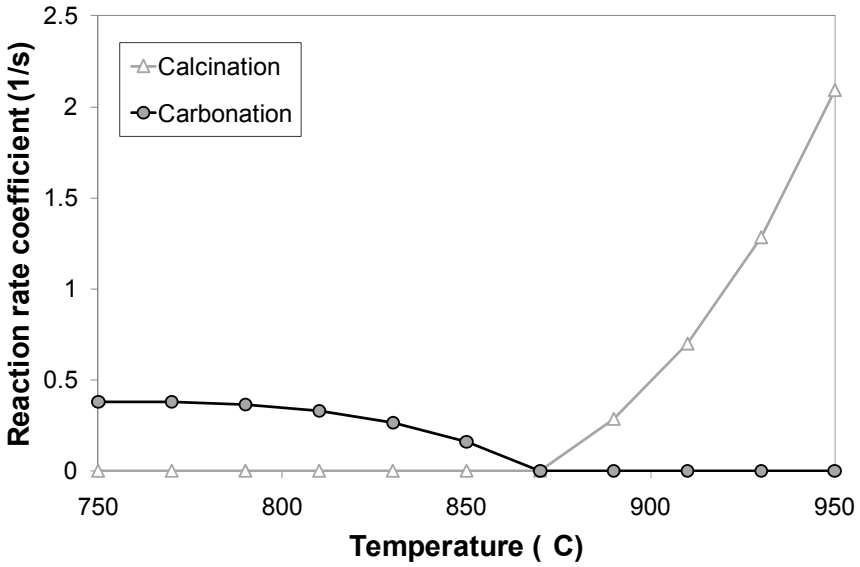

Figure 5.3. Reaction rate coefficients of calcination and carbonation.
Parameters: $a_{calc} = 1$, $a_{carb} = 1$, $p_{CO2} = 0.69$ atm.

5.4 Sulphation and direct sulphation

The sulphur capture can occur by sulphation or direct sulphation:

$$\text{Sulphation} \qquad CaO + SO_2 + \tfrac{1}{2}O_2 \rightarrow CaSO_4 \tag{5.12}$$

$$\text{Direct sulphation} \qquad CaCO_3 + SO_2 + \tfrac{1}{2}O_2 \rightarrow CaSO_4 + CO_2 \tag{5.13}$$

In air-fired CFB combustion at atmospheric pressure, the sulphur capture occurs by normal calcination–sulphation route and the reactions by direct sulphation are insignificant. At high partial pressure of CO_2, the calcination temperature is higher, thus the calcination of limestone may not occur and the direct sulphation can be dominating.

Various bench scale and pilot scale studies show that in normal sulphation, the maximum conversion degree of CaO is limited due to formation of sulphate layer, which prevents the diffusion of gases to the core of the particle (Anthony and Granatstein, 2001). In some correlations, this has been considered by setting a fixed maximum conversion degree. However, if the residence time of the limestone particle is long enough, the conversion will continue, although slowly. Models with a final maximum conversion are not good in a case of long residence time and strong attrition (Saastamoinen, 2007). In direct sulphation, the conversion rate is slower but the maximum conversion degrees can be higher than in normal sulphation (Liu et al., 2000).

In the current model, the sulphation and direct sulphation rates are controlled by the following correlations:

$$k_{sulf,i} = 0.001\, a_{sulf,i} \exp\left(\frac{-2400}{T}\right) \exp\left(-8\, X_{\mathrm{CaSO_4},i}\right) C_{\mathrm{SO_2}} C_{\mathrm{O_2}} A_{m0,\mathrm{CaO}} M_{\mathrm{CaO}} \qquad (5.14)$$
$$\max\left(C_{\mathrm{O_2}}\right) = 0.5\ \mathrm{mol/m^3}$$

$$k_{dirs,i} = 0.01\, a_{dirs,i} \exp\left(\frac{-3031}{T}\right) C_{\mathrm{SO_2}}^{0.9} C_{\mathrm{CO_2}}^{-0.75} C_{\mathrm{O_2}}^{0.001} A_{m0,\mathrm{CaCO_3}} M_{\mathrm{CaCO_3}} \qquad (5.15)$$

The correlation for the normal sulphation includes terms for all the main affecting variables: temperature, molar concentration of SO_2 and O_2, and the effective reaction surface area. The sulphation rate increases as a function of temperature (Han et al., 2005). The decaying conversion rate due to formation of the sulphate layer has been estimated by the exponential term including the molar fraction of $CaSO_4$, which is similar to approach applied by Mattisson and Lyngfelt (1998a). Based on Liu et al. (2000), the oxygen content does not affect the reaction rate if it is above 5%. In this model, the effect of the oxygen concentration has been limited to a maximum value of 0.5 mol/m^3, which corresponds to approximately 5% of oxygen at normal combustion temperatures.

The correlation for direct sulphation is based on Hu et al. (2008). Although the oxygen concentration has not been found to affect the reaction rate, a term C_{O2} has been added to set the reaction rate to zero, if the oxygen concentration is approaching zero. Due to small exponent, the oxygen term is near to unity in oxidizing conditions. The default reaction surface for CaO and $CaCO_3$ has been set to same as above for carbonation and calcination (20 000 m^2/kg and 300 m^2/kg). The actual reaction rate surfaces are dependent on the limestone. For initial estimations and for qualitative studies, the above correlations can be applied without corrections, but for more accurate simulations, the correction terms $a_{sulf,i}$ and $a_{dirs,i}$ should be adjusted to fit the experimental data.

The following figure presents the conversion by the sulphation and direct sulphation rates as a function of time determined by the above equations in a constant environment and compared with experimental values presented by Liu et al. (2000). At the start of the simulation, the molar conversion to $CaSO_4$ has been set to zero. As the sulphation progresses, the conversion rate of normal sulphation decays. The conversion rate of direct sulphation is slower at first but does not decay as a function of conversion degree and thus can reach a higher conversion degree.

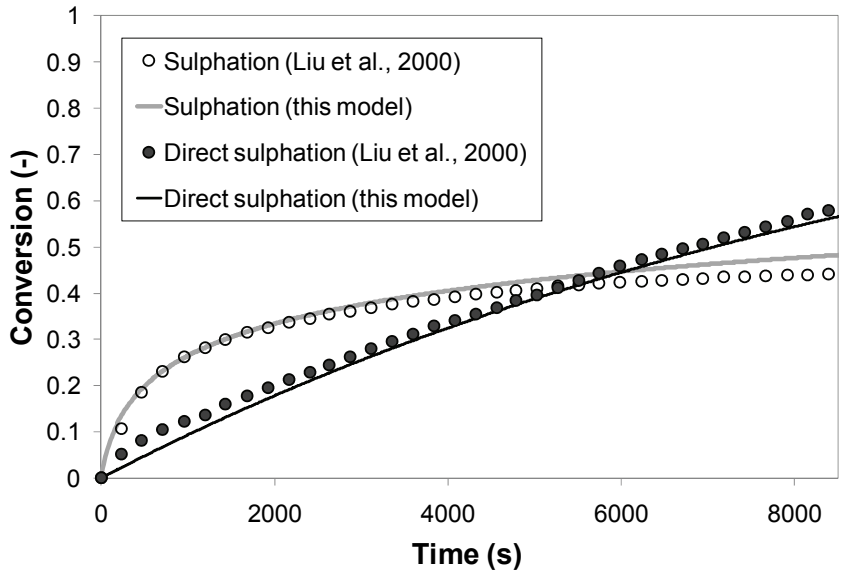

Figure 5.4. Molar conversion degree to $CaSO_4$ in sulphation and direct sulphation. Parameters: $a_{sulf} = a_{dirs} = 0.8$, 1123 K, 10% O_2, 1920 ppm SO_2. CO_2 is 20% and 80% for normal sulphation and direct sulphation, respectively.

5.5 Desulphation

In atmospheric units, the sulphur capture reaches maximum efficiency at about 850°C, but the exact optimum temperature varies considerably depending on the limestone and the unit. The literature gives various explanations for this, for example decomposition of the sulphate in reducing conditions (desulphation), sintering, pore blocking due to increased sulphation at high temperature, and oxygen depletion due to increased volatile combustion. The actual mechanism can be a combination of several affecting phenomena, but many researchers prefer the first explanation that the temperature maximum can best be regarded as competition between sulphation and desulphation, with desulphation becoming more important at higher temperatures (Mattisson and Lyngfelt, 1998b; Zevenhoven et al., 1999; Anthony and Granatstein, 2001; Barletta et al., 2002).

In this model, the desulphation is determined as reaction with CO:

$$\text{Desulphation} \qquad CaSO_4 + CO \rightarrow CaO + SO_2 + CO_2 \tag{5.16}$$

In real conditions, the decomposition of $CaSO_4$ may take place in a reaction with hydrogen as well. Moreover, the possible decomposition routes may involve CaS.

A simple correlation for determining the desulphation rate is attempted:

$$k_{desu,i} = 0.005\, a_{desu,i} \exp\left(\frac{-10\,000}{T}\right) C_{\mathrm{CO}} A_{m0,\mathrm{CaSO_4}} M_{\mathrm{CaSO_4}} \tag{5.17}$$

The desulphation rate is proportional to molar concentration of CO and increases as a function of temperature. The default specific surface area has been set to $A_{m0,CaSO4}$ = 100 m^2/kg. The following figure presents an example of sulphation and desulphation rates as a function of temperature in a constant atmosphere. The values are defined as mol/m^3s, thus the difference between the sulphation and desulphation can be directly compared. With the applied parameters, the correlations produce a maximum sulphur capture at 850 °C. In a three-dimensional furnace process, the conditions are more complicated, as the desulphation occurs locally in areas with reducing conditions and high temperature, the gas composition and the sorbent composition are not constant, and the outcome is difficult to estimate without the support of modelling tools.

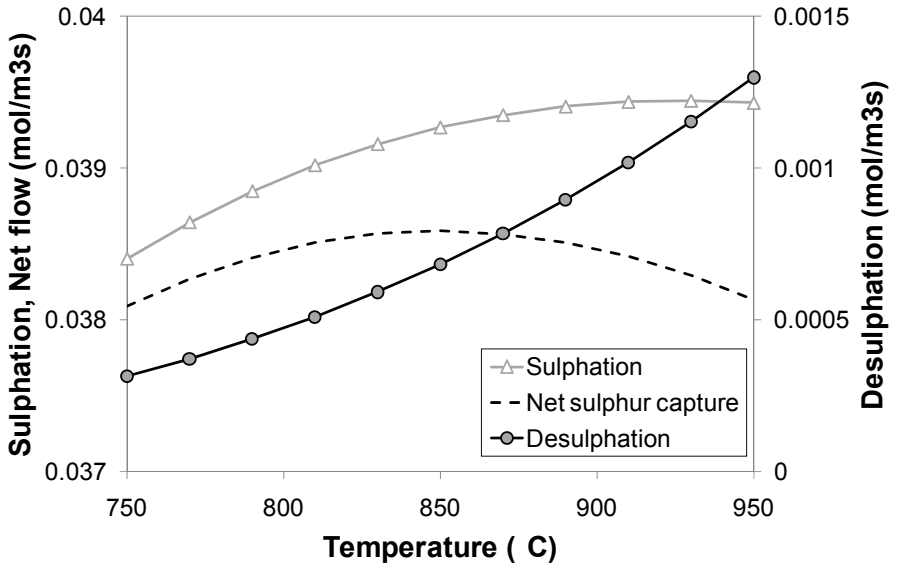

Figure 5.5. Molar sulphation and desulphation rates (mol/m^3s).
Parameters: sorbent concentration 1 kg/m^3, 5% CO, 0.1% SO_2, X_{CaSO4}=0.1.

5.6 Enthalpy change in sorbent reactions

The enthalpy change in sorbent reactions is determined based on formation enthalpies and it is included in the energy equation (Equation 3.14). The reaction enthalpies for the different reactions are as follows (negative = exothermic):

$$CaCO_3 \rightarrow CaO + CO_2 \qquad \Delta H_0 = +178.327 \text{ kJ/mol} \qquad (5.18)$$

$$CaO + CO_2 \rightarrow CaCO_3 \qquad \Delta H_0 = -178.327 \text{ kJ/mol} \qquad (5.19)$$

$$CaO + SO_2 + \tfrac{1}{2}O_2 \rightarrow CaSO_4 \qquad \Delta H_0 = -502.115 \text{ kJ/mol} \qquad (5.20)$$

$$CaCO_3 + SO_2 + \tfrac{1}{2}O_2 \rightarrow CaSO_4 + CO_2 \qquad \Delta H_0 = -323.788 \text{ kJ/mol} \qquad (5.21)$$

$$CaSO_4 + CO \rightarrow CaO + SO_2 + CO_2 \qquad \Delta H_0 = +219.151 \text{ kJ/mol} \qquad (5.22)$$

5.7 Sources of sulphur dioxide emissions

The sulphur dioxide emissions originate from the combustion of sulphur containing fuel:

- The volatile sulphur is released as H_2S.
- The sulphur in char is combusted to SO_2 in oxidizing conditions.
- During gasification of char, the sulphur in char is released as H_2S.
- In oxidizing conditions, H_2S can burn to SO_2.

In addition, in oxycombustion, part of the SO_2 entering the furnace originates from the recycled flue gas. This recirculation may have an improving effect on the in-furnace sulphur capture, as the sulphation reactions are occurring at higher SO_2-concentration.

The different sources of sulphur have a high impact on the formation of emissions and the sulphur capture. This should be realized when developing the sub-models for the sorbent reactions. The sub-models for sorbent reactions are the last link in the long chain of different sub-models affecting the phenomena: fluid dynamics and mixing of gas and solids, distribution of elements in char and volatiles, devolatilization, combustion of char, combustion of gaseous species, and heat transfer. If one of these sub-phenomena is not correctly modelled, it will have an effect on the last link, i.e. the sorbent reactions, as well.

6 Applications

6.1 Validation study of a 15 MWe CFB combusting recycled wood

This chapter presents a model validation study, which has been published in Myöhänen et al. (2005).

The object of this study was a 15 MWe CFB boiler plant burning recycled wood. The measurements were carried out during the commissioning of the boiler in 2003. The boiler was operated in steady state conditions and the mass and energy balances of the boiler were determined according to DIN 1942, based on the measured heat recovery, exit gas composition and analyses of the input and output materials.

Figure 6.1 presents the boiler unit and the location of measurement ports on the right side wall of the furnace. Similar ports were located on the opposite wall. The cross-section of the furnace is 5.5 m x 3.6 m and the height of the furnace is 19 m. The measurement ports were standard temperature measurement ports located through the fins in the membrane wall. The hole size was 24 mm, which limited the maximum practical probe diameter to 22 mm.

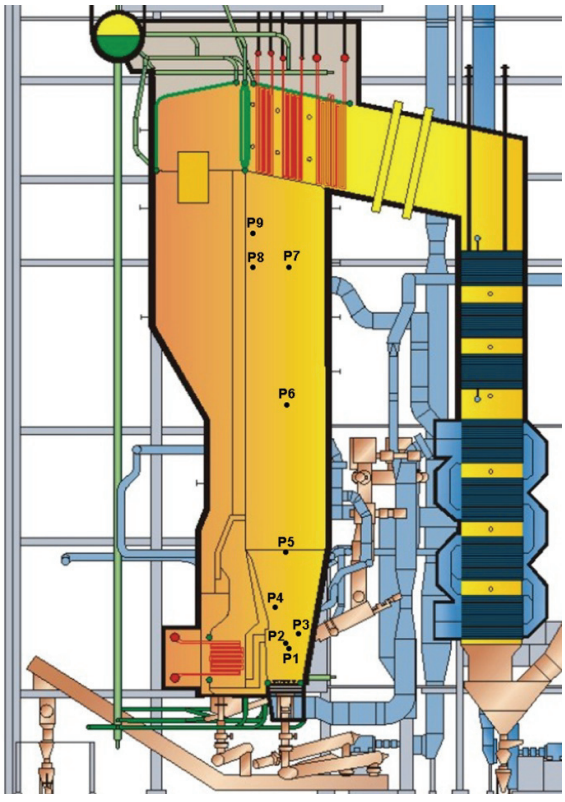

Figure 6.1. 15 MWe CFB boiler unit and measurement ports in furnace.

The fuel is fed to the furnace from two locations at the back wall (wall at the right in Figure 6.1). Fluidization air enters the furnace through the grid and secondary air is injected through nozzles located in two levels at the refractory lined tapered bottom of the furnace. The cooled solid separator is integrated with the furnace and the solids from the separator enter fluidized bed heat exchanger units before they are introduced back to the furnace.

During the profile measurements, the boiler was operated at full load. Operation data are presented in Table 6.1.

Table 6.1: Operation data of the studied boiler unit.

Steam Flow Rate (MCR)	16.4 kg/s
Steam Pressure	90 bar g
Steam Temperature	500 °C
Thermal Output	44 MWt
Power Output	15 MWe
Fuel	Recycled wood
Proximate analysis (as fired)	13% char, 56% volatiles, 2% ash, 29% moisture
Ultimate analysis (d.s.)	50.52% C, 5.76% H, 0.06% S, 1.56% N, 42.10% O
Higher heat value (d.s.)	19.9 MJ/kg
Total flue gas flow rate	17.5 m^3n/s
Average bed temperature	770 °C
Average furnace exit temperature	840 °C (at separator inlet)
Circulating bed	Mixture of fuel ash and make-up sand
Average solid density	approx. 2500 kg/m^3
Average particle size (downcomer)	180 – 200 µm
Circulating mass flow rate	approx. 2 kg/m^2s net flow in furnace
Grid air / total air share	45%
Bottom ash / total ash share	75%
Upper secondary air level from grid	4 m
Combustion efficiency	99.97% carbon conversion

The vertical pressure profile was determined by differential pressure measurements across the measurement ports. The measured pressure differences were corrected by the gas density difference between the inside ($\rho_{g,i}$) and outside ($\rho_{g,o}$) of the furnace and the solid concentration profile was determined from the differential pressures:

$$\Delta P = \Delta P_{meas} - \left(\rho_{g,in} - \rho_{g,out}\right) g\, \Delta h \tag{6.1}$$

$$\Delta P = \varepsilon_s \left(\rho_s - \rho_g\right) g\, \Delta h \approx \varepsilon_s \rho_s g\, \Delta h \tag{6.2}$$

The determined vertical solid concentration profile was fitted to an empirical correlation (Chapter 3.4), which was then used to determine the solid concentration profile in the model.

Temperature and gas concentration profiles were determined from the available measurement ports by using an air-cooled suction probe (Figure 6.2). The length of the probe was 4.6 meters and the maximum diameter 21.3 mm. The analyzed gas components included O_2, CO_2, CO, CH_4, NO and N_2O.

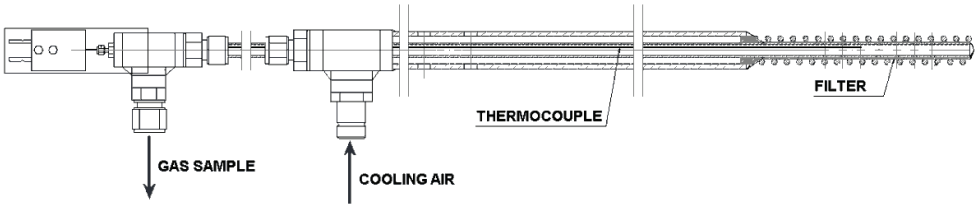

Figure 6.2. Gas suction probe.

Figure 6.3 presents oxygen and carbon monoxide concentration measurements of measurement ports P5 – P7. The carbon monoxide is higher at the left side of the furnace indicating non-uniform fuel feed distribution. The oxygen concentration is increasing along the height of the furnace, which seems surprising at first, since all measurement ports are well above the secondary air nozzles. The reason for this was explained by the modelling study.

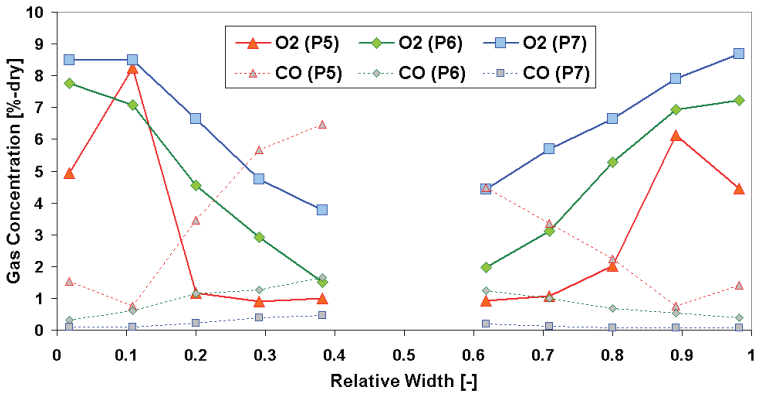

Figure 6.3. Oxygen and carbon monoxide measurements.

A common problem with all modelling and simulation tools is the accurate definition of the boundary conditions. In pilot scale units, the boundary conditions, e.g., fuel feed and air feed rate and distribution, can be determined with reasonable accuracy, but in commercial scale units, this is often difficult. A typical CFB boiler can include 2 – 16 fuel feeding locations and 20 – 60 secondary air nozzles depending on the size of the unit. The total fuel and air feed rates can be determined from overall mass and energy balance, but the distribution of the fuel and air are normally not measured or the

measurements are inaccurate. The usual assumption of uniform distribution may often be incorrect.

As an example, the following figure shows the fuel feeding system of the studied boiler unit. The fuel is discharged from a day silo to a double screw system, which divides the fuel to two fuel lines. The fuel is then fed to the furnace by screw feeders. The fuel feeding system is apparently capable to provide uniform fuel distribution to both fuel lines.

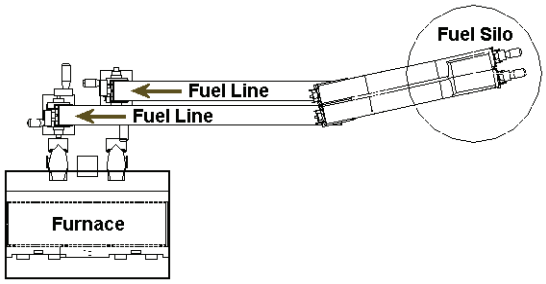

Figure 6.4. Fuel feeding system.

During the commissioning of the boiler, gas profile measurements were carried out in order to check the balance of the fuel feed distribution. These showed, that the concentration of combustible gases was slightly higher on the left side of the furnace indicating higher fuel feeding rate to that side. Further inspection revealed that the double screw system was not dividing the fuel evenly to both lines. The problem was later solved by simple modifications to the fuel system.

In this case, the actual fuel feed distribution was determined with the aid of the model. Figure 6.5 shows the tuning process based on the measured values of CO and CH_4 above the tapered bottom section of the furnace. The modelling was started with uniform 50/50 fuel feed distribution. With uniform distribution, the modelling result differs clearly from the measurements. The modelled results matched the measurements fairly well when the feed fraction of the left fuel feeder was increased to 60%. After the fuel feed distribution had been fixed, the other tunable model parameters, such as the dispersion coefficient of the gas, were fine-tuned based on the measured gas profiles.

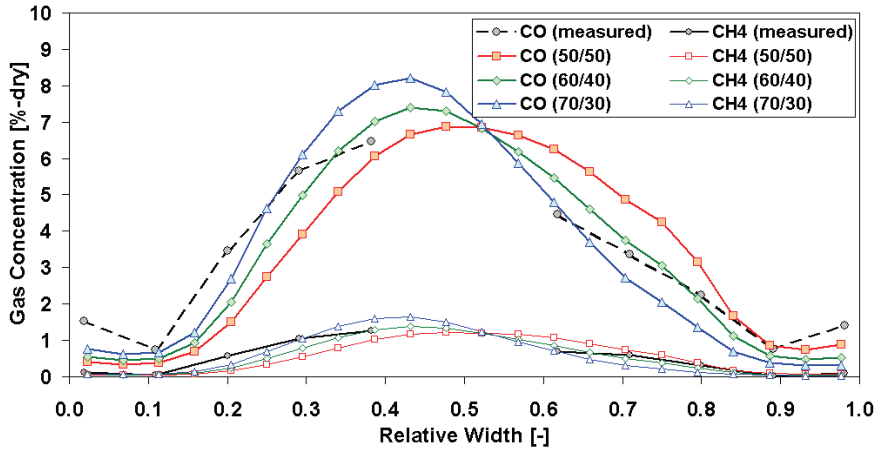

Figure 6.5. Tuning of fuel feed distribution.

Determination of accurate boundary conditions is case-specific and reliable determination is often not possible. If the boundary conditions of the process model are different from the real conditions, then the model is not valid. If profile measurements are available, then the boundary conditions can be determined by using the model. Otherwise a sensitivity study of the effect of non-uniform boundary conditions should be performed.

The characteristics of the feed materials affect the combustion process and must be known in order to model the process successfully. Different characterization methods have been presented by Jäntti et al. (2005). As an example, the following shows model results with different char reactivity values.

Figure 6.6 presents the effect of char reactivity on local char combustion rate and temperature and Figure 6.7 the effect on char fraction in fly ash. The location of the values in Figure 6.6 is at the bottom of the furnace, near the fuel feeding points. In the reference case, the char reactivity is based on the characterization tests. In the two comparison cases, the reactivity constant in Equation 4.14 has been decreased and increased 50% of the reference value.

The effect on the char combustion rate is small compared to the quantity of the change. This is because the char combustion rate is limited by the local char and oxygen concentration and thus dependent on the location of the feeding points and the mixing of char with oxygen. The effect on the temperature field is even smaller, because the temperature is affected by many other variables as well, such as the combustion of gases and heat transfer.

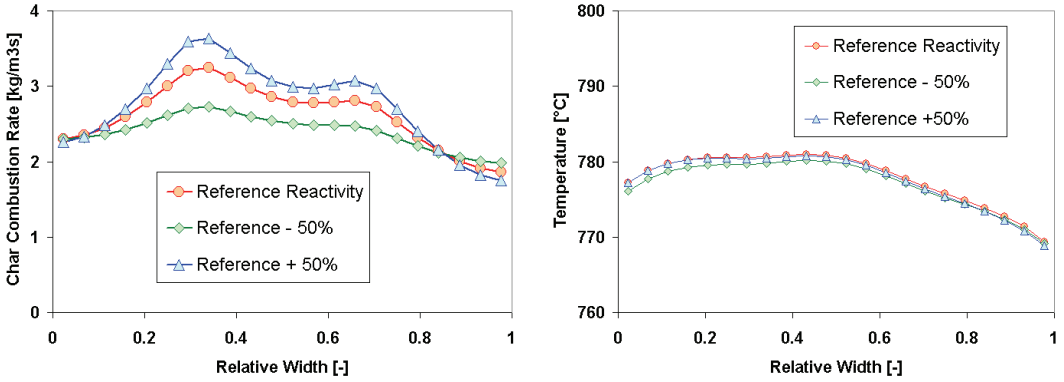

Figure 6.6. Effect of char reactivity on local combustion rate and temperature.

If the reactivity is small, the char reactivity can be determined based on the measured char fraction in the fly ash (Figure 6.7). With high reactivity fuels, the effect is small, thus, the determination of the char combustion rate coefficient is difficult if it is based only on field measurements. In general, the model parameters should be based on characterized values whenever possible in order to reduce the number of tunable parameters during modelling process.

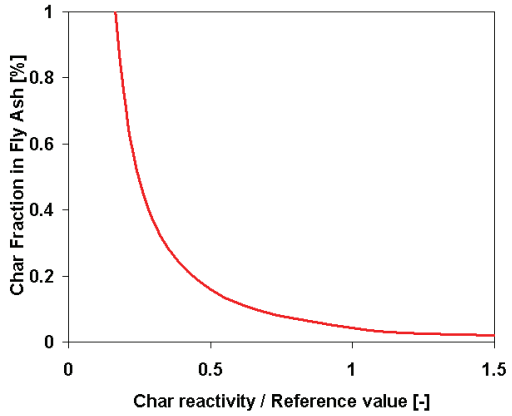

Figure 6.7. Effect of char reactivity on char fraction in fly ash.

After the boundary conditions, the characteristic feed material properties and other explicitly defined model parameters were set, the determination of the adjustable model parameters could be started. The tuning was performed by comparing the measurements to the model results and modifying the appropriate model parameters until the two matched.

The main adjustable parameters affecting the gas concentration and temperature profiles were:

- dispersion coefficients of solid and gaseous species affecting the mixing of fuel, combustible gases and oxygen,
- reaction rate parameters affecting the combustion process and formation of emissions (those parameters, which were not determined by characterization methods),
- parameters affecting the penetration of fuel and secondary air jets,
- parameters affecting the internal circulation, and
- parameters affecting the heat transfer coefficients.

Because many of the adjustable parameters interact with each other, the whole tuning and validation process is iterative and complicated. When several different cases are modelled, generic correlations for determining the different parameters are developed and the number of adjustable parameters is reduced.

The following figure compares different profile measurements to the model results after the tuning process has been completed. The values match well with each other.

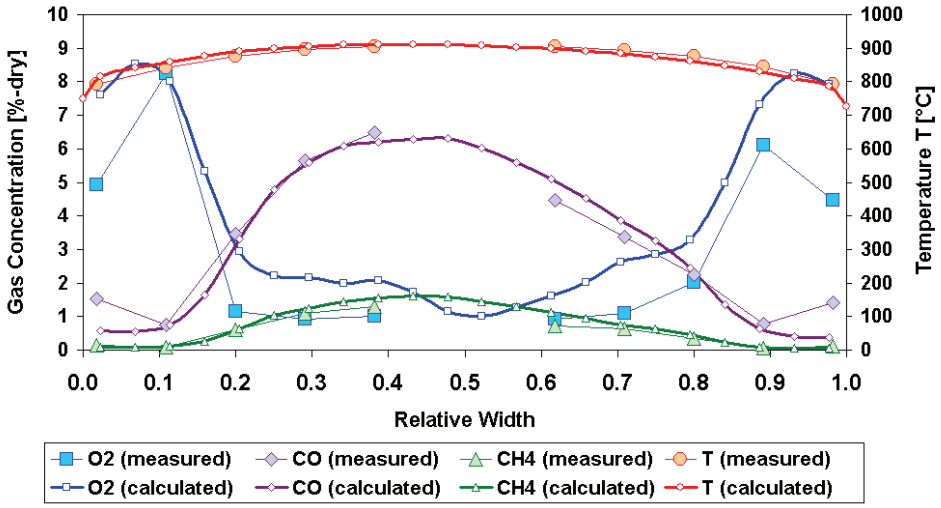

Figure 6.8. Measured and modelled gas concentration and temperature profiles

After the model has been validated, it represents the actual furnace process with good accuracy and it can be used for studying the process in more detail. The following figures are three-dimensional representations of the different process variables.

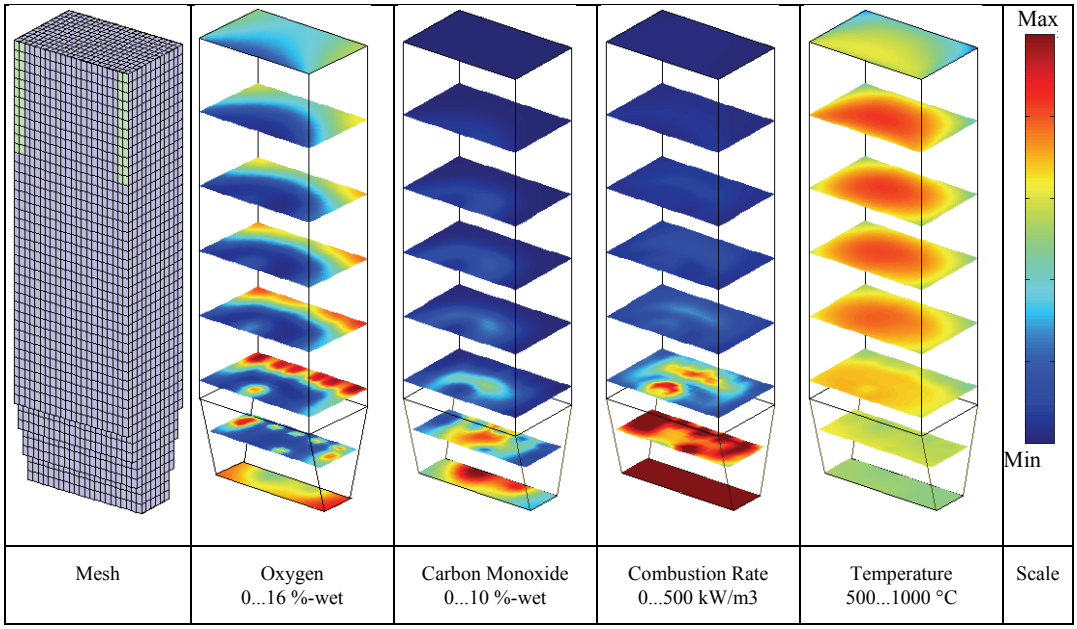

Figure 6.9. Model results.

The modelled oxygen concentration explains why the oxygen measured at the centreline of the furnace increases along the height. Most of the secondary air nozzles are located at the back wall of the furnace. The air from the secondary air nozzles mixes slowly with the main gas stream, consequently, at the centreline, the oxygen content increases towards the top of the furnace. This is presented clearly in Figure 6.10. The oxygen content is higher at the sides of the furnace due to secondary air entering these locations from the start-up burners.

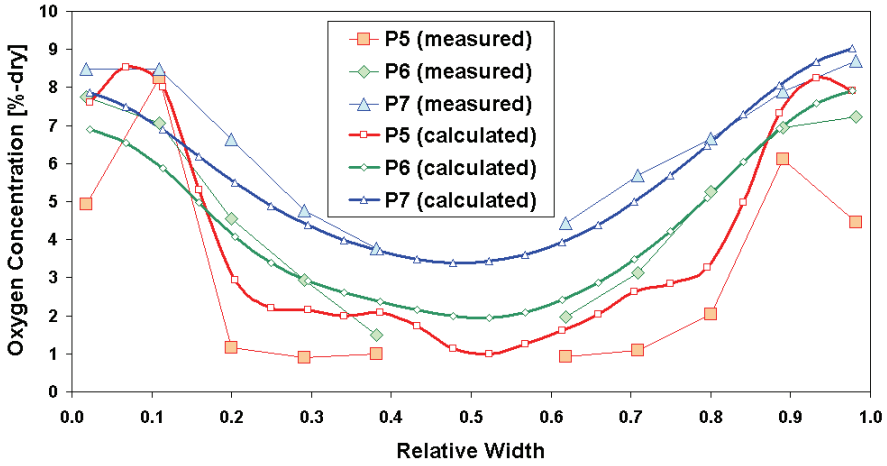

Figure 6.10. Measured and modelled oxygen profiles.

The carbon monoxide profile shows the effect of non-uniform fuel feed distribution. At the bottom part of the furnace, the concentration is higher on the left side. At the top of the furnace, the amount of combustible gases reaches zero indicating good combustion efficiency despite the non-uniform conditions.

The combustion rate is highest in the areas where combustible material mixes with oxygen. In CFB conditions, most of the combustion occurs always at the bottom of the furnace.

The temperature profile is a result of the combustion profile and heat transfer. The temperature profile is typical for this kind of fuel: at the bottom of the furnace, the temperature is lower than above the tapered bottom section of the furnace. At the top part of the furnace, the temperature field is uniform. Non-uniform fuel feed distribution has practically no effect on temperature distribution.

6.2 Conceptual study of an oxy-fuel CFB boiler

The following conceptual study has been presented by Eriksson et al. (2009) and later published by Myöhänen et al. (2009). Some of the modelling results have been reported by Kuivalainen et al. (2009) as well. The objective was to study a full-scale oxygen-fired CFB. In oxy-fuel combustion, the fuel is burned in a mixture of oxygen and recycled flue gas. This generates CO_2 rich flue gas from which the CO_2 can be separated and compressed.

The world's first supercritical CFB boiler, which was constructed at Łagisza, Poland, was selected as a starting point and reference for the studies. The boiler efficiency with supercritical steam conditions is higher than with a conventional subcritical steam cycle, which compensates for the reduction of net power output due to oxygen production and CO_2 capture. The output of the plant is 460 MWe (gross) / 439 MWe (net). The net efficiency is in excess of 43%. The supercritical steam parameters are 27.5 MPa and 560°C. The fuel is bituminous coal sourced from ten local coalmines. A more detailed description of the boiler design is given by Hotta (2009).

The main effect of higher O_2 concentration is the rise of the adiabatic combustion temperature (Figure 6.11). In the hot loop of a CFB furnace (i.e. furnace, separator and return leg), the temperature level is limited by agglomeration temperature of solid particles and it is typically well below 1000 °C. Increasing the adiabatic temperature will increase the need of heat transfer in the CFB furnace as shown in Figure 6.11, which illustrates the share of heat duty in CFB hot loop as a function of adiabatic temperature. Decreased gas flow rate means also that cross-sectional area of the boiler is smaller. Together with higher heat duty share of the hot loop, this means that one of the major challenges with high oxygen concentrations will be the development of CFB boiler design in such a manner that enough cooling surfaces exist.

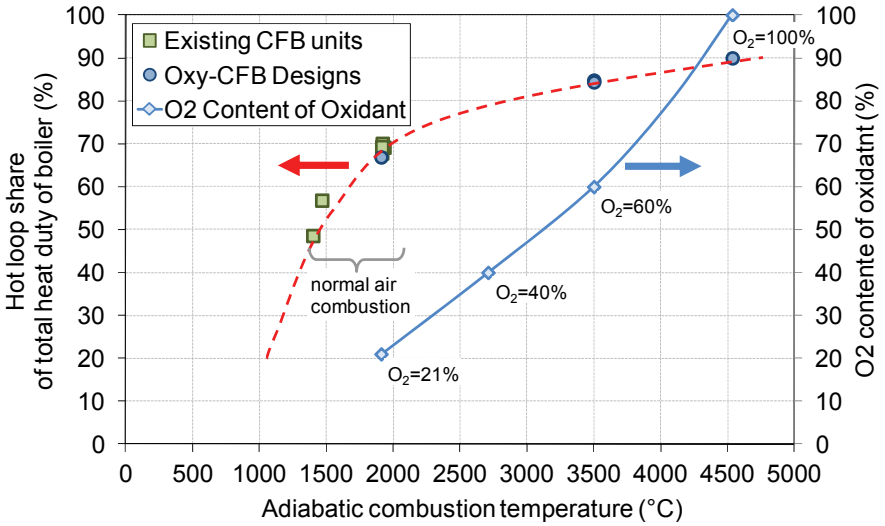

Figure 6.11. Hot loop share of total heat duty as the function of the adiabatic combustion temperature (courtesy of Jouni Miettinen, Foster Wheeler Energia Oy).

Normal boiler designs with reasonable modifications can be applied, if the mixing ratio of oxygen and recycled flue gas ratio is chosen so that the adiabatic combustion temperature is close to that of air firing. In a "dual firing" concept, the plant could be operated either with or without carbon capture, which reduces risks due to failures in the auxiliary equipment. It also enables more flexible production depending on the price of CO_2 allowances and electricity and power requirements.

With moderate oxygen concentration of the combustion gas, the main differences to air-fired combustion are due to much higher concentrations of CO_2 and H_2O. These affect the combustion reactions, fluid dynamics, heat transfer, and emissions formation and reduction mechanisms. Changes occur in the gas density and viscosity, radiation properties of gas and equilibrium of $CaCO_3/CaO$. The latter influences the sulphur capture and particle fragmentation, with further effects on solids circulation and heat transfer.

In this study, the following cases were evaluated:

- Air-firing as the reference case,
- Case 1: oxycombustion with reduced in-furnace heat surfaces,
- Case 2: oxycombustion with original in-furnace heat surfaces,
- Case 3: similar to Case 2, but with reduced flue gas recycle rate (i.e. higher O_2 concentration of oxidant and lower velocities but similar steam capacity).

Table 6.2 presents main process values of different cases.

Table 6.2: Process values of conceptual study.

	Air ref.	Case 1	Case 2	Case 3
Input-O_2 (%-wet)	20.6	23.9	23.9	29.6
Oxidant temp. (°C)	295	252	250	230
Steam capacity (MW)	965	1022	1018	1003
Fuel input (MW)	1020	1069	1068	1044
Furn. velocity (m/s)	5.2	4.5	4.5	3.7
Furn. exit temp. (°C)	864	900	867	899
Flue gas flow (kg/s)	457	461	459	364
Flue gas to stack (kg/s)	457	132	131	130
Excess O2 (%-dry)	3.6	3.7	3.7	3.7
Flue gas CO_2 (%-wet)	14.3	60.6	60.5	60.8
Flue gas H_2O (%-wet)	9.1	32.9	33.0	32.7
Recirc. gas temp. (°C)	-	272	269	254
Flue gas temp. (°C)	123	166	166	153
Boiler efficiency (%)	92.7	95.3	95.0	95.7

The three-dimensional furnace model consisted of about 150 000 hexahedral cells. The actual furnace geometry and the location of different inlets and outlets were modelled as true as possible, given the limited density of the calculation mesh (Figure 6.12). The boundary conditions were defined based on one-dimensional boiler design model.

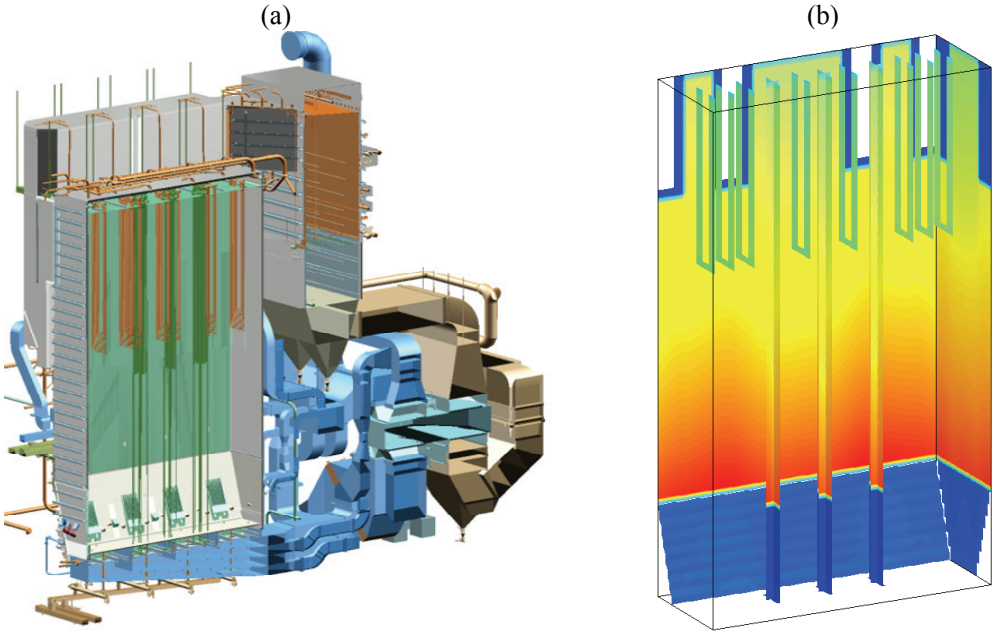

Figure 6.12. Łagisza CFB boiler. (a) Actual layout of the plant. (b) Model geometry.

In oxycombustion cases, the O_2 content in oxidant is relatively low, thus, the oxygen profiles in the air- and oxygen-fired cases are fairly similar. Highest differences were found between Case 3 and the reference case (Figure 6.13). The maximum oxygen concentrations above the secondary air ports are approximately equal, about 16 % in both cases. In the upper furnace, the high local O_2 concentrations are diluted by mixing and by combustion reactions.

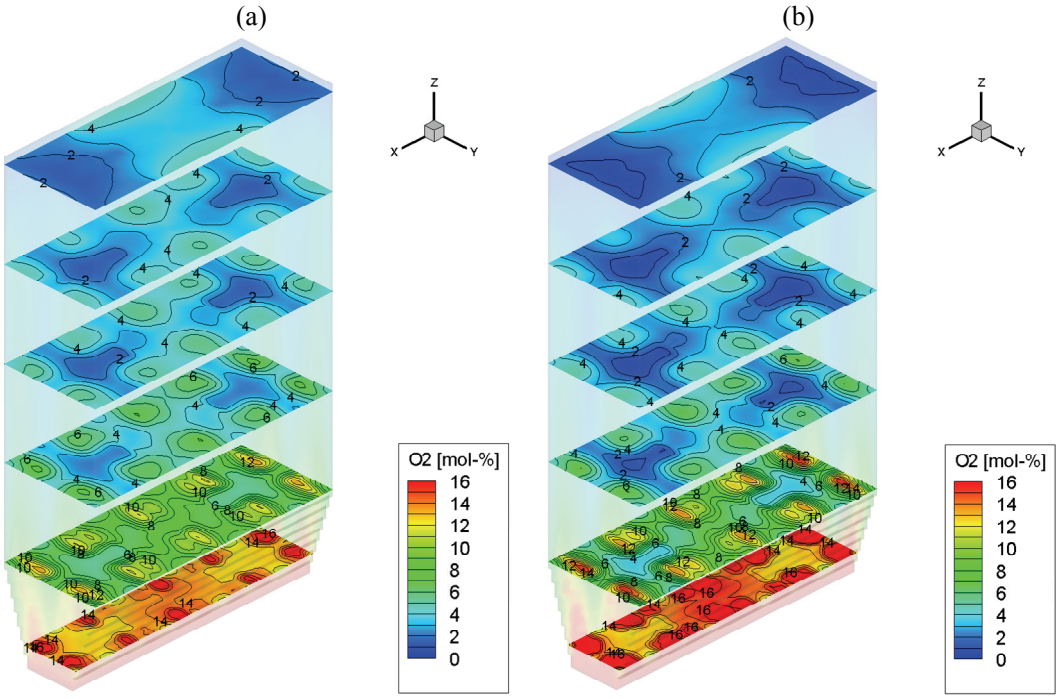

Figure 6.13. Modelled oxygen concentration fields of air-fired case (a) and Case 3 (b).

In oxygen-fired cases, the CO_2 and H_2O levels are higher due to composition of oxidant streams. The CO_2 concentration fields of air-fired case and Case 3 are compared in Figure 6.14. The shape of the profiles is similar, but in oxycombustion case, the CO_2 level is about 47%-units higher.

Figure 6.15 compares the temperature fields between the air-fired case and Case 3. In these cases, the amount of internal heat surfaces was the same, but due to lower recirculation gas flow rate and higher O_2 content of oxidant, the furnace temperatures are higher in Case 3, especially at the lower furnace. The maximum temperatures are still quite moderate.

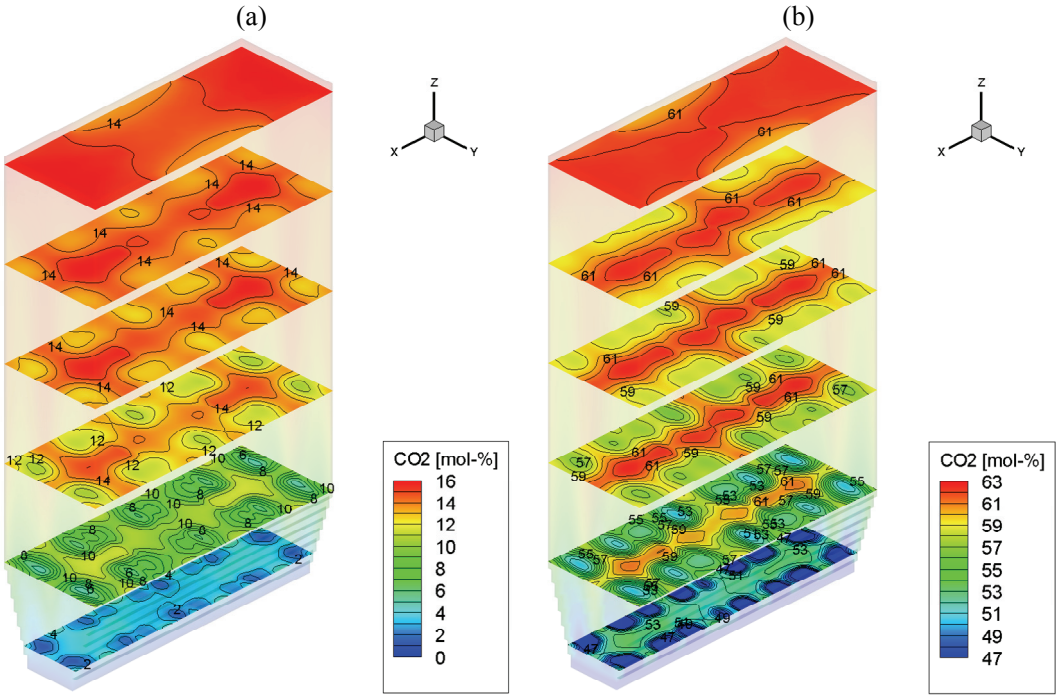

Figure 6.14. Modelled carbon dioxide concentration fields of air-fired case (a) and Case 3 (b).

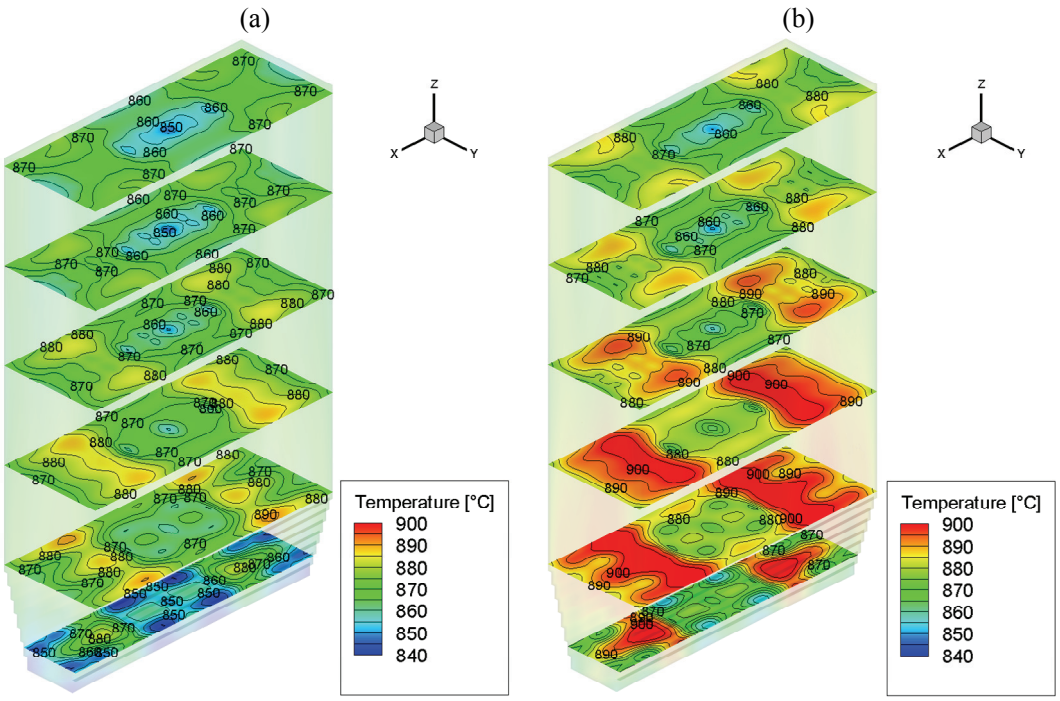

Figure 6.15. Modelled temperature fields of air-fired case (a) and Case 3 (b)

6.3 Modelling of a Flexi-Burn® demonstration plant

A Flexi-Burn® CFB is a concept, in which a circulating fluidized bed (CFB) boiler can be operated both in air-fired and oxygen-fired modes. In the air-fired mode, the operation is similar to a conventional CFB. In the oxygen-fired mode, the fuel is burned in a mixture of oxygen and recycled flue gas, which enables carbon capture and storage (CCS). The flexible operation reduces risks of outage in power generation due to e.g. failures in oxygen production and carbon capture and storage equipment. It also provides a possibility to determine the economically optimum operating mode depending on the power requirements and the price of CO_2 allowances.

A commercial CCS demonstration plant applying the Flexi-Burn concept is under development by a partnership formed by ENDESA Generación, CIUDEN and Foster Wheeler Energia Oy (Kuivalainen et al., 2010). The OXY-CFB-300 project is based on supercritical oxy-combustion concept applying the Flexi-Burn CFB technology. The main target of this demonstration plant is to validate a CCS technology at commercial scale, using a wide range of coals and biomass. The design of the Flexi-Burn CFB furnace is supported by modelling with the tool presented in this thesis. The following modelling results have been presented in Myöhänen et al. (2011).

Figure 6.16 presents a simplified process flow scheme of the power plant. It consists of an air separation unit, a supercritical OTU CFB boiler, a CO2 compression and purification unit, and a turbine island. For oxy-fuel combustion, which is the primary operation mode, oxygen is mixed with recycled flue gases. The absence of air nitrogen produces a flue gas stream with a high concentration of CO_2, making it much easier to separate the CO_2. In the air-firing mode, the ASU and CPU are out of service or in stand-by and the plant is operated like a conventional power plant, leading flue gases to the atmosphere.

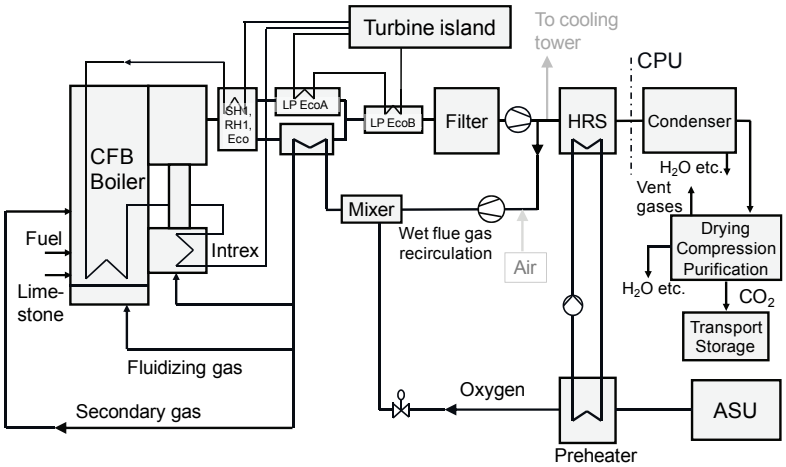

Figure 6.16. Schematic of a Flexi-Burn CFB power plant.

Flexi-Burn is a trademark of Foster Wheeler Energia Oy, registered in the US, EU, Finland.

Two model cases were calculated: an air-fired case and an oxygen-fired case, in which the oxygen content of the inlet gas was about 24%. The fuel was a mixture of anthracite (70%) and petroleum coke (30%). The boiler load was 100% in oxygen-fired case. In air-fired mode, the maximum load was 90%. The calculation mesh and the layout from top are presented in Figure 6.17 showing the locations of the furnace outlets.

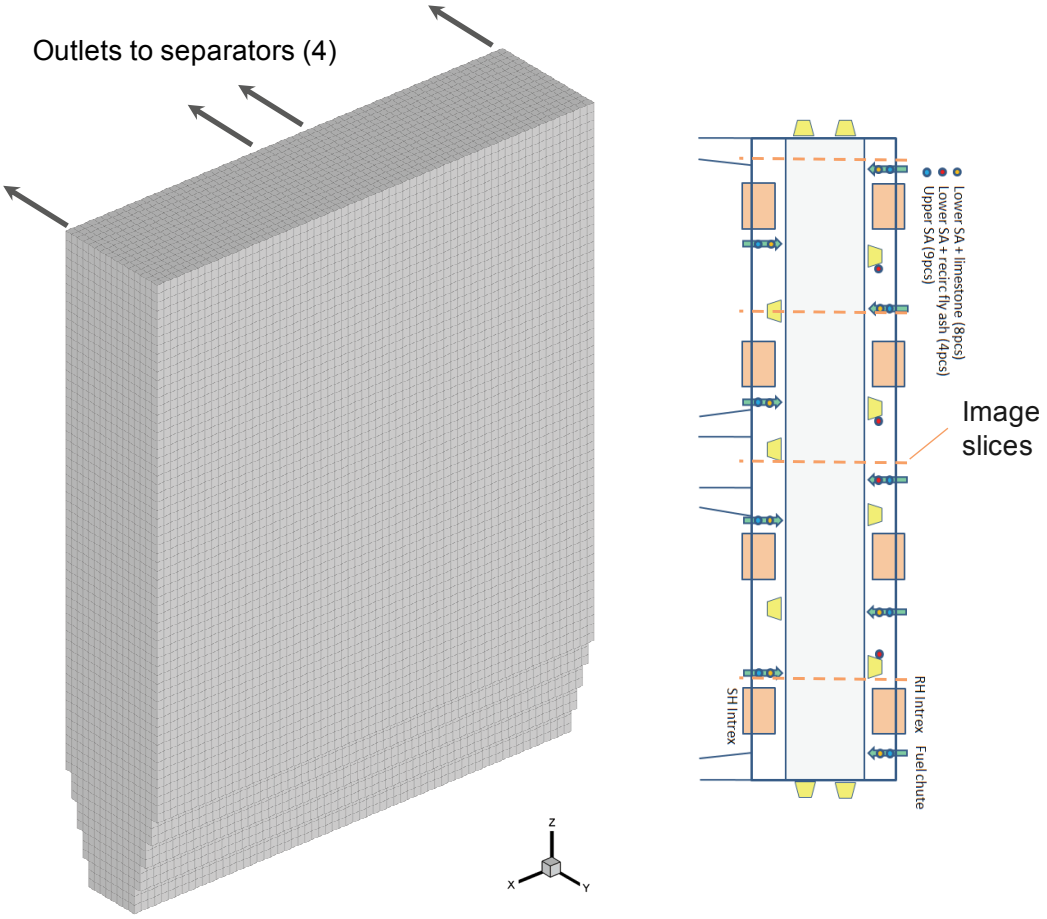

Figure 6.17. Calculation mesh (71 936 calculation cells) and layout from top.

Figure 6.18 illustrates the main differences of the flue gas composition after the furnace in air-fired and oxygen-fired cases. In both cases, the share of oxygen is about 3%. In air-fired combustion, about 75% of the flue gas is nitrogen due to composition of the combustion air. When changing from air-fired to oxygen-fired combustion, the share of carbon dioxide increases from 15% to 69% and the share of water vapour increases from 7% to 22%. The share of nitrogen decreases to 6%. In both cases, the share of other gas species is less than 0.3%.

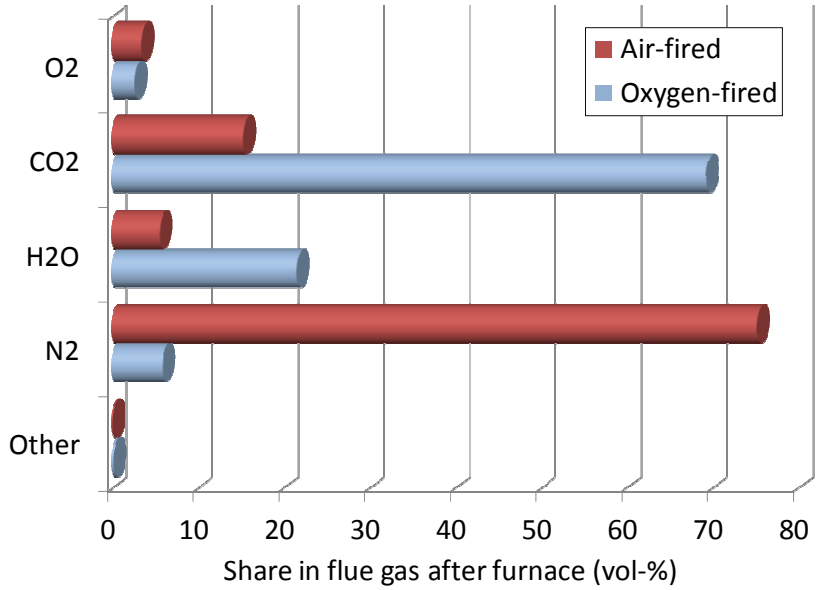

Figure 6.18. Composition of main gas species in the flue gas after the furnace.

Figures 6.19 – 6.32 compare the three-dimensional model results of air-fired and oxygen-fired combustion. Based on this study, the combustion reactions are fairly similar, if the oxygen content of the inlet gas in oxygen-fired mode is close to air-fired mode. The char combustion and devolatilization profiles are similar in shape, but in oxygen-fired mode, the values are slightly higher due to higher boiler load and higher fuel flow rate (Figures 6.19 and 6.20). Consequently, the total heat from reactions is higher as well in oxygen-fired case (Figure 6.21).

Most of the heat originates from combustion of char at the bottom of the furnace. The temperature profiles show some local cold spots at the bottom of the furnace in air-fired case (Figure 6.22). The cold spots are due to cooling effects of cold inlet air, the evaporation of fuel, and the internal circulation of cooled solids at the side walls. In oxygen-fired case, the temperature profile is more uniform because of the exothermic carbonation reactions, which are occurring at locations, where the temperature is below the calcination temperature.

The maximum temperatures are found at the centreline of the furnace. Near the side walls, the gas-solid suspension is cooled by the presence of the cooled walls, but in the centreline, there is no cooling wall. Consequently, near the centreline, the temperature tends to be higher, if the fuel feed and the combustion process are uniform. The same affects the temperature distribution at the furnace outlets: the temperature is higher in the outlets located at the centre compared with the outlets located in the corners.

The oxygen profiles are quite similar in both cases (Figure 6.23). The locations and the effects of the secondary air feeds above the fuel inlets are clearly visible as local higher concentrations. At the bottom of the furnace, the profiles are non-uniform showing lower oxygen content on the sides of the fuel inlets. In oxygen-fired case, the local maximums are slightly higher than in the air-fired case due to slightly higher oxygen concentration in the input streams. The oxygen profiles indicate that at the centreline of the furnace, the oxygen concentration is lower, thus a lower fuel input or more secondary air would be needed in this area to make the combustion process more uniform.

The shapes of the carbon dioxide profiles are fairly similar, but naturally, in oxygen-fired case, the values are much higher due to replacing the nitrogen of air with recycling of flue gas (Figure 6.24). In both cases, the CO_2 concentration increases towards the upper part of the furnace due to combustion reactions. In oxygen-fired case, local minimums can be noticed at the bottom of the furnace at left and right sides, and in the corner near the roof. These are due to carbonation reactions, which consume CO_2 in these locations, where the local temperature is below the calcination temperature.

The concentration fields of carbon monoxide and hydrogen illustrate the basic difference between the formation of combustible gases from char and volatiles (Figures 6.25 and 6.26). Carbon monoxide is formed during devolatilization and combustion of char, while hydrogen and hydrocarbons are mainly formed during devolatilization only. Consequently, hydrogen is found only near the fuel inlets, while carbon monoxide is found across the whole bottom of the furnace as a result of burning char. The values are slightly higher in the oxygen-fired case due to higher fuel input.

The calcination and carbonation rates show how the limestone reaction mechanisms are largely affected due to high partial pressure of CO_2 in oxygen-fired mode (Figures 6.27 and 6.28). In air-fired combustion, the fresh limestone calcines near the feeding points and the carbonation is almost non-existent. In oxygen-fired combustion, the calcined limestone may re-carbonate in locations, where the local temperature is below the calcination temperature. In this calculation, these locations are found near the side walls at the bottom of the furnace, near the secondary air feed points, and near the corners of furnace walls. The re-carbonation produces $CaCO_3$, which again is re-calcined at areas with higher temperature.

The cycling calcination-carbonation reactions affect the local gas composition (mainly CO_2), temperature profiles and velocity fields and need to be carefully considered during the operation of the unit. During steady operation, the effect of calcination-carbonation cycling can be beneficial as it produces a more uniform temperature field due to exothermal and endothermal reactions occurring in colder and warmer areas, respectively. However, rapid changes in the operating mode, e.g. when changing from air-fired mode to oxygen-fired mode or when changing to a small boiler load, may have unfavourable effects on the controllability as large proportions of the bed material may carbonate. Moreover, the re-carbonation may cause local sintering of the bed material.

The sulphation and direct sulphation occur mostly at the bottom of the furnace, where the amount of SO_2 is high due to combustion reactions (Figures 6.29 and 6.30). In oxygen-fired case, the sulphation rate is higher mainly due to higher SO_2 concentration. In air-fired case, the amount of direct sulphation is practically zero. In oxygen-fired case, the direct sulphation is possible near the side walls, where the concentration of $CaCO_3$ is higher due to recarbonation.

Figure 6.31 presents the desulphation rates. The desulphation rate is highest at the bottom of the furnace and near the centreline, where the local concentration of carbon monoxide is high.

The sulphur dioxide profiles in Figure 6.32 are the result of different sources and sinks inside the furnace, which are mainly due to SO_2 originating from combustion reactions and consumed by sulphation reactions. In oxygen-fired case, the SO_2 concentration is higher, which is produced by higher fuel flow rate and the input of SO_2 in the recirculated gas. The SO_2-concentration is higher at the centre of the furnace, where the temperature and the CO-concentration are higher, which promote the desulphation.

Figure 6.33 compares the integrated sources and sinks of sulphur dioxide. In both cases, the SO_2 originates mainly from combustion of char, because with the applied fuels, most of the sulphur is found in char. The sulphur capture occurs mainly by normal sulphation. In the oxygen-fired case, the target was to operate the furnace at a temperature level above the calcination temperature. Consequently, the reduction of SO_2 is about 20 times higher by sulphation than by direct sulphation.

The SO_2 from the desulphation has been marked as a source to evaluate its effect on the sulphur capture. Based on this study, the desulphation has a clear effect and it should be considered in the sulphur capture model. In oxygen-fired case, the desulphation is clearly higher due to higher CO-concentrations at the bottom of the furnace, where the desulphation is occurring.

In oxygen-fired case, some of the SO_2 originates from the gas feed due to recirculated flue gas. In this modelling, the composition of the feed gas was determined based on conservative estimations of the overall performance and sulphur capture. Based on the model calculations, the molar flow of SO_2 in the recirculated gas is slightly smaller than the molar flow of SO_2 in the feed gas. The calculation could be continued by adjusting the composition of the input gas and recalculating the results. Another alternative would be to couple the solved flue gas composition to the composition of the recirculated gas, but this method is more prone to convergence problems. For the analysis of the different main features and phenomena, the continuation of the calculation would have insignificant effect, however.

The actual emission of SO_2 to flue gas is smaller in oxygen-fired case than in air-fired case, although the fuel feed is higher. This is because in the oxygen-fired case, the

partial pressure of SO_2 in the furnace is higher due to effect of SO_2 in the recirculated gas, which then increases the sulphation rate.

Figure 6.34 presents a similar analysis of the sources and sinks of carbon dioxide. In air-fired case, most of the CO_2 originates from combustion reactions added by a small proportion from the calcination of fresh limestone and a very small amount due to shift conversion. In oxygen-fired case, in addition to above, the inlet gas contains a large proportion of CO_2 coming from recirculated gas. This results in high molar flow of CO_2 through the system and consequently, a high concentration of CO_2 in the furnace and in the flue gas. A small proportion of CO_2 is consumed by carbonation, but this is again released by re-calcination. The mass flows of CO_2 due to direct sulphation, desulphation, and Boudouard reaction were omitted from the chart, because their share was less than 0.1% of the total molar flows.

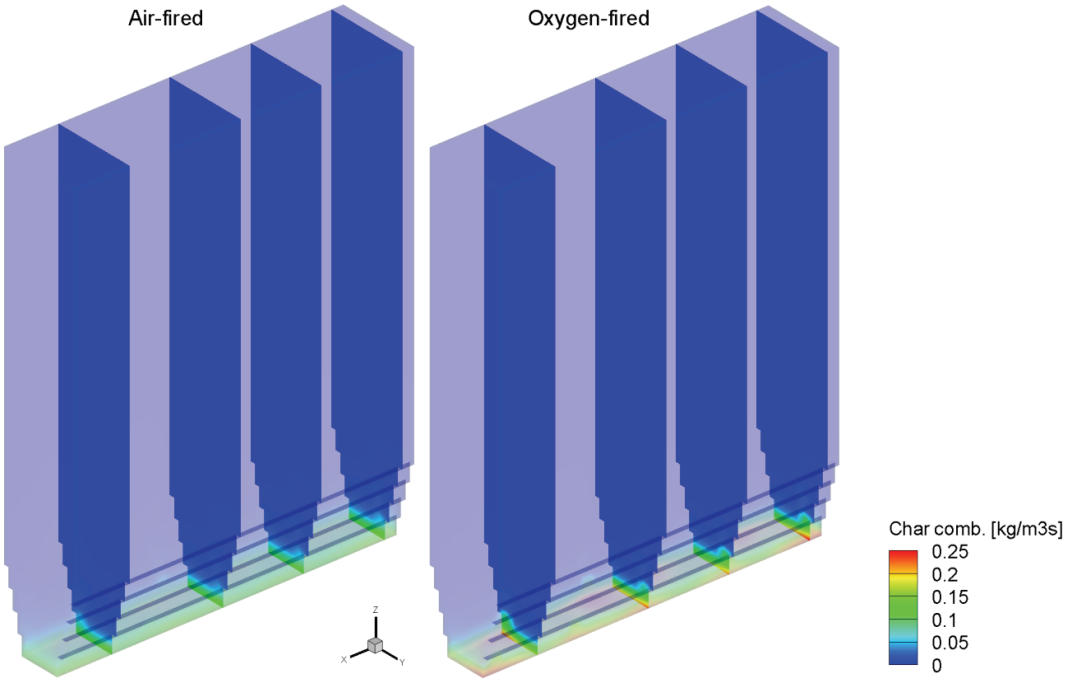

Figure 6.19. Char combustion rate.

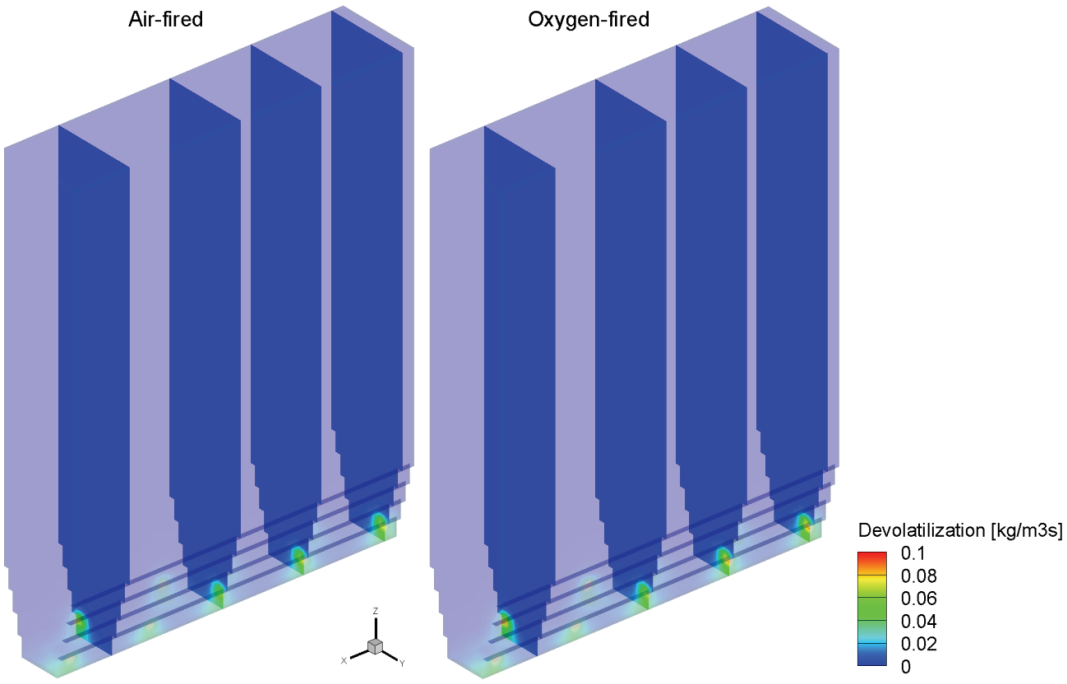

Figure 6.20. Devolatilization rate.

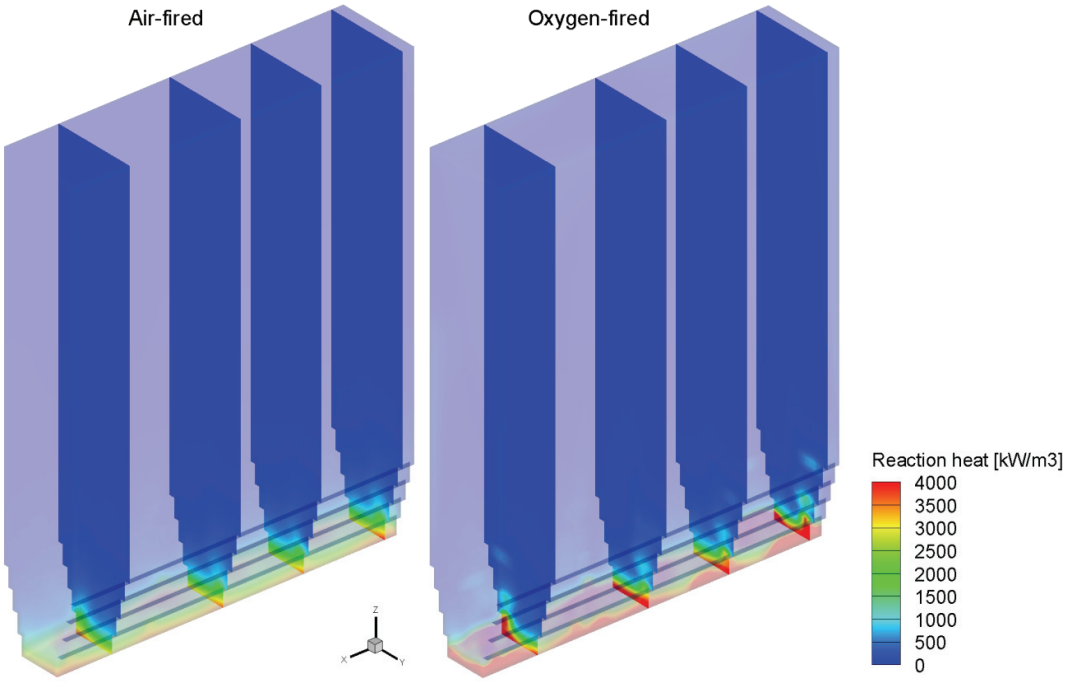

Figure 6.21. Total heat from reactions.

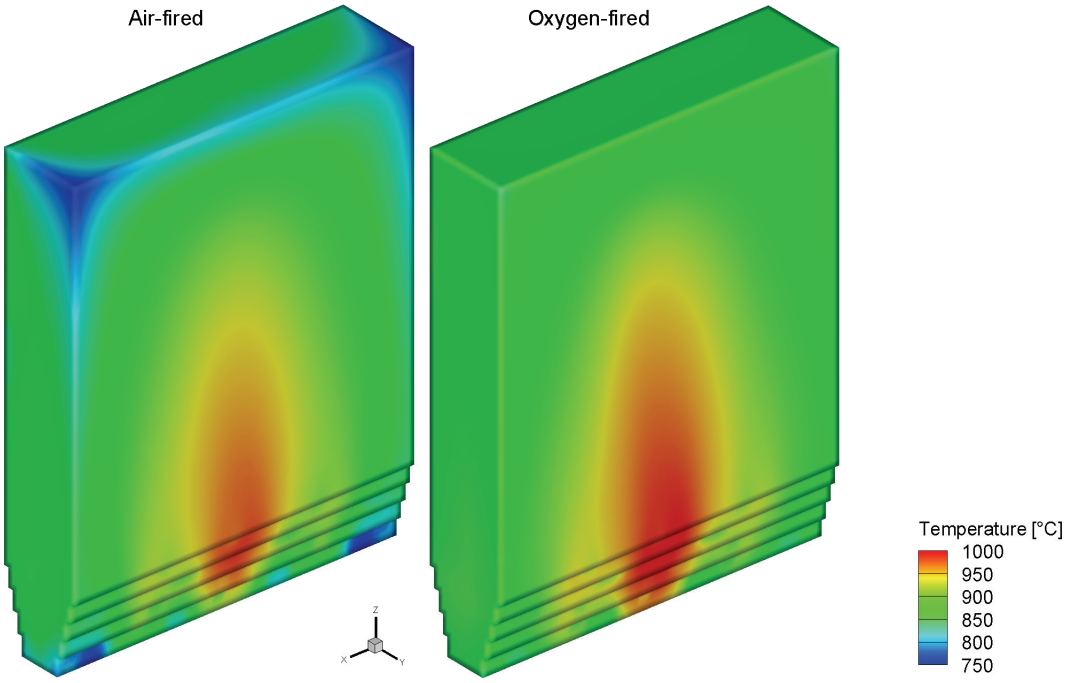

Figure 6.22. Temperature fields.

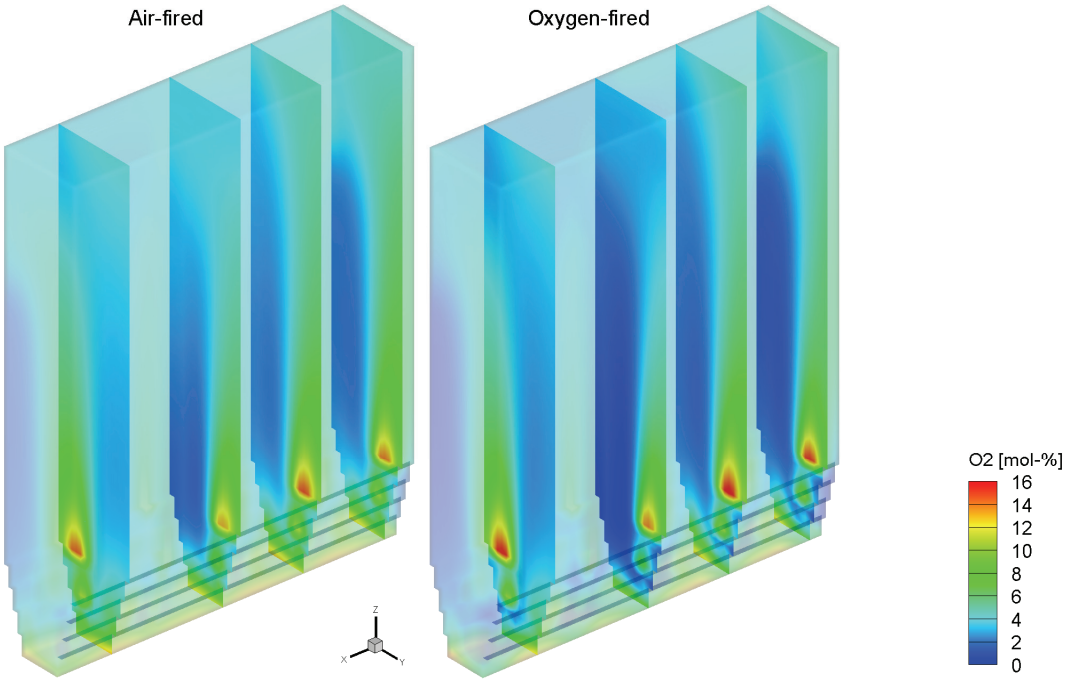

Figure 6.23. Oxygen concentration.

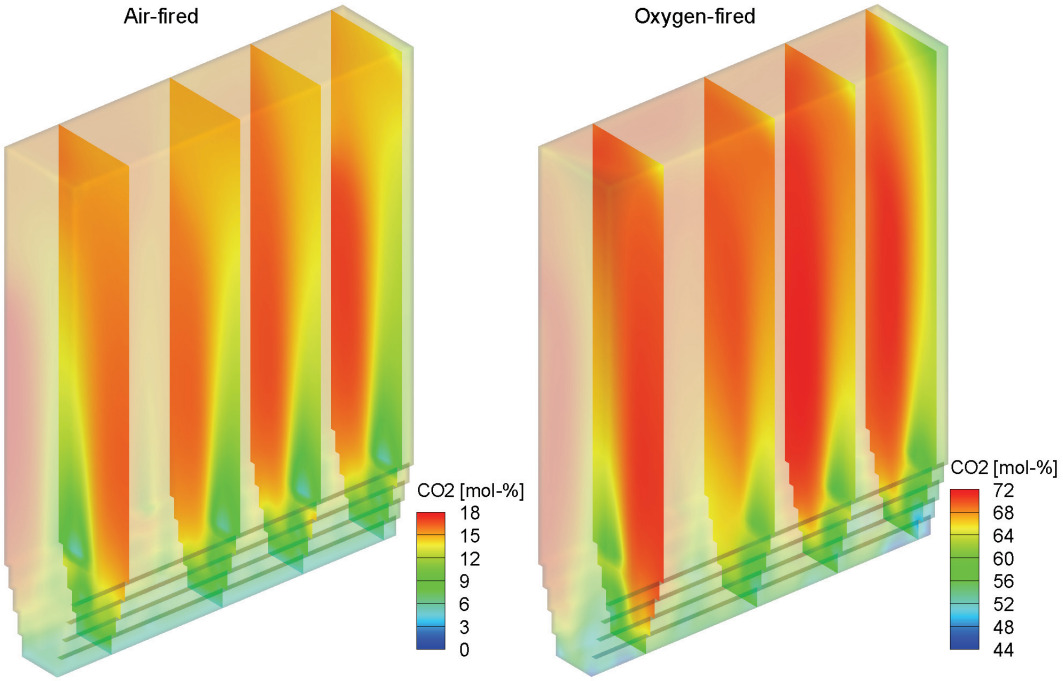

Figure 6.24. Carbon dioxide concentration.

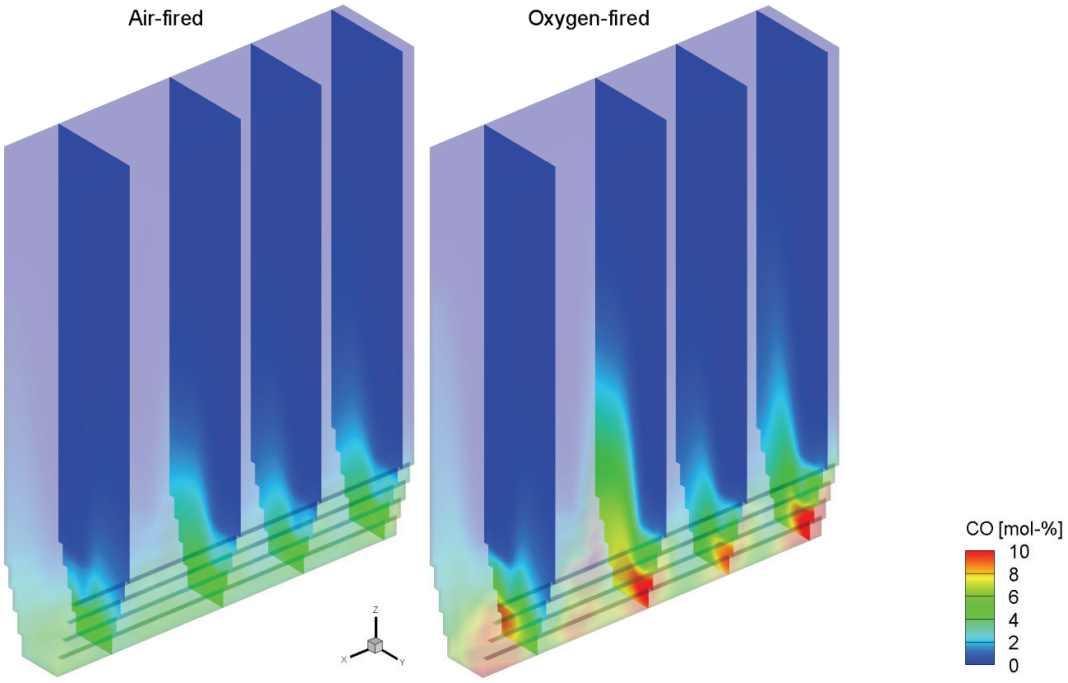

Figure 6.25. Carbon monoxide concentration.

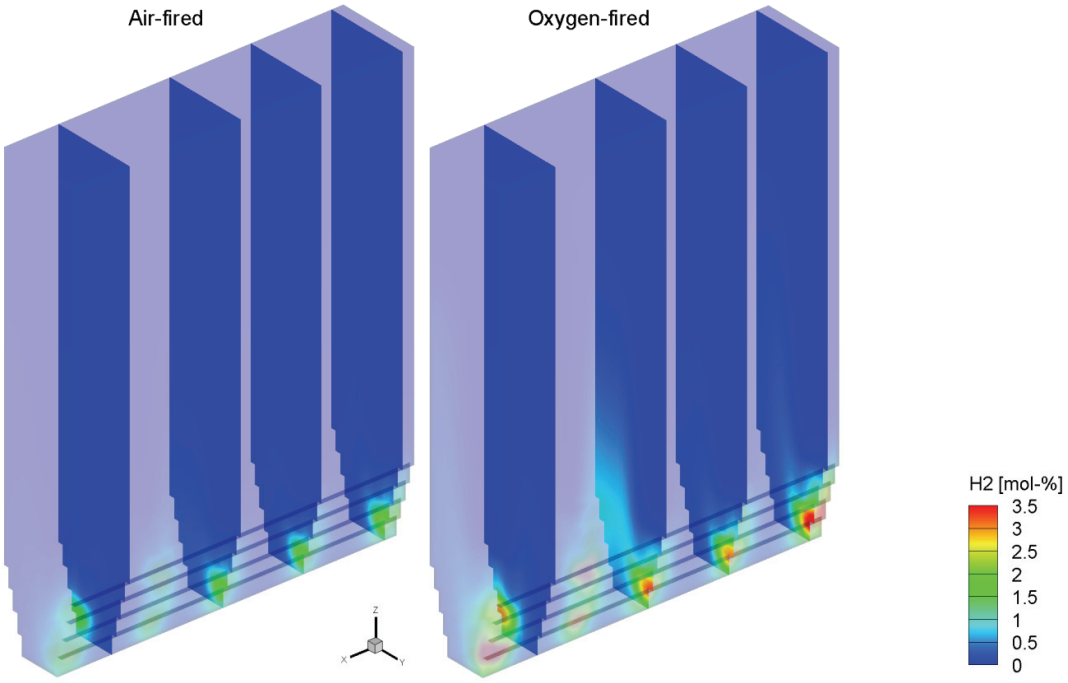

Figure 6.26. Hydrogen concentration.

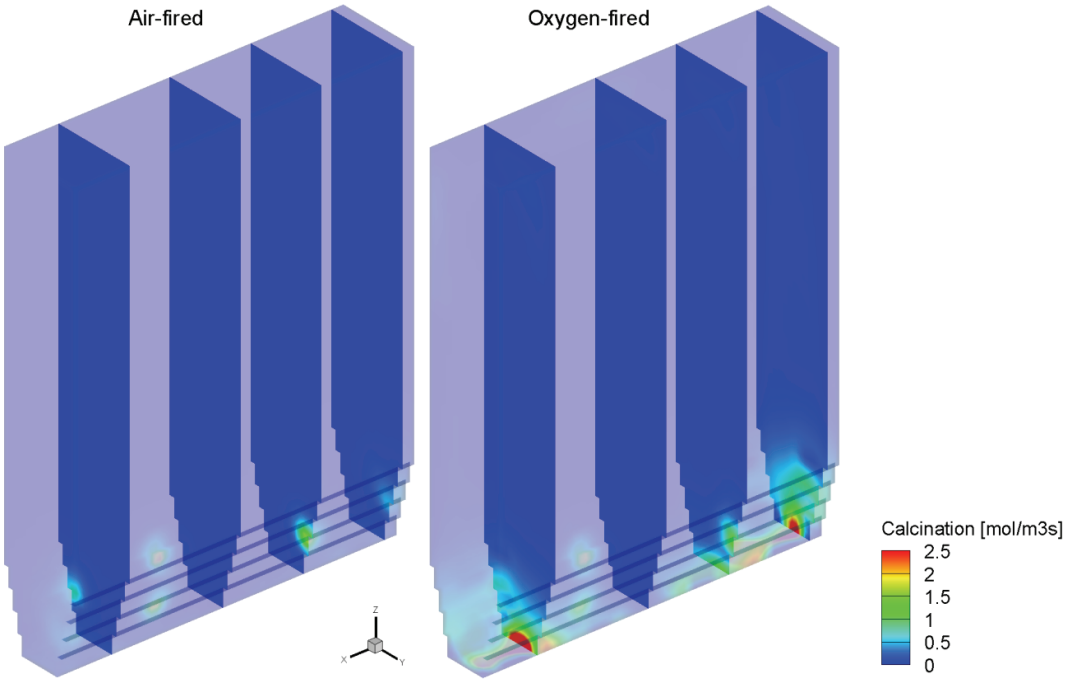

Figure 6.27. Calcination rate.

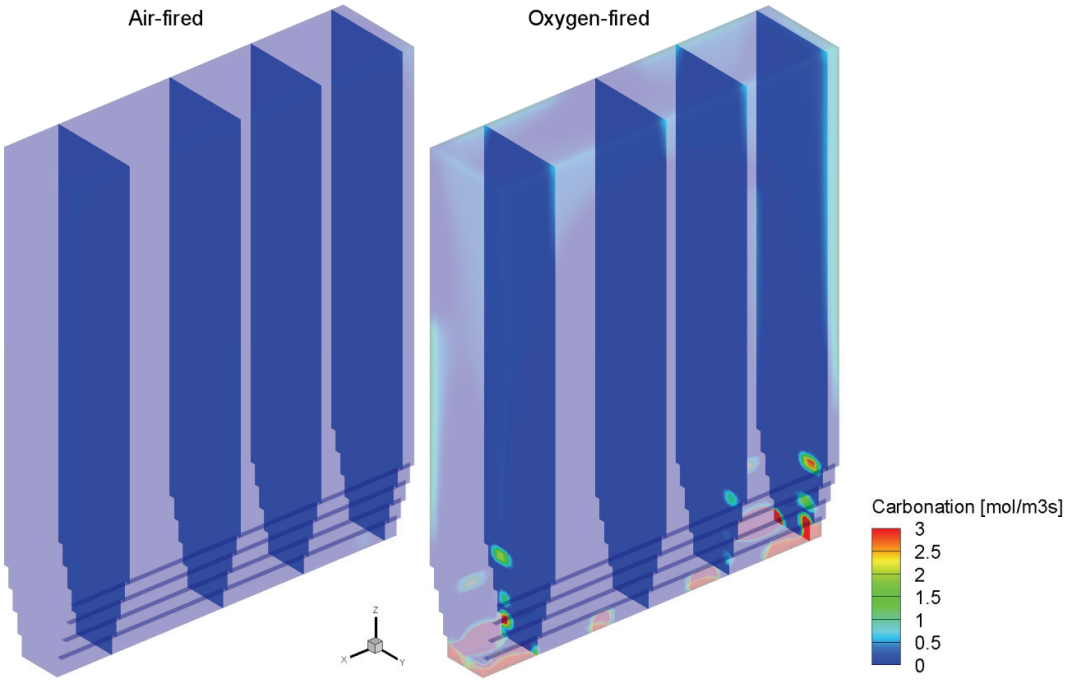

Figure 6.28. Carbonation rate.

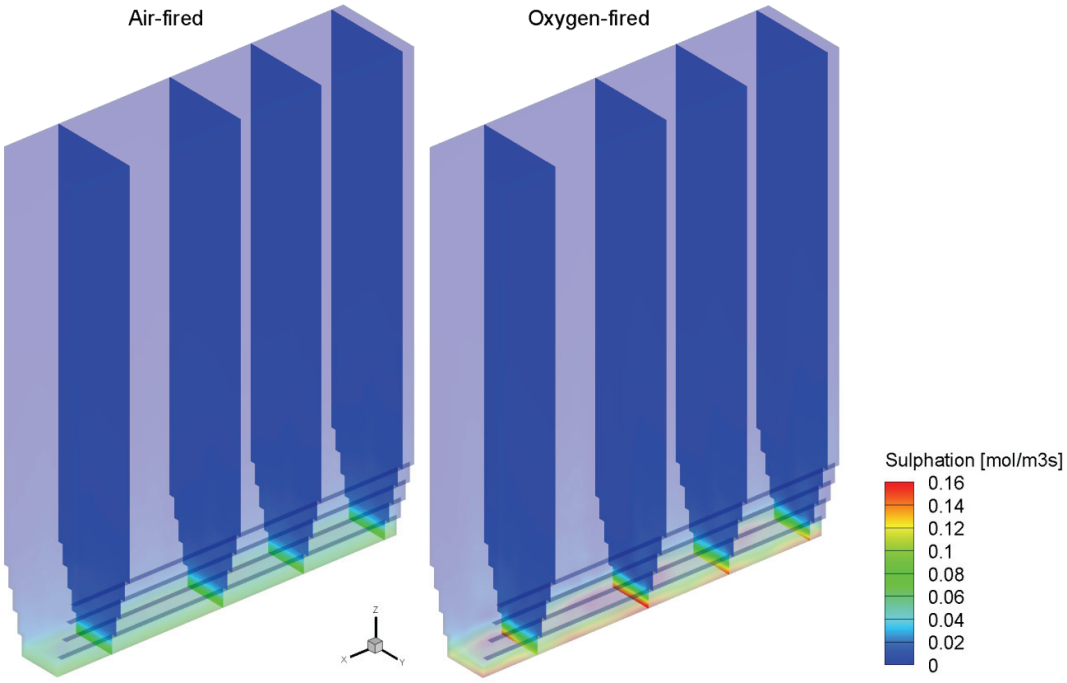

Figure 6.29. Sulphation rate.

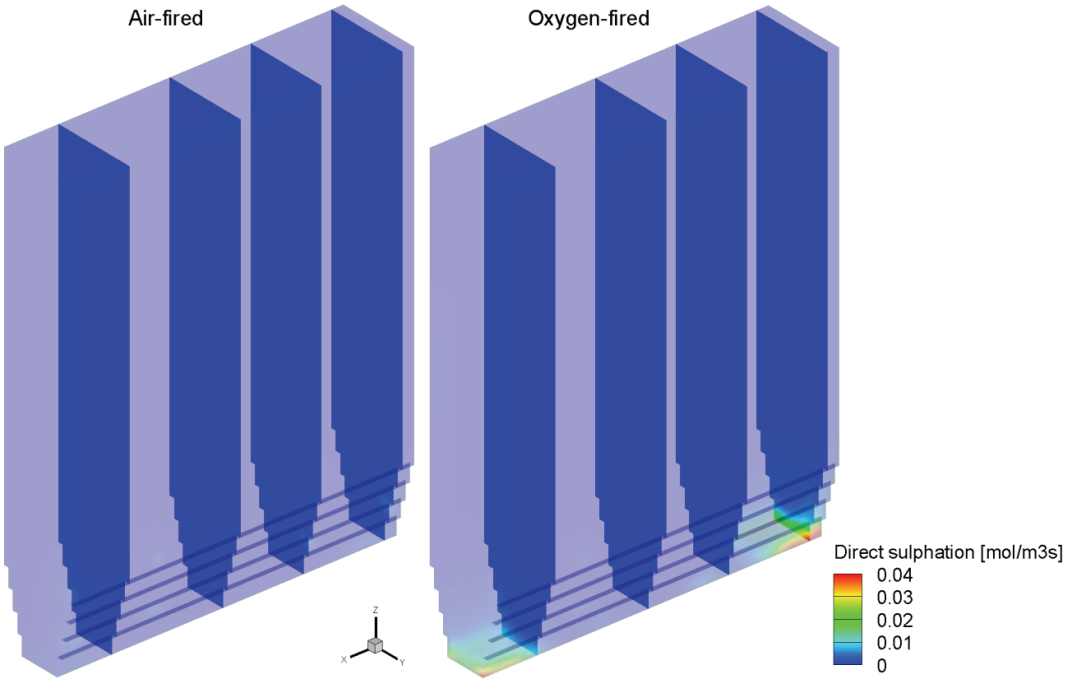

Figure 6.30. Direct sulphation rate.

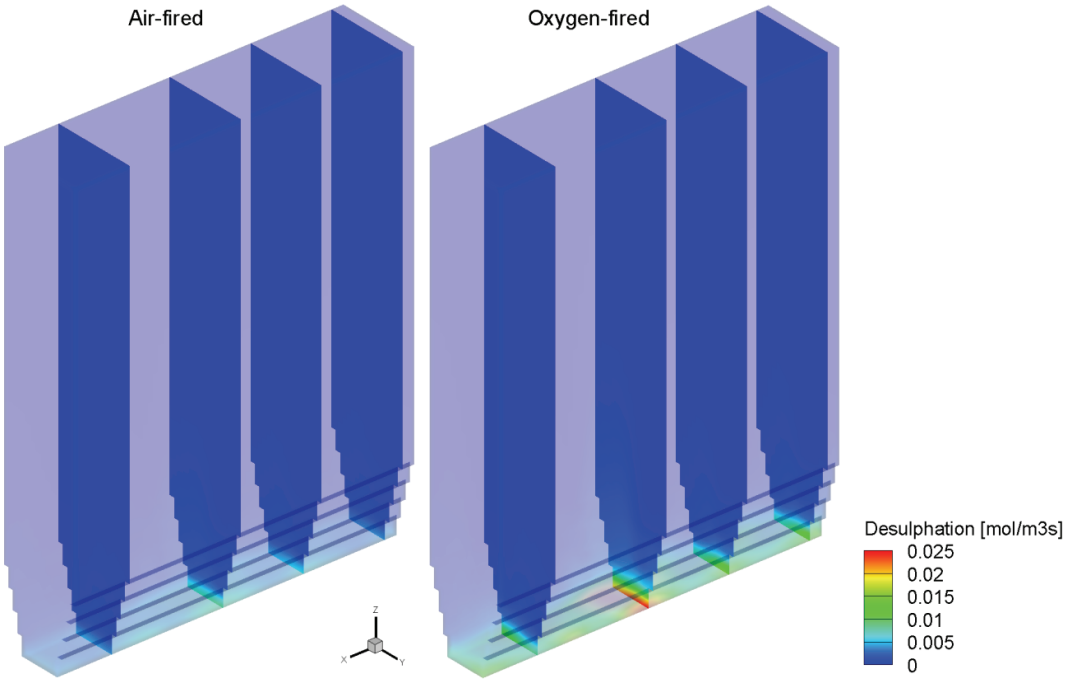

Figure 6.31. Desulphation rate.

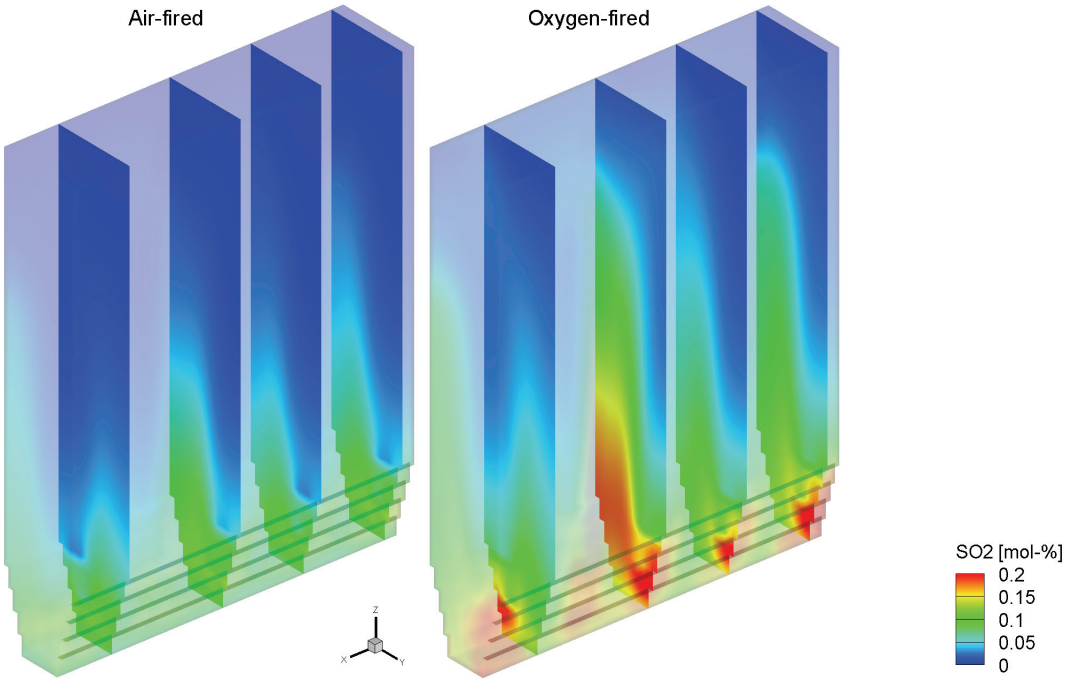

Figure 6.32. Sulphur dioxide concentration.

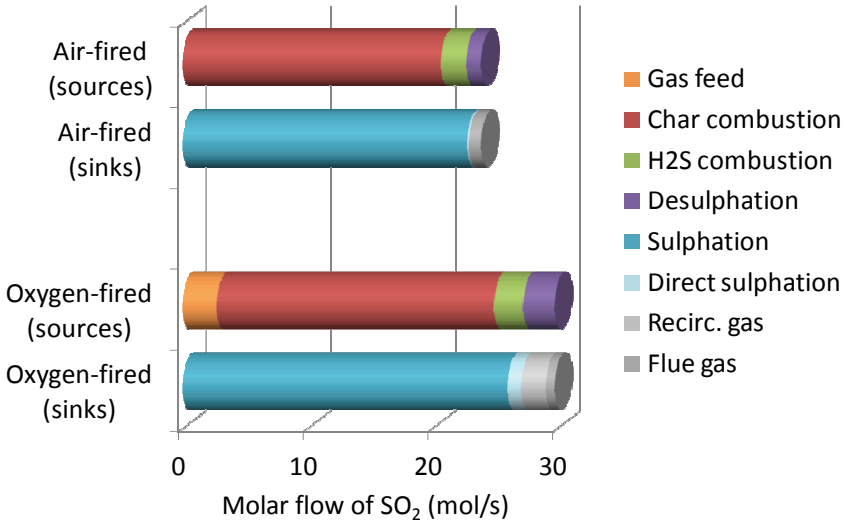

Figure 6.33. Sources and sinks of sulphur dioxide in air-fired and oxygen-fired cases.

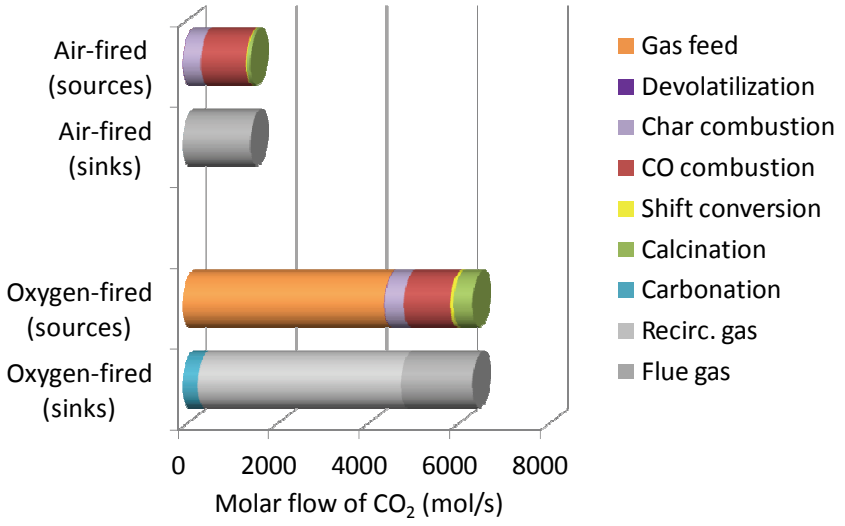

Figure 6.34. Sources and sinks of carbon dioxide in air-fired and oxygen-fired cases.

7 Discussion

The circulating fluidized bed systems can be studied using a wide selection of model approaches, ranging from micro-scale particle models and meso-scale multiphase models to lumped scale empirical models. The fundamentals-oriented CFD methods are starting to be applied for industrial scale, but for a comprehensive three-dimensional modelling of large-scale CFB furnaces, including the modelling of reactions, comminution, and heat transfer, the only alternative is still the semi-empirical model approach. In future, the borders between the semi-empirical models and CFD models will be fading as the calculated data of flow dynamics by CFD models can be incorporated to semi-empirical models, and the CFD models can be applied to a larger scale.

The benefits of a valid three-dimensional CFB furnace model are quite clear: with a support of such a model, the placement of the feeding points and heat transfer surfaces can be designed optimally, and the model can be applied for various trouble-shooting and risk assessment studies. Thus, there should be a driving force to develop such models as the development work pays for itself quickly by enhanced design work, improved efficiency, and the availability of the boiler units. However, based on the published data, the number of such models is extremely small.

The probable hindrances which have prevented the wider development of 3D-models are related to the complexity of the CFB process. Getting all the pieces together for building a comprehensive model is a tedious job, and there is a lack of knowledge of many phenomena. However, just the building of the process helps to identify the problem areas, from which more data is needed, and to support the development of methods for getting the data.

Especially the modelling of emissions is challenging, as the formation of emissions is dependent on all the other phenomena: fluid dynamics, mixing, combustion reactions, comminution, and heat transfer. If one of these areas is modelled falsely, it affects the modelling of the emissions as well. The three-dimensional description of the emission formation can be a very valuable tool when optimizing the emission control and minimizing the emissions, thus more work should be focused in this area.

One major problem area in the modelling is the characterization of the feed materials (e.g. fuel and sorbent). The feed materials can be characterized by bench scale and pilot scale tests, but scaling the results to industrial scale is not always straightforward. The actual conditions in a large-scale furnace may be different from the conditions in a small-scale test apparatus. For example, the flow patterns in a pilot scale can be different compared to full-scale, leading to a direct impact on the mixing and thus on the reactions.

Another challenge common to all model approaches is the correct definition of the boundary conditions. If the boundary conditions are not correct, the model results are hardly correct either. In industrial CFB boilers, the number and the accuracy of the measurements are limited. For example, the actual fuel feed distribution to individual feed points cannot usually be determined. If profile measurements of gas concentrations and temperatures are available, three-dimensional modelling can be applied for determining the actual boundary conditions. When modelling new units, sensitivity studies should be carried out to determine the effect of off-design values.

The final and biggest challenge is the validation of the models in industrial scale. The physical dimensions of the commercial CFB boilers are huge, and even a large number of measurement points can cover only a small proportion of the whole furnace. Moreover, the measurement probes can only extend few meters inside the furnace, while the depth of the furnace can be in the order of ten meters or more. Furthermore, the detailed measurements in industrial units are often regarded as commercially sensitive data by the industry, and the dissemination of this data is restricted.

The presented model includes a comprehensive description of the different phenomena occurring inside a CFB furnace. However, it is still only a tool for thought with limited prediction ability. A large number of validation studies on different scales, applying various feed materials and conditions should be carried out in order to improve the general validity and the accuracy of the model. The persons carrying out the modelling work should already have a good knowledge and understanding of the process, and preferably, the developers and users of the code should have first-hand experiences of operating the units and carrying out field measurements. Only then, the accuracy – or inaccuracy – of the measured values and the various sub-models could be properly evaluated and the development work targeted to critical areas, which need the most attention.

8 Conclusions

The development of the circulating fluidized bed processes requires modelling tools which can simulate the complex process phenomena and model full-scale units. The combustion process in a CFB furnace is inhomogeneous due to the limited number of feeding points and limited mixing rate. A natural choice to simulate such a process is to model it three-dimensionally. The comprehensive simulation of large-scale CFB units is possible using semi-empirical models, but the number of such models is small. Moreover, except for the present model, none of the published models is capable of calculating the sorbent reactions and the sulphur capture in the three-dimensional flow environment of the CFB furnace.

The objective of this work was to develop a model frame for simulating a CFB process and to develop sub-models describing the combustion and sorbent reactions in air-fired and oxygen-fired combustion. The objective was reached and the developed model has been successfully used for studying different industrial scale CFB units, combusting different fuel types.

The main contribution of this work is the three-dimensional model frame for modelling CFB furnaces. Other major contributions are the developed correlations and sub-models for modelling the combustion and limestone reactions. In addition, a classification of the different model approaches for fluidized bed systems was presented, which helps to categorize the different models and to justify the different modelling approaches on different scales.

As further contributions, the work presents studies of the combustion and sorbent reactions illustrating the different sub-phenomena in air-fired and oxygen-fired CFB combustion. The studies reveal some of the potential hazards related to sorbent reactions at high CO_2 concentrations. For the future CFB boilers applying oxycombustion and carbon capture, the changing limestone reaction mechanisms have to be considered in the design in order to optimize the performance and the emission control, and to avoid operational problems.

The prediction ability of the developed model is still limited due to the small amount of available measurement data for validating the correlations. Many of the sub-models and correlations are based on literature data, and they have not yet been extensively validated by field measurements. The future work should be targeted for performing validation studies with different fuels and sorbents, and in air-fired and oxygen-fired modes. Based on the validation studies, different empirical correlations can be tuned, and the prediction ability of the model improved.

The sub-models will be continuously improved and extended, and several plans already exist for the further development. For example, the heat transfer model can be improved by implementing a separate radiation model which can simulate the long distance radiation. Implementing a momentum balance equation for the fuel would improve the

ability to simulate fuels which are easily entrained, such as peat and different biomasses. The effective reactivity of char could be investigated by detailed transient CFD simulations of burning char in inhomogeneous bed environment, and the results could be applied for improving the macroscopic correlations. The sorbent model could simulate the actual reactions and temporal effects better using the integration of a separate particle model and Lagrangian modelling of the sorbent particles in the Eulerian model frame. The integration of the comprehensive process model and flow modelling by CFD could improve the description of the flow dynamics and mixing. All of these items are already being developed in various ongoing projects.

The development of the model is a continuous process: the different sub-models can be always improved as more knowledge is achieved. The main achievement of this work is the overall model frame which can be utilized for the further development and testing of new sub-models and theories, and for concentrating the knowledge gathered from experimental and computational studies carried out at bench scale, pilot scale, and industrial scale apparatus.

References

Abanades, J.C. and Alvarez, D. (2003). Conversion limits in the reaction of CO2 with lime. *Energy & Fuels*, 17, pp. 308-315.

Abanades, J.C., Alonso, M., and Rodriguez, N. (2011). Experimental validation of in situ CO2 capture with CaO during the low temperature combustion of biomass in a fluidized bed reactor. *International Journal of Greenhouse Gas Control*, 5, pp. 512-520.

Adánez, J., de Diego, L.F., Gayán, P., Armesto, L., and Cabanillas, A. (1995). A model for prediction of carbon combustion efficiency in circulating fluidized bed combustors. *Fuel*, 74(7), pp. 1049-1056.

Adánez, J., Gayán, P., and Garcia-Labiano, F. (1996). Comparison of mechanistic models for the sulfation reaction in a broad range of particle sizes of sorbents. *Industrial & Engineering Chemistry Research*, 35, pp. 2190-2197.

Adánez, J., Gayán, P., Grasa, G., de Diego, L.F., Armesto, L., and Cabanillas, A. (2001). Circulating fluidized bed combustion in the turbulent regime: modelling of carbon combustion efficiency and sulphur retention. *Fuel*, 80, pp. 1405-1414.

Agrawal, K., Loezos, P.N., Syamlal, M., and Sundaresan, S. (2001). The role of meso-scale structures in rapid gas-solid flows. *Journal of Fluid Mechanics*, 445, pp. 151-185.

Alonso, M., Rodriguez, N., Grasa, G., and Abanades, J.C. (2009). Modelling of a fluidized bed carbonator reactor to capture CO2 from a combustion flue gas. *Chemical Engineering Science*, 64, pp. 883-891.

Anderson, T.B. and Jackson, R. (1967). A fluid mechanical description of fluidized beds. *Industrial & Engineering Chemistry Fundamentals*, 6, pp. 527-539.

Andrews, M.J. and O'Rourke, P.J. (1996). The multiphase particle-in-cell (MP-PIC) method for dense particulate flows. *International Journal of Multiphase Flow*, 22, pp. 379-402.

Andrews, A.T., Loezos, P.N., and Sundaresan, S. (2005). Coarse-grid simulation of gas-particle flows in vertical risers. *Industrial & Engineering Chemistry Research*, 44, pp. 6022-6037.

Anthony, E.J. (1995). Fluidized bed combustion of alternative solid fuels; status, successes and problems of the technology. *Progress in Energy and Combustion Science*, 21(3), pp. 239-268.

Anthony, E.J. and Granatstein, D.L. (2001). Sulfation phenomena in fluidized bed combustion systems. *Progress in Energy and Combustion Science*, 27, pp. 215-236.

Arastoopour, H. (2001). Numerical simulation and experimental analysis of gas/solid flow. *Powder Technology*, 119, pp. 59-67.

ASTM D388 (1992). *Standard Classification of Coals by Rank*. West Conshohocken, PA, USA: ASTM International.

Bagnold, R.A. (1954). Experiments on a gravity-free dispersion of large solid spheres in a Newtonian fluid under shear. *Proceedings of the Royal Society of London. Series A, Mathematical and Physical Sciences*, 225, pp. 49-63.

Barisic, V., Zabetta, E.C., and Sarkki, J. (2009). Prediction of agglomeration, fouling, and corrosion tendency of fuels in CFB co-combustion. In: Yue, G., Zhang, H., Zhao, C., and Luo, Z., eds, *Proceedings of the 20th International Conference on Fluidized Bed Combustion*. Beijing: Tsinghua University Press.

Barker, R. (1973). The reversibility of the reaction CaCO3 - CaO + CO2. *Journal of Applied Chemistry & Biotechnology*, 23, pp. 733-742.

Barletta, D., Marzocchella, A., and Salatino, P. (2002). Modelling the SO2-limestone reaction under periodically changing oxidizing/reducing conditions: the influence of cycle time on reaction rate. *Chemical Engineering Science*, 57, pp. 631-641.

Barner, H.E., Chartier, J.S., Beisswenger, H., and Schmidt, H.W. (1985). Application of circulating fluid bed technology to the combustion of waste materials. *Environmental Progress*, 4(2), pp. 125-130.

Baskakov, A.P. and Leckner, B. (1997). Radiative heat transfer in circulating fluidized bed furnaces. *Powder Technology*, 90, pp. 213-218.

Basu, P. and Nag, P.K. (1987). An investigation into heat transfer in circulating fluidized beds. *International Journal of Heat and Mass Transfer*, 30(11), pp. 2399-2408.

Basu, P. and Nag, P.K. (1996). Heat transfer to walls of a circulating fluidized-bed furnace. *Chemical Engineering Science*, 51(1), pp. 1-26.

Basu, P. (2006). *Combustion and gasification in fluidized beds*. Boca Raton, FL, USA: CRC Press.

Basu, P., Acharya, B., and Dutta, A. (2009). Gasification in fluidized beds - present status & design. In: Yue, G., Zhang, H., Zhao, C., and Luo, Z., eds, *Proceedings of the 20th International Conference on Fluidized Bed Combustion*. Beijing: Tsinghua University Press.

Beetstra, R., van der Hoef, M.A., and Kuipers, J.A.M. (2007). Drag force of intermediate Reynolds number flow past mono- and bidisperse arrays of spheres. *AIChE Journal*, 53(2), pp. 489-501.

Belin, F., Maryamchik, M., Walker, D.J., and Wietzke, D.L. (2001). Babcock & Wilcox CFB boilers - design and experience. In: Geiling, D.W., ed., *Proceedings of the 16th International Conference on Fluidized Bed Combustion*. New York: ASME.

Bell, R.A. (2000). *Numerical modelling of multi-particle flows in bubbling gas-solid fluidized beds*. Ph.D. thesis. Swinburne University of Technology.

Biba, V., Macak, J., Klose, E., and Malecha, J. (1978). Mathematical model for gasification of coal under pressure. *Industrial & Engineering Chemistry Process Design and Development*, 17(1), pp. 92-98.

Boivin, M., Simonin, O., and Squires, K.D. (1998). Direct numerical simulation of turbulence modulation by particles in isotropic turbulence. *Journal of Fluid Mechanics*, 375, pp. 235-263.

Bouquet, E., Leyssens, G., Schönnenbeck, C., and Gilot, P. (2009). The decrease of carbonation efficiency of CaO along calcination-carbonation cycles: Experiments and modelling. *Chemical Engineering Science*, 64, pp. 2136-2146.

Boyd, T.J. and Friedman, M.A. (1991). Operation and test program summary at the 110 MWe Nucla CFB. In: Basu, P., Horio, M., and Hasatani, M., eds, *Proceedings of the 3rd International Conference on Circulating Fluidized Beds*, pp. 297-312. Oxford: Pergamon Press.

Breault, R.W. (2006). A review of gas-solid dispersion and mass transfer coefficient correlations in circulating fluidized beds. *Powder Technology*, 163, pp. 9-17.

Buhre, B.J.P., Elliott, L.K., Sheng, C.D., Gupta, R.P., and Wall, T.F. (2005). Oxy-fuel combustion technology for coal-fired power generation. *Progress in Energy and Combustion Science*, 31, pp. 283-307.

Cheng, L., Chen, B., Liu, N., Luo, Z., and Cen, K. (2004). Effect of characteristic of sorbents on their sulfur capture capability at a fluidized bed condition. *Fuel*, 83, pp. 925-932.

Chu, K.W. and Yu, A.B. (2008). Numerical simulation of complex particle-fluid flows. *Powder Technology*, 179, pp. 104-114.

Corella, J. and Sanz, A. (2005). Modeling circulating fluidized bed biomass gasifiers. A pseudo-rigorous model for stationary state. *Fuel Processing Technology*, 86, pp. 1021-1053.

Costa, B., Faille, D., Lamquet, O., Marchiondell, C., and Spelta, S. (2001). Dynamic modeling of a 250 MWe CFB boiler. In: Geiling, D.W., ed., *Proceedings of the 16th International Conference on Fluidized Bed Combustion*. New York: ASME.

Cundall, P.A. and Strack, O.D. (1979). A discrete numerical model for granular assemblies. *Geotechnique*, 29(1), pp. 47-65.

Czakiert, T., Bis, Z., Muskala, W., and Nowak, W. (2006). Fuel conversion from oxy-fuel combustion in a circulating fluidized bed. *Fuel Processing Technology*, 87, pp. 531-538.

Dalla Valle, J.M. (1948). *Micromeritics*. London: Pitman.

De Wilde, J., Heynderickx, G.J., and Marin, G.B. (2007). Filtered gas-solid momentum transfer models and their application to 3D steady-state riser simulations. *Chemical Engineering Science*, 62, pp. 5451-5457.

Deen, N.G., Van Sint Annaland, M., and Kuipers, J.A.M. (2006). Detailed computational and experimental fluid dynamics of fluidized beds. *Applied Mathematical Modelling*, 30, pp. 1459-1471.

Deen, N.G., Van Sint Annaland, M., Van der Hoef, M.A., and Kuipers, J.A.M. (2007). Review of discrete particle modeling of fluidized beds. *Chemical Engineering Science*, 62, pp. 28-44.

Deng, Z., Xiao, R., Jin, B., Song, Q., and Huang, H. (2008). Multiphase CFB modeling for a chemical looping combustion process (fuel reactor). *Chemical Engineering & Technology*, 31(12), pp. 1-14.

Ding, J. and Gidaspow, D. (1990). A bubbling fluidization model using kinetic theory of granular flow. *AIChE Journal*, 36, pp. 523-538.

Doherty, W., Reynolds, A., and Kennedy, D. (2009). The effect of air preheating in a biomass CFB gasifier using Aspen Plus simulation. *Biomass and Bioenergy*, 33, pp. 1158-1167.

Dutta, A. and Basu, P. (2002). An experimental investigation into the heat transfer on wing walls in a circulating fluidized bed boiler. *International Journal of Heat and Mass Transfer*, 45(22), pp. 4479-4491.

Dutta, A. and Basu, P. (2003). An improvement of cluster-renewal model for estimation of heat transfer on the water-walls of commercial CFB boilers. In: Pisupati, S., ed., *Proceedings of the 17th International Conference on Fluidized Bed Combustion*. New York: ASME.

EPRI (2002). *Atmospheric Fluidized-Bed Combustion Guidebook - 2002 Update*. Interim report. Palo Alto, CA: Electric Power Research Institute. 1004493.

Ergun, S. (1952). Fluid flow through packed columns. *Chemical Engineering Progress*, 48(2), pp. 89-94.

Eriksson, T., Nuortimo, K., Hotta, A., Myöhänen, K., Hyppänen, T., and T., P. (2009). Near zero CO2 emissions in coal firing with oxyfuel CFB boiler. In: Yue, G., Zhang, H., Zhao, C., and Luo, Z., eds, *Proceedings of the 20th International Conference on Fluidized Bed Combustion*. Beijing: Tsinghua University Press.

Feng, Y.T., Han, K., and Owen, D.R.J. (2010). Combined three-dimensional lattice Boltzmann method and discrete element method for modelling fluid-particle interactions with experimental assessment. *International Journal for Numerical Methods in Engineering*, 81, pp. 229-245.

Ferziger, J.H. and Peric, M. (2002). *Computational Methods for Fluid Dynamics*, 3rd edn. Berlin: Springer. ISBN 3-540-42074-6.

Flour, I. and Boucker, M. (2002). Numerical simulation of the gas-solid flow in the furnace of a CFB cold rig with Estet-Astrid code. In: Grace, J.R., Zhu, J., and de Lasa, H., eds, *Proceedings of the 7th International Conference on Circulating Fluidized Beds*, pp. 467-474. Ottawa: Canadian Society for Chemical Engineering.

Garcia-Labiano, F., Adánez, J., Hampartsoumian, E., and Williams, A. (1996). Sulfur release during the devolatilization of large coal particles. *Fuel*, 75, pp. 585-590.

Garside, J. and Al-Dibouni, M.R. (1977). Velocity-voidage relationships for fluidization and sedimentation. *Industrial & Engineering Chemistry Process Design and Development*, 16, pp. 206-214.

Gayán, P., de Diego, L.F., and Adánez, J. (1997). Radial gas mixing in a fast fluidized bed. *Powder Technology*, 94, pp. 163-171.

Gidaspow, D., Syamlal, M., and Seo, Y. (1986). Hydrodynamics of fluidization of single and binary size particles: supercomputer modelling. In: Østergaard, K. and Sørensen, A., eds, *Proceedings of the 5th Engineering Foundation Conference on Fluidization*. New York: Engineering Foundation.

Gidaspow, D., Bezburuah, R., and Ding, J. (1992). Hydrodynamics of circulating fluidized beds: kinetic theory approach. In: Potter, O.E. and Nicklin, D.J., eds, *Proceedings of the 7th Engineering Foundation Conference on Fluidization*, pp. 75-82. New York: Engineering Foundation.

Gidaspow, D., Jung, J., and Singh, R.K. (2004). Hydrodynamics of fluidization using kinetic theory: an emerging paradigm. *Powder Technology*, 148, pp. 123-141.

Glowinski, R., Pan, T.-W., Hesla, T.I., and Joseph, D.D. (1999). A distributed Lagrange multiplier/fictitious domain method for particulate flows. *International Journal of Multiphase Flow*, 25, pp. 755-794.

Gnanapragasam, N.V. and Reddy, B.V. (2008). Numerical modeling of bed-to-wall heat transfer in a circulating fluidized bed combustor based on cluster energy balance. *International Journal of Heat and Mass Transfer*, 51, pp. 5260-5268.

Goidich, S.J. and Lundqvist, R.G. (2002). The utility CFB boiler - present status, short and long term future with supercritical and ultra-supercritical steam parameters. In: *PowerGen Europe*.

Goldschmidt, M.J.V., Beetstra, R., and Kuipers, J.A.M. (2002). Hydrodynamic modelling of dense gas-fluidized beds: Comparison of the kinetic theory of granular flow with 3D hard-sphere discrete particle simulations. *Chemical Engineering Science*, 57, pp. 2059-2075.

Golriz, M.R. and Grace, J.R. (2002). Predicting heat transfer in large-scale CFB boilers. In: Grace, J.R., Zhu, J., and Lasa, H.d., eds, *Proceedings of the 7th International Conference on Circulating Fluidized Beds*, pp. 121-128. Ottawa: Canadian Society for Chemical Engineering.

Gui, N. and Fan, J. (2009). Numerical simulation of motion of rigid spherical particles in a rotating tumbler with an inner wavelike surface. *Powder Technology*, 192, pp. 234-241.

Gungor, A. and Eskin, N. (2008). Two-dimensional coal combustion modeling of CFB. *International Journal of Thermal Sciences*, 47, pp. 157-174.

Gungor, A. (2009a). A study on the effects of operational parameters on bed-to-wall heat transfer. *Applied Thermal Engineering*, 29, pp. 2280-2288.

Gungor, A. (2009b). One dimensional numerical simulation of small scale CFB combustors. *Energy Conversion and Management*, 50, pp. 711-722.

Han, K., Lu, C., Cheng, S., Zhao, G., Wang, Y., and Zhao, J. (2005). Effect of characteristics of calcium-based sorbents on the sulfation kinetics. *Fuel*, 84, pp. 1933-1939.

Hartge, E.-U., Luecke, K., and Werther, J. (1999). The role of mixing in the performance of CFB reactors. *Chemical Engineering Science*, 54, pp. 5393-5407.

Hartge, E.-U., Budinger, S., and Werther, J. (2005). Spatial effects in the combustion chamber of the 235 MWe CFB boiler Turow No 3. In: Cen, K., ed., *Proceedings of the 8th International Conference on Circulating Fluidized Beds*, pp. 675-682. Beijing: International Academic Publishers.

Hartge, E.-U., Ratschow, L., Wischnewski, R., and Werther, J. (2009). CFD-simulation of a circulating fluidized bed riser. *Particuology*, 7, pp. 283-296.

Hayhurst, A.N. and Lawrence, A.D. (1995). The devolatilization of coal and a comparison of chars produced in oxidizing and inert atmospheres in fluidized beds. *Combustion and Flame*, 100, pp. 591-604.

He, Y., Deen, N.G., van Sint Annaland, M., and Kuipers, J.A.M. (2009). Gas-solid turbulent flow in a circulating fluidized bed riser: numerical study of binary particle systems. *Industrial & Engineering Chemistry Research*, 48, pp. 8098-8108.

Hill, R.J., Koch, D.L., and Ladd, A.J.C. (2001). Moderate-Reynolds-number flows in ordered and random arrays of spheres. *Journal of Fluid Mechanics*, 448, pp. 243-278.

Hiltunen, M., Barisic, V., and Coda Zabetta, E. (2008). Combustion of different types of biomass in CFB boilers. In: Schmid, J., Grimm, H.-P., Helm, P., and Grassi, A., eds, *16th European Biomass Conference*. Valencia, Spain, June 2-6, 2008.

Hoomans, B.P.B., Kuipers, J.A.M., Briels, W.J., and Van Swaaij, W.P.M. (1996). Discrete particle simulation of bubble and slug formation in a two-dimensional gas-fluidized bed: a hard-sphere approach. *Chemical Engineering Science*, 51, pp. 99-118.

Hotta, A. (2009). Foster Wheeler's solutions for large scale CFB boiler technology: features and operational performance of Łagisza 460 MWe CFB boiler. In: Yue, G., Zhang, H., Zhao, C., and Luo, Z., eds, *Proceedings of the 20th International Conference on Fluidized Bed Combustion*. Beijing: Tsinghua University Press.

Hotta, A., Kauppinen, K., and Kettunen, A. (2010). Towards new milestones in CFB boiler technology - CFB 800 MWe / new 460 MWe super-critical plant with CFB boiler in Lagisza - first experience update. In: *Power-Gen Europe*.

Hu, H.H. (1996). Direct simulation of flows of solid-liquid mixtures. *International Journal of Multiphase Flow*, 22, pp. 335-352.

Hu, G., Shang, L., Dam-Johansen, K., Wedel, S., and Hansen, J.P. (2008). Initial kinetics of the direct sulfation of limestone. *AIChE Journal*, 54(10), pp. 2663-2673.

Hua, Y., Flamant, G., Lu, J., and Gauthier, D. (2004). Modelling of axial and radial solid segregation in a CFB boiler. *Chemical Engineering and Processing*, 43, pp. 971-978.

Huilin, L., Guangbo, Z., Rushan, B., Yongjin, C., and Gidaspow, D. (2000). A coal combustion model for circulating fluidized bed boilers. *Fuel*, 79, pp. 165-172.

Hyppänen, T., Lee, Y.Y., and Rainio, A. (1991). A three-dimensional model for circulating fluidized bed boilers. In: Anthony, E.J., ed., *Proceedings of the 11th International Conference on Fluidized Bed Combustion*, pp. 439-448. New York: ASME.

Igci, Y., Andrews, A.T., Sundaresan, S., Pannala, S., and O'Brien, T. (2008). Filtered two-fluid models for fluidized gas-particle suspensions. *AIChE Journal*, 54(6), pp. 1431-1448.

Ishii, M. (1975). *Thermo-Fluid Dynamic Theory of Two-Phase Flow*, vol. 22, Collection de la Direction des Etudes et Researches d'Electricite de France. Paris: Eyrolles.

Issangya, A.S., Grace, J.R., Bai, D., and Zhu, J. (2000). Further measurements of flow dynamics in a high-density circulating fluidized bed riser. *Powder Technology*, 111, pp. 104-113.

Jalali, P. and Hyppänen, T. (2010). Verification of continuum models for solids momentum transfer by means of discrete element method. *Industrial & Engineering Chemistry Research*, 49, pp. 5270-5278.

Jenkins, J.T. and Savage, S.B. (1983). A theory for the rapid flow of identical, smooth, nearly elastic spherical particles. *Journal of Fluid Mechanics*, 130, pp. 187-202.

Johansson, A. (2005). *Solids flow pattern in circulating fluidized-bed boilers*. Ph.D. thesis. Göteborg: Chalmers University of Technology.

Johnsson, F. and Leckner, B. (1995). Vertical distribution of solids in a CFB-furnace. In: Heinschel, K.J., ed., *Proceedings of the 13th International Conference on Fluidized Bed Combustion*, pp. 671-679. New York: ASME.

Jäntti, T., Loschkin, M., Pikkarainen, T., Miettinen, J., and Myöhänen, K. (2005). Characterization of CFB feed materials in designing Foster Wheeler CFB boilers. In: Cen, K., ed., *Proceedings of the 8th International Conference on Circulating Fluidized Beds*, pp. 418-425. Beijing: International Academic Publishers.

Jäntti, T. and Parkkonen, R. (2009). Lagisza 460 MWe Supercritical CFB - Design, start-up and initial operation experience. In: *Power Gen Asia*. Bangkok: Pennwell.

Kallio, S. (2005). Comparison of simulated and measured voidage and velocity profiles and fluctuations in a CFB riser. In: Cen, K., ed., *Proceedings of the 8th International Conference on Circulating Fluidized Beds*, pp. 105-112. Beijing: International Academic Publishers.

Kallio, S., Taivassalo, V., and Hyppänen, T. (2008). Towards time-averaged CFD modelling of circulating fluidized beds. In: Werther, J., Nowak, W., Wirth, K.-E.,

and Hartge, E.-U., eds, *Proceedings of the 9th International Conference on Circulating Fluidized Beds*. Hamburg: TuTech Innovation.

Kallio, S., Guldén, M., and Hermanson, A. (2009). Experimental study and CFD simulation of a 2D circulating fluidized bed. In: Yue, G., Zhang, H., Zhao, C., and Luo, Z., eds, *Proceedings of the 20th International Conference on Fluidized Bed Combustion*, pp. 799-804. Beijing: Tsinghua University Press.

Karimipour, S. and Pugsley, T. (2010). Study of gas streaming in a deep fluidized bed containing Geldart's Group A particles. *Chemical Engineering Science*, 65, pp. 3508-3517.

Karppanen, E. (2000). *Advanced control of an industrial circulating fluidized bed boiler using fuzzy logic*. Ph.D. thesis. University of Oulu.

Kavidass, S., Anderson, G.L., and Norton, G.S. (2000). Why build a circulating fluidized bed boiler to generate steam and electric power. In: *Power-Gen Asia*. September 20-22, 2000, Bangkok, Thailand.

Kettunen, A., Hyppänen, T., Kirkinen, A.-P., and Maikkola, E. (2003). Model-based analysis of transient behavior of large-scale CFB boilers. In: Pisupati, S., ed., *Proceedings of the 17th International Conference on Fluidized Bed Combustion*. New York: ASME.

Knoebig, T., Luecke, K., and Werther, J. (1999). Mixing and reaction in the circulating fluidized bed - A three-dimensional combustor model. *Chemical Engineering Science*, 54, pp. 2151-2160.

Kokko, A. and Nylund, M. (2005). Biomass and coal co-combustion in utility scale - operating experience of Alholmens Kraft. In: Li, J., ed., *Proceedings of the 18th International Conference on Fluidized Bed Combustion*. New York: ASME.

Koornneef, J., Junginger, M., and Faaij, A. (2007). Development of fluidized bed combustion—An overview of trends, performance and cost. *Progress in Energy and Combustion Science*, 33, pp. 19-55.

Koski, M. (2010). *Three-dimensional modelling of gasification in a circulating fluidized bed process*. Master's thesis. Lappeenranta University of Technology.

Koski, M., Ritvanen, J., Myöhänen, K., Hyppänen, T., Palonen, J., Häkkinen, K., and Kokki, S. (2011). Three-dimensional modelling study of a circulating fluidized bed gasifier. In: *International Conference on Polygeneration Strategies*. Submitted for publication.

Krishnan, S.V. and Sotirchos, S.V. (1994). Effective diffusivity changes during calcination, carbonation, recalcination and sulfation of limestones. *Chemical Engineering Science*, 49, pp. 1195-1208.

Kruse, M. and Werther, J. (1995). 2D gas and solids flow prediction in circulating fluidized beds based on suction probe and pressure profile measurements. *Chemical Engineering and Processing*, 34, pp. 185-203.

Krzywanski, J., Czakiert, T., Muskala, W., Sekret, R., and Nowak, W. (2010). Modeling of solid fuels combustion in oxygen-enriched atmosphere in circulating fluidized bed boiler. Part 1. The mathematical model of fuel combustion in oxygen-enriched CFB environment. *Fuel Processing Technology*, 91, pp. 290-295.

Kuivalainen, R., Pikkarainen, T., Leino, T., Tourunen, A., Myöhänen, K., Takkinen, S., and Hyppänen, T. (2009). Oxyfuel-CFB boiler scale-up based on integrated experimental and modeling work. In: *Proceedings of the 1st International Oxyfuel Combustion Conference*. Cottbus, Germany, September 8-11, 2009.

Kuivalainen, R., Eriksson, T., Hotta, A., Sacristán, A.S., Jubitero, J.M., Ballesteros, J.C., Lupion, M., Cortes, V., Anthony, B., Jia, L., McCalden, D., Tan, Y., He, I., Wu, Y., and Symonds, R. (2010). Development and demonstration of oxy-fuel CFB technology. In: *The 35th International Technical Conference on Clean Coal & Fuel Systems*. Clearwater, Florida, June 6-11, 2010.

Lackermeier, U., Rudnick, C., Werther, J., Bredebusch, A., and Burkhardt, H. (2001). Visualization of flow structures inside a circulating fluidized bed by means of laser sheet and image processing. *Powder Technology*, 114, pp. 71-83.

Leboreiro, J., Joseph, G.G., Hrenya, C.M., Snider, D.M., S.S., B., and Galvin, J.E. (2008). The influence of binary drag laws on simulations of species segregation in gas-fluidized beds. *Powder Technology*, 184, pp. 275-290.

Lee, Y.Y. and Hyppänen, T. (1989). A coal combustion model for circulating fluidized bed boilers. In: Manaker, A.M., ed., *Proceedings of the 10th International Conference on Fluidized Bed Combustion*, 2, pp. 753-764. New York: ASME.

Lefebvre, S., Chaouki, J., and Guy, C. (2004). Phase mixing modeling in multiphase reactors containing gas bubble: a review. *International Journal of Chemical Reactor Engineering*, 2.

Lemasle, J.-M. and Sculy-Logotheti, I.-M. (2004). Baima: China's first large-scale CFB. *Modern Power Systems*, 24(2), pp. 26-27.

Li, Y. and Kwauk, M. (1980). The dynamics of fast fluidization. In: Grace, J.R. and Matsen, J.M., eds, *Fluidization*, pp. 537-544. New York: Plenum Press.

Li, X., Luo, Z., Ni, M., and Cen, K. (1995). Modeling sulfur retention in circulating fluidized bed combustors. *Chemical Engineering Science*, 50(14), pp. 2235-2242.

Li, X.T., Grace, J.R., Lim, C.J., Watkinson, A.P., Chen, H.P., and Kim, J.R. (2004). Biomass gasification in a circulating fluidized bed. *Biomass and Bioenergy*, 26, pp. 171-193.

Li, Q.H., Zhang, Y.G., and Meng, A.H. (2009). Design and application of novel horizontal circulating fluidized bed boiler. In: Yue, G., Zhang, H., Zhao, C., and Luo, Z., eds, *Proceedings of the 20th International Conference on Fluidized Bed Combustion*. Beijing: Tsinghua University Press.

Lim, K.S., Zhu, J.X., and Grace, J.R. (1995). Hydrodynamics of gas-solid fluidization. *International Journal of Multiphase Flow*, 21, pp. 141-193.

Lim, K.S., Zhu, J.X., and Grace, J.R. (1995). Hydrodynamics of gas-solid fluidization. *International Journal of Multiphase Flow*, 21, pp. 141-193.

Liu, H., Katagiri, S., Kaneko, U., and Okazaki, K. (2000). Sulfation behavior of limestone under high CO2 concentration in O2/CO2 coal combustion. *Fuel*, 79, pp. 945-953.

Liu, X. and Xu, X. (2009). Modelling of dense gas-particle flow in a circulating fluidized bed by distinct cluster method (DCM). *Powder Technology*, 195, pp. 235-244.

Liu, D. and Chen, X. (2010). Lateral solids dispersion coefficient in large-scale fluidized beds. *Combustion and Flame*, 157, pp. 2116-2124.

Loschkin, M. (2001). *Modelling of fractional solid material mass balance of a circulating fluidized bed boiler*. Master's thesis. Lappeenranta University of Technology.

Loth, E. (2006). Overview of multiphase modeling. In: Crowe, C.T., ed., *Multiphase Flow Handbook*, chap. 13.1. Boca Raton: CRC Press. ISBN 978-0-8493-1280-9.

Luecke, K., Hartge, E.-U., and Werther, J. (2004). A 3D model of combustion in large-scale circulating fluidized bed boilers. *International Journal of Chemical Reactor Engineering*, 2. Article A11.

Lun, C.K., Savage, S.B., Jeffrey, D.J., and Chepurniy, N. (1984). Kinetic theories for granular flow: inelastic particles in Couette flow and slightly inelastic particles in a general flow field. *Journal of Fluid Mechanics*, 140, pp. 223-256.

Lyngfelt, A., Leckner, B., and Mattisson, T. (2001). A fluidized-bed combustion process with inherent CO2 separation; application of chemical-looping combustion. *Chemical Engineering Science*, 56, pp. 3101-3113.

Ma, D. and Ahmadi, G. (1990). A thermodynamical formulation for dispersed multiphase turbulent flows. *International Journal of Multiphase Flow*, 16, pp. 323-351.

Ma, L. (2006). *Combustion and gasification of chars in oxygen and carbon dioxide at elevated pressure*. Ph.D. thesis. Stanford University.

Makkonen, P. (1999). *Artificially intelligent and adaptive methods for prediction and analysis of superheater fireside corrosion in fluidized bed boilers*. Ph.D. thesis. Lappeenranta University of Technology.

Marchetti, M.M., Czarnecki, T.S., Semedard, J.C., Devroe, S., and Lemasle, J.-M. (2003). Alstom's large CFBs and results. In: Pisupati, S., ed., *Proceedings of the 17th International Conference on Fluidized Bed Combustioni*. New York: ASME.

Mathiesen, V., Solberg, T., and Hjertager, B.H. (2000). An experimental and computational study of multiphase flow behavior in a circulating fluidized bed. *International Journal of Multiphase Flow*, 26, pp. 387-419.

Mattisson, T. and Lyngfelt, A. (1998a). A sulphur capture model for circulating fluidized-bed boilers. *Chemical Engineering Science*, 53(6), pp. 1163-1173.

Mattisson, T. and Lyngfelt, A. (1998b). Reaction between sulfur dioxide and limestone under periodically changing oxidizing and reducing conditions - effect of cycle time. *Energy & Fuels*, 12, pp. 905-912.

Mickley, H. and Fairbanks, D. (1955). Mechanism of heat transfer to fluidized beds. *AIChE Journal*, 1, pp. 374-384.

Migliavacca, G., Parodi, E., Bonfatti, L., Faravell, T., Pierucci, S., and Ranzi, E. (2005). A general mathematical model of solid fuels pyrolysis. *Energy*, 30, pp. 1453-1468.

Morin, J.-X. (2003). Recent Alstom Power large CFB and scale up aspects including steps to supercritical. In: *47th International Energy Agency Workshop on Large Scale CFB*. October 13, 2003, Zlotnicki, Poland.

Muir, J.R., Brereton, C., Grace, J.R., and Lim, J. (1997). Dynamic modeling for simulation and control of a circulating fluidized-bed combustor. *AIChE Journal*, 43, pp. 1141-1152.

Myöhänen, K., Hyppänen, T., Miettinen, J., and Parkkonen, R. (2003). Three-dimensional modeling and model validation of circulating fluidized bed combustion.

In: Pisupati, S., ed., *Proceedings of the 17th International Conference on Fluidized Bed Combustion*. New York: ASME.

Myöhänen, K., Hyppänen, T., and Loschkin, M. (2005). Converting measurement data to process knowledge by using three-dimensional CFB furnace model. In: Cen, K., ed., *Proceedings of the 8th International Conference on Circulating Fluidized Beds*, pp. 306-312. Beijing: International Academic Publishers.

Myöhänen, K., Tanskanen, V., Hyppänen, T., Kyrki-Rajamäki, R., and Nevalainen, T. (2006). CFD modelling of fluidized bed systems. In: Juuso, E., ed., *SIMS 2006: Proceedings of the 47th Conference on Simulation and Modelling*, pp. 88-93. Helsinki: Finnish Society of Automation.

Myöhänen, K., Hyppänen, T., and Vepsäläinen, A. (2006). Modelling of circulating fluidized bed combustion with a semi-empirical three-dimensional model. In: Juuso, E., ed., *SIMS 2006: Proceedings of the 47th Conference on Simulation and Modelling*, pp. 194-199. Helsinki: Finnish Society of Automation.

Myöhänen, K. and Takkinen, S. (2009). *Happipolttokonseptit: Kiertoleijupolton prosessimallinnuksen kehittäminen ja sovelluslaskennat [Oxyconcepts: Development of process modelling of circulating fluidized bed combustion and application studies]*. Report for Finnish Technology Agency Tekes. Lappeenranta University of Technology. In Finnish.

Myöhänen, K., Hyppänen, T., Pikkarainen, T., Eriksson, T., and Hotta, A. (2009). Near zero CO2 emissions in coal firing with oxy-fuel CFB boiler. *Chemical Engineering & Technology*, 32(3), pp. 355-363.

Myöhänen, K. (2010). *Initial 3D-calculations of selected cases*. Deliverable D6. European Community's Seventh Framework Programme (FP7/2007-2013) under grant agreement n° 239188.

Myöhänen, K. and Hyppänen, T. (2011). A three-dimensional model frame for modelling combustion and gasification in circulating fluidized bed furnaces. *International Journal of Chemical Reactor Engineering*, 9. Article A25, 55 p.

Myöhänen, K., Ritvanen, J., Eriksson, T., Kuivalainen, R., and Hyppänen, T. (2011). Three-dimensional modelling of a 300 MWe Flexi-Burn CFB for multifuel combustion in oxygen-fired and air-fired modes. In: *2nd Oxyfuel Combustion Conference*. 12-16 September 2011, Queensland, Australia. IEA Greenhouse Gas R&D Programme.

Nicolai, R., Goedicke, F., Tanner, H., and Reh, L. (1993). Particle induced heat transfer between walls and gas-solid fluidized beds. In: Avidan, A.A., ed., *Proceedings of the 4th International Conference on Circulating Fluidized Beds*, pp. 305-310. New York: AIChE.

Nikolopoulos, A., Rampidis, I., Nikolopoulos, N., Grammelis, P., and Kakaras, E. (2009). Numerical investigation of 3-D transient combusting flow in a 1.2MWth pilot power plant. In: Yue, G., Zhang, H., Zhao, C., and Luo, Z., eds, *Proceedings of the 20th International Conference on Fluidized Bed Combustion*, pp. 839-844. Beijing: Tsinghua University Press.

Ogawa, S., Umemura, A., and Oshima, N. (1980). On the equations of fully fluidized granular materials. *Journal of Applied Mathematics and Physics*, 31, pp. 483-493.

O'Rourke, P.J., Zhao, P., and Snider, D. (2009). A model for collisional exchange in gas/liquid/solid fluidized beds. *Chemical Engineering Science*, 64, pp. 1784-1797.

Pai, D. and Engström, F. (1999). Fluidized bed combustion: the past, present and future. *Modern Power Systems*, 19(11), pp. 21-26.

Pallarès, D.J. and Johnsson, F. (2002). Fluid dynamic modeling of large CFB units. In: Grace, J.R., Zhu, J., and de Lasa, H., eds, *Proceedings of the 7th International Conference on Circulating Fluidized Beds*, pp. 387-394. Ottawa: Canadian Society for Chemical Engineering.

Pallarès, D. and Johnsson, F. (2006a). A novel technique for particle tracking in cold 2-dimensional fluidized beds - simulating fuel dispersion. *Chemical Engineering Science*, 61, pp. 2710-2720.

Pallarès, D. and Johnsson, F. (2006b). Macroscopic modelling of fluid dynamics in large-scale circulating fluidized beds. *Progress in Energy and Combustion Science*, 32, pp. 539-569.

Pallarès, D. and Johnsson, F. (2008a). Modeling of fuel mixing in fluidized bed combustors. *Chemical Engineering Science*, 63, pp. 5663-5671.

Pallarès, D., Johnsson, F., and Palonen, M. (2008b). A comprehensive model of CFB combustion. In: Werther, J., Nowak, W., Wirth, K.-E., and Hartge, E.-U., eds, *Proceedings of the 9th International Conference on Circulating Fluidized Beds*, pp. 577-582. Hamburg: TuTech Innovation.

Pan, T.-W., Joseph, D.D., Bai, R., Glowinski, R., and Sarin, V. (2002). Fluidization of 1204 spheres: simulation and experiment. *Journal of Fluid Mechanics*, 451, pp. 169-191.

Park, C.K. and Basu, P. (1997). A model for prediction of transient response to the change of fuel feed rate to a circulating fluidized bed boiler furnace. *Chemical Engineering Science*, 52(20), pp. 3499-3509.

Patankar, N.A. and Joseph, D.D. (2001). Lagrangian numerical simulation of particulate flows. *International Journal of Multiphase Flow*, 27, pp. 1685-1706.

Patel, S. (2009). Operation of world's first supercritical CFB steam generator begins in Poland. *Power*, September 1.

Peltier, R. (2006). Nova Scotia Power's Point Aconi plant overcomes CFB design problems to become rock of reliability. *Power*, September 15.

Perry, R.H. and Green, D.W. (1997). *Perry's Chemical Engineers' Handbook*, 7th edn, chap. 27.

Petersen, I. and Werther, J. (2005a). Experimental investigation and modeling of gasification of sewage sludge in the circulating fluidized bed. *Chemical Engineering and Processing*, 44, p. 717–736.

Petersen, I. and Werther, J. (2005b). Three-dimensional modeling of a circulating fluidized bed gasifier for sewage sludge. *Chemical Engineering Science*, 60, pp. 4469-4484.

Pikkarainen, T. (2001). *Characterization method for comminution behavior of limestone and fuel ash in a circulating fluidized bed boiler*. Master's thesis. Lappeenranta University of Technology.

Pugsley, T.S. and Berruti, F. (1996). A predictive hydrodynamic model for circulating fluidized bed risers. *Powder Technology*, 89, pp. 57-69.

Qi, H., Li, F., Xi, B., and You, C. (2007). Modeling of drag with the Eulerian approach and EMMS theory for heterogeneous dens gas-solid two-phase flow. *Chemical Engineering Science*, 62, pp. 1670-1681.

Rainio, A. (1989). *Kolmiulotteisen kaksifaasivirtauksen matemaattinen mallintaminen [Mathematical modelling of a three-dimensional two-phase flow]*. Master's thesis. Lappeenranta University of Technology. In Finnish.

Reh, L. (1986). The circulating fluid bed reactor - its main features and applications. *Chemical Engineering and Processing*, 20(3), pp. 117-127.

Reh, L. (2003). Development potentials and research needs in circulating fluidized bed combustion. *China Particuology*, 1(5), pp. 185-200.

Roeck, D.R. (1982). *Technology overview: circulating fluidized-bed combustion.* Technical report PB-82-240185. Bedford: GCA Corp.

Ross, D.P., Heidenreich, C.A., and Zhang, D.K. (2000). Devolatilization times of coal particles in a fluidised-bed. *Fuel*, 79, pp. 873-883.

Rowlands, I.H. (2005). The European directive on renewable electricity: conflicts and compromises. *Energy Policy*, 33, pp. 965-974.

Saastamoinen, J. (2006). Simplified model for calculation of devolatilization in fluidized beds. *Fuel*, 85, pp. 2388-2395.

Saastamoinen, J. (2007). Particle-size optimization for SO2 capture by limestone in a circulating fluidized bed. *Industrial & Engineering Chemistry Research*, 46, pp. 7308-7316.

Salamov, A.A. (2007). Circulating fluidized bed boilers abroad. *Thermal Engineering*, 54(6), pp. 501-505.

Sapy, G. (1998). CFB: scaling up to 600 MWe. *Modern Power Systems*, 18(8), pp. 19-21.

Schlichthaerle, P. and Werther, J. (2001). Solids mixing in the bottom zone of a circulating fluidized bed. *Powder Technology*, 120, pp. 21-33.

Shah, S., Klajny, M., Myöhänen, K., and Hyppänen, T. (2009). Improvement of CFD methods for modeling full scale circulating fluidized bed combustion systems. In: Yue, G., Zhang, H., Zhao, C., and Luo, Z., eds, *Proceedings of the 20th International Conference on Fluidized Bed Combustion*, pp. 792-798. Beijing: Tsinghua University Press.

Silcox, G.D., Kramlich, J.C., and Pershing, D.W. (1989). A mathematical model for the flash calcination of dispersed CaCO3 and Ca(OH)2 particles. *Industrial & Engineering Chemistry Research*, 28, pp. 155-160.

Sinclair, J.L. and Jackson, R. (1989). Gas-particle flow in a vertical pipe with particle-particle interactions. *AIChE Journal*, 35, pp. 1473-1486.

Smolders, K. and Baeyens, J. (2001). Hydrodynamic modelling of the axial density profile in the riser of a low-density circulating fluidized bed. *Canadian Journal of Chemical Engineering*, 79, pp. 422-429.

Snider, D.M. (2001). An imcompressible three-dimensional multiphase particle-in-cell model for dense particle flows. *Journal of Computational Physics*, 170, pp. 523-549.

Snider, D. and Banerjee, S. (2010). Heterogeneous gas chemistry in the CPFD Eulerian-Lagrangian numerical scheme (ozone decomposition). *Powder Technology*, 199, pp. 100-106.

Sotudeh-Gharebaagh, R., Legros, R., Chaouki, J., and Paris, J. (1998). Simulation of circulating fluidized bed reactors using ASPEN PLUS. *Fuel*, 77(4), pp. 327-337.

Squires, A.M. (1986). The story of fluid catalytic cracking: the first "circulating fluid bed". In: Basu, P., ed., *Proceedings of the First International Conference on*

Circulating Fluidized Beds. Nova Scotia, Canada, November 18-20, 1985. Toronto: Pergamon Press.

Stanmore, B.R. and Gilot, P. (2005). Review - calcination and carbonation of limestone during thermal cycling for CO2 sequestration. *Fuel Processing Technology*, 86, pp. 1707-1743.

Sternéus, J., Johnsson, F., and Leckner, B. (2000). Gas mixing in circulating fluidized-bed risers. *Chemical Engineering Science*, 55, pp. 129-148.

Stratton, R.E. and Wensrich, C.M. (2010). Modelling of multiple intra-time step collisions in the hard-sphere discrete element method. *Powder Technology*, 199, pp. 120-130.

Subbarao, D. and Basu, P. (1986). A model for heat transfer in circulating fluidized beds. *International Journal of Heat and Mass Transfer*, 29, pp. 487-489.

Sun, P., Grace, J.R., Lim Jim, C., and Anthony, E.J. (2008). Determination of intrinsic rate constants of the CaO-CO2 reaction. *Chemical Engineering Science*, 63, pp. 47-56.

Syamlal, M. (1987). *Particle-particle drag term in a multiparticle model of fluidization*. Topical report. Morgantown: Morgantown Energy Technology Center. DOE/MC/2135-2373.

Syamlal, M. and O'Brien, T.J. (1989). Computer simulation of bubbles in a fluidized bed. *AIChE Symposium Series*, 85, pp. 22-31.

Syamlal, M., Rogers, W., and O'Brien, T.J. (1993). *MFIX Documentation Theory Guide*. Technical note. Morgantown: Morgantown Energy Technology Center. DOE/METC-94/1004.

Tanaka, T., Yonemura, S., Kiribayashi, K., and Tsuji, Y. (1996). Cluster formation and particle-induced instability in gas-solid flows predicted by the DSMC method. *JSME International Journal, Series B*, 39(2), pp. 239-245.

Tannehill, J.C., Anderson, D.A., and Pletcher, R.H. (1997). *Computational Fluid Mechanics and Heat Transfer*, 2nd edn. Philadelphia: Taylor & Francis. ISBN 1-56032-046-X.

Tanskanen, V. (2005). *CFD study of penetration and mixing of fuel in a circulating fluidized bed furnace*. Master's thesis. Lappeenranta University of Technology.

Tenneti, S., Garg, R., Hrenya, C.M., Fox, R.O., and Subramaniam, S. (2010). Direct numerical simulation of gas-solid suspensions at moderate Reynolds number:

Quantifying the coupling between hydrodynamic forces and particle velocity fluctuations. *Powder Technology*, 203, pp. 57-69.

Thunman, H., Niklasson, F., Johnsson, F., and Leckner, B. (2001). Composition of volatile gases and thermochemical properties of wood for modeling of fixed or fluidized beds. *Energy & Fuels*, 15, pp. 1488-1497.

Thunman, H., Davidsson, K., and Leckner, B. (2004). Separation of drying and devolatilization during conversion of solid fuels. *Combustion and Flame*, 137, pp. 242-250.

Tossavainen, V., Karvinen, R., and Ylitalo, M. (2003). Modeling air jet penetration into gas-particle suspension cross-flow. In: Pisupati, S., ed., *Proceedings of the 17th International Conference on Fluidized Bed Combustion*. New York: ASME.

Tourunen, A., Saastamoinen, J., and Nevalainen, H. (2009). Experimental trends of NO in circulating fluidized bed combustion. *Fuel*, 88, pp. 1333-1341.

Tsuji, Y., Kawaguchi, T., and Tanaka, T. (1993). Discrete particle simulation of two-dimensional fluidized bed. *Powder Technology*, 77, pp. 79-87.

Tsuji, Y. (2007). Multi-scale modeling of dense phase gas-particle flow. *Chemical Engineering Science*, 62, pp. 3410-3418.

Tsuji, T., Yabumoto, K., and Tanaka, T. (2008). Spontaneous structures in three-dimensional bubbling gas-fluidized bed by parallel DEM-CFD coupling simulation. *Powder Technology*, 184, pp. 132-140.

Utt, J., Hotta, S., and Goidich, S. (2009). Utility CFB goes "supercritical" - Foster Wheeler's Lagisza 460 MWe operating experiences and 600-800 MWe designs. In: *Coal-Gen 2009*. Charlotte, North Caroline, U.S.A., August 19-21.

van der Hoef, M.A., van Sint Annaland, M., and Kuipers, J.A.M. (2004). Computational fluid dynamics for dense gas-solid fluidized beds: a multi-scale modeling strategy. *Chemical Engineering Science*, 59, pp. 5157-5165.

van Wachem, B.G.M., Schouten, J.C., van den Bleek, C.M., Krishna, R., and Sinclair, J.L. (2001b). Comparative analysis of CFD models of dense gas-solid systems. *AIChE Journal*, 47(5), pp. 1035-1051.

Wan, G., Sun, G., Xue, X., and Shi, M. (2008). Solids concentration simulation of different size particles in a cyclone separator. *Powder Technology*, 183, pp. 94-104.

Wang, J. (2010). Flow structures inside a large-scale turbulent fluidized bed of FCC particles: Eulerian simulation with an EMMS-based sub-grid scale model. *Particuology*, 8, pp. 176-185.

Wang, W., Lu, B., Zhang, N., Shi, Z., and Li, J. (2010). A review of multiscale CFD for gas-solid CFB modeling. *International Journal of Multiphase Flow*, 36, pp. 109-118.

Wang, X.Y., Jiang, F., Xu, X., Fan, B.G., Lei, J., and Xiao, Y.H. (2010). Experiment and CFD simulation of gas-solid flow in the riser of dense fluidized bed at high gas velocity. *Powder Technology*, 199, pp. 203-212.

Wang, X.S., Gibbs, B.M., Rhodes, M.J., and Geldart, D. (1996). Convective wall-to-suspension heat transfer in circulating fluidized bed risers. *AIChE Journal*, 42(8), pp. 2112-2117.

Wang, Q., Luo, Z., Li, X., Fang, M., Ni, M., and Cen, K. (1999). A mathematical model for a circulating fluidized bed (CFB) boiler. *Energy*, 24, pp. 633-653.

Wang, Q., Luo, Z., Ni, M., and Cen, K. (2003). Particle population balance model for a circulating fluidized bed boiler. *Chemical Engineering Journal*, 93, pp. 121-133.

Wang, S., Li, X., Lu, H., Yu, L., Ding, J., and Yang, Z. (2009). DSMC prediction of granular temperatures of clusters and dispersed particles in a riser. *Powder Technology*, 192, pp. 225-233.

Vassilev, S.V., Baxter, D., Andersen, L.K., and Vassileva, C.G. (2010). An overview of the chemical composition of biomass. *Fuel*, 89, pp. 913-933.

Wen, C.-Y. and Yu, Y.H. (1966). Mechanics of fluidization. *Chemical Engineering Progress Symposium Series*, 62, pp. 100-111.

Vepsäläinen, A., Myöhänen, K., Hyppänen, T., Leino, T., and Tourunen, A. (2009). Development and validation of a 3-dimensional CFB furnace model. In: Yue, G., Zhang, H., Zhao, C., and Luo, Z., eds, *Proceedings of the 20th International Conference on Fluidized Bed Combustion*, pp. 757-763. Beijing: Tsinghua University Press.

Werther, J. and Hirschberg, B. (1997). Solids motion and mixing. In: Grace, J.R., Avidan, A.A., and Knowlton, T.M., eds, *Circulating Fluidized Beds*, pp. 119-144. London: Blackie Academic and Professional.

Werther, J. (2005). Fluid dynamics, temperature and concentration fields in large-scale CFB combustors. In: Cen, K., ed., *Circulating Fluidized Bed Technology VIII*. Beijing: International Academic Publishers.

Winkler, F. (1922). *Verfahren zum Herstellen von Wassergas*. Pat. German patent No. 437971.

Wischnewski, R., Ratschow, L., Hartge, E.-U., and Werther, J. (2010). Reactive gas-solids flows in large volumes - 3D modeling of industrial circulating fluidized bed combustors. *Particuology*, 8, pp. 67-77.

Xianbin, S. and Minhua, J. (2009). Research and development of large capacity CFB boilers in TPRI. In: Yue, G., Zhang, H., Zhao, C., and Luo, Z., eds, *Proceedings of the 20th International Conference on Fluidized Bed Combustion*. Beijing: Tsinghua University Press.

Yang, N., Wang, W., Ge, W., and Li, J. (2003). CFD simulation of concurrent-up gas-solid flow in circulating fluidized beds with structure-dependent drag coefficient. *Chemical Engineering Journal*, 96, pp. 71-80.

Yerushalmi, J., Turner, D.H., and Squires, A.M. (1976). The fast fluidized bed. *Industrial and Engineering Chemistry Process Design and Development*, 15(1), pp. 47-53.

Yoon, H., Wei, J., and Denn, M.M. (1978). Model for moving bed coal gasification reactors. *AIChE Journal*, 24(5), pp. 885-903.

Yue, G.X., Yang, H.R., Nie, L., Wang, Y.Z., and Zhang, H. (2008). Hydrodynamics of 300MWe and 600MWe CFB boilers with asymmetric cyclone layout. In: Werther, J., Nowak, W., Wirth, K.-E., and Hartge, E.-U., eds, *Proceedings of the 9th International Conference on Circulating Fluidized Beds*. Hamburg: TuTech Innovation.

Yue, G.X., Yang, H.R., Lu, J.F., and Zhang, H. (2009). Latest development of CFB boilers in China. In: Yue, G., Zhang, H., Zhao, C., and Luo, Z., eds, *Proceedings of the 20th International Conference on Fluidized Bed Combustion*. Beijing: Tsinghua University Press.

Zevenhoven, C.A.P., Yrjas, P.K., and Hupa, M. (1998). Product layer development during sulfation and sulfidation of uncalcined limestone particles at elevated pressures. *Industrial & Engineering Chemistry Research*, 37, pp. 2639-2646.

Zevenhoven, R., Yrjas, P., and Hupa, M. (1999). Sulfur capture under periodically changing oxidizing and reducing conditions. In: Reuther, R.B., ed., *Proceedings of the 15th International Conference on Fluidized Bed Combustion*. New York: ASME.

Zhang, W., Johnsson, F., and Leckner, B. (1993). Characteristics of the lateral particle distribution in circulating fluidized bed boilers. In: Avidan, A.A., ed., *Proceedings of the 4th International Conference on Circulating Fluidized Beds*, pp. 266-273. New York: AIChE.

Zhang, W., Johnsson, F., and Leckner, B. (1995). Fluid-dynamic boundary layers in CFB boilers. *Chemical Engineering Science*, 50, pp. 201-210.

Zhang, D.Z. and VanderHeyden, W.B. (2002). The effects of mesoscale structures on the macroscopic momentum equations for two-phase flows. *International Journal of Multiphase Flow*, 28, pp. 805-822.

Zhang, N., Lu, B., Wang, W., and Li, J. (2008). Virtual experimentation through 3D full-loop simulation of a circulating fluidized bed. *Particuology*, 6, pp. 529-539.

Zhang, N., Lu, B., Wang, W., and Li, J. (2010). 3D CFD simulation of hydrodynamics of a 150 MWe circulating fluidized bed boiler. *Chemical Engineering Journal*, 162, pp. 821-828.

Zhao, B.T. and Su, Y.X. (2007). Particle collection theory for cyclone separators: Summary and comparison. *Particle & Particle Systems Characterization*, 23, pp. 484-488.

Zhao, C.S., Duan, L.B., Chen, X.P., and Liang, C. (2009). Latest evolution of oxy-fuel combustion technology in circulating fluidized bed. In: Yue, G., Zhang, H., Zhao, C., and Luo, Z., eds, *Proceedings of the 20th International Conference on Fluidized Bed Combustion*. Beijing: Tsinghua University Press.

Zhou, H., Flamant, G., Gauthier, D., and Lu, J. (2002). Lagrangian approach for simulating the gas-particle flow structure in a circulating fluidized bed riser. *International Journal of Multiphase Flow*, 28, pp. 1801-1821.

Zhu, H.P., Zhou, Z.Y., Yang, R.Y., and Yu, A.B. (2007). Discrete particle simulation of particulate systems: Theoretical developments. *Chemical Engineering Science*, 62, pp. 3378-3396.

Özel, A., Fede, P., and Simonin, O. (2009). 3D numerical prediction of gas-solid flow behavior in CFB risers for Geldart A and B particles. In: Yue, G., Zhang, H., Zhao, C., and Luo, Z., eds, *Proceedings of the 20th International Conference on Fluidized Bed Combustion*, pp. 805-811. Beijing: Tsinghua University Press.

ACTA UNIVERSITATIS LAPPEENRANTAENSIS

407. JOKINEN, MARKKU. Centralized motion control of a linear tooth belt drive: Analysis of the performance and limitations. 2010. Diss.

408. KÄMÄRI, VESA. Kumppanuusohjelman strateginen johtaminen – Monitapaustutkimus puolustushallinnossa. 2010. Diss.

409. KARJALAINEN, AHTI. Online ultrasound measurements of membrane compaction. 2010. Diss.

410. LOHTANDER, MIKA. On the development of object functions and restrictions for shapes made with a turret punch press. 2010. Diss.

411. SIHVO, VILLE. Insulated system in an integrated motor compressor. 2010. Diss.

412. SADOVNIKOV, ALBERT. Computational evaluation of print unevenness according to human vision. 2010. Diss.

413. SJÖGREN, HELENA. Osingonjakopäätökset pienissä osakeyhtiöissä. Empiirinen tutkimus osakeyhtiölain varojenjakosäännösten toteutumisesta. 2010. Diss.

414. KAUPPI, TOMI. Eye fundus image analysis for automatic detection of diabetic retinopathy. 2010. Diss.

415. ZAKHVALINSKII, VASILII. Magnetic and transport properties of $LaMnO_{3+\delta}$, $La_{1-x}Ca_xMnO_3$, $La_{1-x}Ca_xMn_{1-y}Fe_yO_3$ and $La_{1-x}Sr_xMn_{1-y}Fe_yO_3$. 2010. Diss.

416. HATAKKA, HENRY. Effect of hydrodynamics on modelling, monitoring and control of crystallization. 2010. Diss.

417. SAMPO, JOUNI. On convergence of transforms based on parabolic scaling. 2010. Diss.

418. TURKU. IRINA. Adsorptive removal of harmful organic compounds from aqueous solutions. 2010. Diss.

419. TOURUNEN, ANTTI. A study of combustion phenomena in circulating fluidized beds by developing and applying experimental and modeling methods for laboratory-scale reactors. 2010. Diss.

420. CHIPOFYA, VICTOR. Training system for conceptual design and evaluation for wastewater treatment. 2010. Diss.

421. KORTELAINEN, SAMULI. Analysis of the sources of sustained competitive advantage: System dynamic approach. 2011. Diss.

422. KALJUNEN, LEENA. Johtamisopit kuntaorganisaatiossa – diskursiivinen tutkimus sosiaali- ja terveystoimesta 1980-luvulta 2000-luvulle. 2011. Diss.

423. PEKKARINEN, SATU. Innovations of ageing and societal transition. Dynamics of change of the socio-technical regime of ageing. 2011. Diss.

424. JUNTTILA, VIRPI. Automated, adapted methods for forest inventory. 2011. Diss.

425. VIRTA, MAARIT. Knowledge sharing between generations in an organization – Retention of the old or building the new 2011. Diss.

426. KUITTINEN, HANNA. Analysis on firm innovation boundaries. 2011. Diss.

427. AHONEN, TERO. Monitoring of centrifugal pump operation by a frequency converter. 2011. Diss.

428. MARKELOV, DENIS. Dynamical and structural properties of dendrimer macromolecules. 2011. Diss.

429. HÄMÄLÄINEN, SANNA. The effect of institutional settings on accounting conservatism – empirical evidence from the Nordic countries and the transitional economies of Europe. 2011. Diss.

430. ALAOUTINEN, SATU. Enabling constructive alignment in programming instruction. 2011. Diss.

431. ÅMAN, RAFAEL. Methods and models for accelerating dynamic simulation of fluid power circuits. 2011. Diss.

432. IMMONEN, MIKA. Public-private partnerships: managing organizational change for acquiring value creative capabilities. 2011. Diss.

433. EDELMANN, JAN. Experiences in using a structured method in finding and defining new innovations: the strategic options approach. 2011. Diss.

434. KAH, PAUL. Usability of laser - arc hybrid welding processes in industrial applications. 2011. Diss.

435. OLANDER, HEIDI. Formal and informal mechanisms for knowledge protection and sharing. 2011. Diss.

436. MINAV, TATIANA. Electric drive based control and electric energy regeneration in a hydraulic system. 2011. Diss.

437. REPO, EVELIINA. EDTA- and DTPA-functionalized silica gel and chitosan adsorbents for the removal of heavy metals from aqueous solutions. 2011. Diss.

438. PODMETINA, DARIA. Innovation and internationalization in Russian companies: challenges and opportunities of open innovation and cooperation. 2011. Diss.

439. SAVITSKAYA, IRINA. Environmental influences on the adoption of open innovation: analysis of structural, institutional and cultural impacts. 2011. Diss.

440. BALANDIN, SERGEY, KOUCHERYAVY, YEVGENI, JÄPPINEN, PEKKA, eds. Selected Papers from FRUCT 8 .2011.

441. LAHTI, MATTI. Atomic level phenomena on transition metal surfaces. 2011. Diss.

442. PAKARINEN, JOUNI. Recovery and refining of manganese as by-product from hydrometallurgical processes. 2011. Diss.

443. KASURINEN, JUSSI. Software test process development. 2011. Diss.

444. PEKKANEN, PETRA. Delay reduction in courts of justice – possibilities and challenges of process improvement in professional public organizations. 2011. Diss.

445. VANHALA, MIKA. Impersonal trust within the organization: what, how, and why? 2011. Diss.

446. HYNYNEN, KATJA. Broadband excitation in the system identification of active magnetic bearing rotor systems. 2011. Diss.

447. SOLONEN, ANTTI. Bayesian methods for estimation, optimization and experimental design. 2011. Diss.

448. JABLONSKA, MATYLDA. From fluid dynamics to human psychology. What drives financial markets towards extreme events. 2011. Diss.